The University Of Sheffield.

Novel materials and routes for rare-earth-free $BaTiO_3$-based ceramics for MLCC applications.

By:

Philip Foeller

Thesis Supervisors:

Prof. Derek C. Sinclair and Prof. Ian M. Reaney

A thesis submitted in partial fulfilment of the requirements for the degree

of

Doctor of Philosophy

The University of Sheffield

Faculty of Engineering

Department of Materials Science and Engineering

September 2017

Table of Contents

Abstract

The $NaNbO_3$-$BaTiO_3$ (NNBT) solid solution was studied as a novel RE-free material for MLCC applications. Relaxor behaviour was found for $NaNbO_3$ (NN)-concentrations as low as 2 mol%. The solid solution changes its behaviour with increasing NN-concentration from ferroelectric, to mixed ferroelectric-relaxor, to relaxor, to mixed behaviour again and finally ferroelectric. Broad permittivity profiles could therefore be obtained for a number of compositions with a wide range of T_{max}, $Na_{0.9}Ba_{0.1}Nb_{0.9}Ti_{0.1}O_3$ (90NNBT) possessed an industry standard (X7R) of TCC = ±15 % from -55 to 125 °C with low dielectric loss and a RT permittivity of ~ 800.

Bilayers were then used to imitate CS microstructures and improve TCC. Optimisation of 'core'-like material, i.e. BT, and a 'shell'-like material, i.e. 2.5NNBT, in a bilayer at a volume ratio of 0.67 2.5NNBT with 0.33 BT resulted in a TCC of ±6% over the temperature range of 25 to 125 °C whilst maintaining a RT permittivity ~3000 and low dielectric loss. Utilising simulations of bilayer permittivity profiles reduced the number of trial and error compositions required to achieve permittivity and TCC targets. One limitation, however, was the interfaces that form, as they add an additional unaccounted component to the series model used. Their impact was reduced through careful processing.

BT-2.5NNBT-90NNBT trilayers resulted in extended temperature range for low TCC applications, pushing the upper temperature up to over 150 °C. 0.33(BT)-0.33(2.5NNBT)-0.33(90NNBT) maintains a TCC of ±15 % to over 150 °C, with RT permittivity values above 100 and low dielectric loss. Adapted ternary phase diagrams were used to identify compositions that led to lower TCCs.

Several important observations were drawn from the bi- and trilayer systems which suggested that that low TCC capacitors may be developed for any temperature range by the following protocols: (i) choose a temperature range, i.e. 100-200 °C; (ii) choose a material that possesses a T_{max} of around 100 °C; (iii) choose a material with T_{max} a little above 200 °C and (iv) choose a third material that possesses a T_{max} that sits in the middle of the previous two materials, or has a broad shoulder that spans the gap between the other two T_{max}s. The number of materials are varied depending on the required temperature range. In general, the lowest number of materials that gives the required TCC should be chosen. This concept was tested for the creation of a temperature stable plateau

between 100 and 200 °C by a BT-85NNBT-90NNBT trilayer. The permittivity-temperature profile shows a plateau between ~100 and ~200 °C with permittivity changes of ~ ±10 % in that temperature range.

Industrial MLCC prototypes based on the hypotheses from this work were made by AVX Ltd in Coleraine. The devices possessed comparable TCC and better lifetimes compared with equivalent commercial products.

Acknowledgments

I would like to express my sincere gratitude to my supervisors Prof. Ian M. Reaney and Prof. Derek C. Sinclair for their supervision and support throughout my PhD research. I benefitted greatly from their insights, experience and scientific thinking. I am also grateful for their financial support, which gave me the opportunities to attend conferences during my time as a PhD student.

I would like to give special thanks to Dr. Julian S. Dean for his support and encouragement. I would like to thank him in particular for his patience when explaining to me and showing me how to undertake FEM modelling to support my work.

My thanks also go to Dr. Rebecca Boston, Dr. Whitney Schmidt, Dr. Fan Yang and Dr. Dawei Wang for their support and guidance and countless discussion related to our work, which gave me great inside and a significant boost to my scientific knowledge. I would also like to thank Dr. Fan yang for supplying me with data for undoped $NaNbO_3$. I would like to thank Mr. George Kerridge for supplying me with the ternary phase diagrams for BT-2.5NNBT-90NNBT trilayers.

I would also like to thank all other members of the Sheffield Functional Materials Group for their support and friendship, which helped particularly in times were the work did not go as planned.

Finally I would like to thank my girlfriend and my family, as they have always supported me when I needed them.

List of publications to date:

- **P. Y. Foeller**, J. S. Dean, I. M. Reaney, and D. C. Sinclair, *Design of a bilayer ceramic capacitor with low temperature coefficient of capacitance*, Appl. Phys. Lett., 2016, **109**, 082904.

- J. S. Dean, **P. Y. Foeller**, I. M. Reaney and D. C. Sinclair, *A resource efficient design strategy to optimise the temperature coefficient of capacitance of BaTiO3-based ceramics using finite element modelling*, J. Mater. Chem. A, 2016, **4**, 6896-6901.

- F. H. Morshead, **P. Y. Foeller**, C. L. Freeman, H. Zhang, I. M. Reaney, D. C. Sinclair and J. S. Dean, *How to extract reliable core-volume fractions from core-shell polycrystalline microstructures using cross sectional TEM micrographs*, Journal of the European Ceramic Society, 2017, **37**, 2795–2801.

- R. Boston, **P. Y. Foeller**, D. C. Sinclair, and I. M. Reaney, *Synthesis of Barium Titanate Using Deep Eutectic Solvents*, Inorg. Chem., 2016, **56**, 542–547.

Chapter 1: Introduction

1.1 Rare-earth-doped $BaTiO_3$-based MLCCs

Multilayer ceramic capacitors (MLCCs) are an important component in the market of modern electronics, such as computing, automotive and aerospace. Increasing demands in that market has led to the need for development of high performance MLCCs, with production projected to reach 3 trillion units per annum in 2020.[1] An MLCC consists of stacked layers of dielectric materials that are separated by internal metal electrodes, figure 1.1.

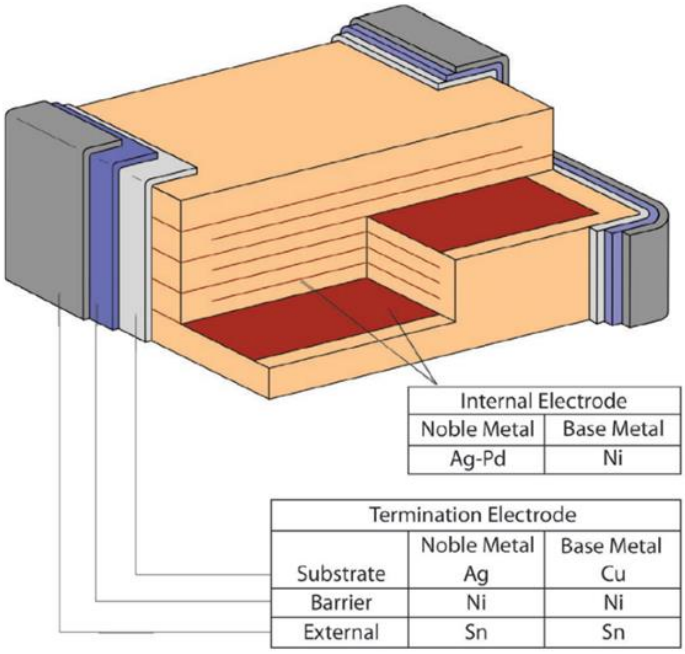

Figure 1.1. Schematic of a MLCC.[2] ©2011 IEEE.

The majority of commercial MLCCs are based on $BaTiO_3$ (BT) due to its excellent dielectric properties, i.e. high permittivity and low dielectric loss. Ferroelectric BT possesses a room temperature (RT) permittivity of ~1500 and a sharp permittivity maximum of ~10,000 at its Curie temperature (T_C) of ~120 °C. The downside is BT's poor Temperature Coefficient of Capacitance (TCC). To fit the capacitance requirements across common operational temperatures (i.e. TCC = ±15% between -55 to +125 °C for a XR7 capacitor, figure 1.2) dopants and additives are used.[3] TCC is calculated by the following equation:

$$TCC = \frac{\Delta\varepsilon}{\varepsilon_{25}\Delta T}, \qquad (1.1)$$

where $\Delta\varepsilon/\Delta T$ is the difference in permittivity at any temperature and the permittivity at RT and ε_{25} is the permittivity at RT.

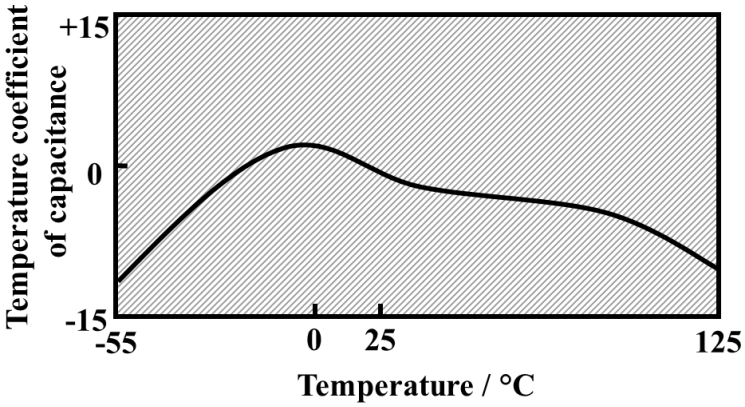

Figure 1.2. Representative TCC profile for an X7R capacitor.

The most commonly used dopant group are rare-earths (RE),[4] which under the right processing conditions form 'core-shell'-type (CS) microstructures, Fig. 1.3. Intermediate sized RE's and in particular Dy are the commonest dopants, as they can substitute on both the A- and B-sites of BT.[5] Limiting dopant diffusion in the processing leads to a core of undoped BT surrounded by a shell of doped BT with a distribution of dopant(s) concentrations. This leads to suppression of BTs T_C to lower temperatures and broadens the permittivity profile sufficient to fit commercial requirements.[6] Previous work by Jeon *et al.* has shown that the volume fractions of core- and shell-material play a crucial role in determining the degree of permittivity peak broadening to control TCC.[7]

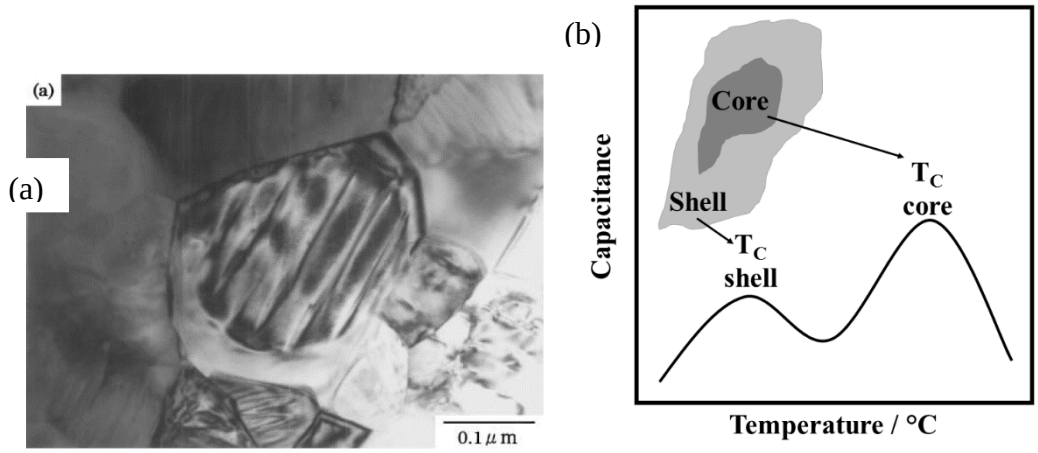

Figure 1.3. (a) TEM micrograph showing a core-shell microstructure (Copyright 2003 The Japan Society of Applied Physics.)[8] and (b) a schematic of a permittivity profile being broadened due to a CS microstructure.

Increasing demand for MLCCs can therefore be linked to increased demand for RE's and puts pressure on the supply, particularly as the demand for RE's is not limited to this field. Figure 1.4 shows a prediction that indicates a significant demand-and-supply gap by 2020 at the latest. With the looming possibility that not enough RE's will be available to meet the demand it is prudent to look for alternatives. Secondly, whilst a CS microstructure does help in modifying TCC appropriately, it requires a long and iterative process to optimise, particularly for previously unused dopant(s).

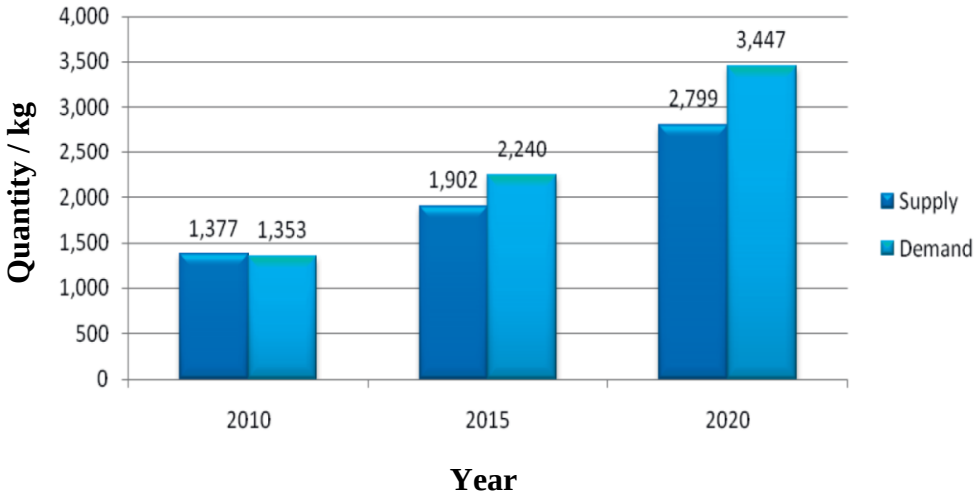

Figure 1.4. Forecasting worldwide supply-and-demand of Dy_2O_3.[9]

1.2 Aims and Objectives

The work carried out in this thesis is focused on how to improve the TCC of BT-based systems without the use of RE's, ideally without the need for a CS microstructure and to further the understanding of RE-free BT-based materials for MLCC applications. An alternative to a CS microstructure is to use layers of different materials to obtain a similar TCC profile, as explained in more detail below.

The material system chosen here as a RE-free alternative is the $xNaNbO_3$-$(1-x)BaTiO_3$ (NNBT) solid solution. NN is an antiferroelectric material with an orthorhombic unit cell and a RT permittivity of ~300 that increases to ~1500 at its Curie temperature (T_C) at ~365 °C.[10,11] The reasons for choosing this system are: (i) NNBT forms a complete solid solution, allowing for a large range of materials to be selected, with the two end members possessing a high T_C (i.e. NN) and large ε_r (i.e. BT) at room temperature. (ii) NN acts as

a donor-acceptor dopant system in BT, therefore imitating the intermediate RE^{3+} dopants commonly used. The idea is that the self-compensation mechanism of this kind of doping reduces the number of oxygen vacancies, which is believed to improve the lifetime of MLCCs. (iii) NNBT is known to exhibit relaxor behaviour with NN concentrations below 5 mol%. This is beneficial as it helps to broaden the permittivity profile of the material and brings it closer to the TCC requirements for commercial use. (iv) The dopants are cheaper than RE-dopants, particularly Na^{+}. This is important, as commercial use requires a saving on costs to entice a company to consider exchanging previously used and well-known materials. Improved knowledge of the NNBT-solid solution series can be seen as a good start to find a RE-free BT-based material for MLCC applications and will be useful to provide a model component for the bilayered structures.

Bilayered structures offer an alternative to CS structures for reducing the TCC of a system to better fit commercial applications. The reasons why they are investigated are: (i) they combine two materials, whose permittivity profiles can be chosen to be 'core'- and 'shell'-like, hence combining the essential parts of a CS system; (ii) unlike a CS system, high control of the volume ratios of components is easily achieved making the processing conditions more reliable; (iii) once the components are decided upon, simple modelling of their permittivity profiles can give an indication of which ratios to choose to optimise TCC; and (iv) materials that were previously unsuitable for MLCC applications can be used, as the components themselves don't have to individually fit the required TCC profile. This can open up a whole group of potential RE-free materials, as a CS microstructure to reduce TCC is no longer necessary. The only limitation is that the shrinkage rates of the materials need to be comparable to be suitable for co-sintering. It is therefore interesting to investigate the use of layered structures to obtain lower TCCs.

The structure of the thesis is as follows. Chapter 2 reviews the fundamentals of undoped and doped BT and a general review of MLCCs. This provides a basic level of understanding of this research field and the associated technology as well as how to develop potential RE-free BT-based MLCC materials. Chapter 3 describes the experimental procedures used within the thesis.

In Chapter 4 the solid solution series of NNBT is investigated, particularly compositions close to the end members. These materials provide the input for the RE-free 'shell'-like material for the layered structures to be considered later in the thesis. Chapter

5 investigates another material from the NNBT-SS series, 90NNBT, which has the potential to be useful for X7R MLCC applications. The focus is on its dielectric properties and its suitability for MLCC processing. The concept of layered structures is proven in Chapter 6 using a 2.5NNBT-BT bilayered system. This is the simplest layered system to model and process and is therefore viewed as the best starting point when looking into layered systems. A number of characteristics regarding layered systems are discussed in Chapter 7, such as how the choice of materials and number of layers influence TCC. It also highlights that improvements to TCC are not just limited to the bilayer system discussed in the previous chapter. This discussion extends to trilayered systems in Chapter 8 and the use of modelled ternary phase diagrams of permittivity-temperature profiles to find the lowest possible TCCs from the three end members. Results from bilayer-prototypes made by AVX Ltd. are discussed in Chapter 9.

In Chapter 10 the main results and conclusions are summarised, along with an outlook for further research.

1.3 References

1 S. Hoenderdaal, L. T. Espinoza, F. Marscheider-Weidemann and W. Graus, *Energy*, 2013, **49**, 344-355.

2 M.-J. Pan and C. A. Randall, *IEEE Electr. Insul. Mag.*, 2010, **26**, 44–50.

3 Murata - Chip Monolithic Ceramic Capacitors, http://www.murata.com/~/media /webrenewal/support/library/catalog/products/capacitor/mlcc/c02e.ashx?la=en-us. (accessed 16.01.2017).

4 K.-J. Park, C.-H. Kim, Y.-J. Yoon, S.-M. Song, Y.-T. Kim and K.-H. Hur, *J. Eur. Ceram. Soc.*, 2009, **29**, 1735–1741.

5 D. Makovec, Z. Samardzija and M. Drofenik, *J. Am. Ceram. Soc.*, 2004, **87**, 1324-1329.

6 S.-C. Jeon, C.-S. Lee and S.-J. L. Kang, J *J. Am. Ceram. Soc.*, 2012, **95**, 2435-2438.

7 S.-C. Jeon, B.-K. Yoon, K.-H. Kim and S.-J. Kang, *J. Adv. Ceram.*, 2014, **3**, 76-82.

8 H. Kishi, Y. Mizuno and H. Chazono, *Jpn. J. Appl. Phys.*, 2003, **42**, 1–15.

9 R. L. Moss, E. Tzimas, H. Kara, P. Willis and J. Kooroshy, Critical Metals in Strategic Energy Technologies, European Union, Luxembourg, 2011.

10 D.-K. Kwon, Y. Goh, D. Son, B.-H. Kim, H. Bae, S. Perini and M. Lanagan, *J. Elec. Mat.*, 2016, **45**, 631-638.

11 R. Aoyagi, S. Bannno and M. Maeda, *2014 Joint IEEE International Symposium on the Applications of Ferroelectric, International Workshop on Acoustic Transduction Materials and Devices & Workshop on Piezoresponse Force Microscopy*, 2014, 1-4.

Chapter 2: Literature Review

2.1. ABO_3 Perovskites

2.1.1 The ABO_3 Perovskite Structure

The origin of the term Perovskite dates back to 1839, when mineralogist working for L. A. Perovsky discovered $CaTiO_3$.[1] From then onwards materials that are isostructural to $CaTiO_3$ are referred to as perovskites,[1] with the general formula ABX_3.

A is representative for a large cation, B for a mid-sized cation and X an anion. The ideal perovskite structure has a cubic unit cell. The cations occupying the A site are surrounded by twelve X anions in a cubo-octahedral coordination and the cations occupying the B site are surrounded by six anions in an octahedral coordination. In turn the X anions are coordinated by two B- and four A- site cations.[2]

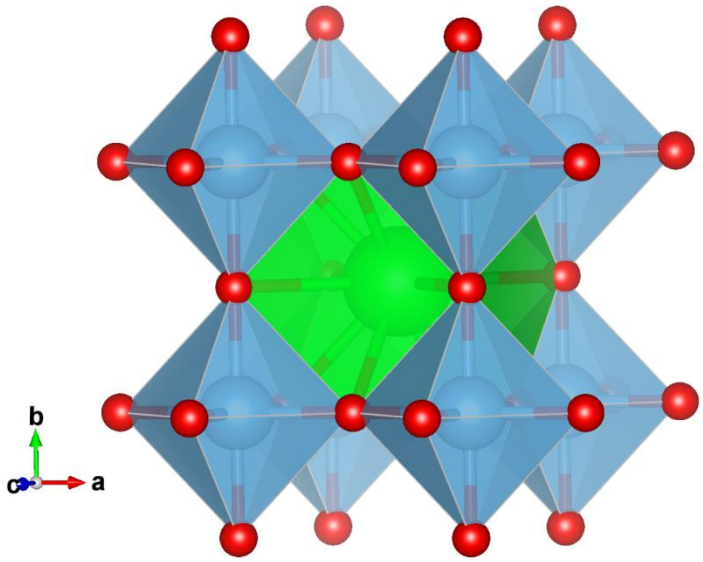

Figure 2.1. Octahedral three-dimensional framework of ABX_3 perovskites. A sits at the centre of eight octahedra, whilst B sits at the centre of each octahedron and X on the vertices of each octahedron, created with Vesta.[3]

Another way of representing the ideal cubic perovskite structure is a framework structure with corner-sharing BX_6 octahedra with A being set into the twelve-coordinate centre.[4] It is noteworthy that each X in the structure is shared by two BX_6 octahedra, leading to a linear B – X – B arrangement. The octahedra link at all their corners to form a three-dimensional framework, as shown in Figure 2.1.

2.1.2 Types of ABO_3 Perovskites

The most common anion in the X site of an ABX_3 perovskite is oxygen. There are compounds that contain other anions, such as halogens. An example for these are fluoride perovskites.[5] Due to the nature of this project, the focus of this review is limited to oxide perovskites of general form ABO_3.

For oxide perovskites the combined oxidation state of the contained cations is 6 and can be achieved *via* the following combinations: $A^{1+}B^{5+}O_3$, $A^{2+}B^{4+}O_3$ and $A^{3+}B^{3+}O_3$.[4] Common examples for compounds of the $A^{1+}B^{5+}O_3$ type are $KTaO_3$, $NaTaO_3$, $KNbO_3$ and $NaNbO_3$. Compounds of type $A^{2+}B^{4+}O_3$ have a larger variety of examples, as A^{2+} can be alkaline earth ions, Cd^{2+} or Pb^{2+} and B^{4+} can be for example Ce^{4+}, Fe^{4+}, Sn^{4+} or Ti^{4+}. Considering compounds of the $A^{3+}B^{3+}O_3$ type, examples for A^{3+} are rare earth cations and Bi^{3+} and examples for B^{3+} are Cr^{3+}, Al^{3+} and Fe^{3+}.

2.1.3 Tolerance Factor, Distorted and Complex ABO_3 Perovskites

According to Goldschmidt the ideal cubic perovskite structure requires the A-cation to be of a size that fits exactly into the 12-coordinate site.[6] That means the face-diagonal of the unit cell is given by $2(r_A + r_O)$, where r_A and r_O are the ionic radii of the A and O ions, respectively. This results in a unit cell edge that is equal to $\sqrt{2}(r_A + r_O)$. However, the unit cell edge is also given by $2(r_B + r_O)$, where r_B is the ionic radius of B. From this it can be concluded that the ideal relationship of ionic radii in an ideal cubic perovskite is given by

$$(r_A + r_O) = \sqrt{2}(r_B + r_O) \qquad (2.1)$$

To represent the degree of variation that is allowed by perovskite structures, equation 1 can be rearranged to give the Goldschmidt tolerance factor, t.

$$t = \frac{r_A + r_O}{\sqrt{2}(r_B + r_O)} \qquad (2.2)$$

The flexibility over bond lengths in perovskites means that perovskites are formed when t is between $0.8 < t < 1.06$.[7] If an A-cation is too large for the dodecahedral site, $t > 1$ and the BO_6 octahedra are distorted. If the A-cation is too small, $t < 1$ and tilting of the BO_6 octahedra occurs, compensating for the increased A-O distance.[7–9]

Another range of perovskites are complex perovskites, where the structure contains more than one "perovskite unit". This arises when there is more than one type of cation present in a given crystallographic site, *i.e.* more than one cation present in the A site, (AA')BO_3, the B site, A(BB')O_3, or both, (AA')(BB')O_3.[4,10,11] If a complex perovskite possesses a structure that involves the sharing of A- and/or B-sites by two or more cations of complementary valency, it is possible that cation ordering occurs.[4,12] This is due to factors such as the difference in size of B-site ions,[13] the difference in charge of B-site ions[11] and thermal annealing.[14] There are many examples for the different types of ordering in the literature.[10,15,16]

2.2. Ferroelectrics

Ferroelectrics are materials that possess spontaneous polarisation, which can be switched by applied electric fields.[12,17–20] The Curie temperature (T_C) is the phase transition between a polar ferroelectric phase and a non-polar paraelectric phase, *e.g.* a tetragonal to cubic transition in perovskites. In its paraelectric state a ferroelectric obeys the Curie-Weiss (CW) law:

$$\varepsilon_r - 1 = \frac{C}{T - T_0}, \qquad (2.3)$$

where ε_r is the relative permittivity, C is the Curie constant and T_0 is the Curie-Weiss temperature. Since the relative permittivity of a ferroelectric is significantly larger than 1, the following assumption is usually made:

$$\varepsilon_r - 1 \approx \varepsilon_r. \qquad (2.4)$$

The CW for a ferroelectric can therefore be plotted as $1/\varepsilon_r$ vs. T and T_0 can be obtained via extrapolation as seen in figure 2.2. For a 1st order transition $T_0 < T_C$ due to the sudden change in the order parameter at T_C.[17,20] For a second order transition, $T_0 = T_C$.

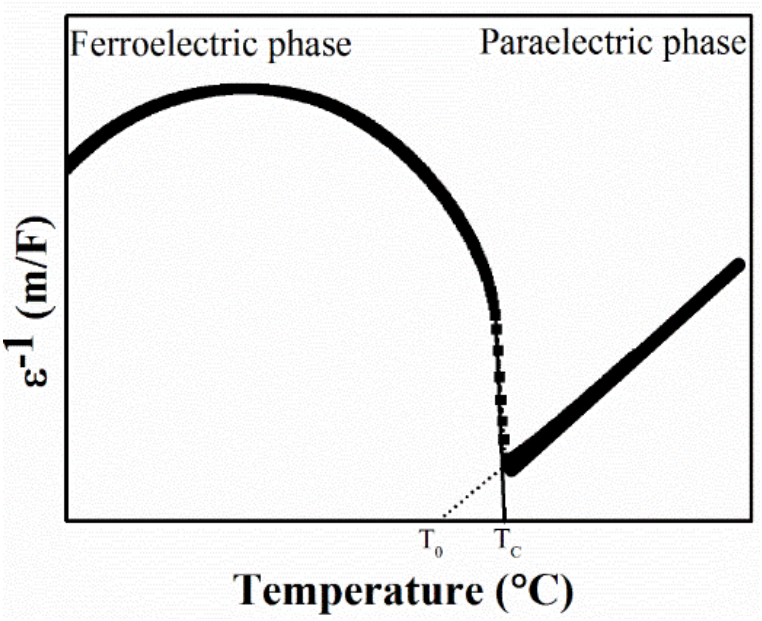

Figure 2.2. Schematic of a CW plot, $1/\varepsilon_r$ vs. T.

2.2.1 Relaxor ferroelectrics

Some perovskites do not show sharp but instead diffuse phase transitions (DPT) are observed. They are classed as relaxor ferroelectrics or relaxors.[21,22] Common features in relaxors are compositional disorder and high dielectric properties around their DPT. This and the improved temperature dependence caused by the DPT make relaxors attractive for capacitor applications.

Figure 2.3 illustrates some relaxor characteristic temperatures. Similar to normal ferroelectrics, the CW law is obeyed in the high temperature paraelectric phase. At the Burns temperature (T_B) relaxors enter an ergodic (ER) phase. This does not involve a structural change, however the dielectric properties change. This has been attributed to the development of polar nano-regions (PNRs). These regions show dynamic behaviour, which is slowed down with decreasing temperature.

At low enough temperatures, non-canonical relaxors will form ferroelectric phases from the ER phase. This happens at T_C, as in normal ferroelectrics. In canonical relaxors, the material enters the non-ergodic (NER) phase at temperatures below the freezing temperature (T_f). In this state the PNRs are frozen in random orientations but an applied high electric field can transform the non-polar state into a FE state.[23]

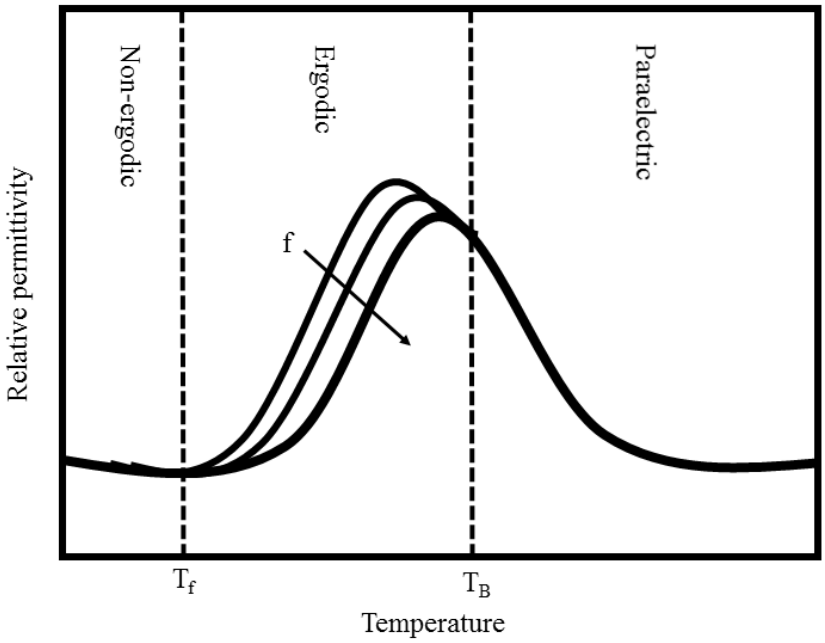

Figure 2.3. Schematic of permittivity versus temperature response for a relaxor.

There have been several explanations for the origins of PNRs,[23–29] but they are out of the scope for this work. However, two approaches sum up most models. They either consider PNRs to be (a) frustrations that are in a cubic matrix, or (b) nano-domains separated by a domain wall, as shown in figure 2.4.[23]

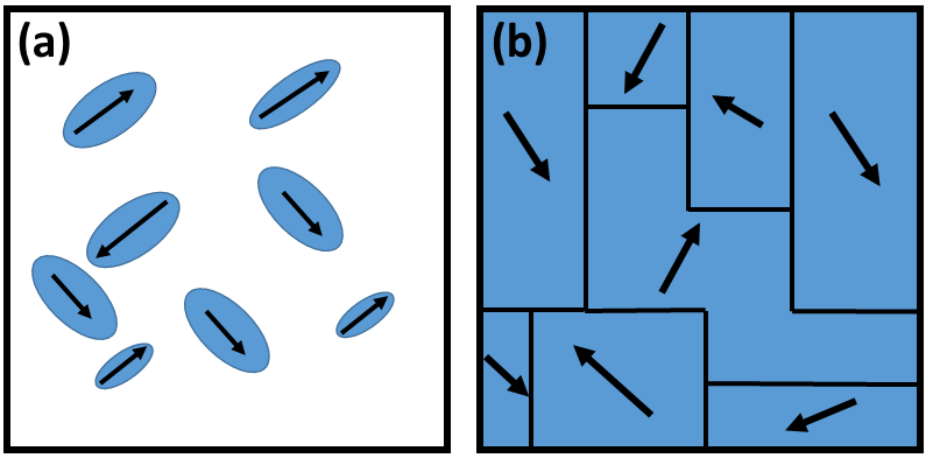

Figure 2.4. Schematic representation of PNRs in relaxors.

2.3. $BaTiO_3$ – Barium Titanate crystal structure, electrical properties and characteristic behaviour

2.3.1. The $BaTiO_3$ Structure

The crystal structure of perovskite $BaTiO_3$ is cubic above the material's Curie temperature, T_C (about 130 °C).[30,31] In cubic $BaTiO_3$, the Ba^{2+} ions are at the centre of the cubic unit cell, the Ti^{4+} ions at its corners and the O^{2-} ions on the centre of the cells edges, Figure 2.1.

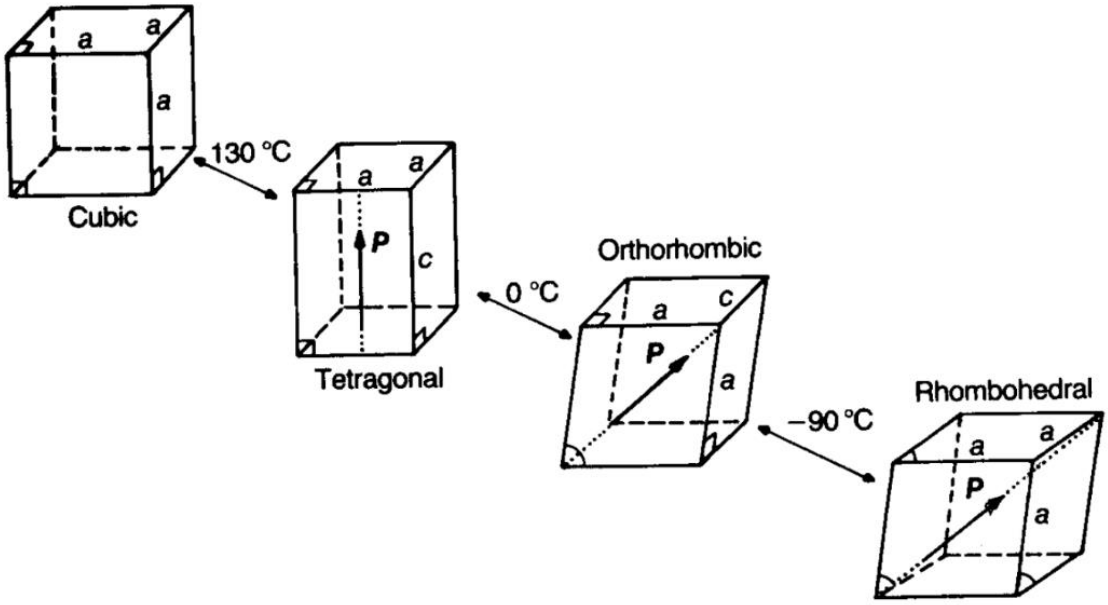

Figure 2.5. Distortions of the cubic unit cell of $BaTiO_3$ with decreasing temperature (Copyright © 2003 John Wiley & Sons Ltd., reprinted with permission from publisher).[30]

This cubic structure of $BaTiO_3$ distorts to a tetragonal structure at temperatures between T_c and 0 °C, resulting in a dipole moment along the c-direction, Figure 2.5. Between 0 and –80 °C $BaTiO_3$ will adopt an orthorhombic structure with a dipole moment along its diagonal face. Finally, there is a rhombohedral phase which forms below –80 °C.[12,30] with a dipole moment along the body diagonal.

2.3.2. Ferroelectricity in $BaTiO_3$

Cubic $BaTiO_3$ is paraelectric and there is no net dipole moment present. This is due to the centrosymmetric position of Ti^{4+} ions in the TiO_6 octahedra resulting in no net charge displacements within any of the octahedra.[30] Below T_C there is a phase transition from cubic to tetragonal $BaTiO_3$ resulting in the occurrence of a net dipole moment in the crystal structure, making $BaTiO_3$ ferroelectric.[32] This is due to the TiO_6 octahedra losing their centre of symmetry because the Ti^{4+} ions are displaced from their centrosymmetric position towards one of the six apical oxygens.[12,30] This leads to spontaneous polarisation in tetragonal $BaTiO_3$ and parallel displacement in adjacent $BaTiO_3$ unit cells results in ferroelectric domains of polarisation in the material.

2.3.3 Ferroelectric domains in $BaTiO_3$.

The alignment of adjacent dipoles leads to net polarisation as discussed previously. Ferroelectric domains are regions of aligned dipoles, as shown in Figure 2.6. The domains are separated by domain walls and differ in the direction of their net polarisation. They are formed because they result in an electrically neutral body, minimising the electrostatic energy.[30,33,34]

At T_C, $BaTiO_3$ undergoes both spontaneous polarisation and strain. This manifests as a distortion in the crystal structure from a higher to a lower symmetry crystal class, *i.e.* cubic to tetragonal. Ferroelectric domains therefore not only serve to minimise macroscopic polarisation but also to minimise the stress that is occurring due to the distortion. In an applied electric field the electric dipoles will align and are coupled to the deformation on a unit cell level. This gives rise to the piezoelectric response in ferroelectric ABO_3 perovskites.[30]

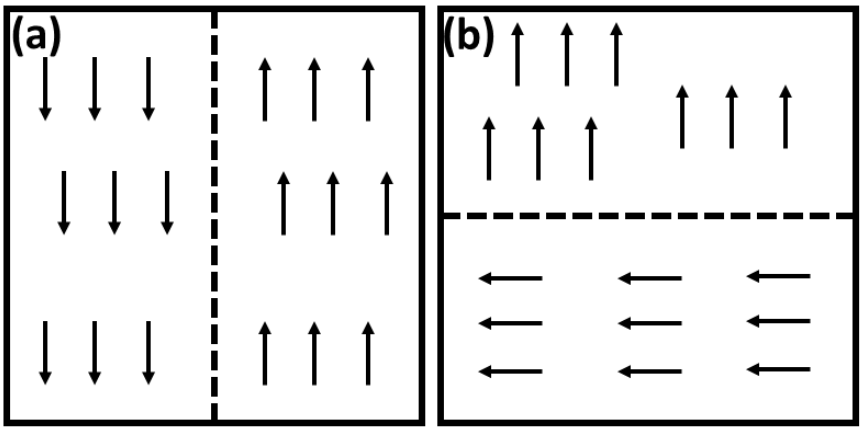

Figure 2.6. Schematic of 180 and 90º ferroelectric domains in $BaTiO_3$.

2.3.4 Hysteresis loops in $BaTiO_3$

The phase transition from the non-polar paraelectric cubic phase to the polar ferroelectric tetragonal phase allows for the polarisation in ferroelectric $BaTiO_3$ to be reversible. To observe this it is possible to plot the macroscopic polarisation against the applied electric field, resulting in a hysteresis loop, when plotting polarisation (P) versus applied electric field (E), Figure 2.7.[30,35] Increasing E leads to a common alignment (or at least a component of alignment) of the domains in the ceramic with the direction of E. This results in a dramatic increase in P, Figure 2.7. Removal of the applied E does not lead to an instant decrease in P due to remnant polarisation.[36] This effect is due to some domains within the crystal retaining their P (or at least a component of it) with the direction of the poling field, due to an energy barrier to return to its un-poled state. Application of a reversed E results in a reversal of P and gives rise to the P-E hysteresis loop.

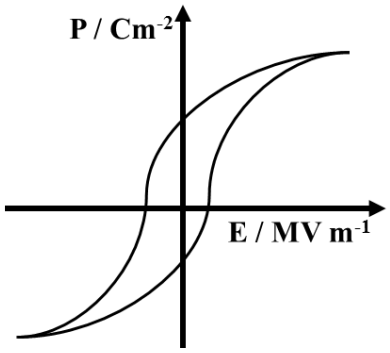

Figure 2.7. Schematic of a hysteresis loop observed in $BaTiO_3$ ceramics, when plotting the polarisation, P vs. the applied field, E.

2.3.5 Permittivity properties of $BaTiO_3$

One of the most useful properties of ferroelectric $BaTiO_3$ is its very high permittivity, even at room temperature. The change in relative permittivity of $BaTiO_3$ with temperature is shown in Figure 2.8. It is possible to observe sudden increases in permittivity with maxima at temperatures that correspond to the various phase transitions of $BaTiO_3$.[30,36] The largest of these maxima corresponds to T_C. It is also possible to see evidence of anisotropic behaviour, as the permittivity of $BaTiO_3$ measured along its c-axis is lower than that measured along its a-axis, Figure 2.8.[30]

Polycrystalline $BaTiO_3$ ceramics behave differently, as grain boundaries and stress play a role and it is more difficult to align the random crystallographic axes into domains.

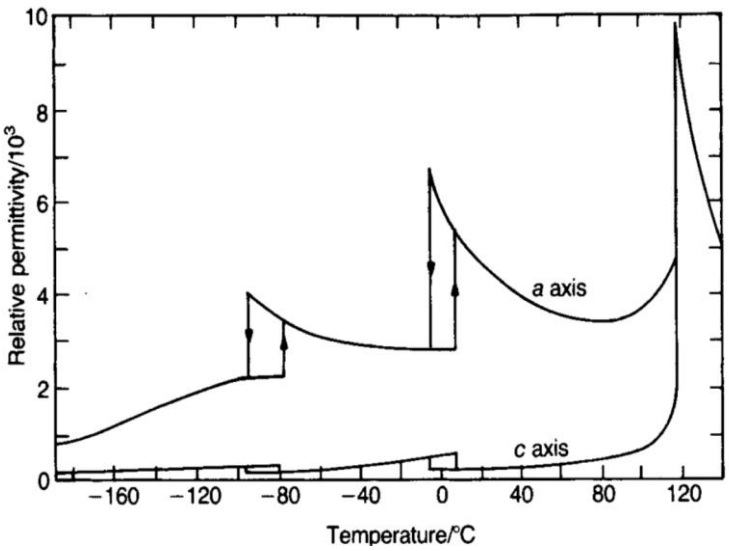

Figure 2.8. Relative permittivity along different axis versus temperature for $BaTiO_3$ (Copyright © 2003 John Wiley & Sons Ltd., reprinted with permission from publisher).[30]

2.3.6 Properties affecting the permittivity and T_C

There are many factors that affect T_C and permittivity of $BaTiO_3$, especially since undoped $BaTiO_3$ will always contain some accidental impurities, which influence both permittivity and T_C. This will be discussed further in section 2.4, where doped $BaTiO_3$ is

reviewed. This section concentrates on the influence of grain size and Ba / Ti ratio on the permittivity and T_C of undoped $BaTiO_3$.

2.3.6.1 The effect of grain size on T_C and permittivity

As mentioned previously, the grain size of $BaTiO_3$ affects both its permittivity and phase transition temperatures. Decreasing the grain size from ca. ~ 50 to 1 µm will result in an increase in permittivity of the ferroelectric state for $BaTiO_3$, whereas there is no correlation in its paraelectric state.[30,37–42] Figure 2.9 illustrates the relationship in a ferroelectric $BaTiO_3$ ceramic, which was first observed by Kneikamp *et al.* and is considered to be due to increasing internal stress in the grains.[37–40,43,44]

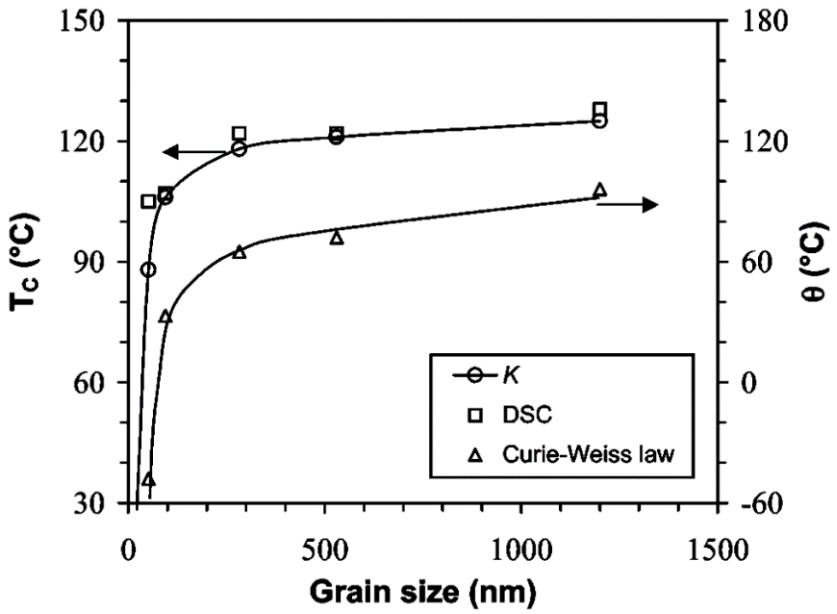

Figure 2.9. Relationship between decreasing grain size and increasing permittivity in $BaTiO_3$ ceramics for grains larger than 1 µm. Reprinted figure with permission from Zhao et al.[39] Copyright (2004) The American Physical Society.

For grains decreasing in size below 1 µm it is possible to observe a decrease in permittivity, Figure 2.10. This was initially attributed to the disappearance of ferroelectricity below a critical limit of ca. ~ 0.20 µm.[39] A better explanation has been provided by Hoshina *et al.* who established a core-shell model,[45] where a ceramic grain is made up of a tetragonal core surrounded by a cubic shell.

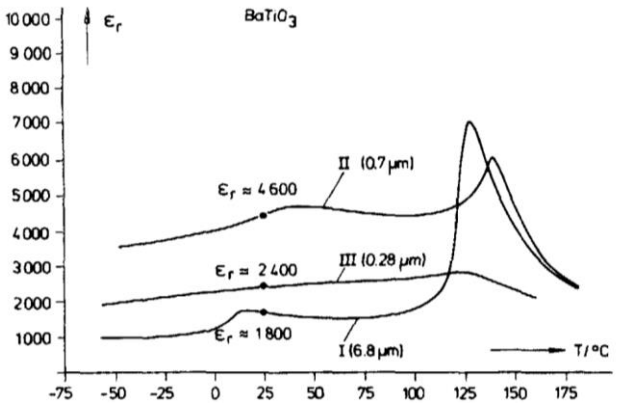

Figure 2.10. Relationship between decreasing grain size and decreasing permittivity in $BaTiO_3$ ceramics for grains smaller than 1 µm. Reprinted from Arlt *et al.*,[46] with the permission of AIP Publishing.

2.3.6.2 The effect of the Ba/Ti ratio on permittivity and T_C

It has been reported that $BaTiO_3$ is capable of accommodating small excess amounts BaO and TiO_2.[47,48,49] Smyth et al. have reported the solid solubility limit in both cases lies around the 100 ppm mark.[48,49] The excess of either component leads to a decrease in T_C.[47,50]

2.4. Doped $BaTiO_3$

There are two types of $BaTiO_3$ doping that are considered, isovalent and aliovalent doping of the Ba^{2+} and Ti^{4+} sites. Isovalent doping refers to ions used for doping that are of the same charge as the parent ion on that site.[7] If the dopant is of a different charge to that of the ion on the parent site it is referred to as aliovalent doping.[7] The ions used for doping are not only chosen for their ionic charge but also their ionic radii. This is because the $BaTiO_3$ structure can accommodate ionic dopants of specific sizes, as was mentioned previously in accordance with the tolerance factor. In general, the Ba-site can accommodate ions ranging from ca. ~ 130 to 160 pm in size and the Ti-site allows for dopants to range from ca ~ 60 to 75 pm.[30]

To gain a better understanding of doped BT it is important to know the defects and doping mechanisms. Section 2.4.1 contains a summary of defects in BT and possible doping mechanisms. This can be referred to when discussing different dopants.

2.4.1 Defect chemistry of $BaTiO_3$

2.4.1.1 Intrinsic defects

There are two kinds of point defects which can occur in crystals, Schottky and Frenkel defects. Intrinsic defects are present because of thermodynamic reasons and are often known as point defects. Schottky defects are vacancies in otherwise perfect crystal lattices, whereas Frenkel defects are atoms/ions which are displaced from their usual lattice site into an interstitial site. In both cases the overall charge/stoichiometry of the lattice remains unaffected.

In BT intrinsic defects are limited to Schottky defects, as the perovskite structure has no interstitial sites for ions to be displaced to. In a full Schottky defect the following vacancies occur:

$$V_{Ba} + V_{Ti} + 3V_O \qquad \text{(Equation 2.5)}$$

However, partial Schottky defects are possible, with vacancies only on the Ba- or Ti-site:

$$V_{Ba} + V_O \qquad \text{(Equation 2.6)}$$

$$V_{Ti} + 2V_O \qquad \text{(Equation 2.7)}$$

2.4.1.2 Defects due to reducing processing atmospheres

There are other defects that occur in BT, which are not intrinsic, but caused by other factors. A common one is the reduction of Ti^{4+} to Ti^{3+}. This is a common thing, particularly as many industrial processes, such as the production of MLCCs, involve sintering in a reducing H_2-containing atmosphere. The result is the loss of oxygen and the creation of Ti^{3+}. This can be a problem, as this changes BT from an insulator into a conducting material. Equations 2.8 and 2.9 show how the loss of O^{2-} ions from the lattice leads to free electrons, which in turn reduce the Ti-ions.

$$O^{2-} \rightarrow \frac{1}{2}O_{2(g)} + 2e^- \qquad \text{(Equation 2.8)}$$

$$2e^- + 2Ti^{4+} \rightarrow 2Ti^{3+} \qquad \text{(Equation 2.9)}$$

2.4.1.3 Extrinsic defects

Extrinsic defects can be unwanted, in case of impurities, or wanted, *i.e.* dopants. There are two general groups of extrinsic defects to be considered in BT, stoichiometric and non-stoichiometric. A brief summary of the doping mechanisms is given here, more detailed examples and explanations can be found in sections 2.4.2 and 2.4.3.

In general there are two classes of doping mechanisms, ionic and electronic. In the case of ionic doping mechanisms, the overall charge of the lattice is maintained by the use of ions and vacancies. Electronic mechanisms use the creation of electrons (e^-) and holes (h^+) to maintain a neutral lattice.

In stoichiometric defects, ions on the Ba- and/or the Ti-sites are replaced with ions of the same charge, examples are found below.

$$Ca^{2+} \rightarrow Ba^{2+} \quad \text{(Equation 2.10)}$$

$$Zr^{4+} \rightarrow Ti^{4+} \quad \text{(Equation 2.11)}$$

Non-stoichiometric defects are due to ions on the Ba- and/or the Ti-sites being replaced with ions of different charge present more complex defect mechanisms than the stoichiometric defects. Na^+, RE^{3+} and Nb^{5+} ions will be used as dopants to explain the defect mechanisms taking place. There are three possible doping configurations: A-, B- or AB-doping mechanisms.

For the A-site there are 3 possible ways to cope with the dopants of higher charge. Either there is the formation of an A- or B-site vacancy, which represent the ionic compensation mechanisms, or there is an electronic compensation mechanism.

$$3Ba^{2+} \rightarrow 2RE_A^{3+} + V_A \quad \text{(Equation 2.12)}$$

$$Ba^{2+} + \frac{1}{4}Ti^{4+} \rightarrow RE_A^{3+} + \frac{1}{4}V_B \quad \text{(Equation 2.13)}$$

$$Ba^{2+} \rightarrow RE_A^{3+} + e^- \quad \text{(Equation 2.14)}$$

When doping the A-site with an ion of lower charge, the mechanisms can be either of the following:

$$Ba^{2+} + \frac{1}{2}O^{2-} \rightarrow Na_A^+ + \frac{1}{2}V_O \quad \text{(Equation 2.15)}$$

$$Ba^{2+} \rightarrow Na_A^+ + h^+ \quad \text{(Equation 2.16)}$$

$$Ba^{2+} + V_A \rightarrow 2Na_A^{+}$$ (Equation 2.17)

The last mechanism would require the presence of a partial Schottky defect to begin with, otherwise there will be no A-site vacancies in the lattice.

In 2011 Freeman *et al.* proved that the use of the RE^{3+} electronic doping mechanisms, equation 2.14 is energetically unfavourable (~10 eV) compared to the ionic doping mechanisms, equations 2.12 and 2.13 (~1-3 eV).[51,52] They concluded that changes in conduction properties observed in BT when A-site RE donor doped is not due to the electron compensation scheme, as assumed previously. Instead Ti-vacancies are preferentially formed, equation 2.13 and this promotes oxygen loss at high processing temperatures this is the source of the semiconducting properties, equations 2.8 and 2.9.

Their results also confirmed that the small RE-ions, e.g. Yb prefers to substitute exclusively onto the Ti-site, whereas large RE-ions prefer the A-site, e.g. La and intermediate RE-ions, e.g. Gd follow their energetically most favourable route, the self-compensation mechanism.[51]

When doping the B-site with dopants of a higher charge, the compensation mechanisms possible are as follows:

$$5Ti^{4+} \rightarrow 4Nb_B^{5+} + V_B$$ (Equation 2.18)

$$\frac{1}{2}Ba^{2+} + Ti^{4+} \rightarrow Nb_B^{5+} + \frac{1}{2}V_A$$ (Equation 2.19)

$$Ti^{4+} \rightarrow Nb_B^{5+} + e^{-}$$ (Equation 2.20)

$$Ti^{4+} \rightarrow Nb_B^{5+} + \frac{1}{2}O^{2-}$$ (Equation 2.21)

The last mechanism would require an oxygen deficient lattice to begin with, as otherwise there is no place to go for additional oxygen ions in the perovskite structure.

Doping with an ion of lower valency on the B-site gives the following possible doping mechanisms:

$$Ti^{4+} + \frac{1}{2}O^{2-} \rightarrow RE_B^{3+} + \frac{1}{2}V_O$$ (Equation 2.22)

$$Ti^{4+} \rightarrow RE_B^{3+} + h^{+}$$ (Equation 2.23)

$$3Ti^{4+} + V_B \rightarrow 4RE_B^{3+}$$ (Equation 2.24)

The last mechanism would require the presence of a partial Schottky defect to begin with, otherwise there will be no B-site vacancies in the lattice.

Finally there is the AB-site doping or self-compensation doping mechanism. Here one site is doped with an ion of higher valency, whilst the other side is doped with an ion of lower valency. No vacancies or electronic defects are required to balance the overall charge.

$$Ba^{2+} + Ti^{4+} \rightarrow 2RE_{AB}^{3+} \quad \text{(Equation 2.25)}$$

$$Ba^{2+} + Ti^{4+} \rightarrow Na_{A}^{+} + Nb_{B}^{5+} \quad \text{(Equation 2.26)}$$

2.4.2 Isovalent doping of $BaTiO_3$

2.4.2.1 Isovalent doping of the Ba-site in $BaTiO_3$

Isovalent doping of the Ba-site has significant impact on the phase transitions of $BaTiO_3$ as it shifts T_C but without changing the shape of the permittivity curve, Figure 2.11. Isovalent doping in all cases also changes the phase transition between the tetragonal to the orthorhombic phase and the orthorhombic to the rhombohedral phase.[30] Examples of the effect of isovalent doping on the phase transition temperatures are shown in Figure 2.12.

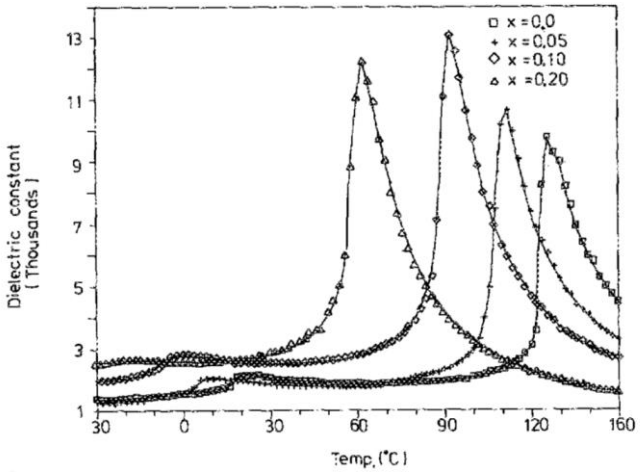

Figure 2.11. An example of permittivity data displaying the shift in T_C with the use of an isovalent dopant (Sr^{2+}) on the Ba-site. Reprinted from Lin *et al.*,[53] with the permission of AIP Publishing.

Commonly used isovalent dopants in the literature for the Ba-site are Ca^{2+}, Sr^{2+} and Pb^{2+}.[53,54,55] Ca^{2+} doping initially increases T_C by ca. 8-10 °C up to 8 mol% then decreases it by ca. 1 °C per mol%.[56] This effect has been attributed to a compromise between ionic radii mismatching and ionic polarisability[56] or the distribution of the Ca-dopant.[57] Another explanation was given by Sinclair *et al.* proposing that the ionic radii mismatch results in strain which leads to an initial increase in T_C.[58]

Increasing the concentration of Sr^{2+} on the Ba-site will lead to a decrease of T_C by ca. 4 °C per mol%.[56] This is due to the difference in ionic radii that exists between Ba^{2+} and the smaller Sr^{2+} dopant, leading to an increasing pressure effect. However, increasing the concentration of Pb^{2+} on the Ba-site leads to an increase of T_C.[30] This is surprising as Pb^{2+} is smaller than Ba^{2+}, however this effect arises due to the higher polarisability of Pb^{2+} compared to Ba^{2+} and the hindrance associated with the $6s^2$ electron lone pair on the Pb-ions.[56]

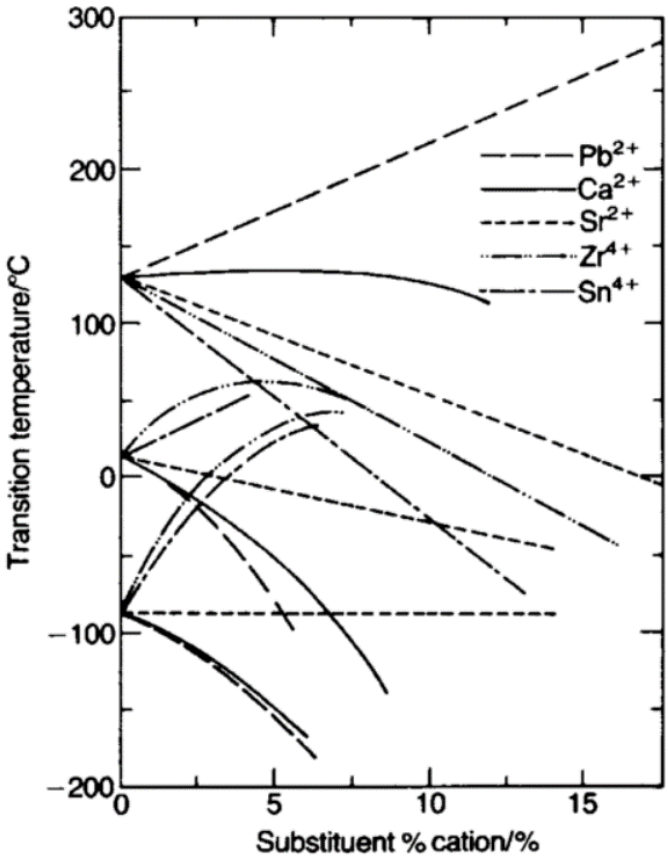

Figure 2.12. The effect of isovalent doping on the Ba- (*e.g.* Ca^{2+}, Sr^{2+} and Pb^{2+}) and Ti-site (*e.g.* Zr^{4+} and Sn^{4+}) on the phase transition temperatures in $BaTiO_3$ (Copyright © 2003 John Wiley & Sons Ltd., reprinted with permission from publisher).[30]

2.4.2.2 Isovalent doping of the Ti-site of $BaTiO_3$

Isovalent doping of the Ti-site also affects all three phase transition temperatures in $BaTiO_3$.[30] Unlike isovalent doping of the Ba-site, however, it also changes the magnitude of the permittivity and leads to diffuse phase transitions.[14,59]

Commonly used isovalent dopants in the literature for the Ti-site are Zr^{4+}, Hf^{4+} and Sn^{4+}, which possess different solid solubility limits in $BaTiO_3$, but affect T_C similarly.[54,59–61] Zr^{4+} has a solid solubility limit of 30 mol% and increasing the concentration of Zr^{4+} in the Ti-site decreases T_C by ca. 5-6 °C per mol%.[54] Similarly, Hf^{4+} decreases T_C by ca. 7-8 °C per mol%.[59] Sn^{4+} decreases T_C in a similar way to Zr^{4+} at a rate of ca. 5-6 °C per mol%.[60,61]

2.4.3 Aliovalent doping of $BaTiO_3$

2.4.3.1 Donor doping of $BaTiO_3$

If a dopant is used with a higher valency than the host ion it is called a donor dopant. In the case of $BaTiO_3$ it is possible to use donor dopants on both the Ba- and Ti-sites. Commonly used donor dopants for the Ba-site are rare earth cations, such as La^{3+},[62–67] Ce^{3+},[65,68–74] Nd^{3+},[75–78] as well as Y^{3+}.[41,79–81] Transition metal cations are commonly used as donor dopants for the Ti-site. Examples are Nb^{5+} [42,82–88] and Ta^{5+}.[82,87]

Donor dopants have a dramatic effect on $BaTiO_3$ processed in air as even small amounts of donor ions on either site are enough to change the electrical properties from insulating to semi-conducting.[67,89]

Using donor dopants also affects the dielectric properties of $BaTiO_3$. There are two main factors that play a role here, the sintering temperature and the atmosphere used during the sintering process.

Sintering donor doped $BaTiO_3$ at high temperatures in reducing atmospheres will lead to dielectrics that possess higher permittivity and dielectric loss compared to undoped $BaTiO_3$.[90,91] This is the result of oxygen being lost from the grains in the bulk material, leading to the occurrence of an additional element to the electronic microstructure at the interface between the sample and contacts or at the grain boundary, which leads to a ‘colossal dielectric constant (CDC)’. [92,93]

Sintering donor doped $BaTiO_3$ at temperatures below 1450 °C or in a flowing oxygen atmosphere will result in materials that do not show either the leaky dielectric behaviour described above or an increase in permittivity. However, this does remove the potential relaxor-type behaviour and increasingly diffuse-type phase transitions, *i.e.* for La-doped or Nb-doped $BaTiO_3$ at dopant concentrations larger than 10 mol%.[63,84]

Furthermore, it is possible to observe that Ba-site doping with large donor dopants, such as La- or Nd- cations, leads to a significant decrease in T_C with increasing concentration.[63,76,94] Reducing the size of the donor dopant on the Ba-site, i.e. using smaller cations such as Eu^{3+}, leads to a lower decrease in T_C with increasing concentration.[72] It is hypothesised that the different ionic sizes impose different strain and polarisability effects on the material, similar to the A-site Ca-doped $BaTiO_3$ discussed previously.[72]

Donor dopants on the Ti-site, such as Nb^{5+} or Ta^{5+}, result in similar behaviour as large donor dopants on the Ba-site.[83]

It has been proposed that when using two dopants, a donor and an acceptor, it is possible to estimate their combined effect on T_C by adding up the individual effects.[63,95,96] An example for this was observed by Parkash *et al*. for $La_xBa_{1-x}Ti_{1-x}Ni_xO_3$.[95] However, limitations to this model have been observed for larger ions, as they impose a larger strain on the lattice.[96]

2.4.3.2 Acceptor doping of $BaTiO_3$

If a dopant is used with a lower valency than the host ion it is called an acceptor dopant. Even though it is possible to use acceptor dopants on both sites of $BaTiO_3$, there is a larger proportion of Ti-site acceptor dopants reported in the literature. This is because Ba-site acceptor dopants are mainly limited to Na^+ and K^+ in the literature, whereas there is a larger range of Ti-site acceptor dopants available. These can be smaller RE-cations, for example Ho^{3+} or Y^{3+}, transition metals, alkaline earth cations (i.e. Mg^{2+} and Ca^{2+}) or group 3 cations.[81,97–105]

Considering so called ‘leaky’ dielectric behaviour of donor doped $BaTiO_3$ mentioned in the previous section, it can be said that acceptor-doped $BaTiO_3$ does not show this kind of behaviour. Instead acceptor-dopants influence permittivity and phase transition

temperatures. However, relaxor-type behaviour can be obtained by using small amounts of Ti-site acceptor-dopants, not only at high concentrations as described previously with donor dopants.[81,97–105]

Ti-site acceptor doping has particularly strong effects on the T_C of a material. The introduction of Mg^{2+} for example leads to a dramatic drop of ca. 20 °C per mol% of acceptor dopant.[101,102] Similarly, large drops in T_C can be observed when using RE-acceptor-dopants, such as Ho^{3+} or Y^{3+}.[99,106] Acceptor-dopants chosen from the transition metals and group 3 cations show another interesting trend. In small concentrations they stabilise the cubic phase.[107,108]

It has been found that oxygen vacancies lead to poor insulating resistances at high temperatures and electric fields,[109] and lead to reduced lifetimes.[30] They are assumed to be important in the degradation process by various models, such as the grain boundary model proposed by Smyth *et al*.[97]

2.4.3.3 Self-compensation mechanism

If a dopant system is used that results in a lower valency on one site and a higher valency on the other site it results in a self-compensating mechanism. Common examples for this are the intermediate RE-ions, as discussed later.[113]

$$Ba^{2+} + Ti^{4+} \rightarrow 2RE^{3+} \qquad (2.27)$$

However, it is also possible to achieve a self-compensating mechanism without using dopants that will sit on both sites. An example for this could be A-site doping with K^+ and B-site doping with Nb^{5+}. Their combined doping mechanism could be:

$$Ba^{2+} + Ti^{4+} \rightarrow Na^{+} + Nb^{5+} \qquad (2.28)$$

This mechanism does not create any new defects, therefore offers a reduced concentration of oxygen vacancies compared to other doing mechanisms. This makes it interesting for device applications, as it is favourable for device lifetime as discussed previously. The use of intermediate RE-ions as dopants will be discussed further in a later section.

2.4.4 Core-shell microstructures: Heterogeneous doping

Doped BT tends to form so-called 'core-shell' type (CS) microstructures, as seen in figure 2.13, when the dopants are not dispersed completely homogeneously throughout the material.[80,114–117] This incomplete mixing leads to regions with higher or lower amounts of dopants present. The formed microstructure can be described as a 'core' of undoped BT, which is surrounded by a 'shell' of doped-BT, which possesses a concentration gradient in terms of dopant levels.[114,118]

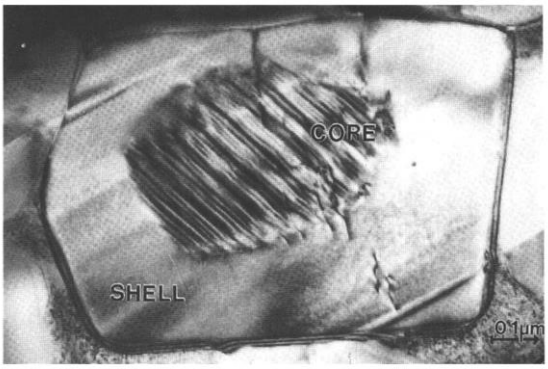

Figure 2.13. TEM micrograph of a CS microstructure.[116] Reproduced with permission.

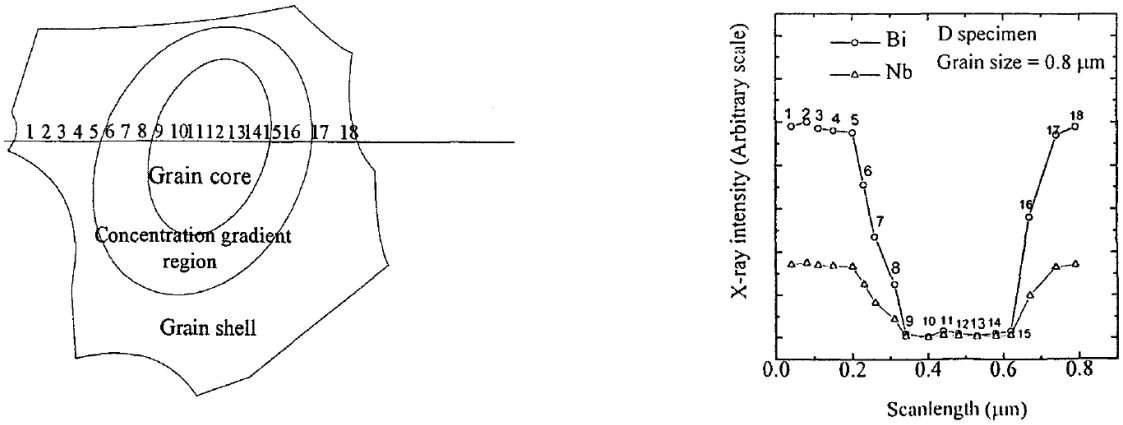

Figure 2.14. Observed concentration gradients in the EDS analysis of Bi and Nb in a CS microstructure.[119] Reproduced with permission.

Generally, the core will exhibit a T_C in the region of the undoped material, whereas the shell will possesses T_Cs corresponding to the range of dopant concentrations present.

An example of the concentration gradient present in CS microstructures is shown in figure 2.14. Figure 2.15 is a schematic of how the presence of shell T_Cs results in a broader permittivity profile. The result is the exhibition of overall diffuse phase transition (DPT) behaviour,[114] which makes CS microstructures a key tool in the capacitor industry as a way of improving temperature stability of the capacitance.

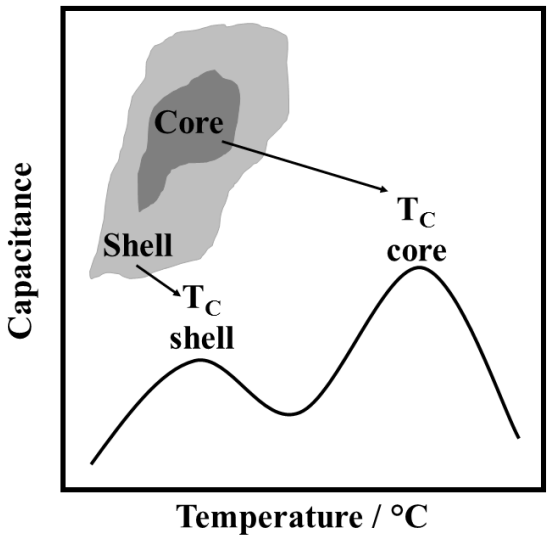

Figure 2.15. Schematic of a permittivity profile of a CS microstructure.

Two factors that play a major role in CS microstructures are the rate of diffusivity of dopants and the volume ratio between the core and shell.[71,120,121] Better diffusivity in the BT lattice allows for a better CS formation under the same processing conditions and the ratio between core and shell has a significant impact on the broadening of the permittivity profile.[122] The CS microstructure of RE-doped BT will be discussed with its relevance to MLCCs later on.

2.4.5 $NaNbO_3$ doped BT

2.4.5.1 $NaNbO_3$ (NN)

Sodium niobate (NN) has been studied with quite some interest in the past due to its large number of polymorphs, some of which are ferroelectric and others that are antiferrolectic.[123,124] NN is an antiferroelectric at RT, where it is found in a distorted orthorhombic phase, as seen in fig. 2.16, and is considered to be one of the most complex

perovskite materials.[123,125] Megaw was the first to report its seven polymorphs in 1974.[126] The phase transitions have been extensively studied, using a variety of techniques, such as XRD, neutron powder diffraction (NPD) and Raman spectroscopy.[127–129] Tan *et al.* have put together a table summarizing the results of various studies as shown in table 2.1.

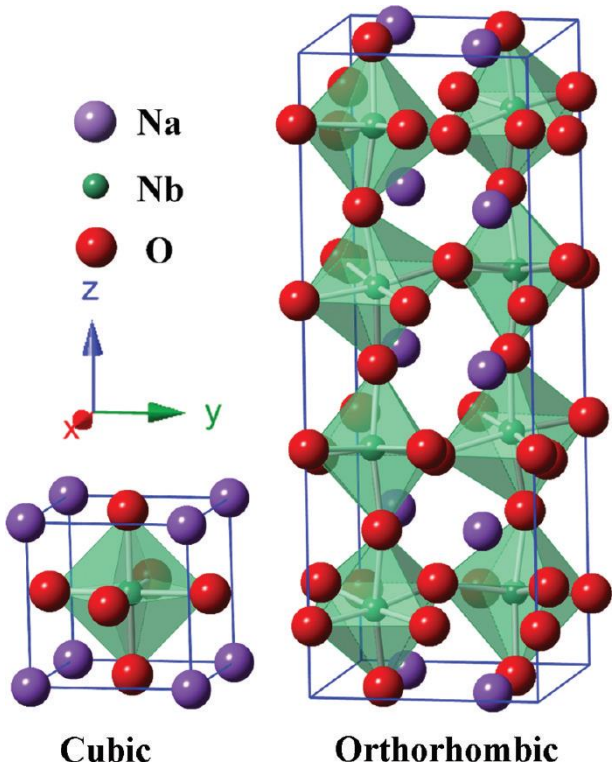

Figure 2.16. Schematic crystal structures of NN. Reprinted with permission from Li *et al.*[130] Copyright 2012 American Chemical Society.

Table 2.1. Summary of NNBT phases, reproduced from Tan *et al.*[127]

	XRD		NPD		XRD/Raman/Dielectric	
Phase	Symmetry	Temp. range (ºC)	Symmetry	Temp. range (ºC)	Symmetry	Temp. range (ºC)
N	Rhombohedral (R3c)	< -100	Rhombohedral (R3c)	< 7	Rhombohedral (R3c)	< -23
P	Orthorhombic (*Pbcm*)	-100 ~ 360	Orthorhombic (*Pbcm*)	-258 ~ 407	P_m: Monoclinic	-23 ~ 137
					INC: Incommensurate	137 ~ 187
					P_O: Orthorhombic	187 ~ 360
R	Orthorhombic (*Pmnm*)	360 ~ 480	Orthorhombic (*Pbnm*)	360 ~ 482	Orthorhombic (*Pmnm*)	360 ~ 480
S	Orthorhombic (*Pnmm*)	480 ~ 520	Orthorhombic (*Pbnm*)	482 ~ 537	Orthorhombic (*Pnmm*)	480 ~ 527
T_1	Orthorhombic (*Ccmm*)	520 ~ 575	Orthorhombic (*Ccmm*)	537 ~ 592	Orthorhombic (*Ccmm*)	527 ~ 575
T_2	Tetragonal (*P4/mbm*)	575 ~ 640	Tetragonal (*P4/mbm*)	592 ~ 677	Tetragonal (*P4/mbm*)	575 ~ 640
U	Cubic (*Pm3m*)	> 640	Cubic (*Pm3m*)	> 677	Cubic (*Pm3m*)	> 640

For the purpose of this thesis the complex phase transitions of NN are insignificant, as the properties investigated below to the orthorhombic-tetragonal transition and above the

rhombohedral-orthorhombic transition. However, the ability of NN to form solid solutions with other perovskite ferroelectrics and for these to possess reasonably high permittivity is significant. NN's dielectric properties are attractive , as seen in figure 2.17, however a RT permittivity of ~300 and a permittivity of ~1500 at a T_C of 375 ^oC are not sufficient on their own for use in MLCC applications.[131] A T_C of ~375 °C makes NN desirable for MLCCs, as it might extend the available operating temperature window.

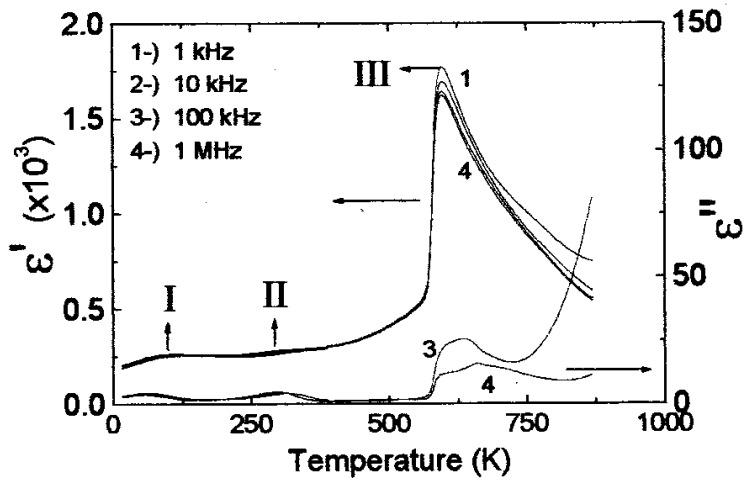

Figure 2.17. Real and imaginary parts of the permittivity of NN ceramics measured at different frequencies and temperatures. Reprinted from Lanfredi *et al.*,[132] with the permission of AIP Publishing

2.4.5.2 NNBT – NN doped BT

Raevskii *et al.* were the first to observe that NN forms a complete solid solution with BT, as seen in figure 2.18.[133] Khemakhem *et al.* also studied this solid solution and concluded it is possible to split it into three categories based on their dielectric responses.[134] According to them, region I shows classical ferroelectric properties for an NN-content below 0.075. When the NN-content is above 0.55 region II is entered and ferro- or anti-ferroelectric behaviour is observed. Finally the intermediate region III shows relaxor-ferroelectric-type diffuse phase transition behaviour. The specific regional boundaries can be debated as Zeng *et al.* observed ferroelectric-relaxor behaviour in compositions with NN-content of $x \geq 0.08$,[135] and Kwon *et al.* recently reported relaxor-type behaviour as low as $x = 0.06$.[131]

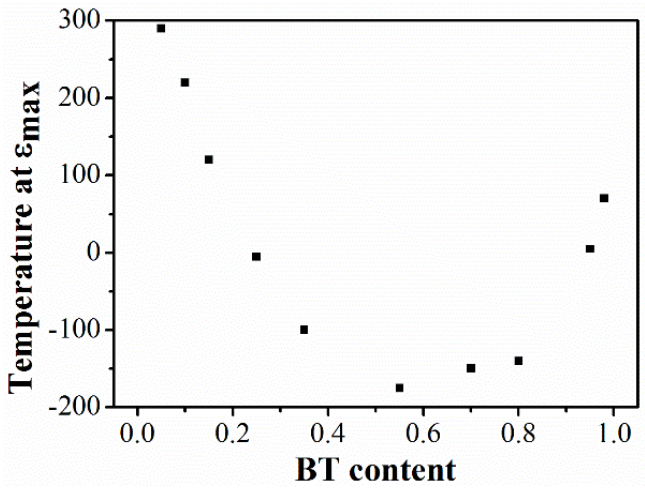

Figure 2.18. Variation of T_{max} with BT content for (1-x)NN-xBT solid solution series, reproduced from data by Raevskii *et al.*[133]

Kwon *et al.* analysed the diffuseness of the dielectric maxima by the following equation developed by Smolenskii and Kirillov:[25,136]

$$\frac{1}{\varepsilon_r} - \frac{1}{\varepsilon_m} = \frac{(T-T_m)^\gamma}{2\varepsilon_m \delta^\gamma}, \qquad (2.28)$$

where ε_r is the relative permittivity, ε_m is the maximum permittivity at T_m, T is the temperature, δ is the diffuseness parameter and γ is the critical exponent. The rule for γ is that it varies from a value of 1 for pure ferroelectrics to a value of 2 for pure relaxors.[131] δ describes the width of the diffuse phase transition and can be obtained from a log-log plot of $(1/\varepsilon_r - 1/\varepsilon_m)$ *vs.* $(T-T_m)$. The graphs slope is equal to γ, whilst the intercept (β) can be used to calculate δ:

$$\delta = \left[\frac{e^{-\beta}}{2\varepsilon_m}\right]^{\frac{1}{\gamma}}. \qquad (2.29)$$

Based on this analysis, they proposed a new set of characteristic regions, which can be seen in figure 2.19. Here, region I shows classic ferroelectric behaviour, region II is a regime with intermediate diffuse phase transition behaviour (DPT) and region III shows relaxor behaviour. Region IV still shows relaxor behaviour, however it is a mix of BT- and NN-based relaxors. x = 0.40 shows relaxor behaviour, however its extraordinarily dispersive phase transition led to a lower than expected γ of 1.6.[131] This large range of relaxor behaviour ($0.06 \geq x \leq 0.70$) makes NN doped BT interesting for capacitor applications, as diffuse phase transitions result in flatter permittivity-temperature profiles.

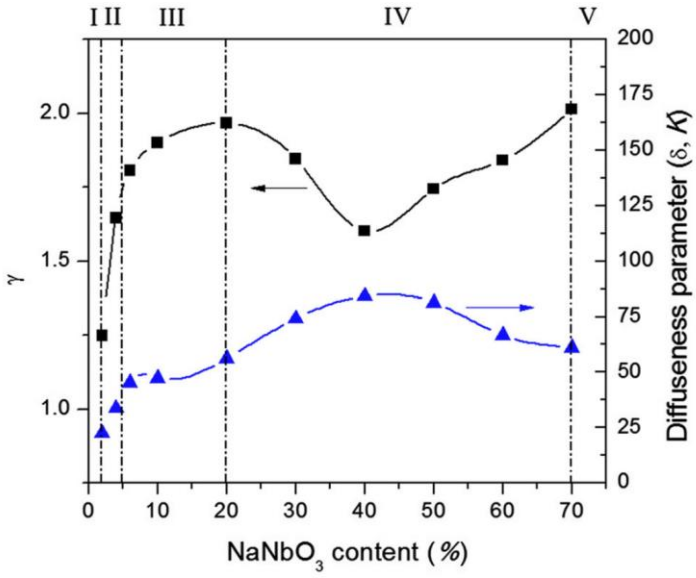

Figure 2.19. Fitting parameters of dielectric data for (1-x)BT-xNN ceramics.[131] ©2015 The Minerals, Metals and Materials Society. Reprinted with permission of Springer.

2.4.6 $BaZrO_3$-doped BT

2.4.6.1 $BaZrO_3$ (BZ)

$BaZrO_3$ is a perfect cubic perovskite, as seen in Fig. 2.20, that does not undergo any phase transitions under ambient pressure up to its melting point.[137,138] BZ therefore lacks the ferroelectric phases that make other perovskites so desirable, e.g. BT. Under high pressures however, a T-C transition can be observed at RT.[139] It is widely studied in solid solutions, particularly with BT, due to the tunability of its structure and electrical properties.[140]

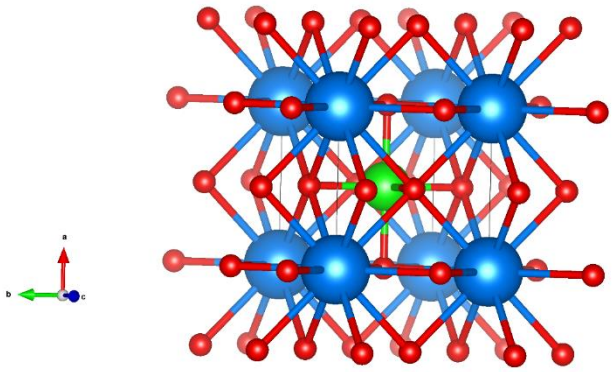

Figure 2.20. Schematic of the BZ unit cell (Ba^{2+} are blue, Zr^{4+} are green and O^{2-} are red), drawn with Vesta.[3]

2.4.6.2 BZTBT – BZ-doped BT

$BaZr_xTi_{1-x}O_3$ possesses several phase transitions, similar to BT, which move closer together with increasing Zr-content and merge into one close to RT for compositions with $x \sim 0.10$, as seen in figure 2.21.[141]

When the Zr-content is increased further, it results in very broad permittivity profiles, showing ferroelectric-relaxor behaviour.[142,143] Furthermore, T_C of BT decreases dramatically with increasing Zr-content.[144] The BZT solid solution is one of the most important for use in MLCC's.[145–147] When analysing the diffuseness of the permittivity profiles, it was observed that a Zr-content of $x > 0.10$ resulted in $\gamma \sim 1.5$ and $x \geq 0.25$ resulted in $\gamma \sim 2$.[142,148]

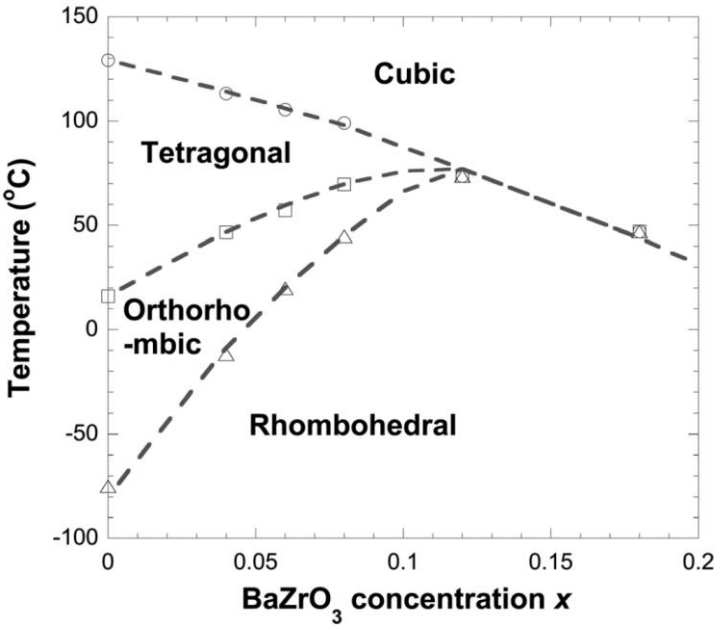

Figure 2.21. Partial phase diagram of the polymorphic phase fields and their transition temperatures in BZT with increasing Zr-content. Reprinted from Dong *et al.*,[148] with the permission of AIP Publishing.

These values for γ can be compared to those observed in NNBT, and therefore BZT also possesses a large range of compositions with ferroelectric-relaxor behaviour. This might prove beneficial, as the effect of Zr-content on T_C leaves a wide range of relaxors that possess permittivity maxima at temperatures comparable to 'shell'-compositions in CS microstructures.

2.5. Multilayer Ceramic Capacitors (MLCC)

2.5.1 Overview

One of the most important applications of $BaTiO_3$ today is its use in MLCCs[147,148] and demand continues to grow as shown in Figure 2.22. For example, Murata (one of the largest capacitor manufacturers) have shown a significant increase in revenue from the capacitor market, as their sales in electronics also increases.[149]

A schematic build-up of an individual MLCC was given in the previous chapter (see Figure 1.1) showing the alternating layers of ceramic material and metal electrodes. The number of layers is not limited to the number of layers shown and commonly exceeds 100 in MLCC's.[121,150]

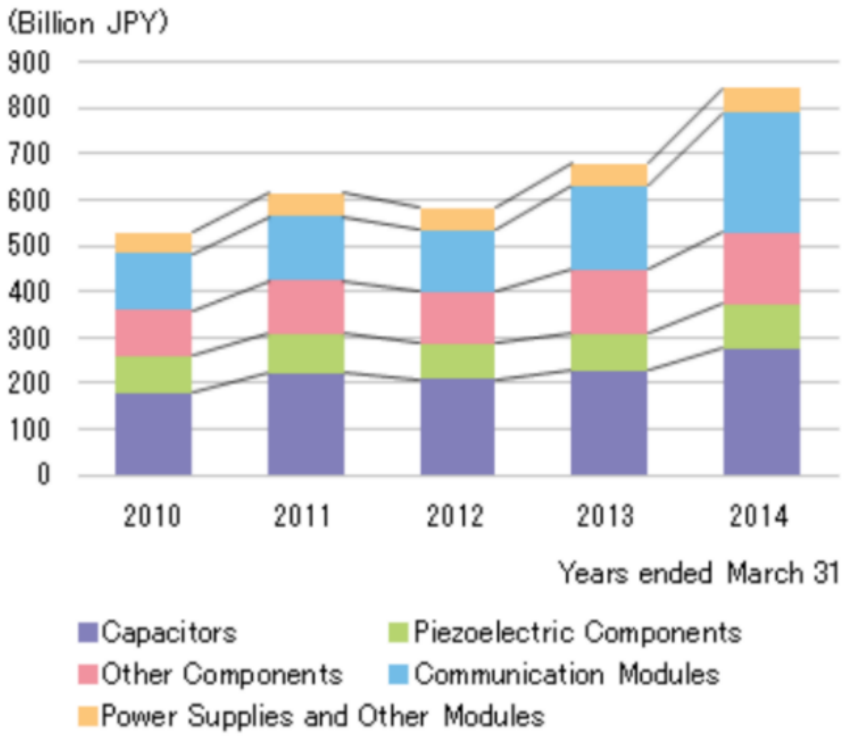

Figure 2.22. Murata Sales by product.[149]

The capacitance of an MLCC can be calculated using the following formula:

$$C = \varepsilon_r \times \varepsilon_0 \times (n-1) \times s / t, \qquad (2.30)$$

where ε_r is the relative permittivity (sometimes also called the dielectric constant, K) of the dielectric ceramic, ε_0 is the permittivity of free space, n is the number of internal

electrode layers, *s* is the overlap area of the internal electrodes and *t* is the thickness of the dielectric ceramic layers. From equation 2.30 it is possible to deduce that large capacitance values can be achieved by a combination of maximising the permittivity of the ceramic, minimising the layer thickness and increasing the number of layers. Other factors that increase the capacitance is to improve the overlap area of the electrodes, as well as improving the stacking quality.

A schematic step-by-step process of making an MLCC from reagent powders is shown in Figure 2.23. The sheeting and printing methods used to form the layers, where a metal electrode paste is printed on the green body sheets are shown. These printed sheets are stacked and then pressed and cut into individual MLCC sized pieces. This is followed by removal of any binder that might have been used and finally the green MLCCs are fired.[88] Knowledge of temperature dependent behaviour of all materials involved as well as their sintering temperatures and periods are required to obtain good MLCCs.

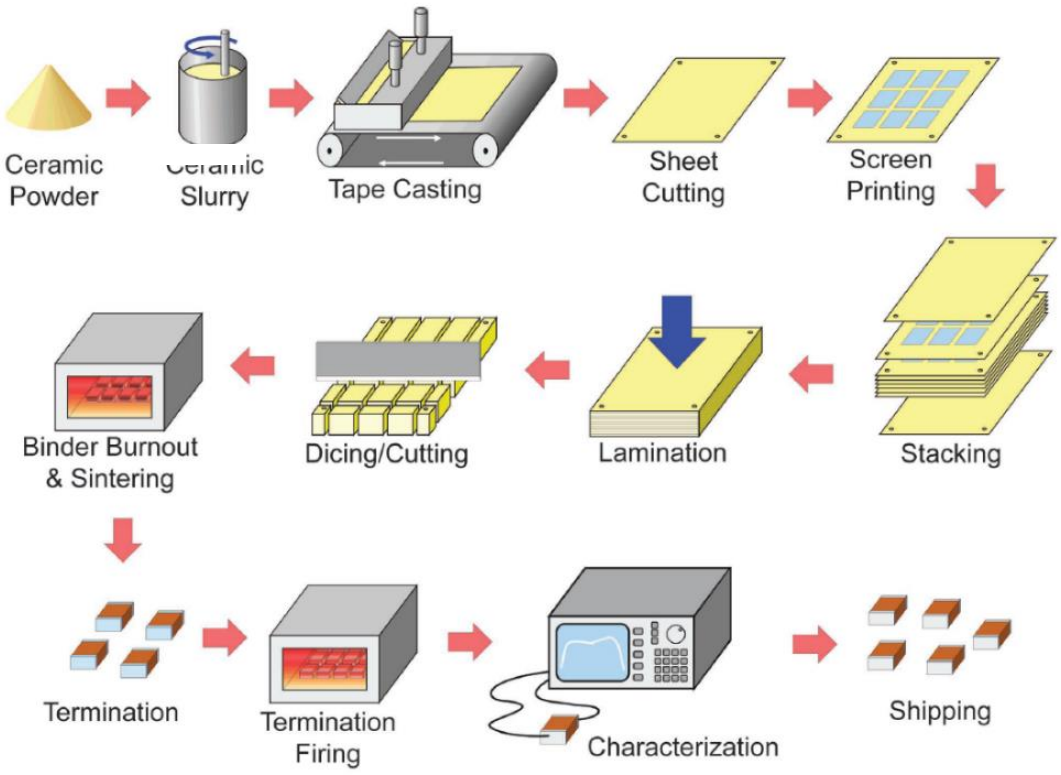

Figure 2.23. Schematic showing the production of MLCCs.[88] ©2011 IEEE.

2.5.2 Properties and classifications

$BaTiO_3$-based MLCCs are classified *via* a code system that takes into account the MLCCs working temperature range and the percentage change of capacitance over this range. The code system is based on the Electronic Industry Alliance (EIA) RS-198 standard and classifies MLCCs with three-digit codes. The first digit is equivalent to the lower operating temperature and is given by a letter, *e.g.* X = -55 °C. The second digit is equivalent to the upper operating temperature and is given as a number, *e.g.* 7 = +125 °C. The last digit gives the percentage change of capacitance over this temperature range and is given another letter, *e.g.* R = ±15 %. Table 2.2 gives examples for the classification of MLCCs using EIA specifications.[71,121]

Table 2.2. Examples of MLCCs classified by EIA specifications, reproduced from [121].

EIA designation	Class	Temp. range (°C)	Temp.-cap. change (%)
X7R	2	-55 to 125	±15
Z5U	2	10 to 85	±22
Y5V	2	-30 to 85	±22

2.5.3 Highly accelerated life test (HALT)

The performance of an MLCC in a highly accelerated life test (HALT) is one of the most important characteristics of the device. They ensure the MLCC will operate within the limits of industrial specifications for extended periods of time. The HALT methodology is used to confirm the reliability of MLCCs. In principle, a temperature and voltage which are in excess of normal operating conditions are applied to MLCCs and the time until failure of the devices is measured.[151] The time recorded can then be extrapolated to the lifetime of the devices under normal operating conditions.

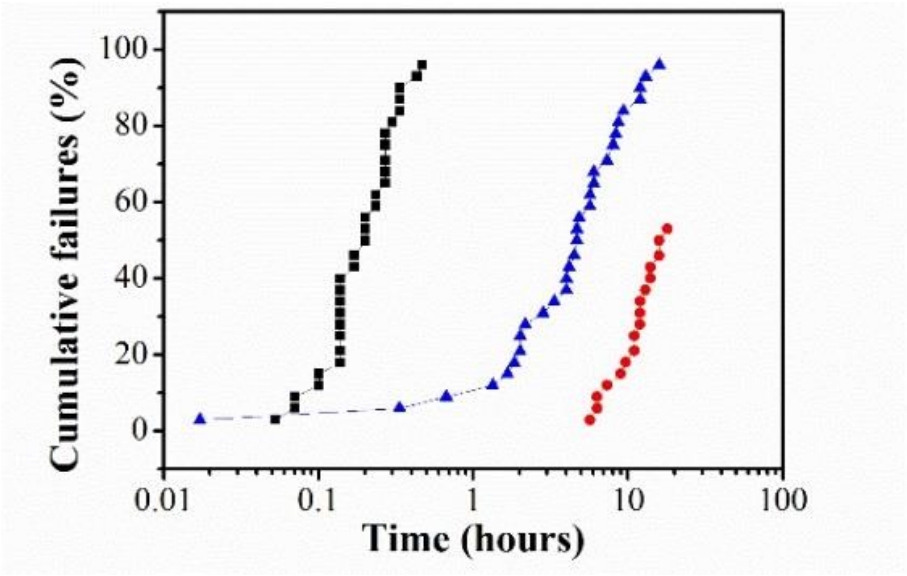

Figure 2.24. Schematic HALT-profiles of varying lifetimes[152].

2.5.4 BME electrodes

Initially the internal electrodes of $BaTiO_3$-based MLCCs were based on platinum (Pt) or palladium (Pd). However, increasing demand for an increase in the number of layers in MLCCs led to a steep increase in cost due to the increasing noble metal content per MLCC unit. This resulted in the search for cheaper alternatives and the development of base-metal-electrode MLCCs.[153] These utilise cheaper base-metals such as nickel (Ni) and copper (Cu) as internal electrodes in combination with non-reducible dielectric ceramics and are fired under reducing atmosphere and subsequently re-oxidised at a lower temperature.[73] Figure 1.1 (Chapter 1) shows examples of noble metal electrodes and those substituted by base-metal-electrodes.

2.5.5. RE-doped $BaTiO_3$ MLCCs

Ni-MLCC is the dominant technology in the MLCC market. This is due to the low cost and high firing temperatures but this development was not trivial, as it meant overcoming the high oxidisability of Ni in air at high temperatures. Hence, firing had to be performed in a reducing atmosphere that prevented Ni from being oxidised, yet did not reduce the dielectric ceramic. Initially, Ti-site acceptor dopants were used to accomplish this in the 1980s.[88,121,154,155] However, the use of acceptor dopants is not favourable for device

lifetime. Due to their limited lifetimes at high fields and temperatures compared to noble-metal electrode MLCCs, they did not become a major success.

This changed in 1990 with the discovery of so-called "magic dopants", especially those rare-earth elements with intermediate ionic radii, such as Dy, Y and Ho.[41,80,115,121,156–158] These are considered to be amphoteric, as they are sufficiently similar in size to Ba^{2+} and Ti^{4+}, enabling them to substitute onto both the A- (as a donor) and the B-site (as an acceptor). The donor-acceptor rare earth-doping enables the achievement of high insulation resistance over a long period of time, enabling thinner dielectric layers and longer lifetimes in MLCCs.[121,159,160] Furthermore, their ability to sit on A- and B-sites decreases the oxygen vacancy concentration in the dielectric ceramic, as self-compensation creates no oxygen vacancies.[88] As discussed previously, oxygen vacancies are considered to be a major contributor to shortened lifetimes and a major issue with exclusive acceptor doping.

One of the most recognised MLCCs systems using donor-acceptor co-substituted doping is $BaTiO_3$-MgO-R_2O_3, where R is a rare earth ion. Saito et al. obtained an Ni-MLCCs fulfilling X7R specifications with a $BaTiO_3$-MgO-Ho_2O_3 system.[71] This review focuses on the use of Ho- and particularly Dy-doped $BaTiO_3$ MLCCs.

2.5.5.1 Dy- and Ho-doped $BaTiO_3$ MLCCs

In rare-earth doping it is found that larger ions, such as La and Sm, substitute on the A-site as donor dopants and smaller ions, such as Yb, substitute on the B-site as acceptors. Intermediate ions, Dy, Ho and Er, substitute on both sites and act as donors and acceptors.[113] Table 2.3 shows the ionic radii of the intermediate rare-earth elements compared to those of barium and titanium.[121]

Kishi *et al.* compared X7R and Y5V Ni-MLCC samples doped with 1 at.% of the different RE-elements and their Highly Accelerated Lifetime test (HALT) at 350 V and 165 °C revealed the use of intermediate sized RE-elements showed a significant increase in lifetime, Figure 2.25.[121]

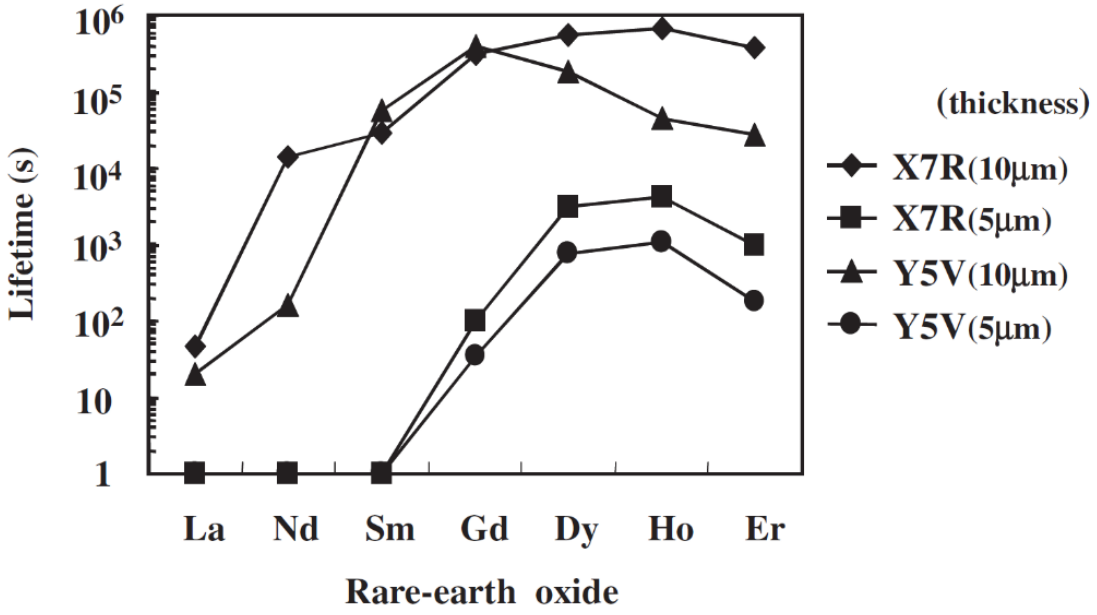

Figure 2.25. Lifetimes of Ni-MLCCs with 1 at.% of different RE-ions.[121] Copyright 2003 The Japan Society of Applied Physics.

Table 2.3. Effective ionic radii of intermediate RE-elements compared to Ba- and Ti-sites, reproduced from Kishi *et al.*[121]

Ion	Ionic radius (Å)	
	6 coordination	12 coordination
Ba^{2+}	-	1.61
Ti^{4+}	0.605	-
Dy^{3+}	0.912	1.255
Ho^{3+}	0.901	1.234
Er^{3+}	0.89	1.234

Furthermore, Kishi *et al.* suggested the improved lifetime of Ho- und Dy-doped MLCCs is due to the ability of intermediate RE-elements to facilitate re-oxidation in the cooling stage after the firing process.[121] This ability results in a lower concentration of oxygen vacancies in the MLCC, which improves the lifetime, as mentioned previously.

Another important aspect investigated was the dielectric loss of MLCCs. It is desirable to keep this as low as possible for device applications and Figure 2.26 shows the results for a load life time tests at 40 °C and 50 V for 1000 hours for Ni-MLCCs containing

different RE-ions.[121] The intermediate RE-doped samples clearly possess lower dielectric loss.

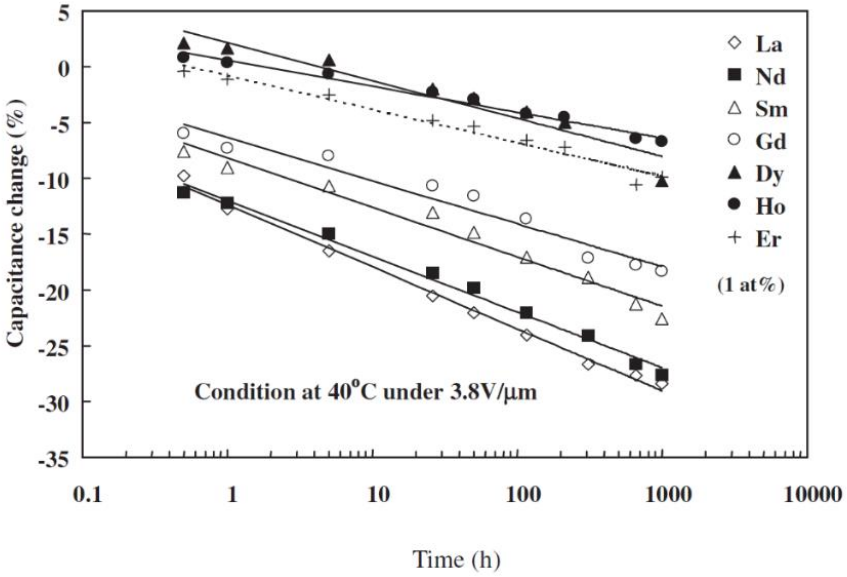

Figure 2.26. Load life time test for X7R Ni-MLCCs containing different RE-dopants.[121] Copyright 2003 The Japan Society of Applied Physics.

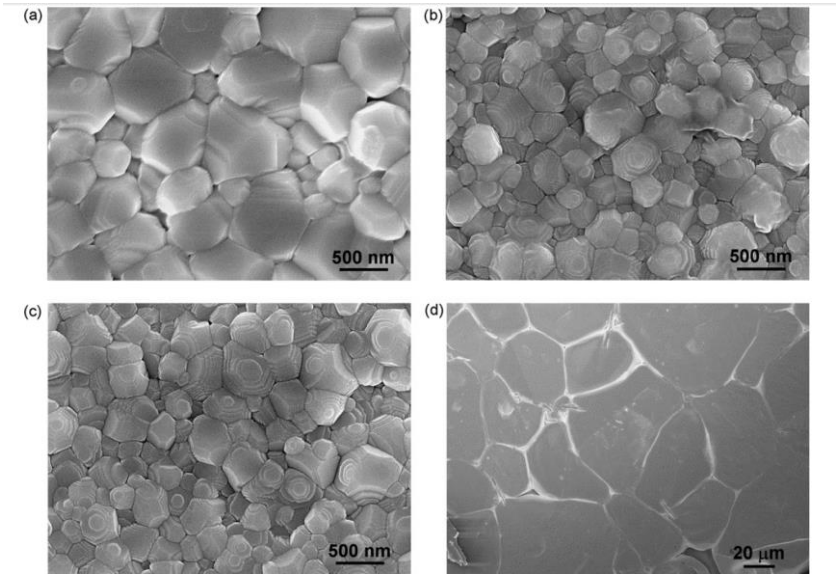

Figure 2.27. SEM micrographs of rare-earth doped samples; a) Dy-doped sintered at 1315 °C, b) Y-doped sintered at 1341 °C, c) Ho-doped sintered at 1341 °C and d) undoped sintered at 1284 °C. Reprinted from J. Eur. Ceram. Soc., 29, K.-J. Park *et al.*, Doping behaviours of dysprosium, yttrium and holmium in $BaTiO_3$ ceramics, 1735–1741, Copyright 2009, with permission from Elsevier.[41]

Dy- and Ho-doped MLCCs are required to form core-shell structures, with a cubic shell in which the RE-ions are dissolved and a tetragonal $BaTiO_3$ core.[117,161] The formation of a core-shell structure is promoted by RE-elements in addition to the previously mentioned stabilisation of the MLCCs dielectric properties.[71,80,162]

Park *et al.* compared the doping behaviours of Ho and Dy and discovered that Dy possessed a higher rate of diffusion in the $BaTiO_3$ lattice, as it displayed the shortest densification rate indicating faster movement of the ions

. This came with the observation that RE-doped samples possessed smaller sized grains than their non-doped counterparts.[41] However, Dy-doped samples possessed larger grains than Ho-doped samples, Figure 2.27. This has been attributed to Dy's improved solubility on the B-site.[41]

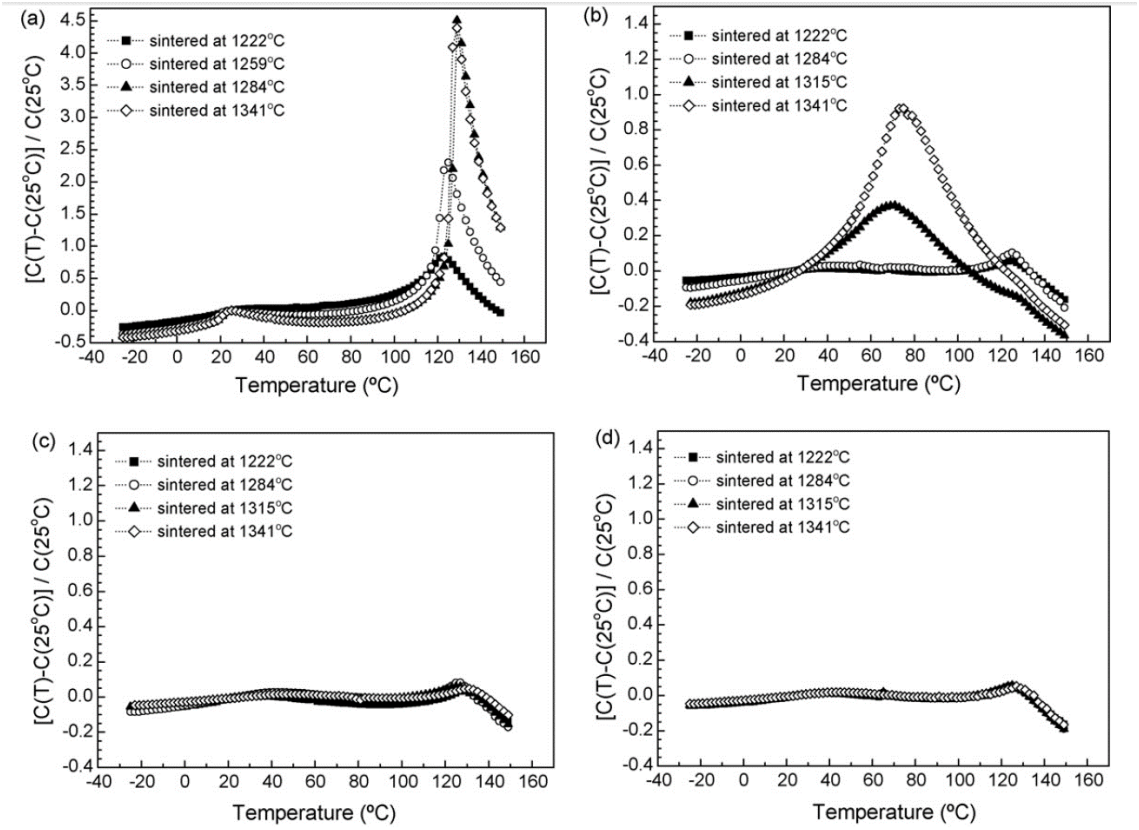

Figure 2.28. Temperature coefficient of capacitance (TCC) versus temperature for various sintering temperatures for, a) undoped, b) Dy-doped, c) Y-doped and d) Ho-doped ceramics. Reprinted from J. Eur. Ceram. Soc., 29, K.-J. Park *et al.*, Doping

behaviours of dysprosium, yttrium and holmium in $BaTiO_3$ ceramics, 1735–1741, Copyright 2009, with permission from Elsevier. [41]

Finally, a study on the temperature coefficient (TCC) of capacitance vs. sintering temperature has been conducted and the results shown in Figure 2.28. Increasing the sintering temperature leads to a significant increase in TCC for Dy-doped samples. The same can be observed for the undoped sample, not however for samples doped with Y or Ho. The reason for this is the inhibited grain growth for Y- and Ho-doped samples due to lower solubility in the bulk material, hence no increase in capacitance is observed.[41]

2.5.6. Sustainable MLCC's: A call for RE-free MLCCs

Considering the significant improvements in performance that RE-element dopants offer to MLCCs, especially Dy, it seems there is no technical reason to look for alternatives. However, the price and the supply-and-demand for Dy is becoming critical worldwide which is considered the most endangered of all RE's.

Dy is an element that naturally occurs only as a trace in various minerals. The estimated worldwide production and reserves of Dy_2O_3 in 2010 are shown in table 2.4.[163] The worldwide reserves are estimated to be 110 million tonnes and about half of these reserves are in China which currently produces almost all the world's supply.

Table 2.4. Worldwide reserves and production of Dy_2O_3 in 2010.[163]

Country	Mine production (estimated)	Reserves (kt)
China	130,000	55,000
India	2,700	3,100
Brazil	550	48
Malaysia	350	30
Commonwealth	-	19,000
USA	-	13,000
Australia	-	1,600
Other countries	-	22,000
World total (rounded)	130,000	110,000

This poses a significant problem, as China has imposed export quotas in the past. This resulted in a significant increase in price since around 2004 and the supply issues cause substantial fluctuations in price, Table 2.5. These restrictions have been tightened further and as shown in Chapter 1, consumer demand will outweigh supply in the future. This will put further pressure on the price and significant increases in price, coupled with an extremely uncertain supply, leads to a need for alternative materials to be used.

Table 2.5. Dysprosium-oxide price development (USD / kg) from 2011 and 2012.[164]

RE	Q1 2011	Q2 2011	Q3 2011	Q4 2011	Q1 2012	Q2 2012
Dy	412.9	921.2	2262.31	2032.31	1366.15	1070

Increasing demands for RE's for use in electronics and other areas will put further stress on supply and pricing for RE-oxides. Figure 1.4 (Chapter 1) shows a prediction that indicates a significant demand-and-supply gap by 2020 at the latest. With that prediction and the importance of electronics in today's day-to-day life in mind, it is important to have alternatives to RE-containing materials, such as RE-doped BT.

2.5 References

1 V. V Lemanov, A. V Sotnikov, E. P. Smirnova, M. Weihnacht and R. Kunze, *Solid State Commun.*, 1999, **110**, 611–614.

2 E. Riedel and C. Janiak, *Anorganische Chemie*, De Gruyter Studium, 8. Edition., 2011.

3 K. Momma and F. Izumi, *J. Appl. Crystallogr.*, 2011, **44**, 1272–1276.

4 G. King and P. M. Woodward, *J. Mater. Chem.*, 2010, **20**, 5785–5796.

5 Y. Zhao, D. J. Weidner, J. B. Parise and D. E. Cox, *Phys. Earth Planet. Inter.*, 1993, **76**, 17–34.

6 V. M. Goldschmidt, *Naturwissenschaften*, 1926, **14**, 477–485.

7 A. R. West, *Solid State Chemistry*, John Wiley & Sons, Ltd, Second Edi., 2014.

8 A. M. Glazer, *Acta Crystallogr. Sect. B Struct. Crystallogr. Cryst. Chem.*, 1972, **28**, 3384–3392.

9 A. M. Glazer, *Acta Crystallogr. Sect. A*, 1975, **31**, 756–762.

10 M. L. Lopez, M. L. Veiga and C. Pico, *J. Mater. Chem.*, 1994, **4**, 547–550.

11 C. I-Wei, L. Ping and W. Ying, *J. Phys. Chem. Solids*, 1996, **57**, 1525–1536.

12 J. Ravez, *C. R. Acad. Sci. Paris, Ser. IIc, Chim.*, 2000, **3**, 267–283.

13 M. P. Harmer, J. Chen, P. Peng, H. M. Chan and D. M. Smyth, *Ferroelectrics*, 1989, **97**, 263–274.

14 N. Setter and L. E. Cross, *J. Appl. Phys.*, 1980, **51**, 4356–4361.

15 G. King and E. Goo, *J. Am. Ceram. Soc.*, 1988, **60**, 454–460.

16 F. Millange, V. Caignaert, B. Domengès, B. Raveau and E. Suard, *Chem. Mater.*, 1998, **10**, 1974–1983.

17 D. Damjanovic, *Rep. Prog. Phys*, 1998, **61**, 1267–1324.

18 M. B. Smith, K. Page, T. Siegrist, P. L. Redmond, E. C. Walter, R. Seshadri, L. E. Brus and M. L. Steigerwald, *J. Am. Chem. Soc.*, 2008, **130**, 6955–6963.

19 G. H. Haertling, *J. Am. Ceram. Soc.*, 1999, **82**, 797–818.

20 K. Uchino, *FerroDevices-1+3-Uchino.pdf*, Marcel Dekker, Inc., New York, 2000.

21 R. Zhang, J. F. Li and D. Viehland, *J. Am. Ceram. Soc.*, 2004, **87**, 864–870.

22 A. A. Bokov and Z. Ye, *Solid State Commun.*, 2000, **116**, 105–108.

23 A. A. Bokov and Z.-G. Ye, *J. Mater. Sci.*, 2006, **41**, 31–52.

24 M. D. Glinchuk and R. Farhi, *J. Phys. Condens. Matter*, 1996, **8**, 6985–6996.

25 G. A. Smolenskii, *J. Phys. Soc. Japan*, 1970, **28**, 26.

26 P. N. Timonin, *Ferroelectrics*, 1997, **199**, 69–81.

27 A. A. Bokov, *Solid State Commun.*, 1994, **90**, 687–691.

28 A. K. Tagantsev and A. E. Glazounov, *Phys. Rev. B*, 1998, **57**, 18–21.

29 V. A. Isupov, *Phys. Status Solidi*, 1999, **213**, 211–218.

30 A. J. Moulson and J. M. Herbert, *Electroceramics - Materials, Properties, Applications*, Chapman & Hall, London, 1990.

31 A. von Hippel, R. G. Breckenridge, F. G. Chesley and L. Tisza, *Ind. Eng. Chem.*, 1946, **38**, 1097–1109.

32 D. Yoon, *J. Ceram. Process. Res.*, 2006, **7**, 343–354.

33 E. C. Subbarao, M. C. McQuarrie and W. R. Buessem, *J. Appl. Phys.*, 1957, **28**, 1194–1200.

34 T. Hiramatsu, T. Tamura, N. Wada, H. Tamura and Y. Sakabe, *Mater. Sci. Eng. B*, 2005, **120**, 55–58.

35 N. Wongdamnern, K. Kanchiang, A. Ngamjarurojana, S. Ananta, Y. Laosiritaworn, A. Charoenphakdee, S. Gupta, S. Priya and R. Yimnirun, *Smart Mater. Struct.*, 2014, **23**, 085022.

36 T. Lee and I. A. Aksay, *Cryst. Growth Des.*, 2001, **1**, 401–419.

37 H. Kniekamp and W. Heywang, *Phys. Rev.*, 1954, **6**, 385–390.

38 K. Kinoshita, *J. Appl. Phys.*, 1976, **47**, 371–373.

39 Z. Zhao, V. Buscaglia, M. Viviani, M. Buscaglia, L. Mitoseriu, A. Testino, M. Nygren, M. Johnsson and P. Nanni, *Phys. Rev. B*, 2004, **70**, 024107.

40 M. Frey and D. Payne, *Phys. Rev. B*, 1996, **54**, 3158–3168.

41 K.-J. Park, C.-H. Kim, Y.-J. Yoon, S.-M. Song, Y.-T. Kim and K.-H. Hur, *J. Eur. Ceram. Soc.*, 2009, **29**, 1735–1741.

42 H. T. Kim and Y. H. Han, *Ceram. Int.*, 2004, **30**, 1719–1723.

43 Y. Enomoto, K. Kinoshita, A. Yamaji and T. Murakami, *J. Am. Ceram. Soc.*, 1977, **60**, 97–101.

44 S. Marković, M. Miljković, Č. Jovalekić, S. Mentus and D. Uskoković, *Mater. Manuf. Process.*, 2009, **24**, 1114–1123.

45 T. Hoshina, S. Wada, Y. Kuroiwa and T. Tsurumi, *Appl. Phys. Lett.*, 2008, **93**, 192914.

46 G. Arlt, D. Hennings and G. de With, *J. Appl. Phys.*, 1985, **58**, 1619–1625.

47 E. Salje, U. Bismayer, B. Wruck and J. Hensler, *Phase Transitions*, 1991, **35**, 61–74.

48 R. K. Sharma, N. H. Chan and D. M. Smyth, *J. Am. Ceram. Soc.*, 1981, **64**, 448–451.

49 Y. h. Hu, M. P. Harmer and D. M. Smyth, *J. Am. Ceram. Soc.*, 1985, **68**, 372–376.

50 S. Lee, Z.-K. Liu, M.-H. Kim and C. a. Randall, *J. Appl. Phys.*, 2007, **101**, 054119.

51 C. L. Freeman, J. A. Dawson, H. Chen, J. H. Harding, L. Ben and D. C. Sinclair, *J. Mater. Chem.*, 2011, **21**, 4861–4868.

52 J. A. Dawson, X. Li, C. L. Freeman, J. H. Harding and D. C. Sinclair, *J. Mater. Chem. C*, 2013, **1**, 1574–1582.

53 J. N. Lin and T. B. Wu, *J. Appl. Phys.*, 1990, **68**, 985.

54 Z. Yu, C. Ang, R. Guo and a. S. Bhalla, *Mater. Lett.*, 2007, **61**, 326–329.

55 L. Zhang, O. P. Thakur, A. Feteira, G. M. Keith, A. G. Mould, D. C. Sinclair and A. R. West, *Appl. Phys. Lett.*, 2007, **90**, 142914.

56 T. Mitsui and W. B. Westphal, *Phys. Rev.*, 1961, **124**, 1354–1359.

57 M. McQuarrie and F. W. Behnke, *J. Am. Ceram. Soc.*, 1954, **37**, 539–543.

58 D. C. Sinclair and J. P. Attfield, *Chem. Commun.*, 1999, **16**, 1497–1498.

59 S. Anwar, P. R. Sagdeo and N. P. Lalla, *J. Phys. Condens. Matter*, 2006, **18**, 3455–3468.

60 N. Baskaran and H. Chang, *J. Mater. Sci. Mater. Electron.*, 2001, **12**, 527–531.

61 S. Marković, M. Mitrić, N. Cvjetićanin and D. Uskoković, *J. Eur. Ceram. Soc.*, 2007, **27**, 505–509.

62 S. Skapin, D. Kolar, D. Suvorov and Z. Samardzija, *J. Mater. Res.*, 1998, **13**, 1327–1334.

63 F. D. Morrison, D. C. Sinclair and A. R. West, *J. Appl. Phys.*, 1999, **86**, 6355–6366.

64 D. Makovec, Z. Samardzija, U. Delalut and D. Kolar, *J. Am. Ceram. Soc.*, 1995, **78**, 2193–2197.

65 D.-Y. Lu, X.-Y. Sun and M. Toda, *J. Phys. Chem. Solids*, 2007, **68**, 650–664.

66 D. Gulwade and P. Gopalan, *Solid State Commun.*, 2008, **146**, 340–344.

67 G. H. Jonker, *Solid. State. Electron.*, 1964, **7**, 895–903.

68 D. Makovec, Z. Samardzija and D. Kolar, *J. Solid State Chem.*, 1996, **123**, 30–38.

69 D. F. K. Hennings, B. Schreinemacher and H. Schreinemacher, *J. Eur. Ceram. Soc.*, 1994, **13**, 81–88.

70 J. H. Hwang and Y. H. Han, *J. Am. Ceram. Soc.*, 2001, **84**, 1750–1754.

71 H. Saito, H. Chazono, H. Kishi and N. Yamaoka, *Jpn. J. Appl. Phys.*, 1991, **30**, 2307–2310.

72 Y. Mizuno, H. Kishi, K. Ohnuma, T. Ishikawa and H. Ohsato, *J. Eur. Ceram. Soc.*, 2007, **27**, 4017–4020.

73 S. Urek and M. Drofenik, *J. Eur. Ceram. Soc.*, 1999, **19**, 913–916.

74 S. Yasmin, S. Choudhury, M. A. Hakim, A. H. Bhuiyan and M. J. Rahman, *J. Mater. Sci. Technol.*, 2011, **27**, 759–763.

75 Z. Yao, H. Liu, Y. Liu, Z. Wu, Z. Shen, Y. Liu and M. Cao, *Mater. Chem. Phys.*, 2008, **109**, 475–481.

76 A. S. Shaikh and R. W. Vest, *J. Am. Ceram. Soc.*, 1986, **69**, 689–694.

77 T. R. N. Kutty and P. Murugaraj, *J. Mater. Sci.*, 1987, **22**, 3652–3664.

78 S. B. Desu and D. A. Payne, *J. Am. Ceram. Soc.*, 1990, **73**, 3407–3415.

79 J. Zhi, A. Chen, Y. Zhi and P. M. Vilarinho, *J. Am. Ceram. Soc.*, 1999, **82**, 1345–1348.

80 C.-H. Kim, K.-J. Park, Y.-J. Yoon, M.-H. Hong, J.-O. Hong and K.-H. Hur, *J. Eur. Ceram. Soc.*, 2008, **28**, 1213–1219.

81 J. H. Jeong, M. G. Park and Y. H. Han, *J. Electroceramics*, 2004, **13**, 805–809.

82 E. C. Subbarao and G. Shirane, *J. Am. Ceram. Soc.*, 1959, **42**, 279–284.

83 N. Maso, H. Beltran, E. Cordoncillo, A. Arenas Flores, P. Escribano, D. C. Sinclair and A. R. West, *J. Mater. Chem.*, 2006, **16**, 3114–3119.

84 N. Masó, H. Beltrán, E. Cordoncillo, D. C. Sinclair and A. R. West, *J. Am. Ceram. Soc.*, 2008, **91**, 144–150.

85 S. Wang, S. Zhang, X. Zhou, B. Li and Z. Chen, *Mater. Lett.*, 2006, **60**, 909–911.

86 M. Kahn, *J. Am. Ceram. Soc.*, 1971, **54**, 452–454.

87 O. I. V'yunov, L. L. Kovalenko and a. G. Belous, *Inorg. Mater.*, 2006, **42**, 1363–1368.

88 M.-J. Pan and C. A. Randall, *IEEE Electr. Insul. Mag.*, 2010, **26**, 44–50.

89 J. Nowotny and M. Rekas, *Solid State Ionics*, 1991, **49**, 135–154.

90 S. Jayanthi and T. R. N. Kutty, *J. Mater. Sci. Mater. Electron.*, 2005, **16**, 269–279.

91 S. Guillemet-Fritsch, Z. Valdez-Nava, C. Tenailleau, T. Lebey, B. Durand and J.-Y. Chane-Ching, *Adv. Mater.*, 2008, **20**, 551–555.

92 P. Lunkenheimer, V. Bobnar, a. Pronin, a. Ritus, a. Volkov and a. Loidl, *Phys. Rev. B*, 2002, **66**, 052105.

93 J. Yu, T. Ishikawa, Y. Arai, S. Yoda, M. Itoh and Y. Saita, *Appl. Phys. Lett.*, 2005, **87**, 252904.

94 F. D. Morrison, D. C. Sinclair and A. R. West, *Int. J. Inorg. Mater.*, 2001, **3**, 1205–1210.

95 O. Parkash, H. S. Tewari, L. Pandey, R. Kumar and D. Kumar, *J. Am. Ceram. Soc.*, 1989, **72**, 1520–1522.

96 A. Feteira, D. C. Sinclair and M. T. Lanagan, *J. Appl. Phys.*, 2010, **108**, 014112.

97 D. Makovec, Z. Samardz and M. Drofenik, *J. Am. Ceram. Soc.*, 2004, **87**, 1324–1329.

98 J. Jeong, E. J. Lee and Y. H. Han, *Jpn. J. Appl. Phys.*, 2005, **44**, 4047–4051.

99 Z. Jing, C. Ang, Z. Yu, P. M. Vilarinho and J. L. Baptista, *J. Appl. Phys.*, 1998, **84**, 983–986.

100 H. Ihrig, *J. Phys. C Solid State Phys.*, 1978, **11**, 819–827.

101 S. H. Cha and Y. H. Han, *Jpn. J. Appl. Phys.*, 2006, **45**, 7797–7800.

102 T. Nagai, K. Iijima, H. J. Hwang, M. Sando, T. Sekino and K. Niihara, *J. Am. Ceram. Soc.*, 2000, **83**, 107–112.

103 S. J. Lee, S. M. Park and Y. H. Han, *Jpn. J. Appl. Phys.*, 2009, **48**, 031403.

104 J. Jeong and Y. H. O. Han, *J. Electroceramics*, 2004, **13**, 549–553.

105 Y. H. O. Han, J. B. Appleby and D. M. Smyth, *J. Am. Ceram. Soc.*, 1987, **70**, 96–100.

106 Y. Liu and A. R. West, *J. Eur. Ceram. Soc.*, 2009, **29**, 3249–3257.

107 P. Baxter, N. J. Hellicar and B. Lewis, *J. Am. Ceram. Soc.*, 1959, **42**, 465–470.

108 N. Maso, H. Beltran, E. Cordoncillo, P. Escribano and A. R. West, *J. Mater. Chem.*, 2006, **16**, 1626–1633.

109 S. Sumita, M. Ikeda, Y. Nakano, K. Nishiyama and T. Nomura, *J. Am. Ceram.*

Soc., 1991, **74**, 2734–2746.

110 E. Loh, *J. Appl. Phys.*, 1982, **53**, 6229–6235.

111 K. Lehovec and G. A. Shirn, *J. Appl. Phys.*, 1962, **33**, 2036–2044.

112 J. B. MacChesney, P. K. Gallagher and F. V. DiMarcello, *J. Am. Ceram. Soc.*, 1963, **46**, 197–202.

113 Y. Tsur, A. Hitomi, I. Scrymgeour and C. A. Randall, *Jpn. J. Appl. Phys.*, 2001, **40**, 255–258.

114 S. Jeon, C. Lee and S. L. Kang, *J. Am. Ceram. Soc.*, 2012, **95**, 2435–2438.

115 Z. Tian, X. Wang, H. Gong, T. Song, K. H. Hur and L. Li, *J. Am. Ceram. Soc.*, 2011, **94**, 973–977.

116 C. A. Randall, S. F. Wang, D. Laubscher, J. P. Dougherty and W. Huebner, *J. Mater. Res.*, 1993, **8**, 871–879.

117 S. Yoon, J. Lee and D. Kim, *J. Am. Ceram. Soc.*, 2002, **85**, 3111–3113.

118 L. Bisco, F. Zhu, M. B. Ward, J. Li and S. J. Milne, *Acta Mater.*, 2015, **90**, 204–212.

119 Y. Park and Y. Kim, *J. Mater. Res.*, 1995, **10**, 2770–2776.

120 H. Kishi, Y. Okino, M. Honda, Y. Iguchi, M. Imaeda, Y. Takahashi, H. Ohsato and T. Okuda, *Jpn. J. Appl. Phys.*, 1997, **36**, 5954–5957.

121 H. Kishi, Y. Mizuno and H. Chazono, *Jpn. J. Appl. Phys.*, 2003, **42**, 1–15.

122 S. Jeon, B. Yoon, K. Kim and S. L. Kang, *J. Adv. Ceram.*, 2014, **3**, 76–82.

123 Y. I. Yuzyuk, P. Simon, E. Gagarina, L. Hennet, D. Thiaudiere, V. I. Torgashev, S. I. Raevskaya, I. P. Raevskii, L. A. Reznitchenko and J. L. Sauvajol, *J. Phys. Condens. Matter*, 2005, **17**, 4977–4990.

124 L. Jiang, D. C. Mitchell, W. Dmowski and T. Egami, *Phys. Rev. B*, 2013, **88**, 014105.

125 L. Fu, D. Lin, Q. Zheng, X. Wu, L. Wu, H. Sun, Y. Wan, X. Fan and C. Xu, *Curr. Appl. Phys.*, 2012, **12**, 1523–1528.

126 H. D. Megaw, *Ferroelectrics*, 1974, **7**, 87.

127 X. Tan, C. Ma, J. Frederick, S. Beckman and K. G. Webber, *J. Am. Ceram. Soc.*, 2011, **94**, 4091–4107.

128 J. Macutkevic, A. Molak and J. Banys, *Ferroelectrics*, 2015, **479**, 48–55.

129 S. K. Mishra, R. Mittal, V. Y. Pomjakushin and S. L. Chaplot, *Phys. Rev.*, 2011, **83**, 134105.

130 P. Li, S. Ouyang, G. Xi, T. Kako and J. Ye, *J. Phys. Chem. C*, 2012, **116**, 7621–7628.

131 D. Kwon, Y. Goh, D. Son, B. Kim, H. Bae, S. Perini and M. Lanagan, *J. Electroceramics*, 2016, **45**, 631–638.

132 S. Lanfredi, M. H. Lente and J. A. Eiras, *Appl. Phys. Lett.*, 2002, **80**, 2731–2733.

133 I. P. Raevskii, L. M. Proskuryakova, L. A. Reznichenko, E. K. Zvorykina and L. A. Shilkina, *Sov. Phys. J.*, 1978, **21**, 259–261.

134 H. Khemakhem, A. Simon, R. Von der Mühll and J. Ravez, *J. Phys. Condens. Matter*, 2000, **12**, 5951–5959.

135 J. T. Zeng, K. W. Kwok and H. L. W. Chan, *J. Am. Ceram. Soc.*, 2006, **89**, 2828–2832.

136 V. Kirillov and V. Isupov, *Ferroelectrics*, 1973, **5**, 3–9.

137 Y. Zhang, M. Liu, J. Wang, T. Shimada and T. Kitamura, *J. Appl. Phys.*, 2014, **115**, 224107.

138 S. Parida, S. K. Rout, L. S. Cavalcante, E. Sinha, M. S. Li and V. Subramanian, *Ceram. Int.*, 2012, **38**, 2129–2138.

139 X. Yang, Q. Li, R. Liu, B. Liu, H. Zhang, S. Jiang, J. Liu, B. Zou and T. Cui, *J. Appl. Phys.*, 2014, **115**, 124907.

140 T. Maiti, R. Guo, A. S. Bhalla, T. Maiti, R. Guo and A. S. Bhalla, *Appl. Phys. Lett.*, 2006, **89**, 122909.

141 W. Li, Z. Xu, R. Chu, P. Fu and G. Zang, *Brazilian J. Phys.*, 2010, **40**, 353–356.

142 Q. Xu, D. Zhan, H. Liu, W. Chen, D. Huang and F. Zhang, *Acta Mater.*, 2013, **61**, 4481–4489.

143 P. S. Dobal, A. Dixit, R. S. K. Yu, R. Guo, A. S. Bhalla, P. S. Dobal, A. Dixit and R. S. Katiyar, *J. Appl. Phys.*, 2001, **89**, 8085.

144 B. Garbarz-Glos, K. Bormanis and D. Sitko, *Ferroelectrics*, 2012, **417**, 118–123.

145 S. Mahajan, O. P. Thakur, C. Prakash and K. Sreenivas, *Bull. Mater. Sci.*, 2011, **34**, 1483–1489.

146 X. G. Tang, K. Chew and H. L. W. Chan, *Acta Mater.*, 2004, **52**, 5177–5183.

147 Y. Wang, B. Cui, L. Zhang, Z. Hu and Y. Wang, *Ceram. Int.*, 2014, **40**, 11681–11688.

148 L. Dong, D. S. Stone and R. S. Lakes, *J. Appl. Phys.*, 2012, **111**, 084107.

149 Murata (accessed 05.01.2015), *http://www.murata.com/en-eu/about/ir/financial/products*.

150 D.-H. Kuo, C.-H. Wang and W.-P. Tsai, *Ceram. Int.*, 2006, **32**, 1–5.

151 J. L. Paulsen and E. K. Reed, *Microelectron. Reliab.*, 2002, **42**, 815–820.

152 *AVX Ltd. Priv. Commun.*

153 D. F. K. Hennings, *J. Eur. Ceram. Soc.*, 2001, **21**, 1637–1642.

154 Y. Sakabe, K. Minai and K. Wakino, *Jpn. J. Appl. Phys.*, 1981, **20**, 147–150.

155 I. Burn and G. H. Maher, *J. Mater. Sci.*, 1975, **10**, 633–640.

156 H. Kishi, N. Kohzu, J. Sugino and H. Ohsato, *J. Eur. Ceram. Soc.*, 1999, **19**, 1043–1046.

157 J. Nishikawa, T. Hagiwara, K. Kobayashi, Y. Mizuno and H. Kishi, *Jpn. J. Appl. Phys.*, 2007, **46**, 6999–7004.

158 C.-C. Chou, C.-S. Chen, I.-N. Lin, W.-C. Yang and H.-F. Cheng, *Ferroelectrics*, 2006, **332**, 35–39.

159 H.-J. Hageman and D. Hennings, *J. Am. Ceram. Soc.*, 1981, **64**, 590–594.

160 K. Albertsen, D. Hennings and O. Steigelmann, *J. Electroceramics*, 1998, **2**,

193–198.

161 Y. Fujikawa, Y. Umeda and F. Yamane, *J. Japan Soc. Powder Powder Metall.*, 2004, **51**, 839–844.

162 Y. Sakabe, Y. Hamaji, H. Sano and N. Wada, *Jpn. J. Appl. Phys.*, 2002, **41**, 5668–5673.

163 R. L. Moss, E. Tzimas, H. Kara, P. Willis and J. Kooroshy, *Critical Metals in Strategic Energy Technologies*, European Union, Luxembourg, 2011.

164 S. Massari and M. Ruberti, *Resour. Policy*, 2013, **38**, 36–43.

Chapter 3: Experimental Methods

3.1 Introduction

This chapter describes the fabrication and characterisation techniques used to investigate raw materials, powders and ceramic samples used in this work.

3.2 Characterisation techniques

3.2.1 Density Measurements

3.2.1.1 Archimedes' density

The bulk density of a material can be obtained by dividing its mass by its volume. Improved accuracy is given by the Archimedes method, based on the principle that net upward buoyancy is equivalent to weight of water that is displaced by a body.

The density apparatus MS-DNY-43 from Mettler Toledo (Greifensee, Switzerland) was used to determine ceramic density. Here, a sintered pellet is initially weighed in air and then suspended in H_2O and weighed again. The equipment uses these values along with the temperature to determine the density using the following equation:

$$\rho = \frac{A}{A-B}(\rho_0 - \rho_L) + \rho_L \qquad (3.1)$$

where, ρ: pellet density (g/cm^3), A: weight of pellet in air (g), B: weight in auxiliary liquid (g), ρ_0: density of auxiliary liquid (g/cm^3), ρ_L: density of air (0.0012 g/cm^3).

3.2.1.2 Theoretical density

The theoretical density of ceramics for each composition was calculated from the atomic weight and the dimensions of the unit cell, using the equation:

$$\rho_{th} = \frac{MW \cdot n}{V_{cell} \cdot N_A}, \qquad (3.2)$$

where ρ_{th} is the theoretical density, MW is the molecular weight (g), n is the number of atoms in the unit cell, V_{cell} is the unit cell volume (cm^3) and N_A is the Avogadro number (6.022×10^{23} atoms mol^{-1}). The unit cell volume was calculated from the lattice parameters obtained from the X-ray Diffraction data of fired ceramics.

3.2.1.3 Dilatometry

Thermal expansion of sintered ceramics and shrinkage of green body pellets were determined using a DIL 402 C (Netzsch, Selb, Germany) dilatometer with a heating rate of 5 ºC/min and a temperature range from 25 to 1400 ºC.

3.2.2 Structural and microstructural analysis

3.2.2.1 X-ray diffraction (XRD)

X-ray diffraction (XRD) was performed on raw materials and reacted powders. Powdered samples for XRD were placed in standard Bruker PMMA holders and the surface flattened with a glass slide. XRD data were obtained on a Bruker D2 Phaser (Karlsruhe, Germany) using Cu K-alpha radiation at 30 kV and 10 mA. Data were collected across the 2θ range of 20 to 80 °. The phases were analyzed using the "DIFFRAC.EVA" software by Bruker (Karlsruhe, Germany).

To determine the lattice parameters, XRD data were collected on a PANalytical X'PERT^3 (Almelo, The Netherlands). EXPGUI and GSAS were used to obtain lattice parameters from the peak positions in the XRD patterns.[1,2]

The peak positions can be related to the lattice parameters via the Bragg equation:

$$\lambda = 2\, d_{hkl} \sin \theta_{hkl}, \qquad (3.3)$$

where λ is the wavelength of the incident beam (Cu kα = 1.54 Å), d_{hkl} is the lattice spacing (Å) and θ_{hkl} is the angle between incident and reflected beam (°). For a cubic unit cell a = b = c and therefore,

$$a = \sqrt{d_{hkl}^2 \, x \, h^2 \, x \, k^2 \, x \, l^2} \qquad (3.4)$$

where a is the lattice parameter of the cubic cell (Å) and h,k,l are the Miller indices of the lattice plane. For a tetragonal unit cell a = b ≠ c and therefore the lattice parameters a and c are determined as:

$$a = \sqrt{d_{hkl}^2 \, x \, h^2 \, x \, k^2} \ , \qquad (3.5)$$

$$c = \sqrt{d_{hkl}^2 \, x \, l^2}, \qquad (3.6)$$

An orthorhombic unit cell a ≠ b ≠ c separates all three lattice parameters, a, b and c.

3.2.2.2 Scanning electron microscopy (SEM)

Scanning electron microscopy (SEM) was carried out on the raw materials and final sintered products to determine the particle size, grain structure and general microstructure, as appropriate.

An electron beam scans a sample in an SEM. The incident electrons either back scatter due to elastic collisions or release secondary electrons from inelastic collisions. These electrons, back scattered or secondary, can be detected and resolved into high resolution images.

Powdered samples were prepared by dispensing a small amount of powder on a double-sided sticky carbon pad which was mounted on an aluminium stud.

Pellets were initially polished with 800, 1200 and 2500 grit silicon carbide paper, followed by 6, 3 and 1 µm diamond polish pastes on synthetic polishing cloths. They were then washed with acetone and thermally etched for 1 h at 90% of the sintering temperature. The etched pellets were mounted on aluminium stubs using silver paste (Agar Scientific Ltd., Stansted, UK). Both pellet and powder samples were coated with a conducting gold layer (EMSCOPE SC500A, Quorum Technologies, Laughton, UK) to facilitate Energy Dispersive Spectroscopy (EDS).

Samples were examined using an Inspect F50 FEG (FEI, Hillsboro, Oregon, USA) SEM operating at a spot size of 3.0 and 20 kV for pellets and 15 kV for powders.

3.2.3 Dielectric measurements

Electrical characterisation was carried out on dense sintered ceramics, which had been polished to remove any surface layers. Before measurements, they were coated with silver (Agar Scientific Ltd., Stansted, UK) or gold paste (M-9875 Gold Paste, Metalor Technologies (UK) Ltd., Birmingham, UK) and fired at 600 °C for 30 min or 800 °C for 2h, respectively.

3.2.3.1 Capacitance, permittivity and dielectric loss

Fixed frequency capacitance and tan δ data were measured using an inductance/capacitance /resistance (LCR) meter (Agilent E4980 Precision LCR Meter, Agilent Technologies, Santa Clara, CA, USA) with an applied ac voltage of 100 mV. Data points were collected every 60 s at 5 different frequencies (1, 10, 100 and 250 kHz and 1 MHz) from room temperature to 400 °C. This was performed in a non-inductively wound tube furnace at a rate of 1 °C / min. The relative permittivity of the sample was calculated from the capacitance:

$$\varepsilon_r = \frac{C \cdot t}{\varepsilon_0 \cdot A} \qquad (3.7)$$

where, ε_r is the relative permittivity (F/m), C is the capacitance (F), t is the thickness of sample (m), ε_0 is the permittivity of free space (8.854 x 10^{-12} F/m) and A is the surface area of sample (m^2).

3.2.3.2 Impedance spectroscopy (IS)

The electrical microstructure of ceramics can be investigated using impedance spectroscopy (IS).[3] For an ideal (bulk) dielectric material, the electrical response to an

AC voltage can usually be described by a Resistor-Capacitor (RC)-parallel-circuit, as shown in figure 3.1.

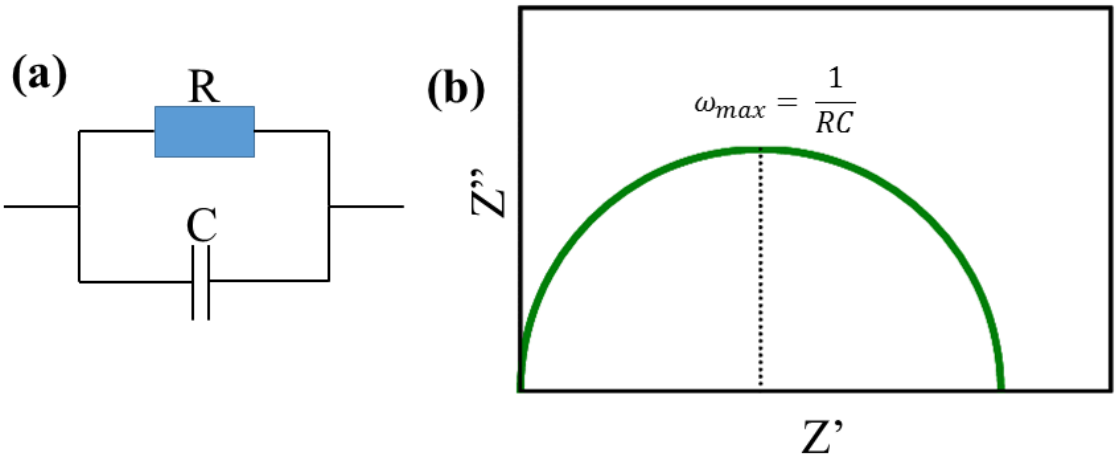

Figure 3.1. Schematic of (a) an RC parallel circuit and (b) a Nyquist plot of impedance for an ideal bulk material.

The Nyquist plot for the RC-parallel-circuit is a single semicircle with the Z'' maximum at R/2 corresponding to the angular frequency $\omega_{max} = 1/RC$, where $\omega_{max} = 2\pi f$. Different electro-active regions of a ceramic (eg bulk, grain boundary etc) can be assigned their own RC-parallel element and time constant, τ, which is responsible for the resolution between regions.

$$\tau = RC \qquad (3.8)$$

The 'brickwork layer model' (BLM) in figure 3.2 shows a schematic of a general ceramic. The bulk part of the grains is clearly surrounded by a grain boundary (gb) and summing electric pathways in series for each equivalent circuit allows for conversion of resistance and capacitance into intrinsic properties, *i.e.* conductivity and permittivity of the bulk. The grain and gb in the BLM possess the same relative permittivity, but the resistivity and therefore the time constant for the gb is much higher than that of the bulk.

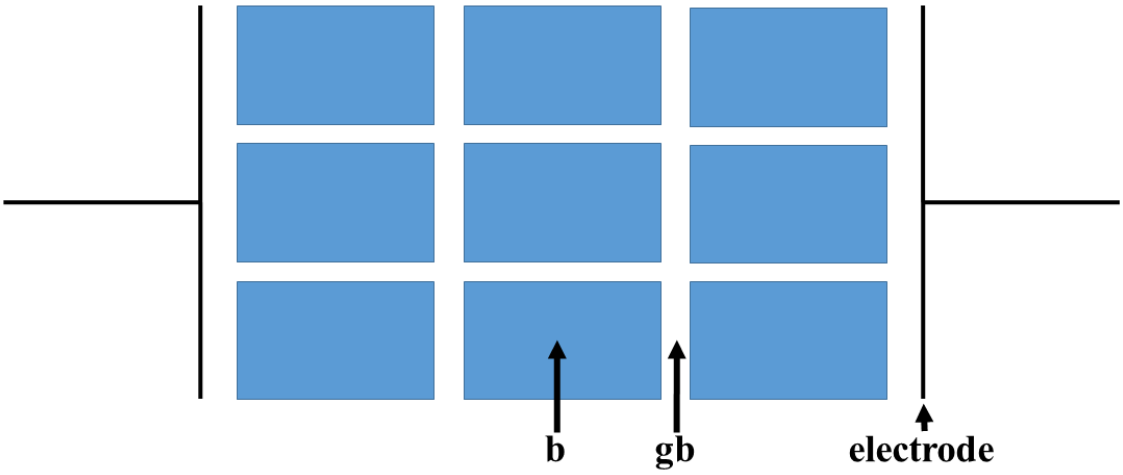

Figure 3.2. Schematic of brickwork layer model of b (bulk) and gb (grain boundary) regions in a ceramic sample.

With the BLM resulting in an isotropic microstructure it is possible to regard the components as two RC elements in series, as shown in figure 3.3. The impedance plots associated with this model allows to simulate impedance data, which can be used to extract the material properties.

In 2014 Dean *et al.* developed a FEM framework that allows comprehensive studies of 3D-heterognous ceramics.[4] Their work showed the importance of microstructure when analysing IS data. A simulated microstructure with a high volume fraction of gb, *i.e.* a small grain volume fraction, resulted in large errors between the properties extracted from the resulting impedance data and the properties that were assigned in the model. These errors were kept below 10% when the gb made up only ~ 1 % of the total thickness of the sample. Therefore, it can be surmised that the BLM and the associated RC-elements are a reasonably close fit to the real values, as long as the gb stays small compared to the grain volume fraction.

A difference of around two orders of magnitude in τ is generally required to obtain well separated semi-circles for the different regions, as shown in figure 3.3. Common ceramic regions are the bulk (b) and grain boundary (gb) regions and their semicircles in the impedance plot allow the extraction of their respective R values from their intercepts on the Z' axis. C values can also be obtained from the impedance plot using equation 3.11.

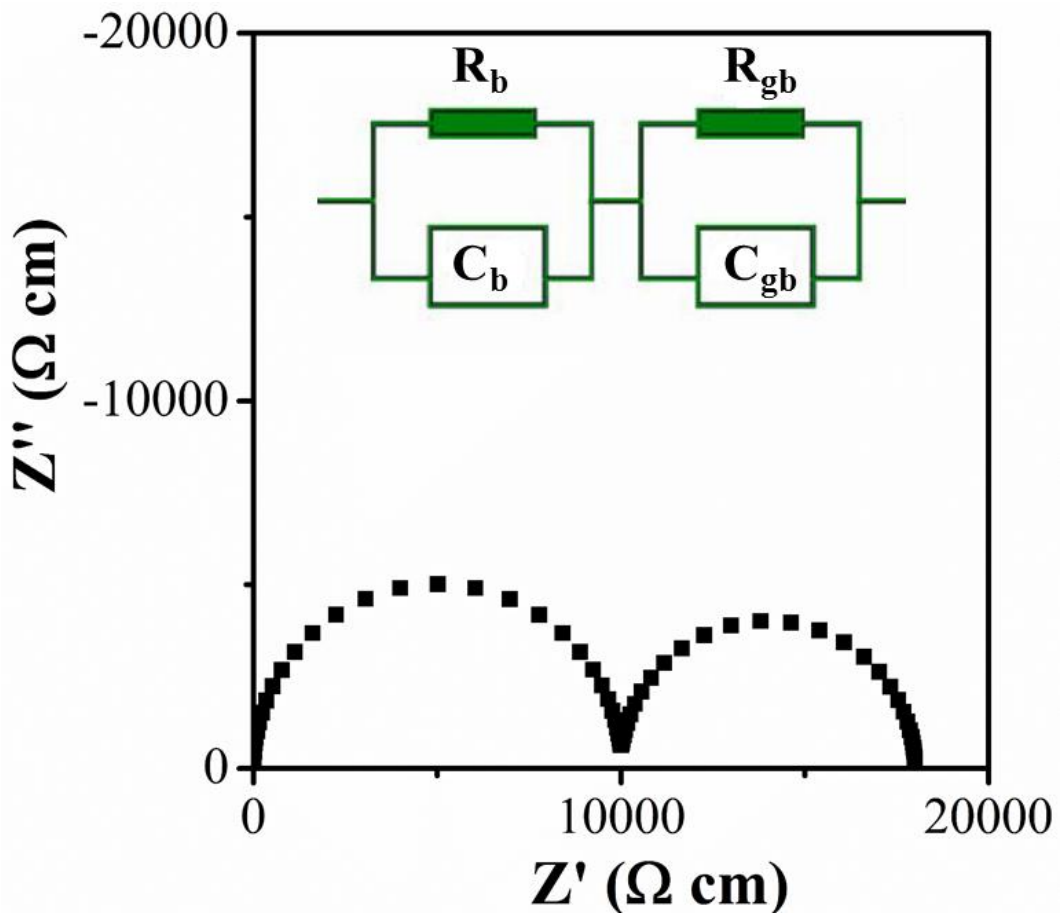

Figure 3.3. Schematic impedance plot for ceramic showing the capacitances and equivalent circuit associated with the sample regions.

The basis of extracting R and C of the bulk and gb are the Z* and M* plots, in particular their imaginary components. Z* and M* are given as:

$$Z^* = Z' - j\,Z'' \qquad (3.9)$$

and

$$M^* = M' + j\,M'', \qquad (3.10)$$

where $j = \sqrt{-1}$.

To obtain the resistance values of different samples and their electro-active regions, Debye peaks in Z" and M" spectroscopic plots were used. The largest Debye peak in the M" plot was used to give grain/bulk data. At the peak maximum:

$$\omega RC = 1, \quad (3.11)$$

and

$$M''_{max} = 1 / (2C_b), \quad (3.12)$$

where, ω is the angular frequency (rad/s), R is the resistance (Ω), C is the capacitance (F), M''_{max} is the maximum M" value (F^{-1}) and C_b is the bulk capacitance (F).

The R and C values of any resistive grain boundaries can be extracted from the Z" plot using equation 3.11 and the maximum Z" value, as

$$Z''_{max} = R/2. \quad (3.13)$$

Characteristic capacitance values for the different regions in a ceramic sample can be found in table 3.1.

Table 3.1. Characteristic capacitances for ceramic samples, reproduced from Irvine *et al.*[3]

Normalised Capacitance in F/cm	Origin of RC element
10E-12	Bulk (ε_r ~ 10)
10E-11	Minor 2° phase
10E-11 - 10E-8	Grain boundary
10E-10 - 10E-9	Bulk ferroelectric (ε_r ~ 100 to 1000)
10E-9 - 10E-7	Surface layer
10E-7 - 10E-5	Sample - electrode interface

Two factors that play a role in IS are the electrodes and the partial oxygen pressure (ρO_2). There are two types of electrodes: blocking and non-blocking electrodes. In non-blocking electrodes the faradaic reactions, *i.e.* electron charge transfer between electrode and electrolyte, are fast and the resistance of charge-transfer is negligible and therefore

not detectable in IS. In the case of blocking electrodes, there are no faradaic reactions, instead there is a buildup of electrically charged layers on the surface of the electrode.

These ion-layers act like a dielectric in a conventional capacitor and possess a double-layer capacitance. This additional capacitance shows up in the Z* plot as a 90° spike at low frequencies. The electrode spike in IS and therefore the buildup of ions in the dielectric are a good indicator of ionic conduction in the material, as ion mobility is required for the ion build up at the electrode. Partially blocking electrodes have spikes that are less than 90° and possess a faradaic-charge-transfer-resistance. Therefore, partially blocking electrodes have their own RC-parallel elements, blocking electrodes only have an extra capacitance component in series to the RC-parallel elements of the grain and gb.

One common kind of ionic conduction in oxides is via oxygen ions. A good way to determine the presence of oxygen ion conduction is ρO_2-dependent IS. Low ρO_2 would lead to less oxygen conduction and therefore the electrode spike would reduce. High oxygen ρO_2 will improve oxygen ion conduction and the spike will increase. This method works with solid electrolytes, which possess only ionic conduction, but not necessarily for systems with mixed ion conduction. Transport measurement numbers of ions are a better way of determining the ionic contribution in mixed conductors. Here a sample is compared to a perfect ionic conductor reference.

ρO_2 can also be used to determine whether the electronic conduction in a sample is n- or p-type. n-type conduction uses e^- as their conduction mechanism. These can often be created by the loss of lattice oxygen, as seen in equation 3.14.

$$O_O^x \rightarrow V_O^{\cdot\cdot} + \frac{1}{2}O_2 + 2e^-. \qquad (3.14)$$

Reducing ρO_2 increases the oxygen loss in the sample and therefore a sample will be n-type if the conductivity increases with decreasing ρO_2. In case of p-type conduction, holes are the charge carriers. They are created by the mechanism shown in equation 3.15.

$$V_O^{\cdot\cdot} + \frac{1}{2}O_2 \rightarrow O_O^x + 2h^{\cdot}. \qquad (3.15)$$

In this case increasing the ρO_2 will lead to an increase in charge carriers and therefore increasing ρO_2 will increase the conductivity of the sample.

The activation energy associated with the bulk and grain boundary conduction processes can be found using Arrhenius plots,

$$\sigma = \sigma_o e^{(Ea / kT)}, \qquad (3.16)$$

where σ is the conductivity (S cm^{-1}), σ_o is the pre-exponential constant (S cm^{-1}), E_a is the activation energy (J or eV), k is the Boltzmann constant (1.38 x 10^{-23} J K^{-1} or 8.6173324 x 10^{-5} eV K^{-1}) and T is the temperature (in K).

When plotting $\log_{10}$ (σ) *vs.* 1000/T(K), E_a (in eV) and the slope, m, of the linear fit of the data corresponds to equation 3.17.

$$E_a = -m\ (0.1986). \qquad (3.17)$$

IS data were collected with an Agilent E4980A Precision LCR Meter with an applied ac voltage of 100 mV. The collected data were analysed using the Zview Impedance Analysis software (Scribner Associates, Inc., Southern Pines, NC) and corrected using the geometric factor of the sample to convert capacitance and resistance into capacitivity and resistivity. The geometry factor is obtained by:

$$GF = \frac{A}{d}, \qquad (3.18)$$

where A is the electrode area (cm^2) and d is the thickness of sample (cm).

3.3 Processing of Materials

3.3.1 Raw Materials

Raw materials used were $BaCO_3$ (≥99%, Sigma-Aldrich, Dorset, UK), TiO_2 (≥99.9%, rutile, Sigma-Aldrich, Dorset, UK), Na_2CO_3 (≥99.5%, Fisher Scientific, Loughborough, UK), Nb_2O_5 (99.999%, Stanford Materials Corporation, USA), V_2O_5 (≥99.6%, Sigma-Aldrich, Dorset, UK) and ZrO_2 (99.9%, Aldrich, Dorset, UK).

3.3.1.1 Drying of raw materials

The electrical properties of $BaTiO_3$-based materials are influenced significantly by the stoichiometry of its components. Therefore it is extremely important to be as accurate as possible when weighing out batches of powders. A significant source of non-stoichiometry can be the amount of water or carbon dioxide in the starting reagents.[5] To remove these potential sources of error from the starting reagents, each powder was dried pre-weighing. Drying temperatures used for each reagent can be found in table 3.2. They were dried overnight and then cooled to 200 °C after which they were transferred to a sealed desiccator to cool to RT.

Table 3.2. Drying temperatures of starting reagents.

Material	Drying temperature / °C
$BaCO_3$	180
TiO_2	900
Na_2CO_3	180
Nb_2O_5	900
V_2O_5	180
ZrO_2	1000

3.3.1.2 Phase analysis of raw materials

The starting reagents were analysed using XRD to confirm their phase purity and to provide information on unit cell parameters.

3.3.2 Processing of ceramics

Polycrystalline samples for the solid solutions listed in Table 3.3 were prepared using the solid state mixed oxide route.

The reagents were used in ~ 50 g stoichiometric batches according to the desired composition. The composition was weighed out with an accuracy of ± 0.001 g and ball-milled using 10 mm diameter Y_2O_3 stabilized zirconia milling media for 12h. Once milled the milling media was removed and the remaining slurry dried at 80 °C for 12h.

Table 3.3. Solid solutions prepared and their respective sintering temperatures.

Solid solution	x-content	Sintering temperature / °C
$Na_xBa_{1-x}Nb_xTi_{1-x}O_3$	0	1400
	0.001	1400
	0.01	1400
	0.02	1400
	0.0225	1400
	0.025	1400
	0.0275	1400
	0.03	1400
	0.04	1400
	0.05	1400
	0.075	1400
	0.1	1400
	0.85	1250
	0.9	1250
	0.95	1250
$BaZr_xTi_{1-x}O_3$	0.1	1400
	0.15	1400
	0.2	1400

The dried sample was then sieved through a 200 µm mesh sieve and the resulting powder was reacted in an alumina crucible for 6 hours. The reaction temperature suitable for all compositions was 1140 °C with a heating rate of 5 °C/min. Following this, the

powder was ball-milled, dried and sieved again, as described above. The formed perovskite structure was confirmed *via* XRD.

The powder obtained by this procedure was pressed into pellets with a 10 mm diameter. This was done in a uniaxial press at ~ 0.3 tonne for ~ 1 min. The green pellet was then placed on Pt-foil in an alumina crucible and sintered in air for 8 h with a ramp rate of 5 °C/min at the appropriate temperature for each composition, as listed in Table 3.3, to achieve >95 % of the theoretical density (for $BaTiO_3$ the theoretical density is 6.012 g/cc). The sintering profile is shown in figure 3.4.

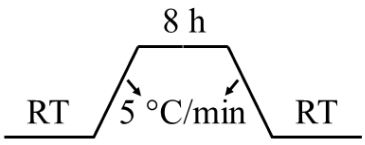

Figure 3.4. Sintering profile for ceramic samples.

3.4 References

1 A. C. Larson and R. B. von Dreele, *'General Struct. Anal. Syst. (GSAS)', Los Alamos Natl. Lab. Rep. LAUR 86-748*, 1994.

2 B. H. Toby, *J. Appl. Crystallogr.*, 2001, **34**, 210–213.

3 J. T. S. Irvine, D. C. Sinclair and A. R. West, *Adv. Mater.*, 1990, **2**, 132–138.

4 J. S. Dean, J. H. Harding and D. C. Sinclair, *J. Am. Ceram. Soc.*, 2014, **97**, 885–891.

5 M. Li, H. Zhang, S. N. Cook, L. Li, J. A. Kilner, I. M. Reaney and D. C. Sinclair, *Chem. Mater.*, 2015, **27**, 629–634.

Chapter 4: $NaNbO_3$-$BaTiO_3$ solid solution series: RE-free donor-acceptor doped BT

4.1 Introduction

$BaTiO_3$ (BT) is one of the most important functional ceramic materials and has a wide range of applications in industry. Rare-earth doped $BaTiO_3$-based materials are the backbone of the multilayer ceramic capacitor (MLCC) industry based on their low temperature coefficient of capacitance (TCC) behaviour.[1–5] A low TCC is commonly achieved *via* a core-shell microstructure (CS), but CS need careful processing and the microstructural analysis can be challenging.[6] Doping BT with $NaNbO_3$ (NN) could offer the opportunity to combine sustainability with easier processing, whilst maintaining the improved TCC of MLCCs associated with donor-acceptor-doping of intermediate RE-ions, such as Dy^{3+}.[7,8]

NN forms a complete solid solution with BT and it is known that even at low NN-contents relaxor-behaviour is observed.[9,10] The NN-content required to obtain relaxor behaviour in NNBT is considered to be between 6-8 mol%.[11,12] Ferroelectric-relaxors possess broadened permittivity responses and the possibility exists to create a large enough temperature stable permittivity plateau for the material due to the relaxor behaviour. For that purpose, the low NN-content side of the NNBT solid solution is of particular interest, as processing might shift the relaxor-onset below the reported 6-8 mol%.

The creation of the temperature stable permittivity plateau should be aided by the fact that Na_2O can be volatile. The assumption is that very small quantities of Na can be lost as Na_2O during the high temperature sintering required to form dense ceramics and therefore result in a heterogeneous distribution of the dopant concentration in the ceramic. Inhomogeneous dopant dispersion can assist in lowering TCC as it can work in a similar manner to the concentration-gradient of dopants in a CS microstructure.

One of the main reasons to use NN as a dopant material is the associated cost and potential supply shortages for RE-ions, in particular Dy^{3+} with its strong price fluctuations and high demand.[13,14] Whilst niobium is not a significantly cheaper substitute it makes up only half of the cation dopants, with the extremely cheap and abundant sodium making up the other 50 %. This would reduce cost significantly, if a similar dopant content to

current RE-doped MLCCs could be used. This again makes the low dopant end of the solid solution more important, as the high end would not be an economical substitute and would only fulfil the sustainability aspect of replacing the scarce RE ions.

Another aspect of choosing NN as a dopant material is the donor-acceptor-doping of intermediate RE-ions in BT. The associated self-compensation mechanism is believed to help improve the lifetime of devices, as it leads to a lower level of oxygen vacancies. Accumulation of oxygen vacancies in a MLCC is considered a significant reason for electrical breakdown of the devices.[5,15–19] NN as a dopant system offers self-compensation, even though the donor and acceptor sites are reversed compared to RE^{3+}-doping.

In this chapter the electrical properties of the NNBT solid solution were studied, with an emphasis placed on relaxor-behaviour and temperature stable permittivity profiles.

4.2 Experimental

The ceramic processing and data collection processes are detailed in chapter 3. The air sintering temperatures for low-doped NNBT was 1400 °C and the highly-doped NNBT samples were sintered at 1250 °C. The sintering temperatures were chosen to achieve dense ceramics.

4.3 Results

4.3.1 Phase composition and microstructure

The materials for this solid solution and their preparation are split and discussed in two subsets. The first subset contains those materials with low NN-concentration (≤ 10 mol %) and the second is with higher NN-concentration (≥ 85 mol %). The high dopant materials were added to establish the properties across the solid solution; however, the main focus was on the lower dopant concentrations.

Room temperature X-ray diffraction (XRD) patterns for the low dopant concentration materials (≤ 10 mol %) are shown in figure 4.1. Peaks may be indexed either according to a single tetragonal perovskite phase or as dopant concentration increases to a cubic phase. This trend is confirmed by the lattice parameters in figure 4.2, as a and c converge

with increasing NN-content, leading to a c/a ratio that reaches 1 for x ≥ 7.5 mol %. This coincides with T_C shifting below room temperature, the temperature at which the XRD data were collected. The c/a ratio was calculated from the tetragonal splitting observed for the (200) peak at 2θ = 45º.

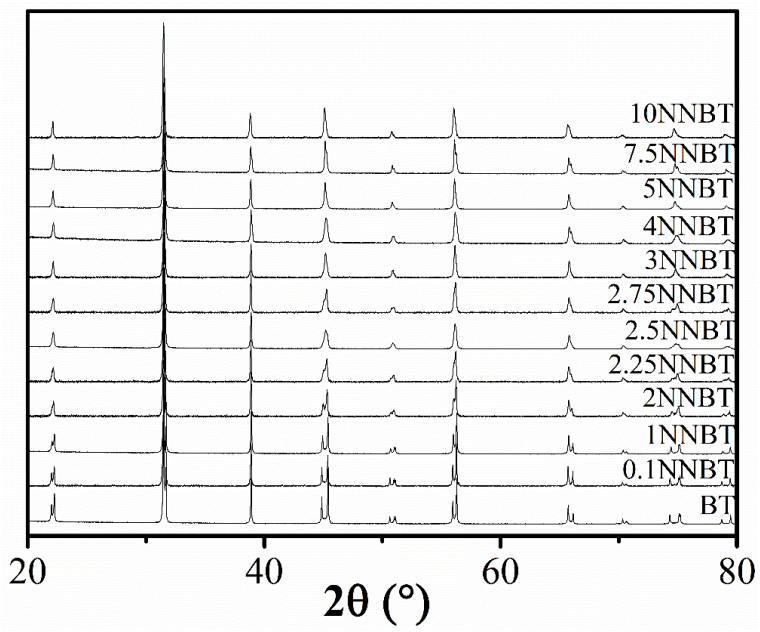

Figure 4.1. Room temperature XRD patterns of low xNNBT, 2θ = 20º - 80º, after sintering at 1400 ºC for 8h.

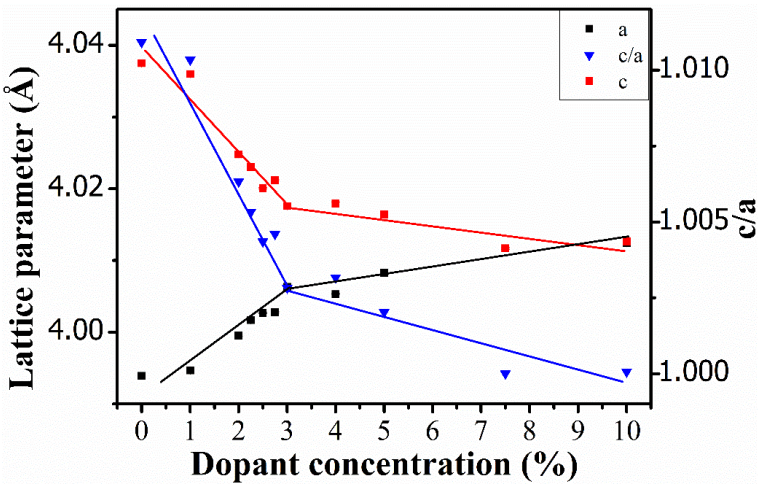

Figure 4.2. Change in lattice parameters and tetragonality, c/a, at 2θ = 45º as a result of NN dopant concentration. Straight lines are to guide the eye.

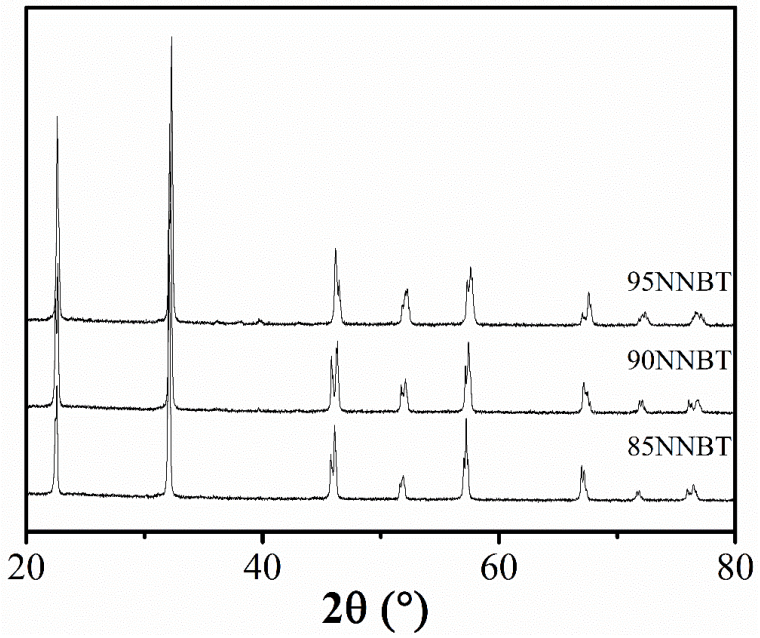

Figure 4.3. XRD patterns of high xNNBT, 2θ = 20º - 80º, after sintering at 1250 ºC for 8h.

Table 4.1. Lattice parameter for xNNBT with x = 85, 90 and 95.

NN-content (%)	a (Å)	b (Å)	c (Å)
85	5.5675 (3)	15.8435 (3)	5.5638 (3)
90	5.5498 (5)	15.8239 (4)	5.5431 (5)
95	5.5789 (2)	15.6222 (4)	5.5373 (2)

For compositions with NN-content ≥85 mol % the main phase is orthorhombic as shown in figure 4.3. Again, there are no secondary phases detected by XRD. Lattice parameters are listed in table 4.1. The significant trend is that cell volume decreases linearly with increasing dopant concentration, as shown in figure 4.4.

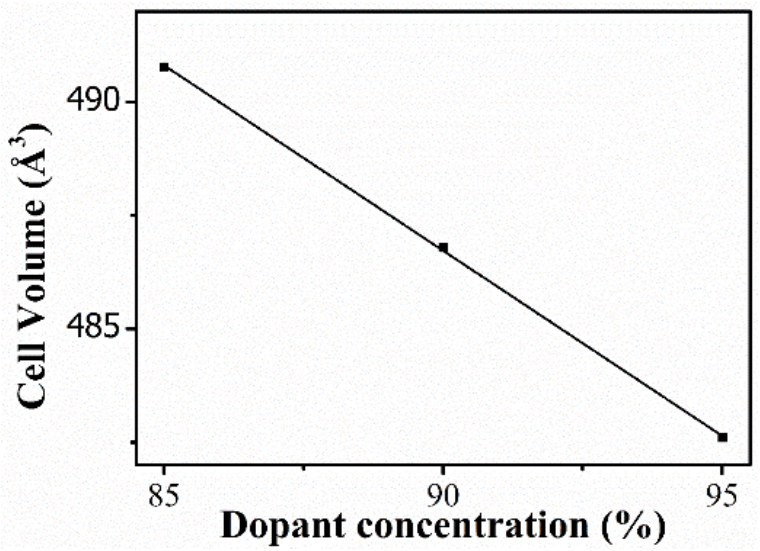

Figure 4.4. Change in cell volume as a result of dopant concentration for ≥85% NN. Straight line

Representative micrographs of the microstructures are displayed in figure 4.5. There is no prevalent grain size, instead a large variety of ~0.5 to several microns. No grains were found to exceed 10 μm. All ceramics showed microstructures consistent with being > 95 % dense (table 4.2).

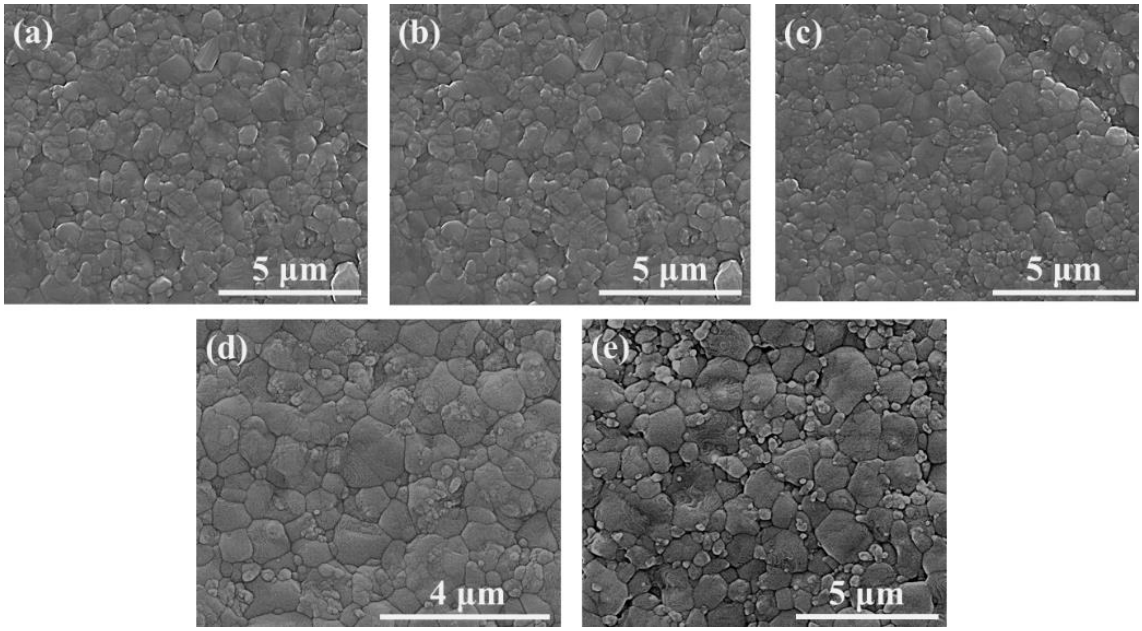

Figure 4.5. SEM micrographs of a (a) 2NNBT, (b) 2.5NNBT, (c) 3NNBT, (d) 5NNBT and (e) 10NNBT ceramic. Sintered at 1400 °C for 8 h, thermally etched at 1260 °C for 0.5 h.

Table 4.2. Theoretical and relative densities for selected compositions of the NNBT series. Compositions with high NN contents were sintered at 1250 ºC and the compositions with low NN content were sintered at 1400 ºC.

NN-content (%)	theo. Density (g/cc)	rel. density (%)	sintering temperature (°C)
0	6.01	96.8	1400
1	6.00	96.7	1400
2	5.98	98.4	1400
2.25	5.97	99.4	1400
2.5	5.97	95.3	1400
2.75	5.96	97.1	1400
3	5.95	98.2	1400
4	5.94	99.7	1400
5	5.91	99.2	1400
7.5	5.86	99.1	1400
10	5.81	99.7	1400
85	4.72	95.5	1250
90	4.66	95.3	1250
95	4.61	93.2	1250

4.3.2 Electrical properties

Permittivity profiles and tan δ for the low NN-content materials are shown in figure 4.6. The general trend for this part of the solid solution series is that T_C shifts to lower temperature with increasing NN-content. Concurrently, a significant broadening of the peak is observed which becomes obvious at concentrations ≥ 2 mol %. tan δ is well below 5 % for the displayed temperature range. The shape of the tan δ profile corresponds to that of the permittivity profile, i.e. the materials that possess sharp peaks in their permittivity profile show similar behaviour in tan δ but as the permittivity profile broadens, no sharp peak is observed in tan δ.

Broadening of the permittivity peak suggests the onset of relaxor behaviour as discussed in the introduction. The onset of broadening at 2 mol % is unexpected as it is significantly lower than that reported in the literature.[10,11] To determine whether this material already exhibits relaxor behaviour it is necessary to inspect the frequency dependency of its permittivity and tan δ profiles. Figure 4.7 compares 2NNBT to 1NNBT which does not show relaxor behaviour.

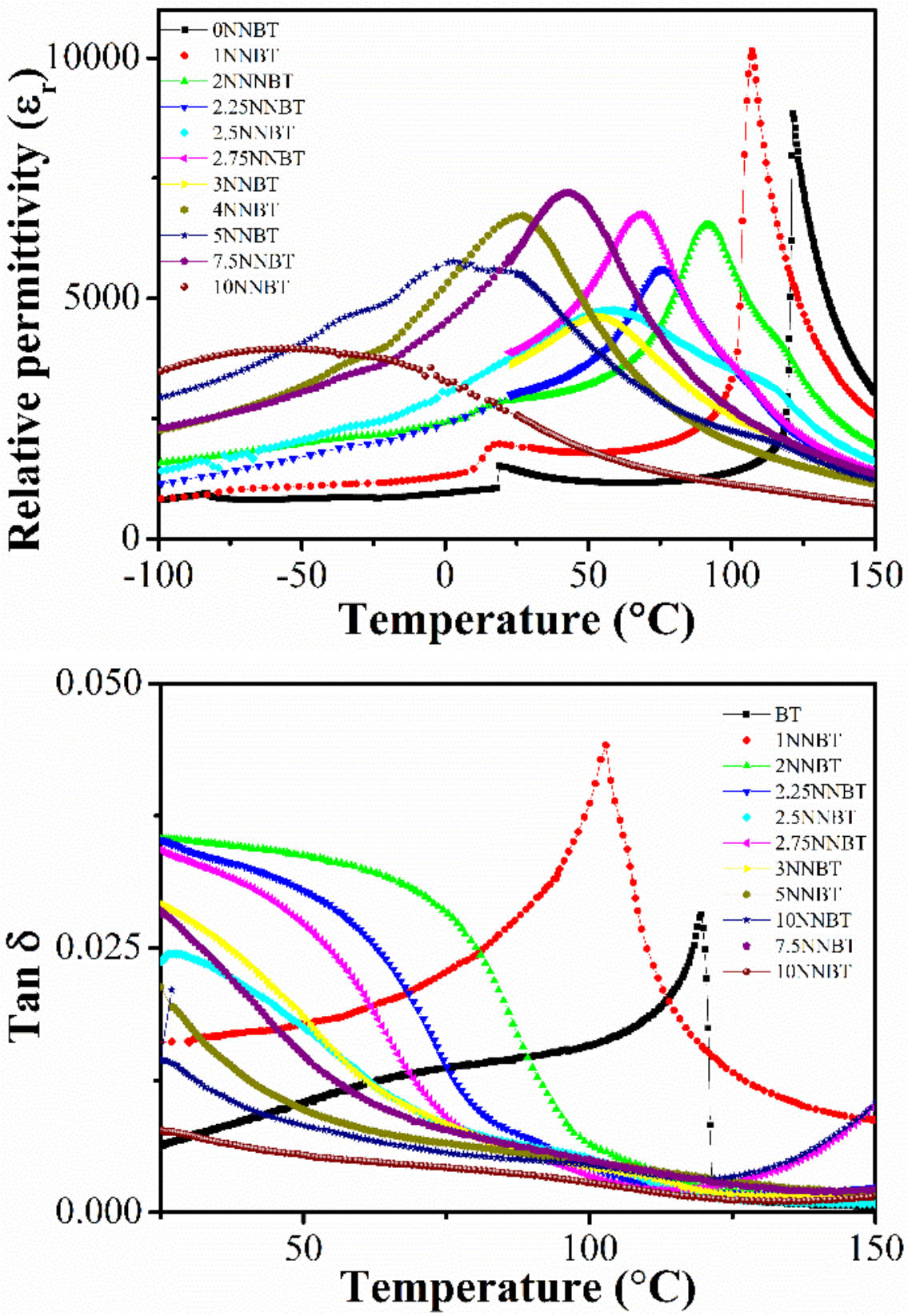

Figure 4.6. (a) Permittivity (100 kHz) *vs.* temperature profiles and (b) dielectric loss (100 kHz) *vs.* temperature profiles for xNNBT ceramics, where x ≤ 10%, after sintering at 1400 ºC for 8h.

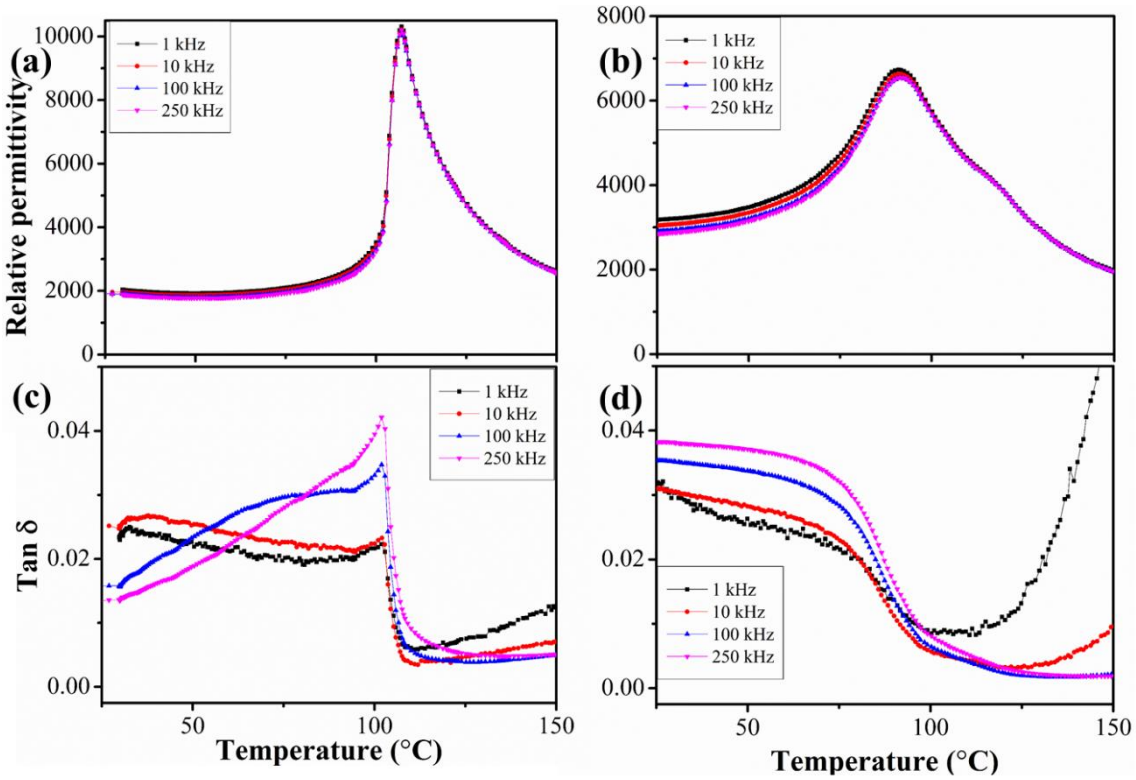

Figure 4.7. Effect of frequency on the permittivity (a, b) and tan δ (c, d) profiles for 1NNBT (a, c) and 2NNBT (b, d) ceramics.

When considering the permittivity profiles of 2NNBT there is a small frequency dependency below T_C with permittivity decreasing with increasing frequency. Above T_C there is no frequency dependent behaviour and the materials therefore exhibit relaxor-type behaviour. This is confirmed on inspection of the tan δ profiles. There is a shift to higher temperatures for the tan δ profile with increasing frequency. The onset of relaxor behaviour for the materials processed here is 2 mol % of NN and therefore at significantly lower concentration than previously reported 4 mol% in the literature.[10,11]

In addition to the relaxor behaviour, 2NNBT shows a weak second peak at ~125 °C, which corresponds to the T_C of undoped-BT and is indicative of a CS microstructure with a BT core. This BT associated peak is observed in most of the permittivity profiles, leading to the conclusion that relaxor behaviour and inhomogeneity play a role in the broadening of the permittivity profiles.

Other compositions of note are 5 and 10NNBT. The profile of 5NNBT shows triple peak behaviour in addition to the BT peak. The triple peak is likely due to the phase transitions in the material which are discussed in more detail later. 10NNBT is the first

profile that appears not to exhibit a BT peak and shows the broadest permittivity plateau. Unfortunately, it is at a temperature that is unsuitable for MLCC applications.

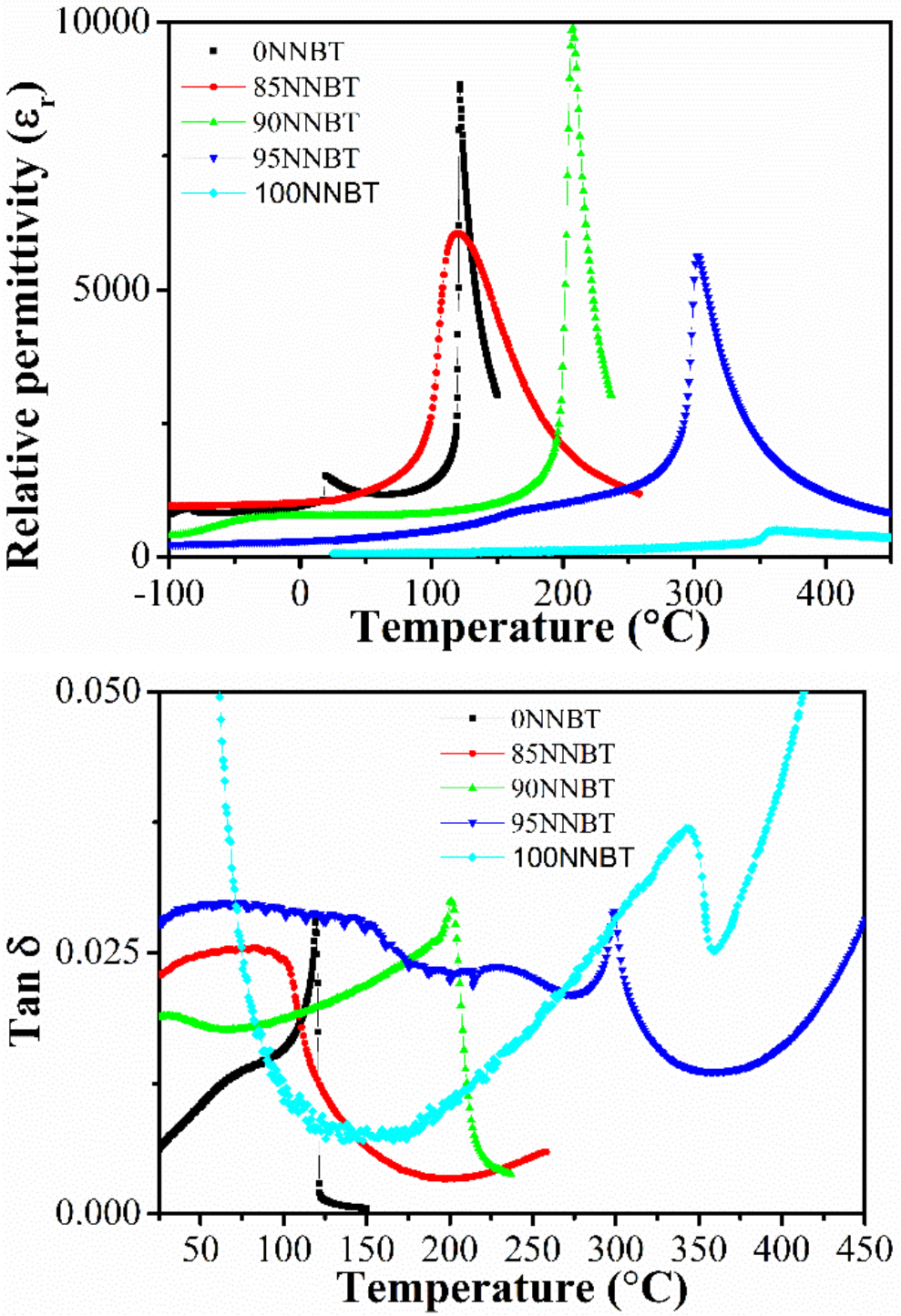

Figure 4.8. (a) Permittivity (100 kHz) *vs.* temperature profiles and (b) dielectric loss (100 kHz) *vs.* temperature profiles for xNNBT ceramics, where x = 0, 85, 90, 95 or 100, after sintering at 1250 ºC for 8h (1200 ºC for 2h for x = 100).

The permittivity and tan δ temperature profiles for NN-content ≥85 mol % materials are shown in figure 4.8. Undoped BT is included as a reference and the trend observed when using BT as a starting point is the opposite of the low-dopant end. Increasing the amount of NN in the material leads to an increase in T_C on this side of the solid solution. An increase in peak broadening is observed in 85NNBT but not in the samples of higher dopant concentrations.

Table 4.3. Summary of TCCs versus xNNBT for different temperature ranges.

xNNBT	max TCC_{Abs} -55 to 125 °C	max TCC_{Abs} -55 to 150 °C
0	185	185
1	515	515
2	125	125
2.25	84	84
2.5	58	33
4	83	78
5	77	68
7.5	78	69
10	80	65
85	473	473
90	30	16
95	134	85

The TCC of the materials in this series are summarised in table 4.3. The closest to the industry norm of ±15 % are 2.5 and 90NNBT. In general, TCC is improved due to relaxor behaviour and processing induced inhomogeneity.

The temperature at ε_{max} changes with increasing dopant concentration for the low NN materials, figure 4.9. In the literature Kwon *et al.* have shown that this temperature drops with increasing NN content up to 40 mol % before rising with further increased dopant levels.[11]

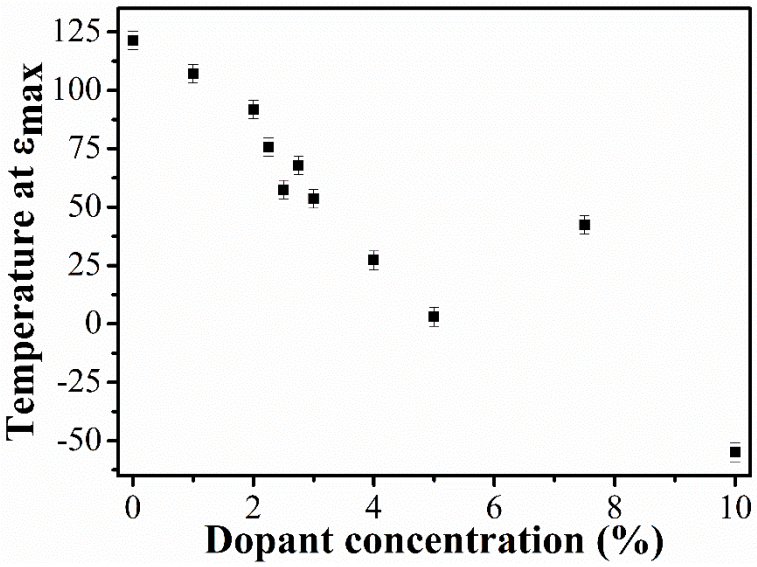

Figure 4.9. The variation of temperature at ε_{max} with NN-content at the low end of the NNBT solid solution.

Figure 4.10 shows how the data from the literature compare to the materials prepared in this work. As shown, the trend in the literature seems to be replicated fairly well for the materials here. Kwon states that at around 40 mol % the behaviour of the materials change from being BT-like to being dominated by NN. This statement is certainly true for the range of compositions prepared here.

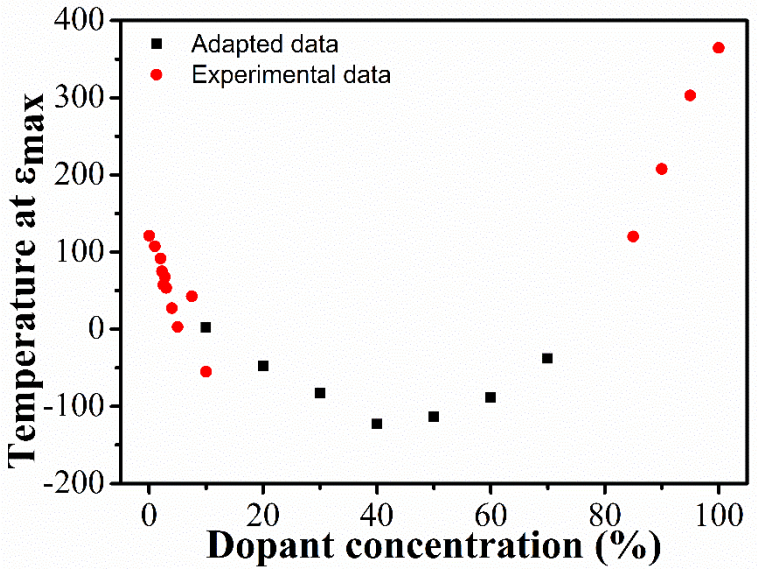

Figure 4.10. The variation in temperature at ε_{max} due to changes in NN-content for data obtained experimentally (red) and that adapted from Kwon *et al*[11] (black).

Initially the drop in T_{max} is due to the change in ionic radii due to the addition of NN. This can be seen in figure 4.11. The drop in the T_{max} profile starts off parallel to the drop in lattice parameter; however, once the relaxor behaviour and CS-like behaviour appear in the permittivity data, it is possible to also observe a deviation from this trend. The change in T_{max} is therefore not only due to ionic size mismatch.

The same thing can be observed on the opposite side of the solid solution. Starting from NN, T_{max} initially drops linearly due to the decrease in tolerance factor but as the peak broadening in the permittivity profiles sets in at around 85NNBT, there is a strong deviation from this trend.

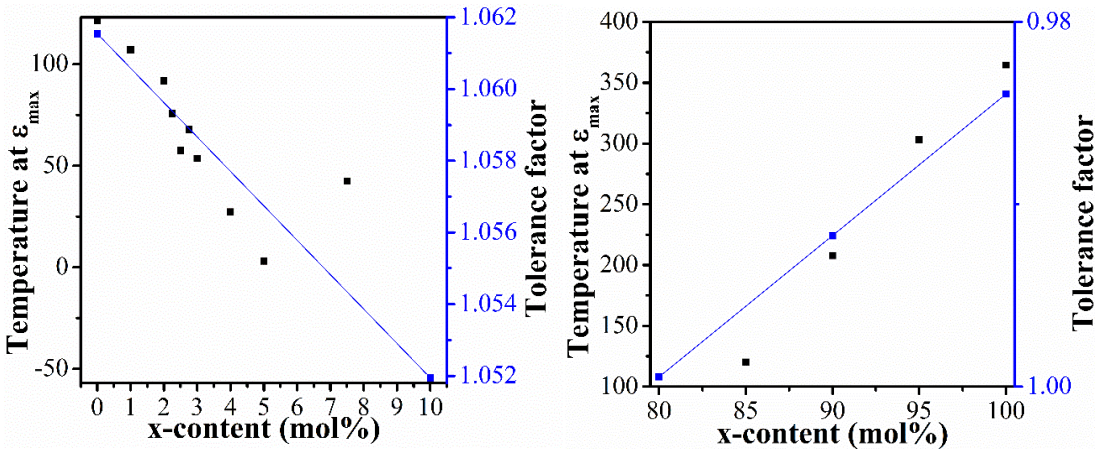

Figure 4.11. Change in T_{max} and tolerance factor with increasing NN-content for (left) low and (right) high NN-contents. Straight lines are the change in tolerance factor with x-content.

One explanation for these trends is that the solid solution possesses two ordered end-members, which maintain their structure with small amounts of dopants and therefore T_{max} changes linearly with ionic size. For those compositions that do not possess relaxor behaviour, T_C corresponds to T_{max}. When the relaxor behaviour starts to occur, there is an increase in disorder of the system with increasing solid solution. This disorder leads to a deviation from linear behaviour. In the middle of the solid solution is where the maximum disorder in the system is found, which stabilises the drop in T_{max} and enables a switch between BT- and NN-dominated order.

Future work should be conducted to look closer at the structural changes occurring throughout this solid solution, particularly at the low temperature range. This might help

in further understanding the behaviour of T_{max} and might provide insight to the formation of the broad permittivity plateaus in this solid solution series. This series provides a large range of broad T_{max}, which makes it a useful platform in the design of new, low TCC materials.

Going back to the low NN side, the trend of a decreasing temperature for the tetragonal-cubic transition (T-C) is accompanied with an increase in the rhombohedral-orthorhombic (R-O) transition, as shown in figure 4.12. In comparison, the orthorhombic-tetragonal (O-T) transition stays nearly constant. Figure 4.11 shows the transitions that are clearly visible in the permittivity profiles. At ≥ 3 mol % it is not possible to observe any distinct transitions and therefore only an R-C transition temperature is given. Extrapolation of the trends in temperature change shows that all three transitions may occur at the same temperature at around 5 mol %. This would account for the three broad peaks observed in the permittivity profile of 5NNBT in figure 4.6.

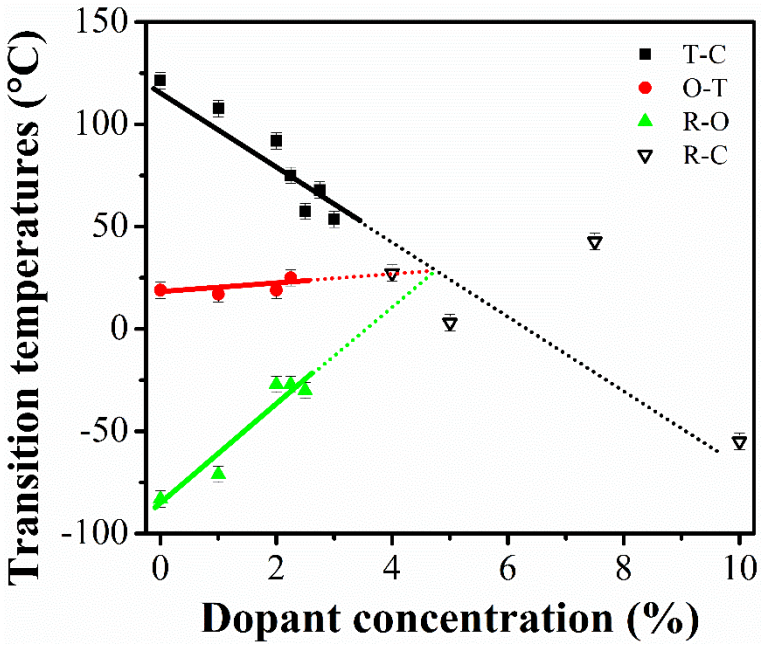

Figure 4.12. Observed change in polymorphic phase transition temperatures with increasing NN-content based on permittivity data. Straight lines are to guide the eye.

Curie-Weiss (CW) plots are a good way of showing phase transitions in ferroelectric materials. The inverse of permittivity at temperatures above T_C often obeys the Curie-Weiss law, which is linear and therefore allows for extrapolation of the Curie temperature, T_0. A summary of the CW plots for low NN-content compositions is shown in figure 4.13

and it is possible to observe a change in behaviour, as there are profiles showing sharp 1st order transitions, as well as profiles that do not show sharp transitions. The different types of transitions are now analysed in more detail.

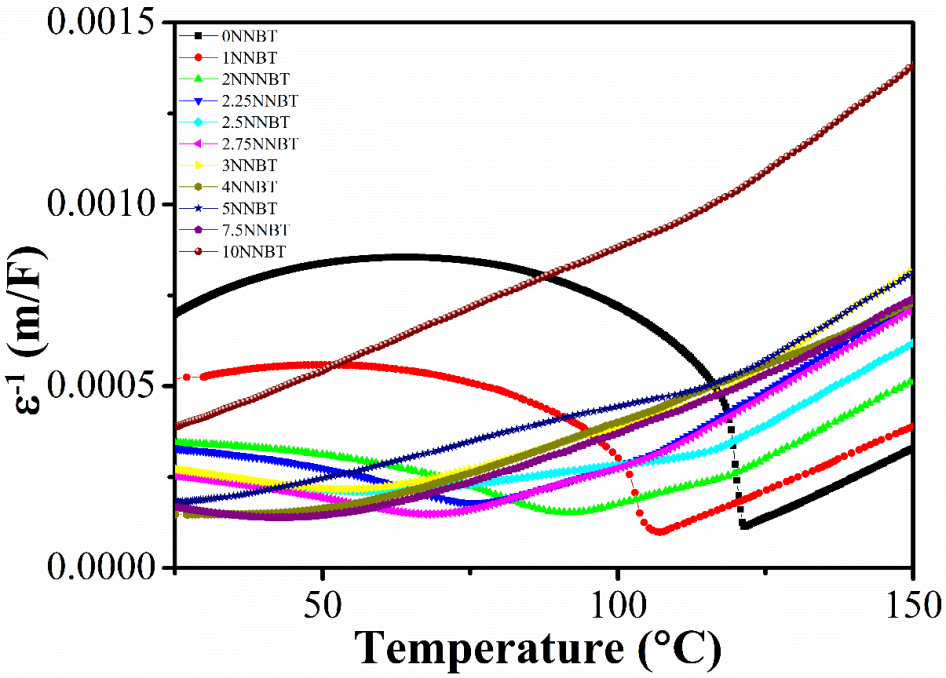

Figure 4.13. Curie-Weiss plots of xNNBT for x ≤ 10.

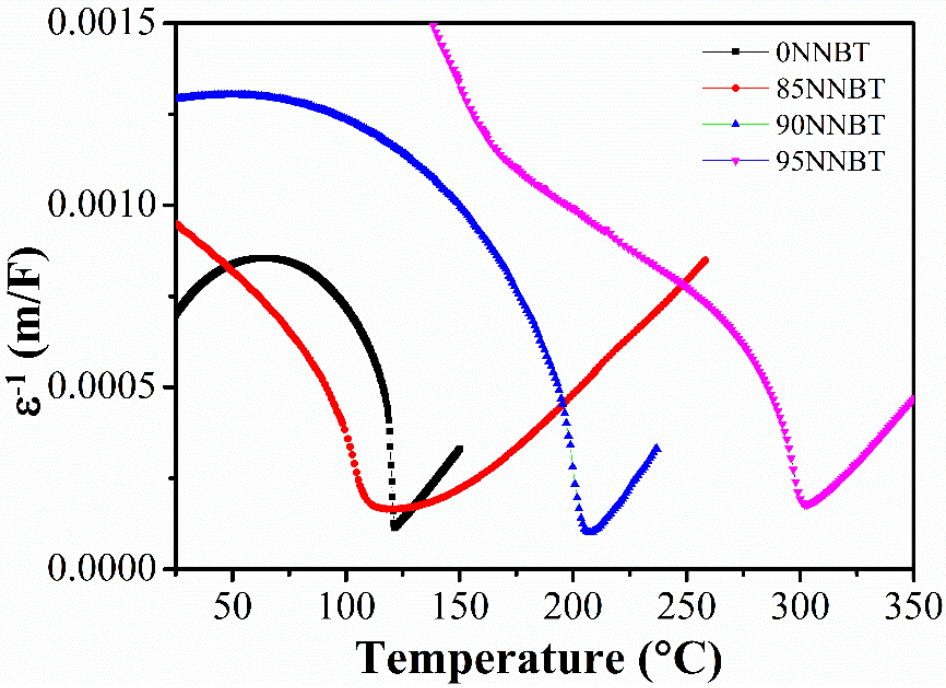

Figure 4.14. Curie-Weiss plots of xNNBT for x ≥ 85.

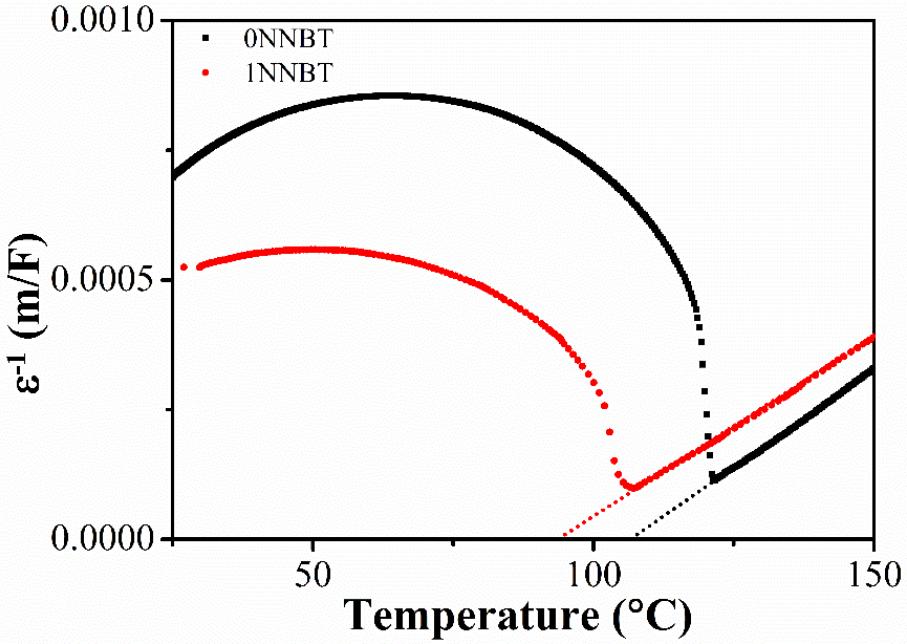

Figure 4.15. Curie-Weiss plots for undoped BT and 1NNBT showing 1st order phase transitions.

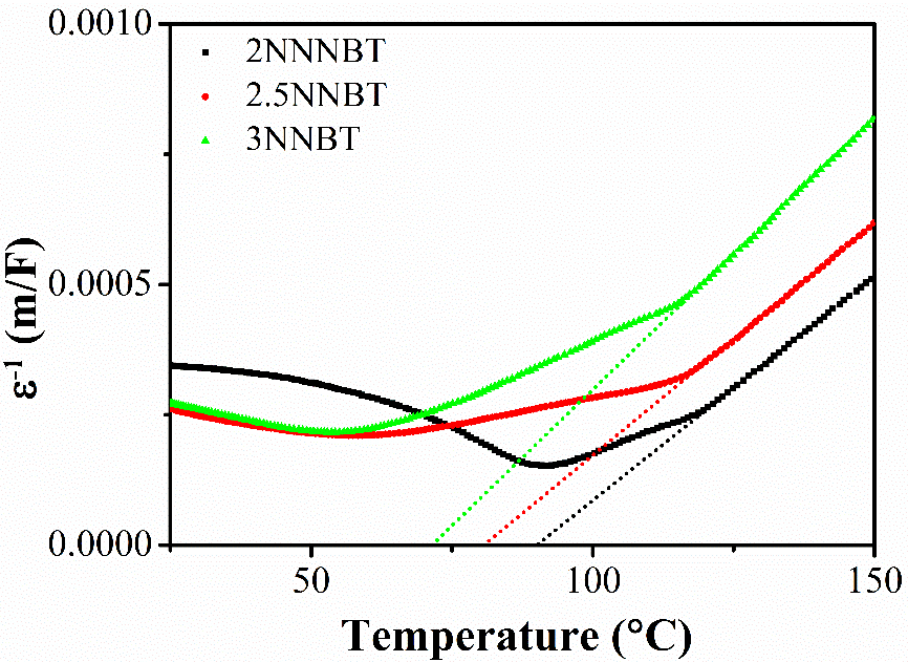

Figure 4.16. Curie-Weiss plots for low xNNBT compositions, 2≤ x <4, showing a transition different to a 1st order-type phase transitions.

A general observation for the low NN-content materials is the gradient change around ~125 °C. This is due to chemical inhomogeneity causing the presence of a BT-'core'. This is observable in the permittivity profiles, however 10NNBT shows this in the CW-plot, but it is not obvious from the permittivity profile.

In contrast, the high NN-content compositions show more similar behaviour. Sharp transitions can be seen in the 90 and 95NNBT samples and even the 85NNBT sample shows some resemblance of a 1st order transition. However, it is clear that it would not be necessary to significantly lower the NN-concentration to lose the 1st order transition completely.

Returning to the low NN-concentration side, the only compositions that show sharp, 1st order-type transitions are undoped BT and 1NNBT. Figure 4.15 shows their CW plots along with the extrapolation of T_0. Increasing the dopant concentration leads to a transition that is clearly not 1st order, as shown in figure 4.16. There is still a significant change in gradient to be able to identify where the data start to deviate from linear CW behaviour. Increasing the dopant concentration to > 4 mol % however puts the materials into the third category. Figure 4.17 shows that it is very difficult to see the exact temperature at which the material starts to deviate from linear CW behaviour. The BT-'core' is maintained throughout this range of compositions.

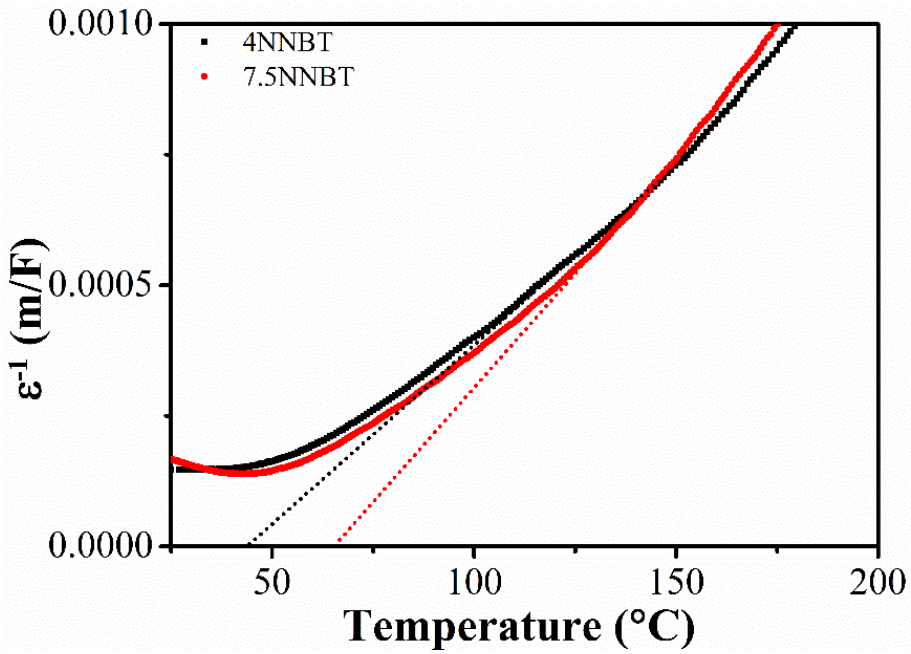

Figure 4.17. Curie-Weiss plots for NNBT compositions, 4≤ x ≤10, showing diffuse transition behaviour.

To get a better understanding of the information presented in the CW plots, figure 4.18 shows a summary of three characteristic temperatures that can be obtained from CW plots. The extrapolated Curie temperature, T_0, the temperature at ε_{max}, T_{max} and the Burns temperature T_d. T_d is the temperature at which the data start to deviate from the CW behaviour and it is found that this temperature shows very little change for compositions with up to 10 mol % NN. This is expected, as the maximum deviation observed in the literature is ~50 °C across the entire compositional range. The magnitude of T_d is ~125 °C, which is the T-C transition temperature for undoped BT. Increasing change in T_d is expected with increasing dopant concentration beyond 10 mol% or changing the processing conditions to limit inhomogeneity.

Both T_0 and T_m decrease with increasing NN-content, however at different rates. This leads to a cross over between the two temperatures at ~2 mol %. Initially T_{max} exceeds T_0, however above 2mol % this trend is reversed and the crossover coincides with the occurrence of relaxor behaviour in the solid solution.

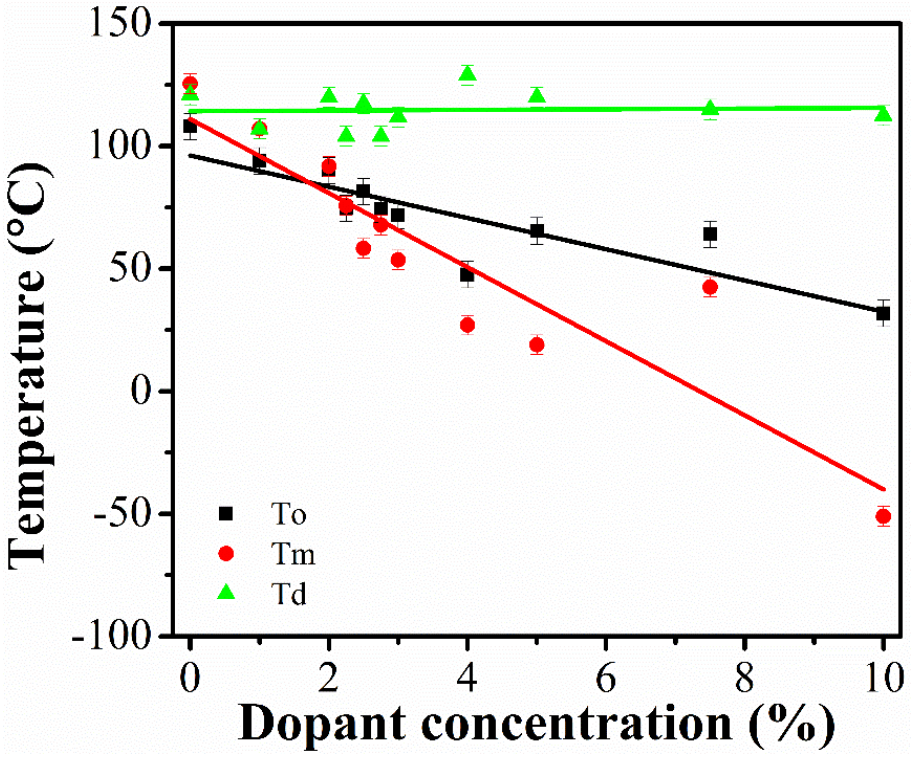

Figure 4.18. Three characteristic temperatures, the extrapolated Curie temperature (T_0), the temperature of dielectric maximum (T_m) and the Burns temperature (T_d) for xNNBT ceramics. Straight lines are to guide the eye.

Another way of analysing CW plots is calculating the fitting parameters δ and γ, as discussed in chapter 2. The critical exponent γ is of particular interest, as it gives a value between 1 and 2, where 1 corresponds to classical ferroelectric behaviour and 2 corresponds to relaxor behaviour. In a log-log plot of $(1/\varepsilon_r - 1/\varepsilon_m)$ *vs.* $(T-T_m)$, γ is the slope of the graph. The diffuseness parameter δ allows a value to be attributed to the broadness of the permittivity profiles. This allows for a qualitative direct comparison of the profiles for the various compositions.

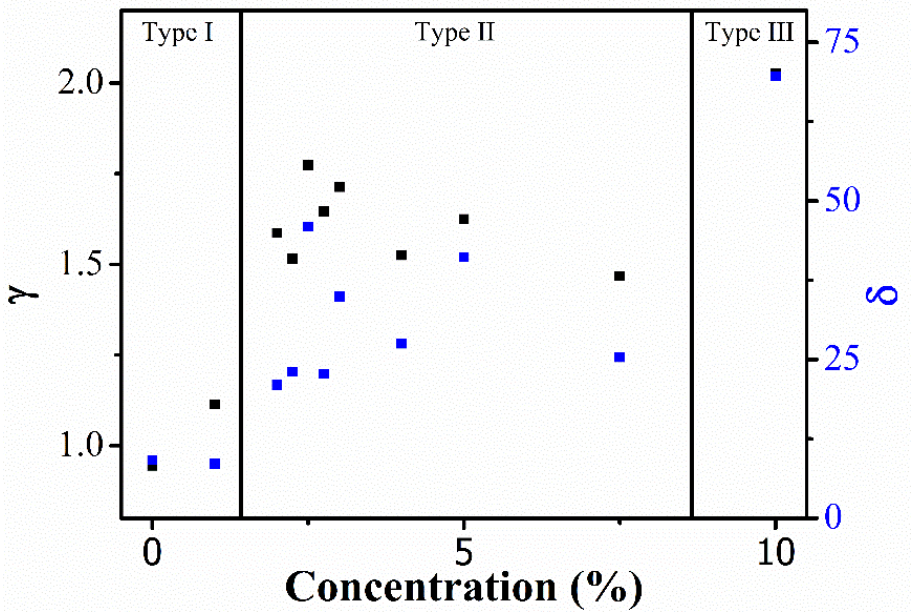

Figure 4.19. Fitting parameters γ and δ of the dielectric data for xNNBT ceramics.

Figure 4.19 shows the results for the fitting parameters. The observed trends for the diffuseness parameter is an increase in diffuseness as the NN-content is increased. This is not surprising as it reflects the first impression given by the permittivity profiles in figure 4.6. There is a less clear trend for γ, even though the overall trend would still show an increase from 0 to 10 mol% NN-content. It is possible, however, to split the compositions into three types, which can be related to γ. Type 1 are the ferroelectric compositions, where $\gamma \sim 1$, Type 2 are the mixed ferroelectric-relaxors, were $\gamma \sim 1.5$ and finally Type 3 are the relaxors with $\gamma \sim 2$.

Table 4.4 summarises the fitting parameters and associates each composition with ferroelectric- , relaxor- or mixed-behaviour. It also lists the intercepts β from the log-log plots of $(1/\varepsilon_r - 1/\varepsilon_m)$ *vs.* $(T-T_m)$, which were used to calculate δ.

Table 4.4. Fitting parameters γ and δ of dielectric data for xNNBT ceramics.

Type	x-content	γ	β	δ
I	0	0.94 (1)	-11.66 (3)	9.17 (3)
	1	1.11 (1)	-12.31 (2)	8.61 (2)
II	2	1.59 (2)	-14.31 (8)	20.97 (8)
	2.25	1.52 (1)	-14.07 (5)	23.06 (5)
	2.5	1.77 (1)	-15.95 (5)	45.94 (5)
	2.75	1.65 (1)	-14.65 (5)	22.75 (5)
	3	1.71 (1)	-15.22 (4)	34.94 (4)
	4	1.53 (1)	-14.56 (2)	27.52 (2)
	5	1.63 (1)	-15.36 (4)	41.14 (4)
	7.5	1.47 (1)	-14.32 (2)	25.35 (2)
III	10	2.03 (2)	-17.57 (8)	69.64 (8)

Table 4.5. Summary of the number of impedance elements observed in the M'', Z'' and Z* formalisms for ceramics in the solid solution series.

Composition	no. of elements	bulk	gb	total	electrode effect
	1-3	M''	Z''	Z*	Z*
0		1	2	2	no
1		1	2	2	no
2		1	1	3	yes
2.25		1	1	2	no
2.5		1	1	3	yes
2.75		1	1	3	yes
3		1	1	2	no
4		1	1	3	yes
5		1	1	3	yes
7.5		1	1	3	yes
10		1	1	3	yes
85		1	1	3	yes
90		1	1	3	yes
95		1	1	3	yes
1 - M'' - largest peak is used for bulk analysis					
2 - Z'' - largest peak used for gb analysis					
3- Z* - total resistivity of ceramic (b + gb)					

Impedance spectroscopy (IS) was carried out on the compositions of this series. Table 4.5 shows which element of the ceramics was analysed using which impedance formalism. The bulk (grain) response was investigated using the largest Debye peak in M" spectroscopic plots, whilst information on the grain boundary (gb) was obtained from the largest Debye-like peak in Z" spectroscopic plots. The capacitances associated with the largest peaks from the M" and Z" spectroscopic plots were in the range of 10^{-10} F cm^{-1}. For the M" plots, this means the largest peak is associated with the bulk response, whereas the Z" plots are generally dominated by the gb response but the presence of a smaller Z'' peak at higher frequency can be identified as the bulk response. The time constants of the bulk and gb are often not different enough to separate them completely. However, this analysis gives the best insight into the gb properties of the materials. The total resistivity of the ceramics was obtained from the low frequency intercept on the real axis of Z* plots, as were the signs of electrode effects, as observed in figure 4.20.

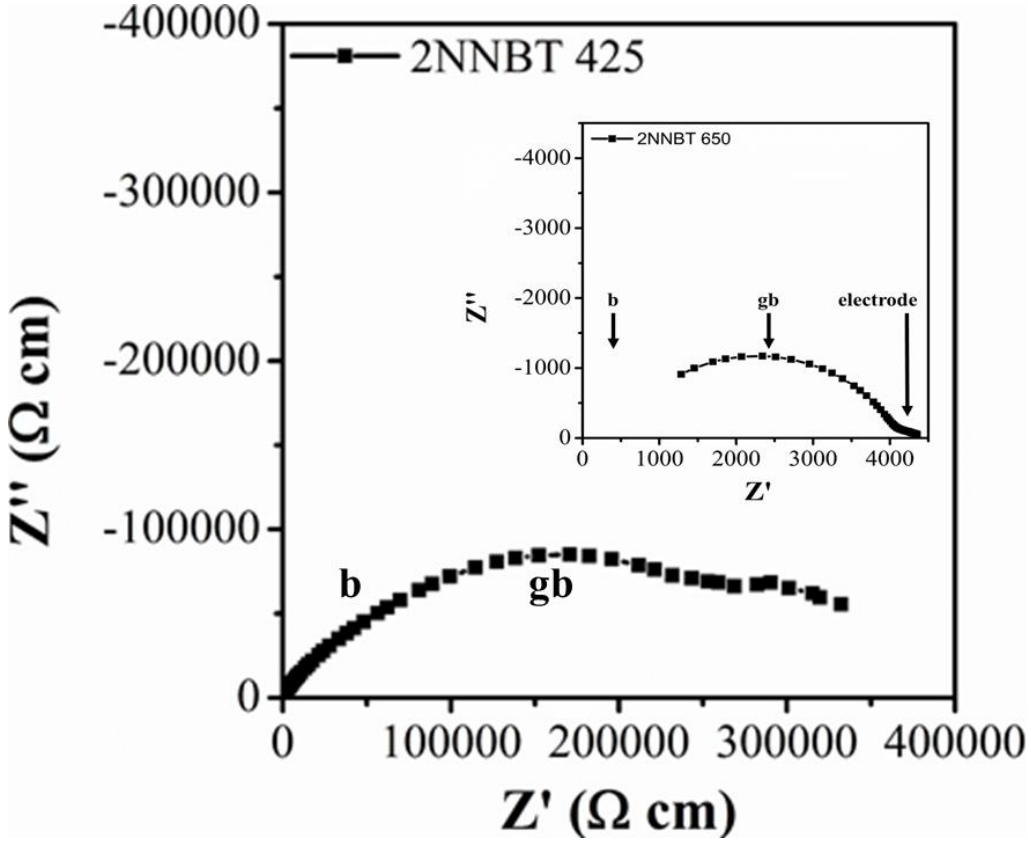

Figure 4.20. Z* plot of 2NNBT at 450 and 650 °C (inset), highlighting the different elements identified. Inset, the bulk element is indicated but not observed in the Z* plot at the higher temperature.

Figure 4.21 is a summary showing selected combined Z” and M” spectroscopic plots. With increasing dopant level there is a switch in the impedance behaviour from the total resistance being dominated by the bulk component (single M’’ and Z’’ peaks that are nearly co-incident), Fig. 4.21 (a) towards grain boundary dominated resistance behaviour (dominant Z” peak becomes increasingly separated from the larger M’’ peak and occurs at lower frequency), Figure 4.21 (b) - (f). The largest peak in the M” spectroscopic plots is attributed to the bulk component of the ceramic. Apart from 0NNBT and 1NNBT, none of the plots show peaks in the Z” plots at 350 ^{o}C. That means only these two materials have significant bulk contributions to their overall resistance, as the other bulk contributions are too small to be observed on Z” plots.

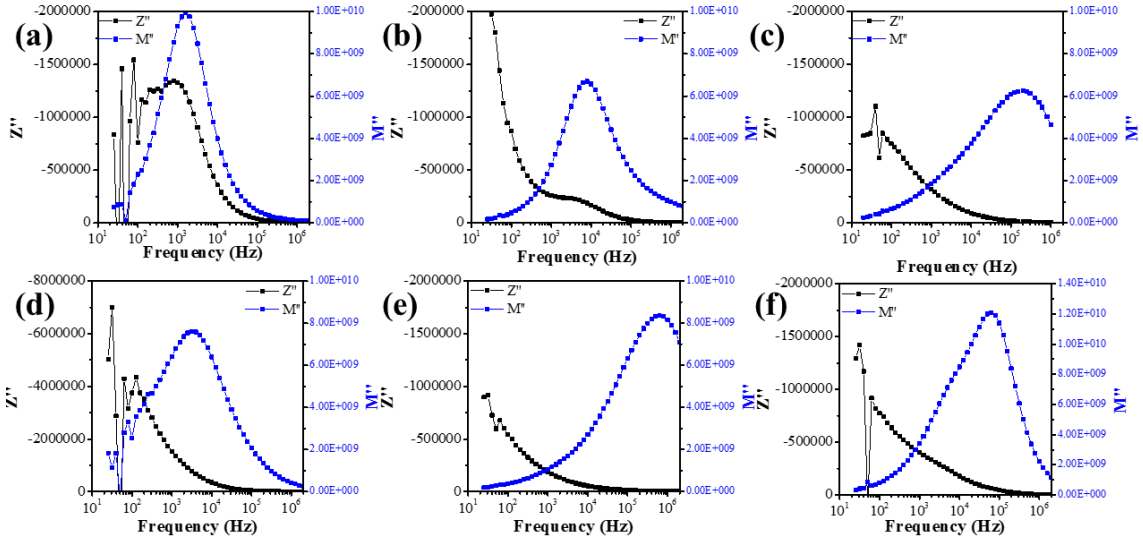

Figure 4.21. Z” and M” vs. log frequency plots for selected compositions of the xNNBT solid solution series at 350 °C, for (a) 0NNBT, (b) 1NNBT, (c) 2NNBT, (d) 2.5NNBT, (e) 5NNBT and (f) 10NNBT.

The most important trend was observed from the M” spectroscopic plots for the low NN-content compositions, figure 4.22. The M’’ peaks were associated with the bulk component of the electrical microstructure and showed significant broadening with increasing dopant level. This coincides with the broadening of the permittivity profiles and is suggestive of inhomogeneous grains resulting in electrical inhomogeneity. The reason for this inhomogeneity might be the existence of regions with small deviations in dopant level compared to each other or the existence of CS microstructures.

There appears to be no trend in f_{max} for the M'' peak in this series. This is significant, as increasing the dopant level should result in a systematic trend in the bulk properties. In this case the processing conditions, whilst favourable for temperature stable permittivity profiles, allow for the bulk components of the materials to reach varying degrees of thermodynamic equilibrium. CS microstructures are based on kinetically limited reactions and the inhomogeneity of the bulk responses indicates significant kinetic-limited reactions have occurred under the processing conditions employed in this study.

This inhomogeneity limits the usefulness of impedance spectroscopy, as the data becomes more processing dependent and less material dependent. In order to investigate the IS bulk properties in this series further, the processing should be modified to try and achieve full thermodynamic equilibrium across the solid solution. Improved homogeneity should be reflected in narrower and better defined Debye peaks in the M'' spectroscopic plots. This investigation should be considered for future work.

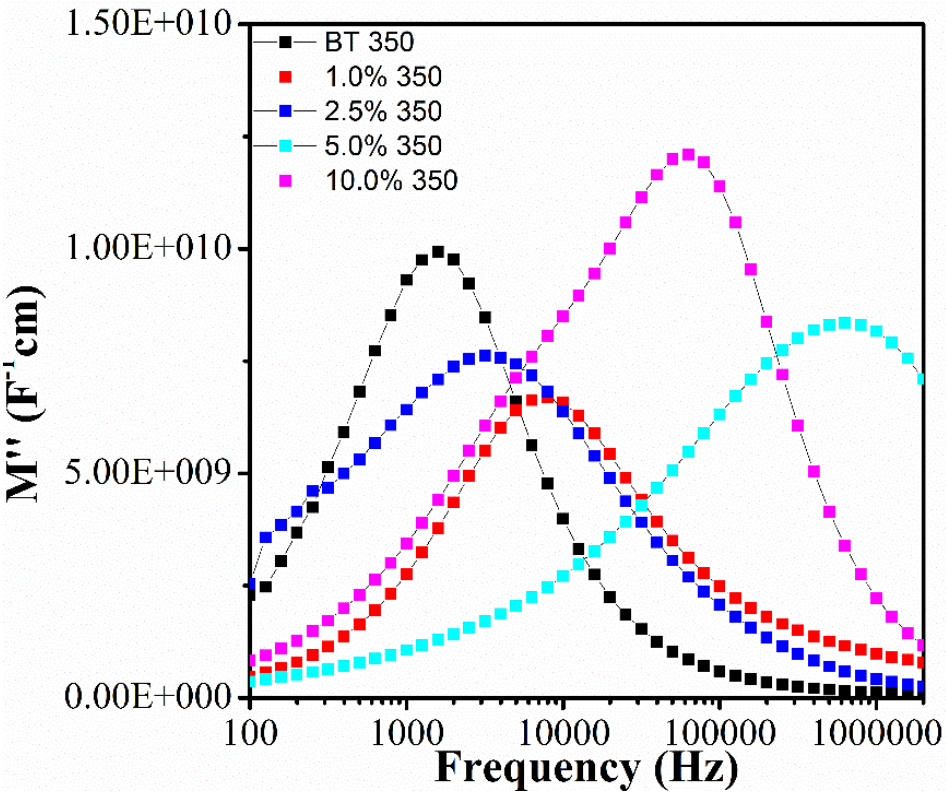

Figure 4.22. M'' vs. log frequency for selected compositions of the xNNBT solid solution series.

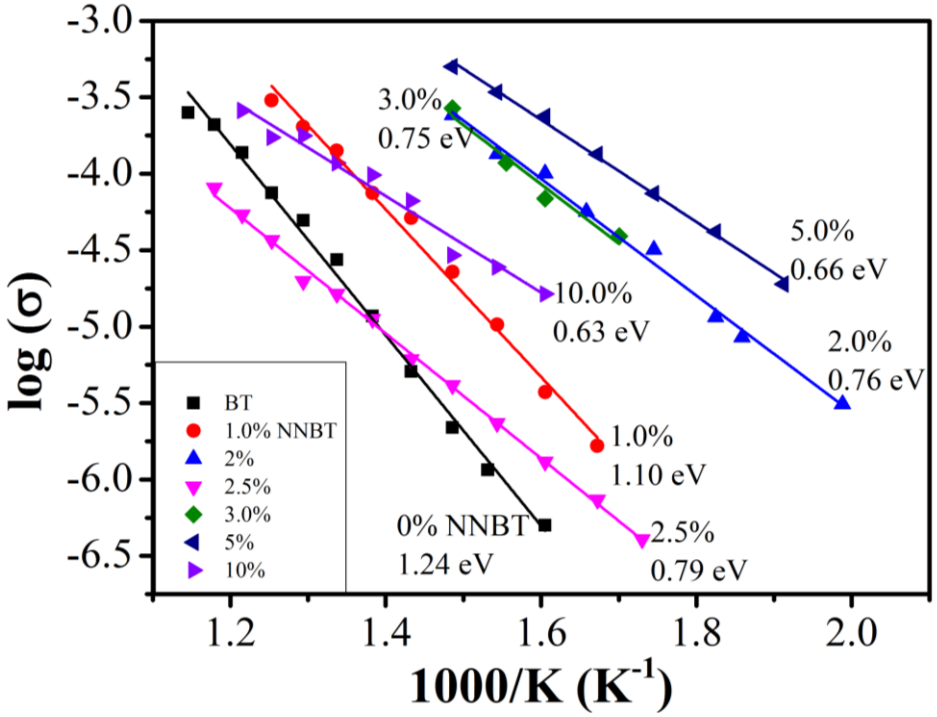

Figure 4.23. Arrhenius behaviour of bulk conductivity data extracted from M'' spectroscopic plots for xNNBT, where x ≤ 10.

Data from the M" spectroscopic plots were analysed and used to determine the activation energy for the bulk conductivity *via* Arrhenius plots, as described in Chapter 3. The Arrhenius plots for some of the low NN-content compositions are shown in figure 4.23. A change in gradient and therefore activation energy can be attributed to a change in conduction behaviour. Looking at the figure, it is possible to see essentially three different gradients. Interestingly, the three gradient regimes and the associated compositions for each gradient coincide with the three classes of materials identified according to their dielectric fitting parameters. This is shown in table 4.6 for the low NN-content materials. It is interesting to observe a general decrease in activation energy with increasing NN-content.

The band gaps for undoped BT and NN are very similar at around ~ 3.2 to 3.4 eV.[20–25] The purely electronic conduction activation energy should be half the band gap (based on intrinsic conduction), however different conduction mechanisms and other extrinsic factors, such as A/B non-stoichiometry, significantly influence the activation energy. From figure 4.23 it can be seen that the electrical conductivity of all materials increases with increasing temperature. This increase can be linked to either of two sources, the increase in the number of charge carriers, or an increase in the mobility of the carriers.

Undoped BT naturally comes with processing induced oxygen vacancies, whose migration enthalpies are found to lie between 0.6-1.1 eV.[26] These values are close to the activation energy obtained here.

Table 4.6. Bulk conduction activation energy values for xNNBT samples.

Type	x-content	Activation energy (eV)
I	0	1.24 (2)
	1	1.10 (2)
II	2	0.76 (1)
	2.5	0.79 (1)
	3	0.75 (5)
	4	0.78 (2)
	5	0.66 (1)
	7.5	0.77 (5)
III	10	0.63 (2)

The decrease in activation energy from BT to 10NNBT can be explained with the volatility of the Na-ions. NN is doped to act as a self-compensation mechanism, which should not increase the number of oxygen vacancies and ideally trap them similar to RE-dopants. Some Na-loss will take place due to the high sintering temperatures. This quantity is small, as the materials remain insulating at low temperatures. However, increasing amounts of NN lead to a greater Na-loss and therefore excess Nb-doping, which is compensated as follows:

$$Ti^{4+} \rightarrow Nb_B^{5+} + e^- \qquad \text{(Equation 4.1)}$$

$$2e^- + 2Ti^{4+} \rightarrow 2Ti^{3+} \qquad \text{(Equation 4.2)}$$

The more excess Nb-ions that are in the lattice the easier the reduction becomes and the number of charge carriers in the system increases. Therefore, a general decrease in activation energy for increasing NN-dopant levels is observed. The oxygen vacancies that are dominant in undoped BT become less relevant.

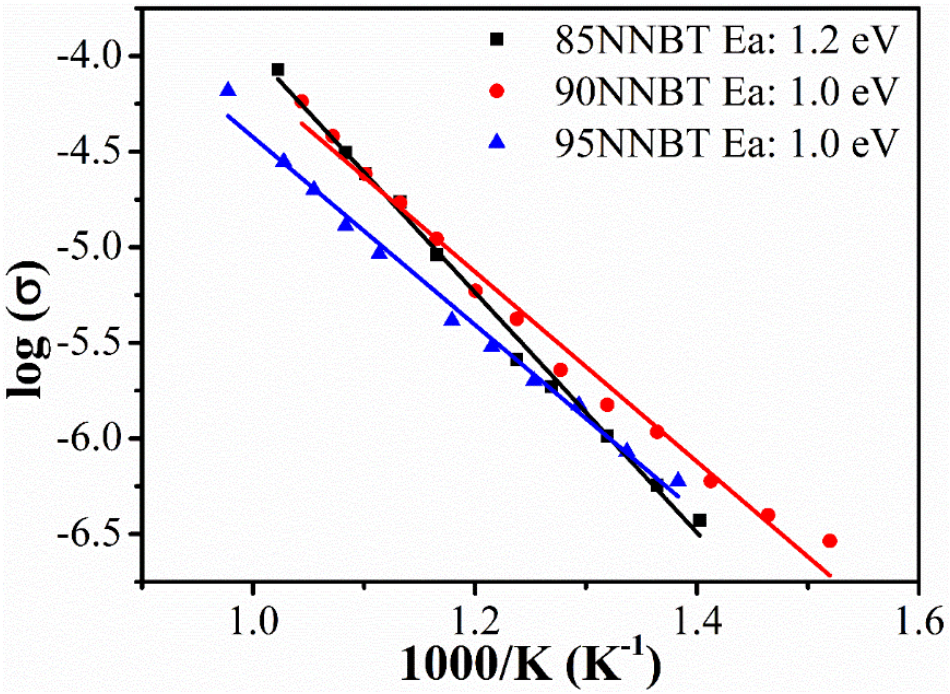

Figure 4.24. Bulk conductivity Arrhenius plot for xNNBT, where x ≥ 85.

For the high NN-content materials, the activation energy values for the bulk conductivity are closer together and fall into the range for a type 1 material, *i.e.* a ferroelectric material, table 4.7. When taking into account the literature and the ferroelectric-relaxor-ferroelectric transition that is observed across the entire solid solution, this does not come as a surprise. The Arrhenius plots of the bulk conductivity for xNNBT, where x ≥ 85, are shown in figure 4.24.

The conduction of the high NN-content materials is also more oxygen vacancies related, as the significantly lower sintering temperatures are inducing less Na-loss.

Table 4.7. Bulk activation energy values for xNNBT samples.

Type	x-content	Activation energy (eV)
I	85	1.24 (2)
	90	1.04 (2)
	95	1.00 (2)

4.3 Conclusions

Compositions of the NNBT solid solution were studied with particular emphasis on the electrical properties of the low NN-concentration side of the solid solution. The permittivity profiles of these showed that small quantities of NN, as little as 2 mol %, are enough to induce relaxor behaviour and lead to substantial broadening of the permittivity-temperature profiles. This is represents a lower concentration of NN to induce relaxor behavior than previously reported in the literature.[11] The chosen processing conditions in this work limit homogeneity and induce CS behaviour. This is favourable for materials that are to be used in MLCC applications but means that 'core'-BT behaviour is found in the permittivity data of these compositions alongside relaxor behaviour.

Further investigation into the electrical properties agreed with the literature and therefore confirmed it is possible to subdivide the compositions into three groups: ferroelectrics, relaxors and a mix of both.[11] From this work and the literature, it appears that this solid solution will change with increasing NN-content from ferroelectric to mixed to relaxor to mixed behaviour and finally reverting back to ferroelectric behaviour. The IS behavior was complex and confirmed significant levels of heterogeneity within the grains of BT-NN materials.

Further work might include changing the processing conditions to obtain thermodynamic equilibrium in all samples and to investigate how this influences the dielectric and conduction properties.

4.4 References

1 H. Saito, H. Chazono, H. Kishi and N. Yamaoka, *Jpn. J. Appl. Phys.*, 1991, **30**, 2307–2310.

2 H. Kishi, N. Kohzu, J. Sugino and H. Ohsato, *J. Eur. Ceram. Soc.*, 1999, **19**, 1043–1046.

3 J. Nishikawa, T. Hagiwara, K. Kobayashi, Y. Mizuno and H. Kishi, *Jpn. J. Appl. Phys.*, 2007, **46**, 6999–7004.

4 Y. Okino, H. Shizuno, S. Kusumi and H. Kishi, *Jpn. J. Appl. Phys.*, 1994, **33**, 5393–5396.

5 M.-J. Pan and C. A. Randall, *IEEE Electr. Insul. Mag.*, 2010, **26**, 44–50.

6 F. H. Morshead, P. Y. Foeller, C. L. Freeman, H. Zhang, I. M. Reaney, D. C. Sinclair and J. S. Dean, *J. Eur. Ceram. Soc.*, 2017, **37**, 2795–2801.

7 D. Makovec, Z. Samardz and M. Drofenik, *J. Am. Ceram. Soc.*, 2004, **87**, 1324–1329.

8 K.-J. Park, C.-H. Kim, Y.-J. Yoon, S.-M. Song, Y.-T. Kim and K.-H. Hur, *J. Eur. Ceram. Soc.*, 2009, **29**, 1735–1741.

9 I. P. Raevskii, L. M. Proskuryakova, L. A. Reznichenko, E. K. Zvorykina and L. A. Shilkina, *Sov. Phys. J.*, 1978, **21**, 259–261.

10 H. Khemakhem, A. Simon, R. Von der Mühll and J. Ravez, *J. Phys. Condens. Matter*, 2000, **12**, 5951–5959.

11 D. Kwon, Y. Goh, D. Son, B. Kim, H. Bae, S. Perini and M. Lanagan, *J. Electroceramics*, 2016, **45**, 631–638.

12 J. T. Zeng, K. W. Kwok and H. L. W. Chan, *J. Am. Ceram. Soc.*, 2006, **89**, 2828–2832.

13 S. Massari and M. Ruberti, *Resour. Policy*, 2013, **38**, 36–43.

14 R. L. Moss, E. Tzimas, H. Kara, P. Willis and J. Kooroshy, *Critical Metals in Strategic Energy Technologies*, European Union, Luxembourg, 2011.

15 A. J. Moulson and J. M. Herbert, *Electroceramics - Materials, Properties, Applications*, Chapman & Hall, London, 1990.

16 S. Sumita, M. Ikeda, Y. Nakano, K. Nishiyama and T. Nomura, *J. Am. Ceram. Soc.*, 1991, **74**, 2734–2746.

17 H. Kishi, Y. Mizuno and H. Chazono, *Jpn. J. Appl. Phys.*, 2003, **42**, 1–15.

18 H.-J. Hageman and D. Hennings, *J. Am. Ceram. Soc.*, 1981, **64**, 590–594.

19 K. Albertsen, D. Hennings and O. Steigelmann, *J. Electroceramics*, 1998, **2**, 193–198.

20 H. Shi, B. Lan, C. Zhang and Z. Zou, *J. Phys. Chem. Solids*, 2014, **75**, 74–78.

21 F. Fresno, P. Jana, P. Reñones, J. M. Coronado and D. P. Serrano, *Photochem. Photobiol. Sci.*, 2017, **16**, 17–23.

22 B. Modak, P. Modak and S. K. Ghosh, *RSC Adv.*, 2016, **6**, 90188–90196.

23 S. Piskunov, E. Heifets, R. I. Eglitis and G. Borstel, *Comput. Mater. Sci.*, 2004, **29**, 165–178.

24 K. Suzuki and K. Kazonuri, *Jpn. J. Appl. Phys.*, 2005, **44**, 2081–2082.

25 S. H. Wemple, *Phys. Rev. B*, 1970, **2**, 2679–2689.

26 M. Kessel, R. A. De Souza and M. Martin, *Phys. Chem. Chem. Phys.*, 2015, **17**, 12587–12597.

Chapter 5: 90NNBT - RE-free X7R TCC profile

5.1 Introduction

The solid solution series xNNBT in Chapter 4 has shown potential at reducing BT's TCC accompanied by a low dielectric loss across the series for temperatures up to 125 to 150 °C. Considering the permittivity and TCC profiles associated with the compositions, only one material in chapter 4 fulfils the industry standard of TCC = ±15 % from -55 to 125 °C by itself.[1] The composition to consider possesses a dopant concentration of x = 0.9 and is referred to as 90NNBT.

90NNBT could offer a RE-free alternative for industry, however it might not be the ideal replacement material. A high RT permittivity (i.e. > 1500) is favourable for industry and 90NNBT possesses a RT value of only ~ 800. This means that more and/or thinner layers would be required to achieve capacitances comparable to current RE-doped MLCCs. In addition, the large dopant concentration (90 % NN means that the BT should really be considered the dopant), results in a negation of any economic advantage this material might have, due to lower priced dopants. However, the increasing demand for RE-dopants and potential supply shortages in the future mean that any alternative involving compromise might be better than no alternative at all.

This chapter looks at the suitability of this composition to be used in the MLCC industry. The most important aspects that were investigated include the effect of processing conditions, such as the sintering temperature and atmosphere (ρ_{O2}). The latter is an extremely important aspect because the electrodes of choice in the MLCC industry are base-metal-electrodes (BME), in particular Ni, due to their low cost.[1–3] Ni-electrodes are currently industrially processed in reducing atmospheres, *i.e.* 1-4 % H_2 in N_2, to prevent Ni from oxidising at temperatures above ca 1100 ^{o}C. Thus, the chemical stability and electrical conductivity of the material under reducing atmospheres and therefore compatibility with BMEs plays a major role in its suitability for large scale MLCC production. If limited to processing in inert or air atmospheres then other (noble metal) electrode materials such as Pt or Ag/Pd would be required and therefore restrict applications to more niche market products, where production and device costs are of secondary concern.

5.2 Experimental

The ceramic processing route described in chapter 3 was followed. The only processing addition was the sintering of sets of 90NNBT ceramics under N_2- and 5 % H_2-atmospheres. This was to obtain information related to the suitability of the material with sintering atmospheres that would be required for industrial production.

Dielectric data were obtained following the procedure described in chapter 3.

5.3 Results and discussion

5.3.1 Phase composition and microstructure.

90NNBT sintered at 1250 °C in air possesses an orthorhombic perovskite structure (Pbcm space group), as determined by XRD in figure 5.1. When changing the processing conditions to higher temperatures, secondary phases are observed in the XRD profiles. They are identified in figure 5.1 and are sintering temperature related and Na-deficient.

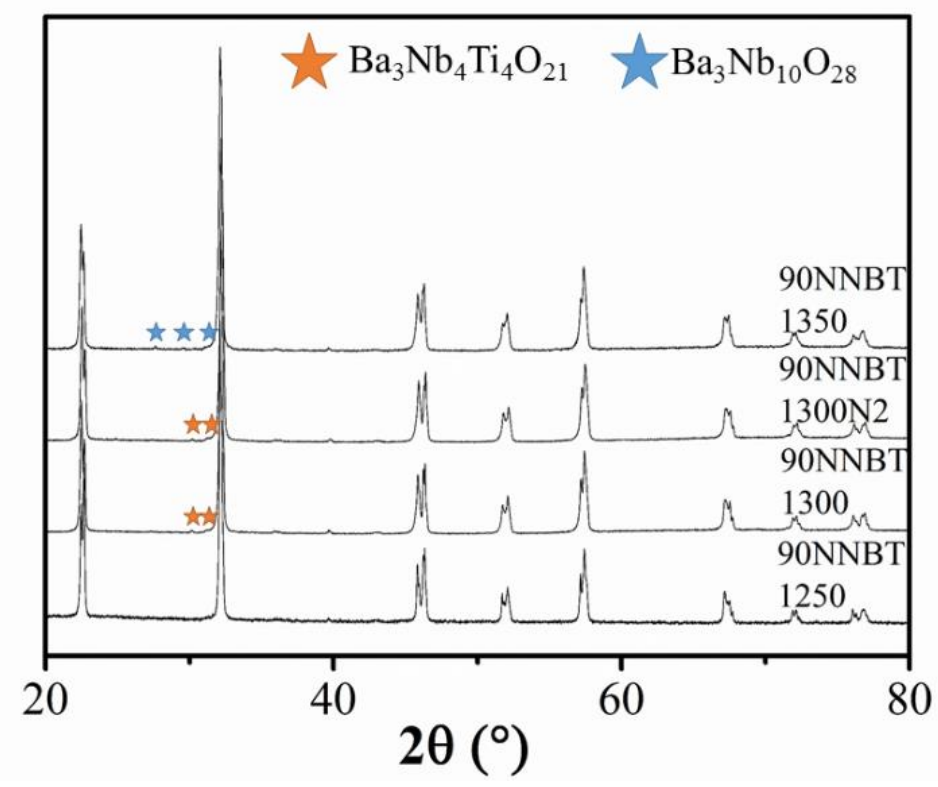

Figure 5.1. XRD patterns of 90NNBT, 2θ = 20º - 80º, after sintering at a range of temperatures for 8h. The highlighted secondary phases were matched to $Ba_3Nb_4Ti_4O_{21}$

(sintering at 1300 °C) and $Ba_3Nb_{10}O_{28}$ (sintering at 1350 °C) and account for Na-loss at higher sintering temperatures.

The secondary phases have a small impact on the cell volume of the single-phase material obtained from sintering at 1250 °C (Volume = 487.8 $Å^3$). The cell volumes of the 1300 (Volume = 487.9 $Å^3$) and 1350 (Volume = 486.6 $Å^3$) samples appear slightly different but can be considered to be within the experimental error. What they have in common is the lack of Na in their secondary phases. This leads to the assumption that the increased sintering temperature leads to an increased loss of Na_2O compared to samples sintered at 1250 °C.

Table 5.1. Summary of lattice parameters for 90NNBT. Information in brackets denote sintering temperature (in degrees Celsius) in air unless stated otherwise.

NN-content (%)	a (Å)	b (Å)	c (Å)
90 (1250)	5.5498 (5)	15.8239 (4)	5.5431 (5)
90 (1300)	5.5985 (7)	15.6547 (15)	5.5664 (7)
90 (1300N2)	5.6006 (6)	15.652 (12)	5.5658 (6)
90 (1350)	5.5915 (6)	15.6562 (12)	5.5589 (7)

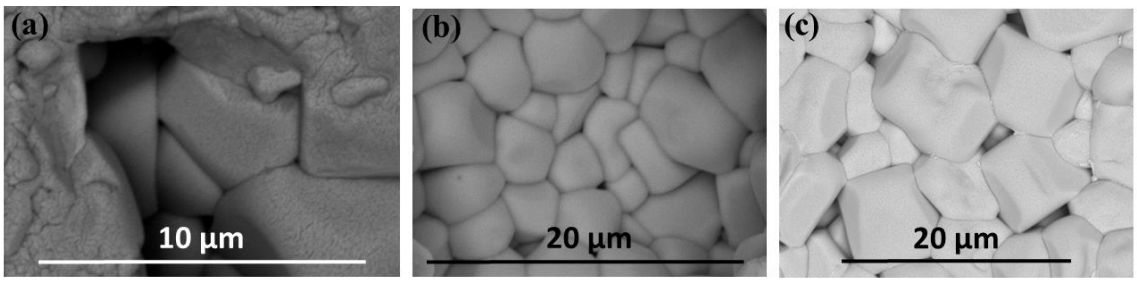

Figure 5.2. SEM micrographs of thermally etched 90NNBT samples sintered at (a) 1250 °C, (b) 1300 °C and (c) 1350 °C.

All samples form ceramics with density > 95%. The SEM micrographs in figure 5.2 show the dense microstructures. Grain sizes appear to be unaffected by the sintering and are in the range between ~0.5 and ~10 µm in all cases.

5.3.2 Electrical properties

The permittivity-temperature profile for 90NNBT is shown in figure 5.3. The RT permittivity of ~ 800 rises to ~10,000 at a T_C of ~205 °C. The permittivity profile is remarkably flat such that TCC fulfills the requirements of an X7R capacitor. It also posseses a remarkably low dielectric loss across the temperature range of -55 to 250 °C.The X7R profile and low tan δ show this material could be considered as a RE-free alternative for the MLCC industry.

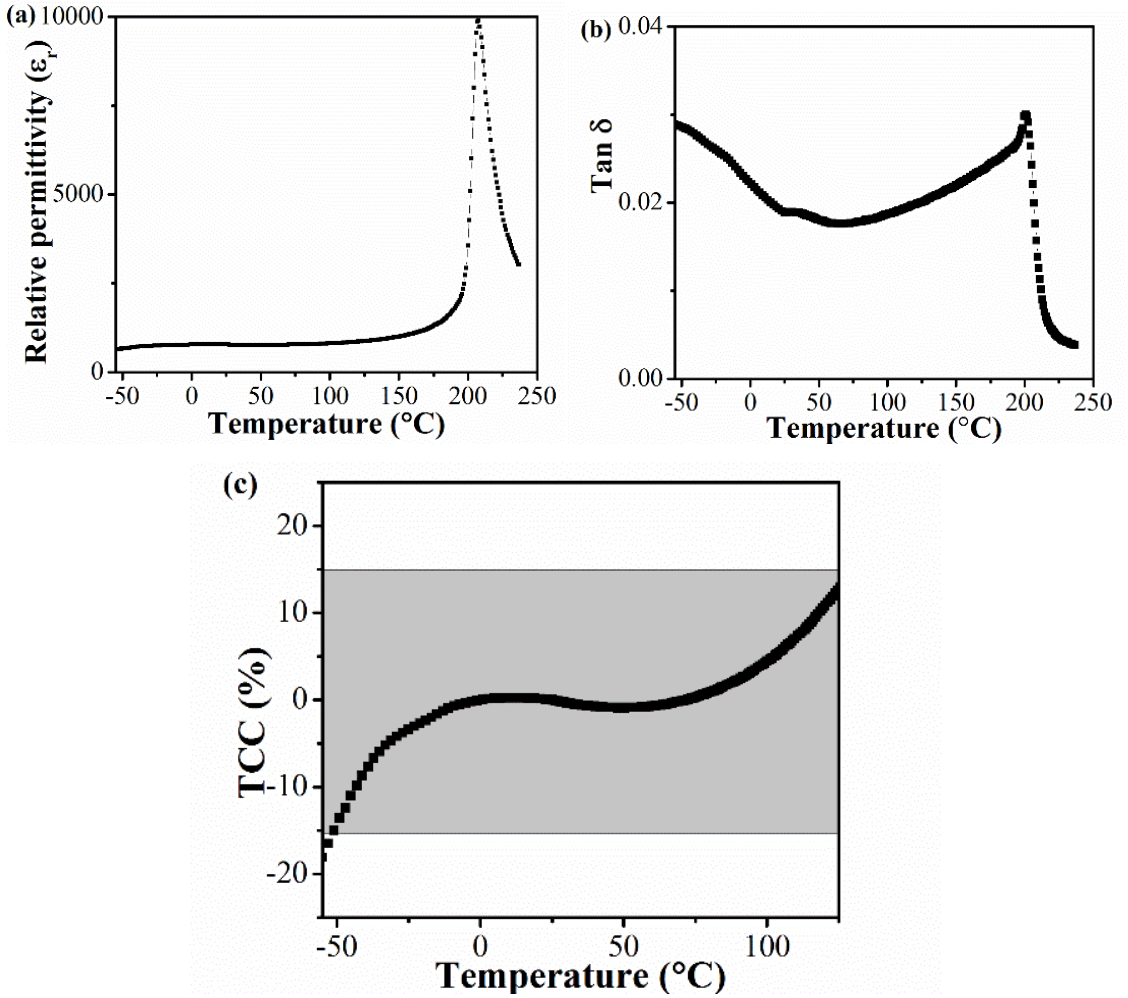

Figure 5.3. The (a) permittivity, (b) tan δ and (c) TCC temperature profiles of 90 NNBT sintered at 1250 ºC.

The permittivity of the material is very sensitive to sintering conditions. Figure 5.4 show the dramatic changes when the sintering temperature is increased from 1250 to 1300 and then 1350 °C (referred to by the number of the sintering temperature hereafter). In

each case, the hold time at the sintering temperature was 8h. The change from 1250 to 1300 °C does not seem to alter the permittivity-temperature profile as only a small shift of T_C to a lower T and a small drop in relative permittivity are observed, figure 5.4.a. However, the TCC profiles show a significant shift at sub ambient temperatures. The TCC for the 1300 sample drops significantly faster and the overall profile drops out of the X7R specification.

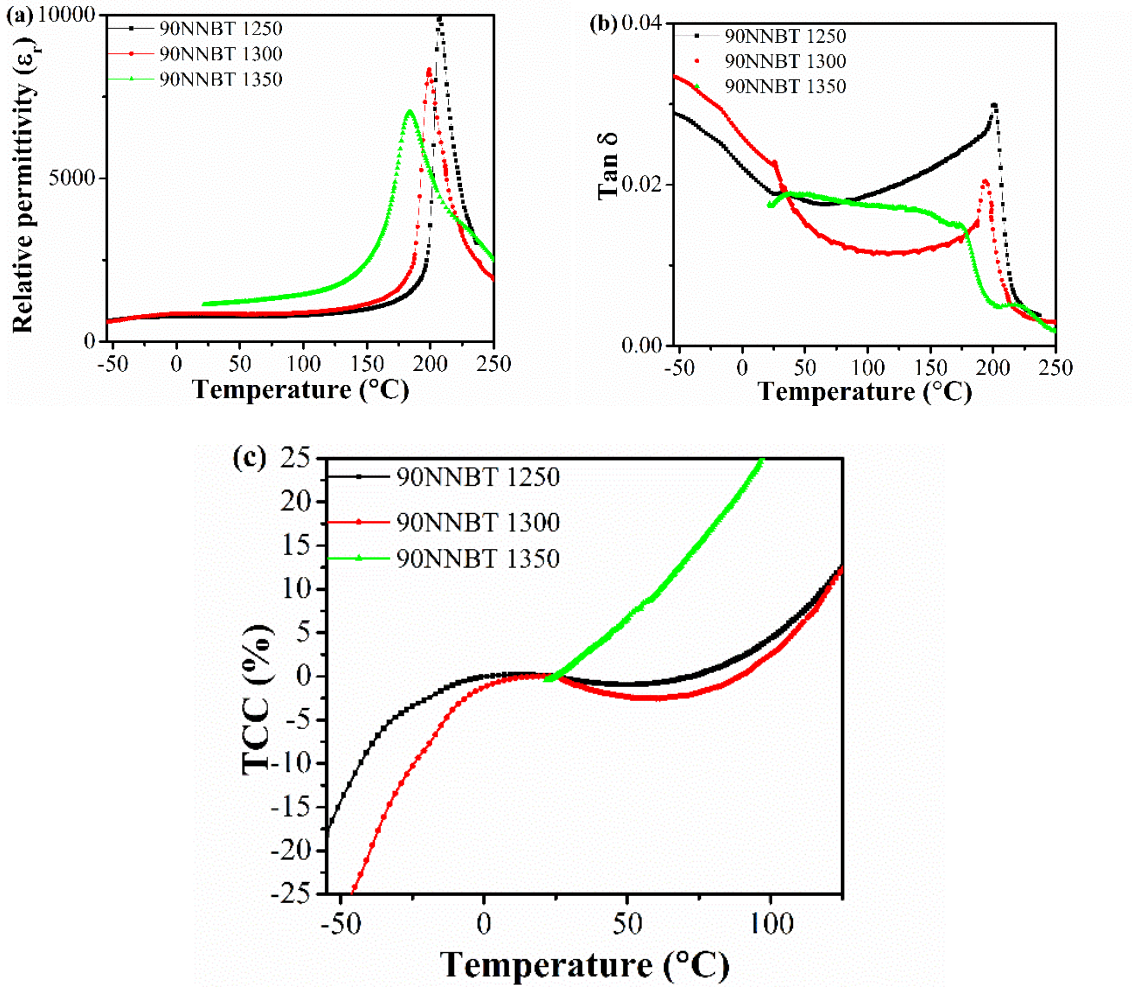

Figure 5.4. The difference in (a) permittivity, (b) tan δ and (c) TCC profiles of 90 NNBT sintered at 1250, 1300 and 1350 °C.

The loss of the X7R specification is even more apparent in case of the 1350 sample. The permittivity-temperature profile shows a significantly broadened peak and the previously flat plateau has disappeared, which becomes particularly apparent in the TCC profile, which shows significant deviation from the previous samples, figure 5.4. All samples maintain a low tan δ of below ~3%. The change in permittivity-temperature and

TCC profiles is attributed to the change in stoichiometry of the main phase due to the occurrence of Na-loss.

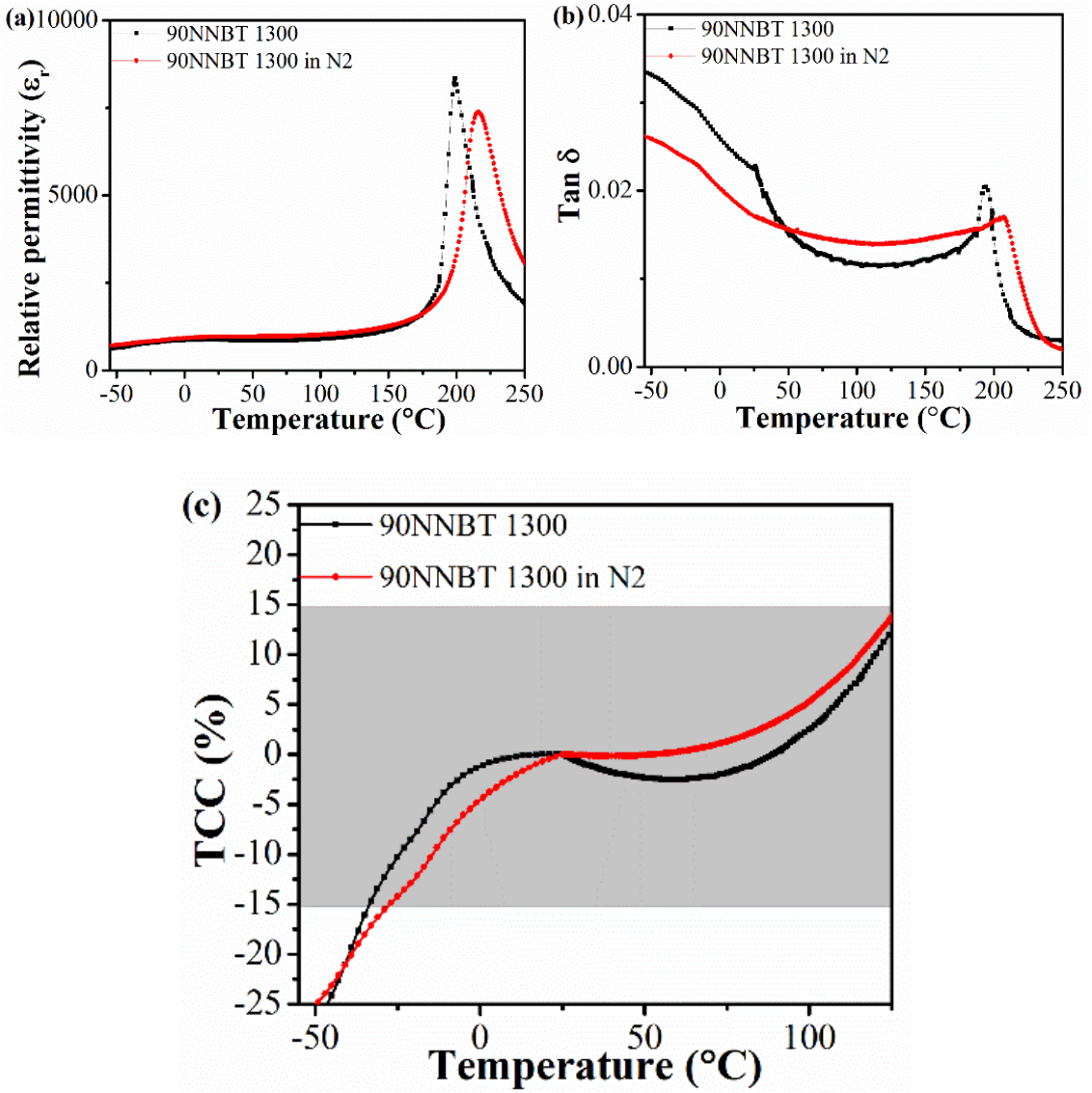

Figure 5.5. The difference in (a) permittivity, (b) tan δ and (c) TCC profiles of 90 NNBT sintered at 1300 ^{o}C in air or under a N_2-atmosphere.

The broadening of the permittivity profile can be explained by the secondary phases. The assumption is that with increasing temperature the local Na-content across the sample starts to deviate from 90 mol%, resulting in a less homogenous distribution. This creates areas, where there might be for example 88NNBT rather than 90NNBT. Each of these areas has their own T_C, which leads to a broadening of the overall transition. Using the data from chapter 4 it is possible to extract the NN concentration corresponding to the

new T_{max} positions. The T_{max} at 1250, 1300 and 1350 °C correspond to NN-concentrations of 90, 89 and 88NNBT, respectively.

As mentioned in the introduction to this chapter the processing atmosphere is important for the commercial use of materials in MLCCs. In order to study the impact of the processing atmosphere, samples were fired in air, nitrogen and a 5 % hydrogen atmosphere and the resulting permittivity-temperature profiles are compared in figure 5.5. Samples fired at 1300 °C were chosen for the comparison even though they may not represent single phase samples, as the higher processing temperature leads to a higher level of reduction in the samples. That means if the sample withstands the atmosphere at 1300 °C it will also withstand it at 1250 °C. The higher temperature also provides a larger temperature range when attempting to co-sinter the 90NNBT with other materials to provide a bilayer system. The reason being that the materials chosen from the low NN-end of the solid solution series prefer sintering temperatures of around 1400 °C. The higher the sintering temperature of 90NNBT the easier it should be to find a common sintering temperature with a low NN-end component in a bilayer arrangement.

The first observation from the comparison is the noticeable absence of data for the sample fired in hydrogen. This is due to the fact that the samples did not survive the sintering process in a 5% H_2/N_2 atmosphere, regardless of sintering temperature (1200 to 1300 °C were tried) the samples reduced visibly (turned black) and melted to varying degrees. This is a significant setback, as reducing atmospheres are required for the processing of Ni-electrodes, which represent the cheapest and therefore most favourable commercial electrodes.

Sintering in N_2 atmosphere on the other hand shows a slight shift of T_C and significant peak broadening in the permittivity-temperature profile as compared to air sintered ceramics, figure 5.5.a. This increase in permittivity is attributed to the existence of regions of different NN-concentrations. Comparing the T_{max} to those from 85, 90, 95 and 100NNBT, the extrapolated NN-concentration associated with this T_{max} is 90.5NNBT. This suggests regions in the material where the NN-concentration is larger than 90NNBT. The assumption is that there will then also be those that are lower than 90NNBT, therefore explaining the observed broadening of the permittivity peak. However, the impact on TCC is small and tan δ is similar for samples processed in air and N_2. This is an

encouraging result, as sintering in N_2 might be an option for 90NNBT MLCCs. This would allow at least for Cu-electrodes, which are cheaper than Pt- or Ag/Pd-electrodes.

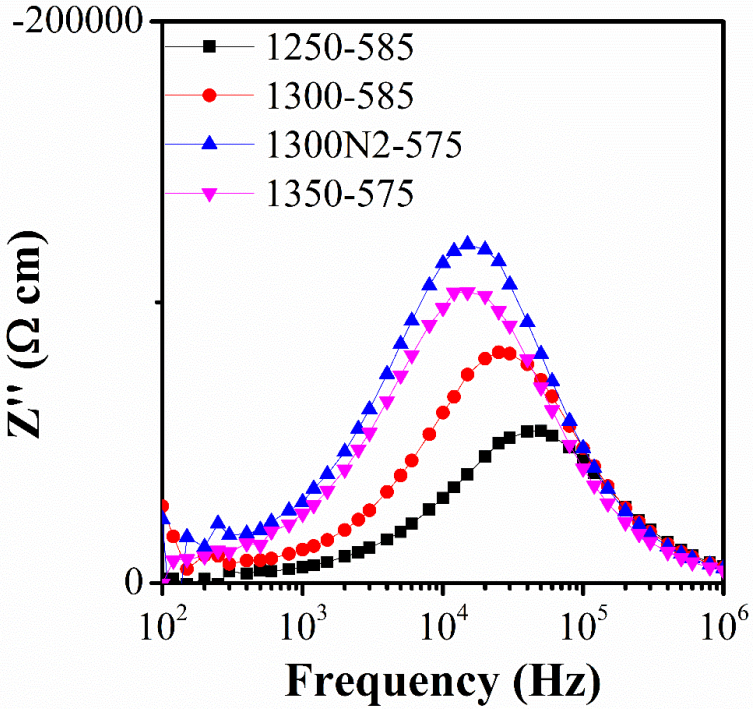

Figure 5.6. Z" versus frequency for 90 NNBT ceramics prepared at various conditions. 575 and 585 refer to the measurement temperature (in °C).

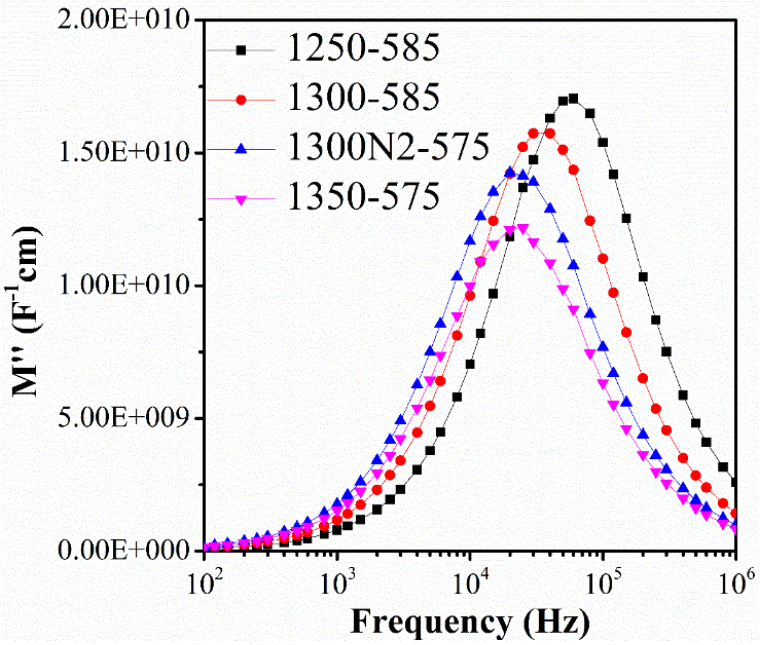

Figure 5.7. M" versus frequency for 90 NNBT ceramics prepared at various conditions. 575 and 585 refer to the measurement temperature (in °C).

The Z" versus frequency plot in figure 5.6 shows that increasing the sintering temperature results in more resistive samples. The peaks in the Z" plot line up fairly well with their corresponding peaks in M" plots, figure 5.7 suggesting the material properties are bulk dominated. From the M" plots it can be observed that the bulk capacitance increases slightly with increasing sintering temperature. There is some gb contribution to the total resistivity, hence the peaks in Z" plots are broader than the corresponding peaks in M" plots.

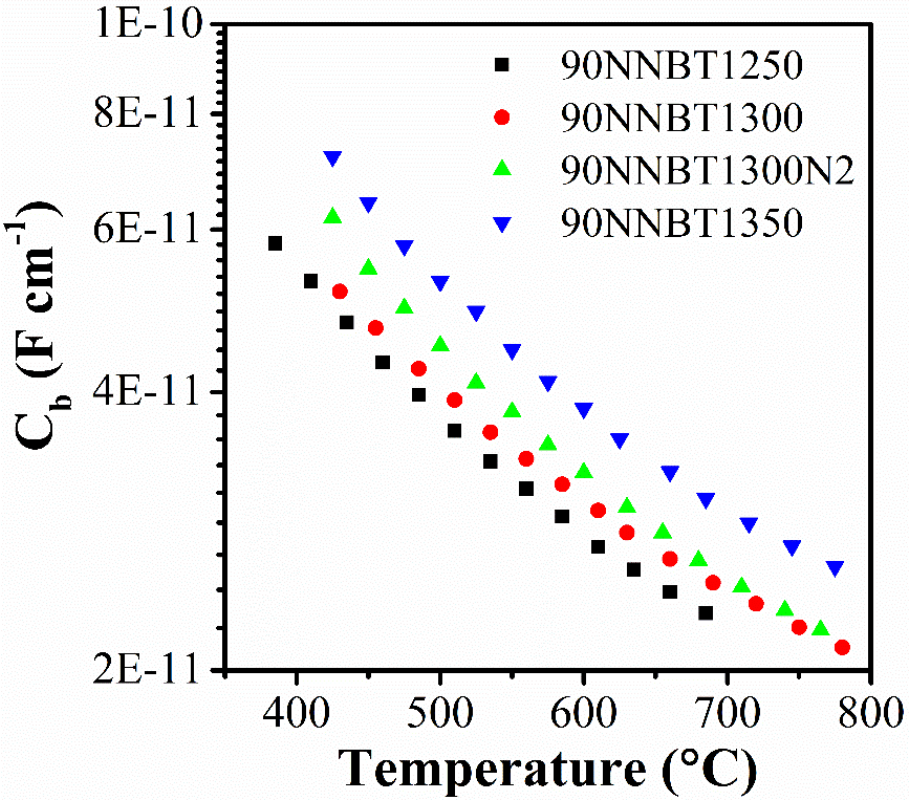

Figure 5.8. Bulk capacitance (from M" plots) versus temperature for 90NNBT ceramics prepared at various conditions.

The increase in bulk capacitance observed in the M" plot is highlighted in figure 5.8. The conclusion is that increasing sintering temperatures do increase the bulk capacitance, whilst at the same time f_{max} decreases, as seen in the M" plot in figure 5.7. However, figure 5.9 shows the change in f_{max} as a function of temperature and no significant changes in f_{max} with sintering temperature are observed.

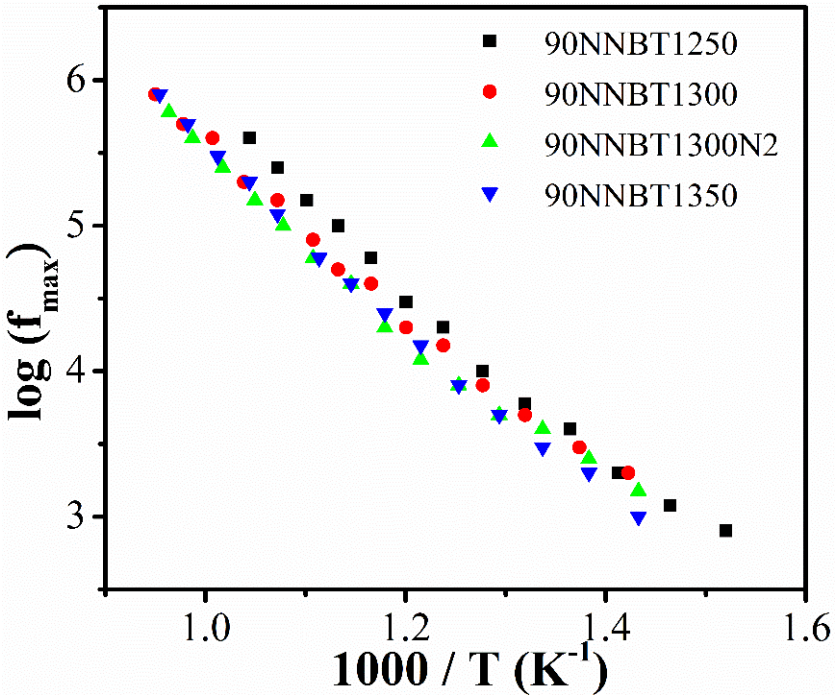

Figure 5.9. Bulk frequency versus 1000/temperature for 90NNBT ceramics prepared at various conditions.

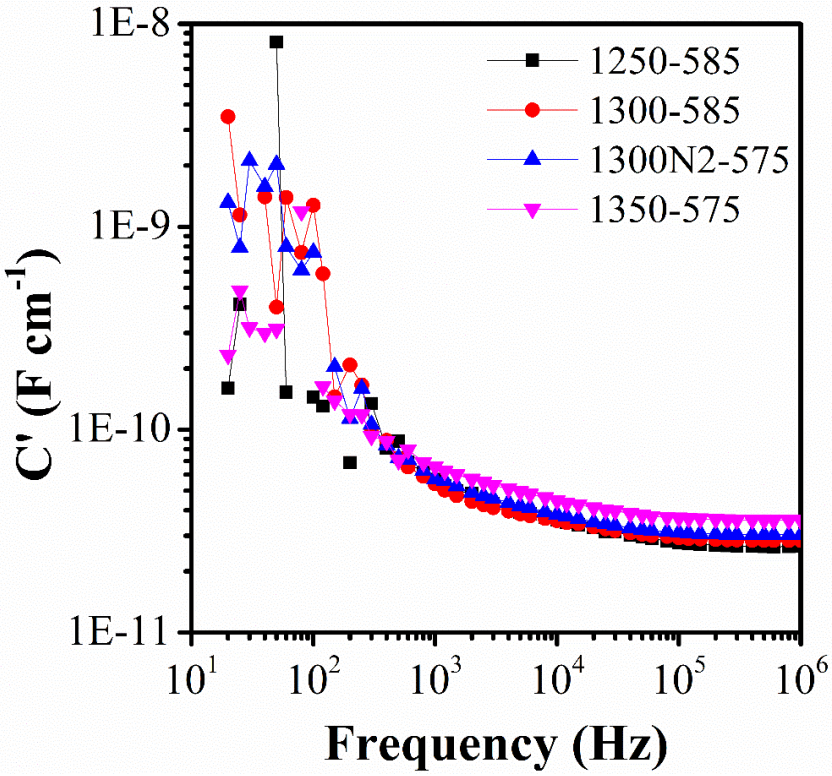

Figure 5.10. C' versus frequency for 90 NNBT ceramics prepared at various conditions. 575 and 585 refer to the measurement temperature (in °C).

When considering the capacitance of the bulk components in figure 5.10 it is possible to see the same trend as in the M" plots and from figure 5.8, increasing sintering temperature leads to an increase in bulk capacitance.

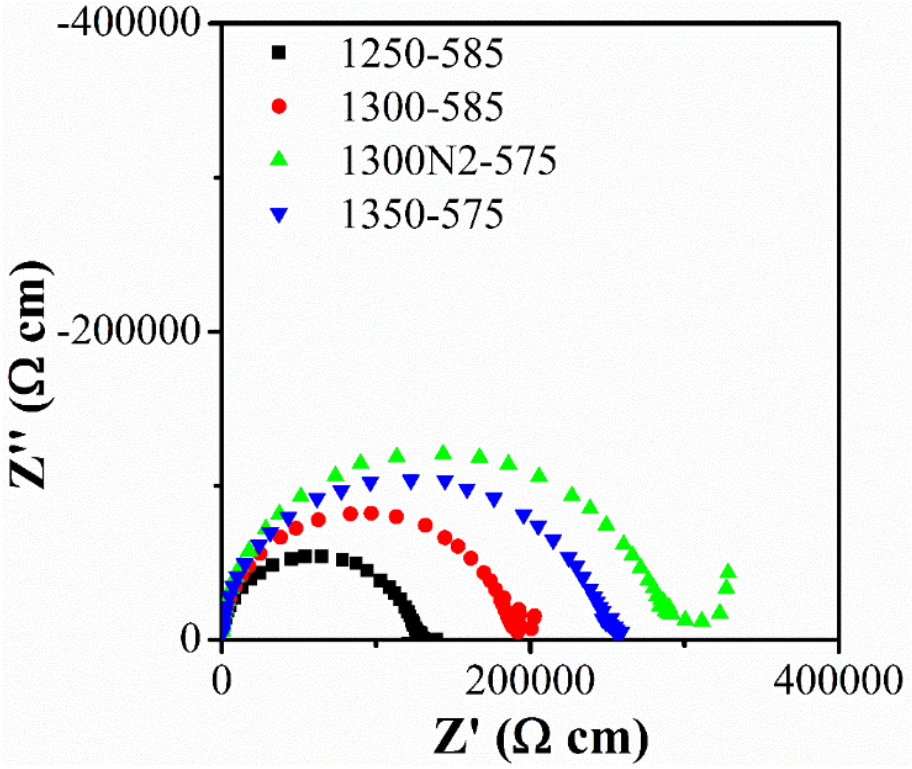

Figure 5.11. Z* plots for 90 NNBT ceramics prepared at various conditions. 575 and 585 refer to the measurement temperature (in °C).

The Z* plot for the materials is shown in figure 5.11 and shows that the material's total resistivity (b + gb) increases with increasing processing temperature.

The bulk activation energy for conduction of the samples was calculated from the M" peaks and plotted as an Arrhenius plot in figure 5.12. They do not change with sintering conditions and remain high at ~1 eV for all samples. This suggests a similar conduction mechanism for all samples.

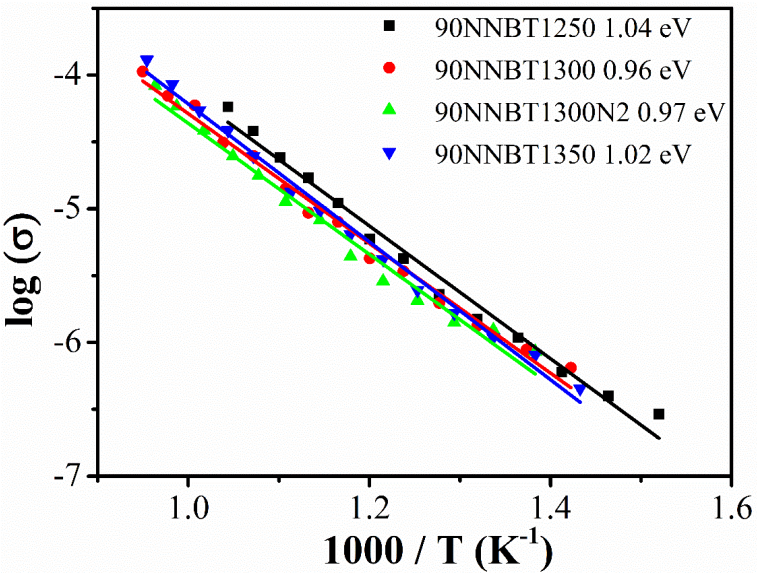

Figure 5.12. log σ versus 1000/T for 90 NNBT ceramics prepared under various conditions.

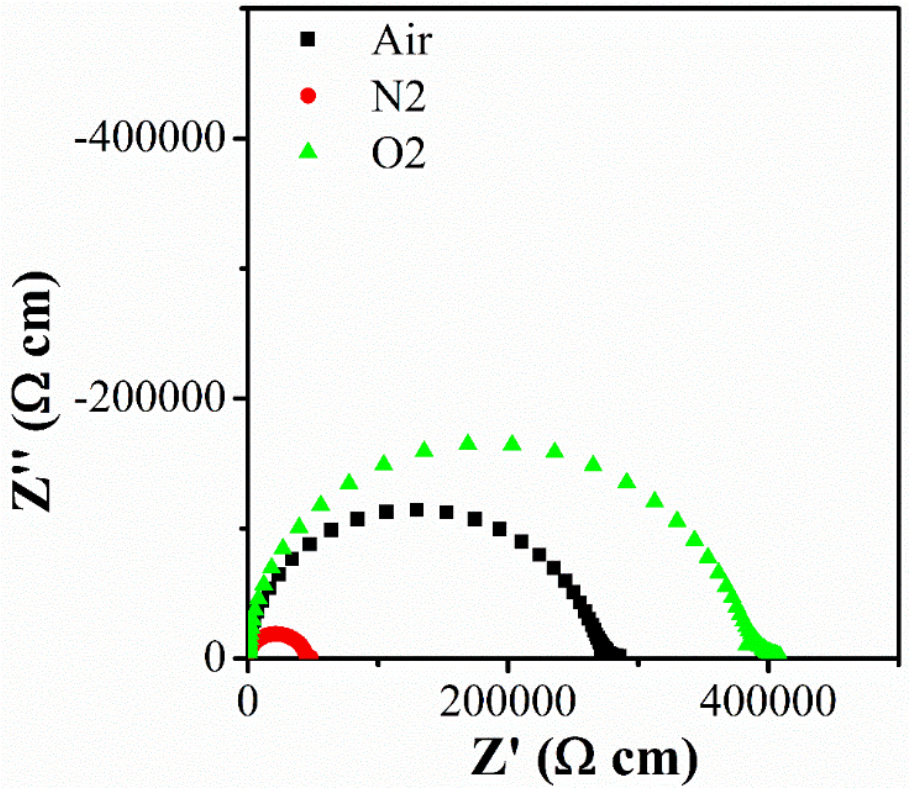

Figure 5.13. Z* plots for 90 NNBT ceramics sintered at 1250 °C and measured at 550 °C. Increasing conductivity with decreasing oxygen partial pressure indicates n-type conduction.

The ρO_2-dependent IS on the 1250 samples showed that their electronic conduction mechanism is n-type, as increasing ρO_2 leads to a decrease in conductivity as shown in figure 5.13. The conduction mechanism therefore is:

$$O_O \rightarrow V_O + \frac{1}{2}O_{2(g)} + 2e^- \quad (5.1)$$

and

$$2e^- + 2Ti^{4+} \rightarrow 2Ti^{3+}. \quad (5.2)$$

Again, there is little evidence for ionic conduction but the large change in bulk resistivity as a function of ρO_2 means that electronic conduction dominates the overall conductivity.

The same ρO_2-dependent study of 1300 samples shows the inverse trend, as seen in figure 5.14. Increasing ρO_2 leads to an increase in conductivity, suggesting that the electronic conduction mechanism is p-type in nature.

$$V_{\ddot{O}} + \frac{1}{2}O_2 \rightarrow O_O^x + 2h^{\cdot} \quad (5.3)$$

At a higher temperature, it might be possible to determine the effect of ρO_2 on the magnitude of the ionic conduction. A change in the electrode spike with ρO_2 would be due to oxygen ion conduction.

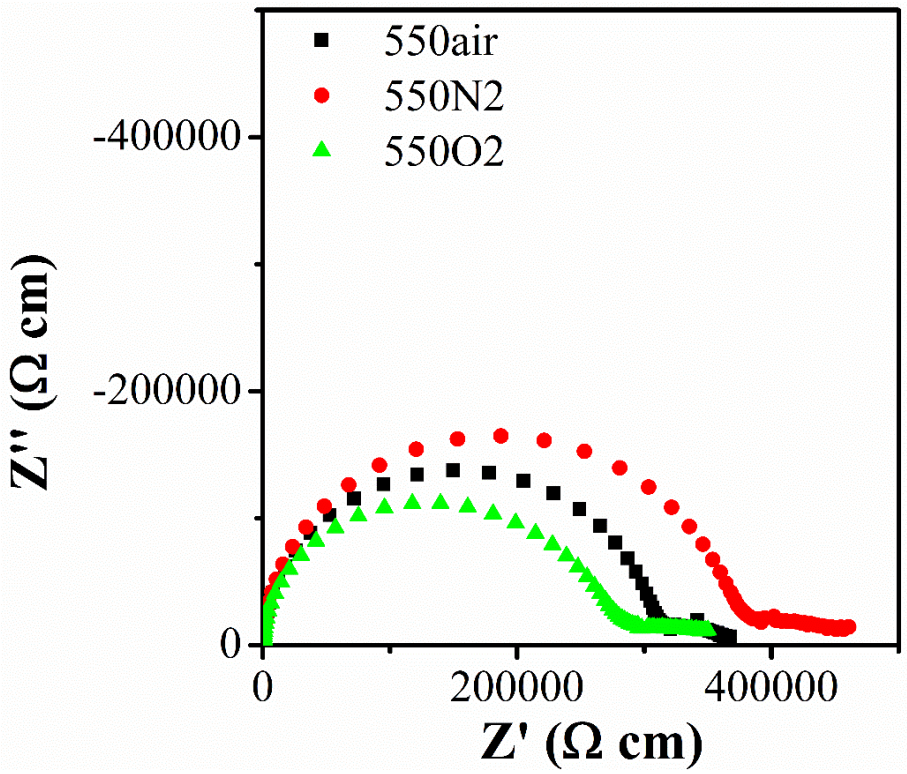

Figure 5.14. Z* plots for 90 NNBT ceramics sintered at 1300 °C. 550 refers to the measurement temperature (in °C). Increasing conductivity with increasing oxygen partial pressure indicates p-type conduction.

The holes created by this conduction mechanism need to be balanced somehow. This can be achieved by oxidising a cation. However, the cations present in this material are Na^{+}, Ba^{2+}, Ti^{4+} and Nb^{5+}. None of these can be oxidised to higher states. This leaves the only anion, O^{2-}, to be oxidised, as suggested in mechanism 5.4.[4] The most likely explanation however are either Fe^{3+} impurities (mechanism 5.5) or the cation vacancies created by the Na-loss (mechanism 5.6).

$$2h^{\cdot} + 2O^{2-} \rightarrow 2O^{-}. \qquad (5.4)$$

$$Fe^{3+} + h^{\cdot} \rightarrow Fe^{4+} \qquad (5.5)$$

$$2V'_{Na} + 2h^{\cdot} \rightarrow 2V_A^{x} \qquad (5.6)$$

It is proposed that Na-loss creates slightly A-site deficient NNBT ($Ba_{1-x}Na_{x-\delta}Ti_{1-x}Nb_xO_{3-\delta}$). The oxygen loss is not large enough to lead to an n-type conduction mechanism, hence it is possible to observe p-type conduction. This suggestion is strengthened by the ρO_2-dependent IS of the 1300 samples at higher temperatures in figure 5.15.

At 850 °C the 1300 samples still shows p-type conduction when decreasing ρO_2 from oxygen to air. When using a N_2 atmosphere the behaviour changes to n-type. The assumption is that ρO_2 this low causes increased loss of oxygen. When a large enough proportion of oxygen is lost the material needs to compensate for it *via* the n-type conduction mechanism and cannot maintain the p-type conduction. Further studies on more controlled A-site deficient NNBT are advisable to study this behaviour in more detail.

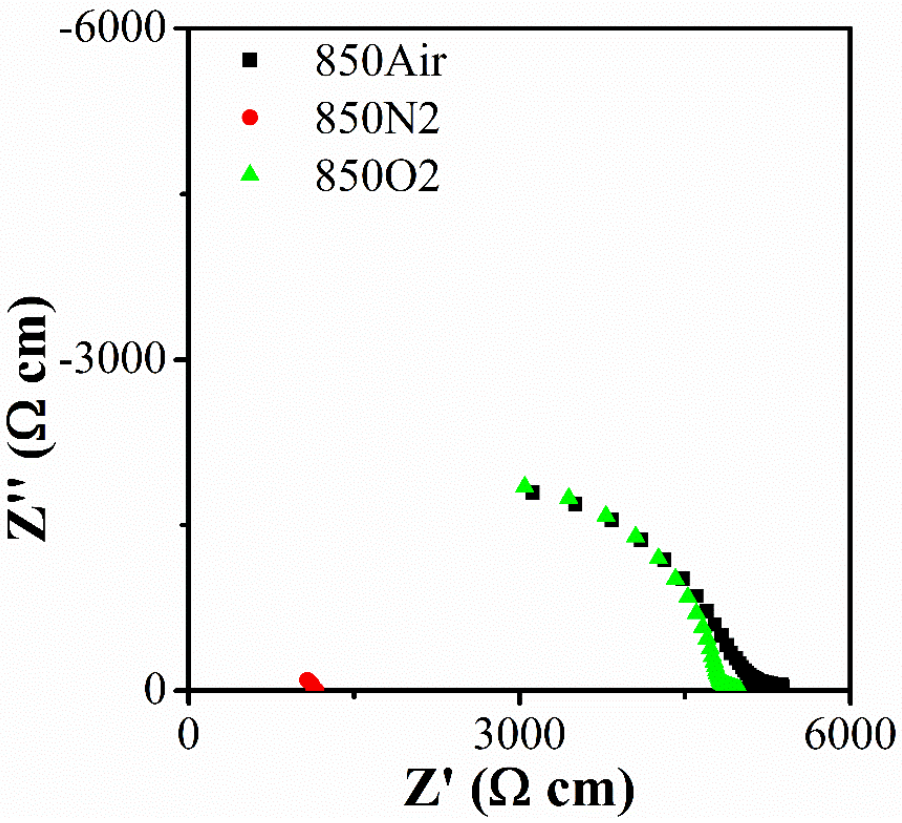

Figure 5.15. Z* plots for 90 NNBT ceramics sintered at 1300 °C. 850 refers to the measurement temperature (in °C).

The higher temperature IS data in figure 5.15 was not able to confirm the presence of oxygen ion conduction, as the electrode spikes do not differ significantly in size. However, ^{18}O measurements would be required to rule it out completely. The other ionic conduction possible is sodium ion conduction. This is significantly harder to prove, as the samples are not conductive enough to test them in a sodium ion battery. For the purposes of this work it is enough to conclude that there is an ionic component present in the conduction mechanism but the electronic conduction is dominant, particularly when n-type conduction is present.

5.3.3 Limitations and possible use

In the introduction it was mentioned that processing temperatures and atmospheres are important for the use of 90NNBT in the MLCC industry. The work in this chapter have shown that a lower sintering temperature is actually favourable to keep this material within the X7R specification. This is favourable, however not favourable enough to offset the issue posed by the non-compatibility of the material with a hydrogen atmosphere. This is likely to rule out Ni-electrodes and lead to higher production costs.

It has to be mentioned that the material was fired in a 5% H_2/N_2 atmosphere. Industry uses lower hydrogen concentrations, often as low as 1%, and therefore the material might survive sintering at these conditions. Especially when it is prepared with acceptor dopants to take up the electrons released due to the reducing atmosphere.

Sohrabi *et al.* have developed a method whereby coating the Ni-particles of the electrode paint in Li_2CO_3 allows for sintering of Ni-electrodes in an oxidative atmosphere.[5] The Li_2CO_3 is believed to decompose and produce CO. The CO creates a locally reducing atmosphere and prevents the formation of NiO. This would make 90NNBT more viable and more work should be done to investigate their suitability.

5.4 Conclusions

The cost of alternative electrodes or the additional processing to use Ni-electrodes in combination with the increased cost associated with the high niobium concentration compared to the small RE-content (~3 mol %) of current commercial MLCCs essentially

rules out 90NNBT as an alternative for current RE-doped formulation on economic terms. It would, however, be an alternative if required due to extreme RE-shortages.

Nonetheless, the $LiCO_3$ coated Ni-particles for the electrodes warrants future investigation. As does the n- to p-type switch due to slight A-site deficiencies in NNBT and the determination of the source of the ionic conduction in the samples. Whilst the material itself is too resistive to be used in batteries, it might prove useful to better understand the nature of the potential sodium ion conduction observed. Particularly as interest in ion battery research seems to be shifting from lithium to sodium.

5.5 References

1 H. Saito, H. Chazono, H. Kishi and N. Yamaoka, *Jpn. J. Appl. Phys.*, 1991, **30**, 2307–2310.

2 H. Kishi, Y. Mizuno and H. Chazono, *Jpn. J. Appl. Phys.*, 2003, **42**, 1–15.

3 S. Wang and G. O. Dayton, 1999, **82**, 2677–2682.

4 A. R. West, *Priv. Commun.*

5 D. Sohrabi, B. Heidary and C. A. Randall, *J. Alloys Compd.*, 2017, **695**, 1448–1454.

Chapter 6: Optimisation of TCC via core-shell (CS) microstructures and bilayers

6.1 Introduction

Ferroelectric BT is the material of choice for the MLCC industry due to its high permittivity. As mentioned previously, however, it has a very strong temperature dependency and the temperature coefficient of capacitance (TCC) is several hundred percent near T_C. Traditionally, industry is using dopants to form core-shell microstructures (CS) to improve the temperature stability to obey industry standards. One of these standards is the X7R capacitor (±15% TCC from -55 to 125 °C).

Recent work by Dean *et al.* used a FEM model to confirm previous findings by Jeon *et al.* that control of the microstructure, *i.e.* the volume ratio between the 'core'- and 'shell'-parts, had a significant impact on the TCC of BT.[1,2] With an exemplary NNBT-doped BT system they were able to show systematic changes in TCC, with changes in the volumetric ratio. This allowed for quick predictions of what CS-systems would generate industry standard TCC responses.

Unfortunately, their model does not remove the lengthy and iterative process of optimising processing conditions. That is still required to reliably manufacture the predicted CS-system. Another weakness to this approach is that the analysis of CS-microstructures relies on transmission electron microscopy (TEM). Obtaining TEM images of CS-microstructures is time consuming and the analysis of the core-to-shell ratio using this technique is not always reliable.[3] Finding a methodology that can compete with the CS microstructures in terms of TCC improvements but allowing for simpler processing and easier control of important factors, such as the volume-ratios, seems prudent.

This led to the proposal of taking two materials displaying 'shell'-like and 'core'-like permittivity profiles and treating them as a layered system. Maurya *et al.* have shown that a layered system can be used to mimic the concentration gradient observed in CS microstructures.[4] They took a set of 70 compositions of varying dopant concentrations and connected them in a layered structure, in parallel and in series. The series capacitor version showed promising results, however the number of layers required utilising this

approach is prohibitively large. This requires substantial time and effort to ensure co-sinterability for so many compositions plus electrodes.

Limiting the series capacitor route to only two components (as opposed to 70) and achieving better temperature stability than Maurya *et al.* could make this a viable option. This chapter concentrates on proving the concept that two capacitors in series can improve TCC sufficiently to make it an alternative to CS-microstructures. The following equation represents capacitors in series and was used to provide model data:

$$\frac{1}{C_{total}} = V_{r1}\frac{1}{C_1} + V_{r2}\frac{1}{C_2} \qquad \text{(Equation 6.1)}$$

where V_r is the volume ratio of a material, C is the capacitance of a material and C_{total} is the total capacitance of the series-type system.

The same materials that Dean *et al.* used for their work on the CS-ratios were chosen, making 2.5NNBT the 'shell'- and BT the 'core'-like layers. There are three effects that need to be considered to explain the differences between the CS-model, the bilayer-model and the experimental bilayer data.

The easiest way to account for is any difference in permittivity between the bilayer model and the corresponding experimental data. The model is based upon the two materials combined with a perfect interface, *i.e.* no interface region but a sharp transition between the two materials. In reality that would not be the case, as some inter-diffusion would take place. Serrano *et al.* recently used the bilayer design and created a co-sintered BZT-BST bilayer.[5] Their modelled and experimental permittivity profiles were in good agreement with only small variations. The experimental and modelled permittivity were in close agreement, however, the temperature dependence of the profiles differ from the modelled to experimental data. This is due to compositional changes in the interface region, which are not present and therefore unaccounted for by the model.

When creating a MLCC based on a bilayer system, the interface between the dielectric layers should not be a significant issue, as the permittivity profile and therefore the TCC is not affected significantly. The additional resistive response might even have positive

effects on the capacitors lifetime. This would need investigation based on actual devices and is beyond the scope of this work.

To eliminate the issue of an interface with a different dopant concentration, the materials in this study were not co-sintered. Instead the two layers were produced and prepared individually and then combined with the application of electrode paste. Even though this process eliminates the occurrence of a significant interface layer, there will be additional electrode interfaces, which due to the restrictive compression between the two layers is likely to yield air gaps due to the shrinkage of the paste during its hardening process. Air gaps can lead to a drop in permittivity, however the shape of the permittivity profile should be preserved better than in the case with a compositionally graded interface region.

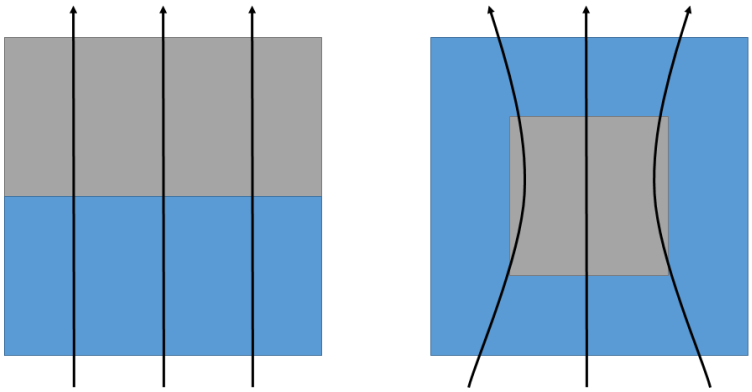

Figure 6.1. Schematic of a bilayer and a CS with a physical 50:50 CS-ratio. The arrows indicate the electric field, which in the case of the CS favours the low resistivity core region (grey) resulting in an electrical CS-ratio that is not 50:50, but skewed towards the core region.

The effect of the resistance and permittivity of the two materials and their effect on the electric field pathways in the respective CS- and bilayer-structures needs to be addressed. Dean *et al.'s* original CS-model used resistances that were chosen to force the field to travel through the core and the shell-parts of the microstructure in a series-type circuit. Therefore a modelled 50-50 CS microstructure corresponded to a 50-50 bilayered model. In this work the resistance of the shell was set to be four orders of magnitude higher than the core, as suggested by the experimental data. Therefore, deviation between the CS and bilayer model are due to differences in the field pathways, created by changes in

resistance. James Heath in his thesis (University of Sheffield) established that the current density in a CS-structure tends to be drawn towards the part of the system with the lower resistivity, as shown in figure 6.1.b.[6] This would distort the 'electrically-observed' volume fractions away from the physically present volume fractions in the microstructure, *i.e.* what is a 50-50 CS-microstructure would in practice tend towards a larger ratio of the lower resistivity material.

This effect of overestimating the low resistivity region is dependent on the core-to-shell volume ratio. As the size of the core-volume (low resistivity phase) decreases, the current curvature effect shown in figure 6.1 will increase. As the curvature of the electric field increases, it leads to an increase in resistivity. This increases the favourability of the current to choose to travel through the shell material, as shown in figure 6.2.

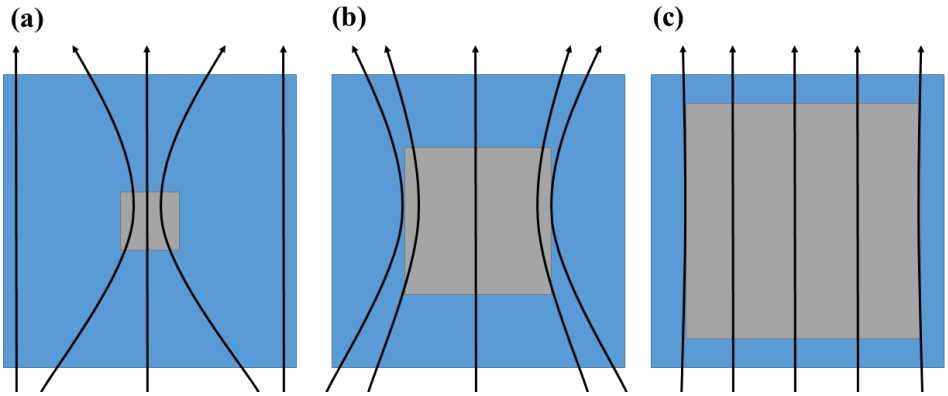

Figure 6.2. Schematic outlining the dependence of current pathway on the CS-ratio which increases from left to right.

The closer the core volume fraction is to 1.0, the closer the simulated permittivity profiles will be to the bilayer model, figure 6.2.c. For small and medium core volume fractions the deviation from the bilayer model should be significant. This is due to the increase in resistivity caused by the electric field trying to bend towards the low resistivity core. This makes the current bending less favourable and therefore the field will be more likely to follow a straight path through the shell, as shown in figure 6.2.a. This is also true for very small core volume fractions, were the current along the outside cannot actually bend enough to reach the core.

The impact of this effect on the observed permittivity profiles on the bilayer and CS model are significant. In the bilayer model the lower permittivity profile will always

dominate, as the model is based on capacitors in series. The CS model has capacitors in series, where the current goes through the core and shell. However if the core is very small, the electric field will travel exclusively through the shell along the edge of the microstructure. This creates a parallel capacitor element. In parallel capacitors the larger permittivity material will dominate. This creates differences in the predicted permittivity profiles of CS microstructures and bilayers.

6.2 Experimental

The ceramics were prepared in accordance with the procedure outlined in chapter 3. The only variation was that the amounts of powder were pre-weighed to control the thickness of the resulting pellet in accordance with the chosen volume ratios. Equation 6.2 was used to calculate the masses required:

$$d = v_f \times \rho, \qquad \text{(Equation 6.2)}$$

where, d is the mass of dielectric material required for the correct thickness, v_f the volume fraction of the dielectric material and ρ the density of the ceramic after sintering at 1400 °C for 8 h. The calculated amount was then adjusted to be as close to 1 g as possible.

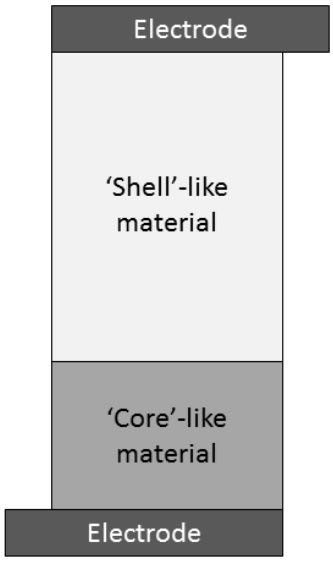

Figure 6.3. Example and schematic of a 2.5NNBT-BT bilayer ceramic.

Using this method, the pellet dimensions turned out within ± 1 % of the desired volume fractions after polishing. The two pellets were then coated with electrodes as outlined in chapter 3 and finally attached to each other *via* the use of Au electrode paste, which was hardened in the same way as the electrodes. This resulted in a bilayer system as shown in figure 6.3.

Note that co-sintering was not considered for this work, as that is a processing step that is not being optimised but exists already. However, dilatometry data for 2.5NNBT and BT shown in figure 6.4 suggested that co-sintering should be possible with minor adjustments.

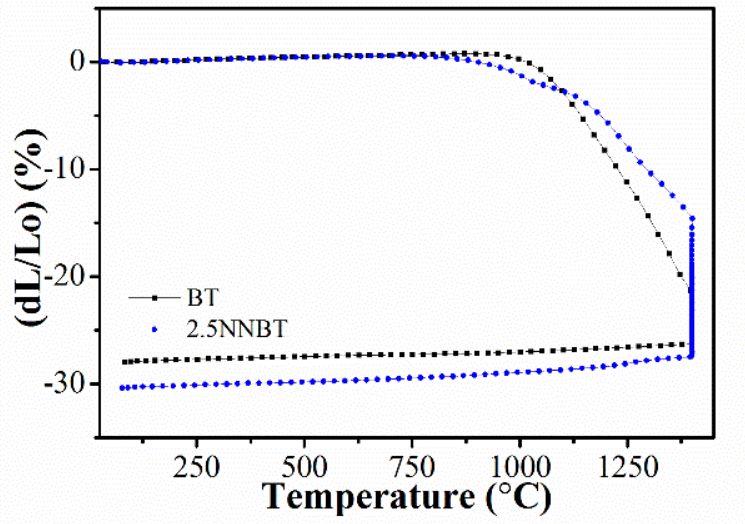

Figure 6.4. Dilatometry profiles for green pellets of 2.5NNBT and BT ceramics.

The finite element package ElCer was used to model the response of the dielectric materials.[7] It uses a time domain finite element method (TDFEM) to solve Maxwell's equations in space and time. This approach allows for the electronic response to be calculated from material properties (here relative permittivity and conductivity) and the ceramic microstructure (here core-shell microstructure).

To ensure confidence in the results a model with realistic grain size and distribution was chosen as the microstructure. The microstructure is generated employing a Voronoi tessellation method. This uses seed points to create a set of surfaces suitable to be used as a granular structure. These seed points are first distributed on a body centred cubic structure to form a collection of irregular tessellated truncated octahedra. The points are then modified using a random jitter to move them from these positions, creating unique irregular shape for each grain. This generates a model of 341 grains that are approximately

500 nm in diameter with a realistic Gaussian distribution to represent the BT grains. Each grain is then shrunk towards its centre to form a core-shell like structure.

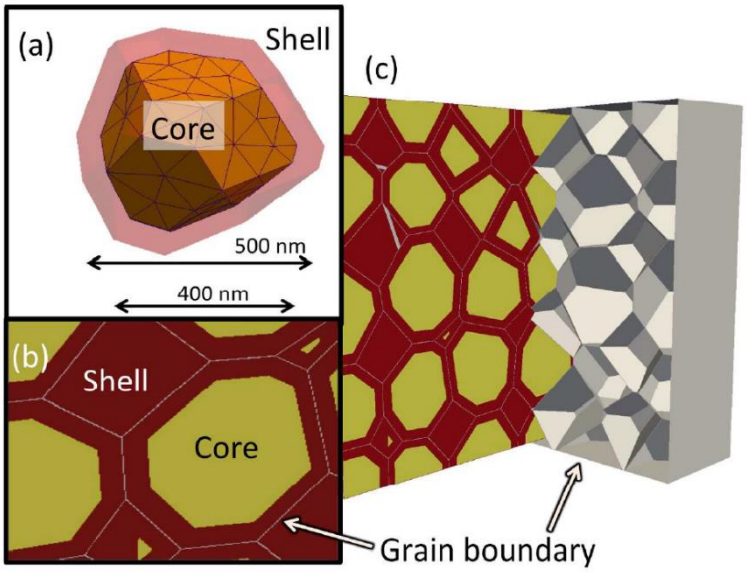

Figure 6.5. Representation of (a) an individual meshed grain with CS microstructure of equal volume fraction, (b) and (c) show slice plots through the 341 individual grains, each with CS volume fraction defined by the user.[2]

The result is an inner surface, which is the core, as seen in figure 6.5. Controlling the shrinkage allows for control of the CS volume ratio. Finally, a thin grain boundary (gb) region is added (ε_r = 100, σ_{gb} = 0.1 μSm^{-1}) between the grains. Each region is then specified with individual material properties of permittivity and conductivity. The gb properties are assumed to be independent from dopant concentration and temperature and are designed to ensure the current flows through the grains (core and shell) and not along the gb. To mimic the temperature response, the core and shell phases are assigned temperature dependent permittivity and conductivity values that were obtained experimentally. The conductivities were chosen so that the shell phase is four orders of magnitude more resistive than the core phase.

The final resulting microstructure is shown in figure 6.5. The microstructure is then meshed using GMSH.[8] A typical model is made up of over 30,000 nodes and 150,000 individual tetrahedra, allowing for fast runs on a desktop computer but ensuring optimised convergence and reliability.

6.3 Results and discussion

6.3.1 Bilayers

The permittivity profiles for BT and 2.5NNBT are shown in figure 6.6. BT has a room temperature (RT) permittivity of ~2500 which rises to ~7000 at its Curie temperature (T_C). The other end member, 2.5NNBT, has a RT permittivity of ~3900 and a broad permittivity maximum of ~4800 around 60 °C. 2.5NNBT also shows evidence of a secondary peak close to the T_C of BT. Both ceramics possess low dielectric loss (< 3 %), however their TCC profiles, figure 6.7, vary significantly, being close to making them mirror images.

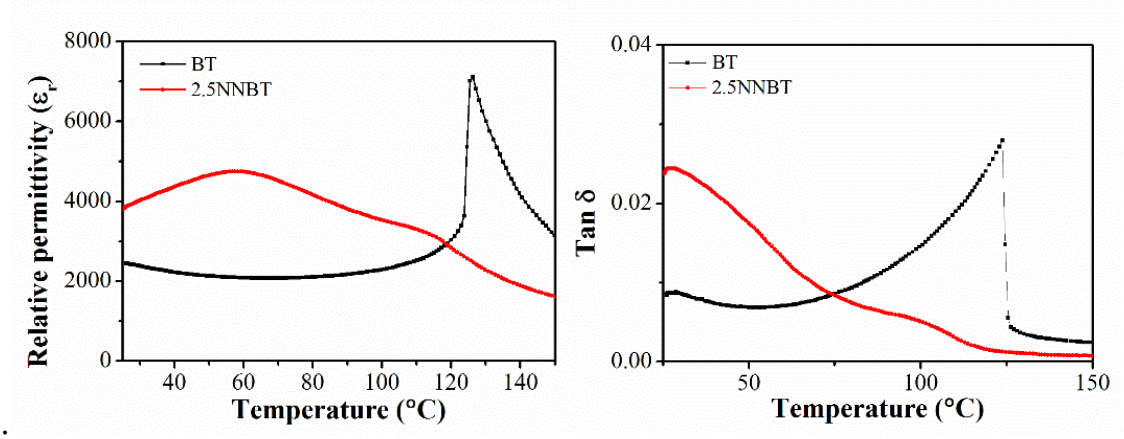

Figure 6.6. Permittivity (left) and tan δ (right) profiles of the 'core'- and 'shell'-like materials, BT and 2.5NNBT, respectively.

Neither of the two materials TCC is close to the chosen benchmark ±15 % in the temperature range of 25 to 125/150 °C. This would automatically rule out both materials for consideration as dielectric components of MLCCs. However, from figure 6.6 it is obvious that individually they would be very well suited to construct 'core'- and 'shell'-like regions from a CS structure, as shown in figure 1.3.b.

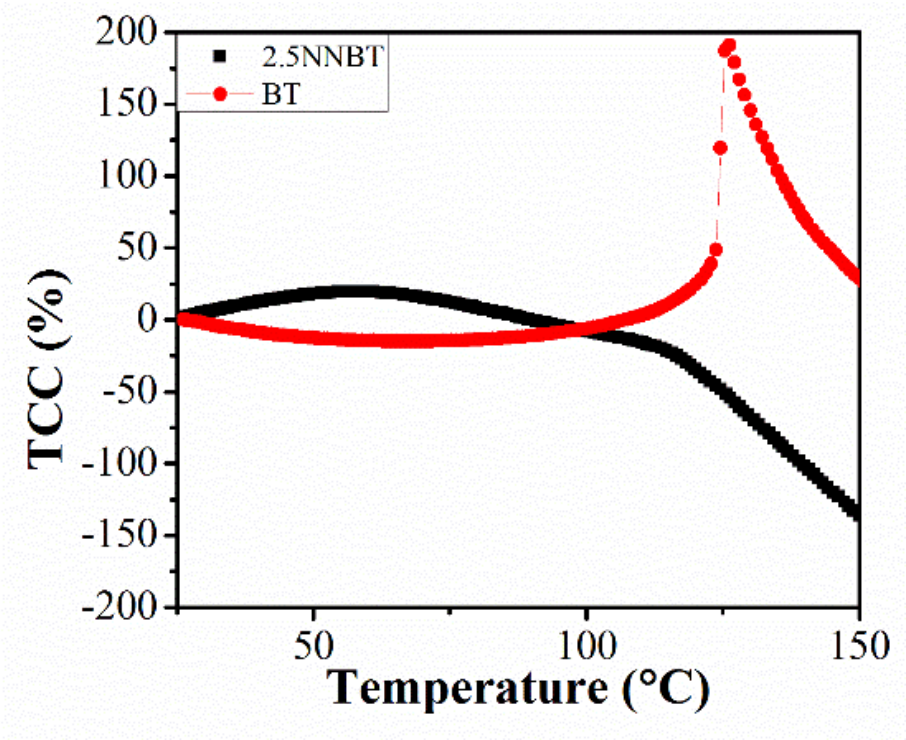

Figure 6.7. TCC profiles of the 'core'- and 'shell'-like materials, BT and 2.5NNBT, respectively.

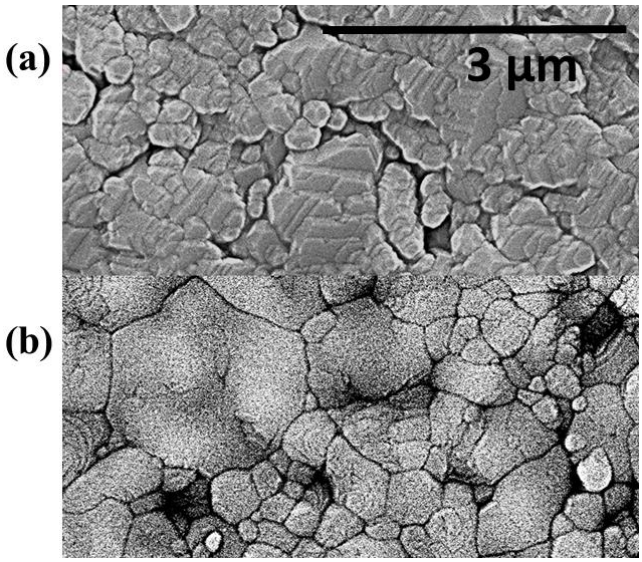

Figure 6.8. SEM micrographs of sintered (a) BT and (b) 2.5NNBT ceramics.

The density of the two end member ceramics was determined to be 98% for BT and 95% for 2.5NNBT, following the sintering process described in chapter 3. SEM, figure 6.8, was carried out to confirm the dense nature of the ceramics, making them suitable for consideration in a bilayered system.

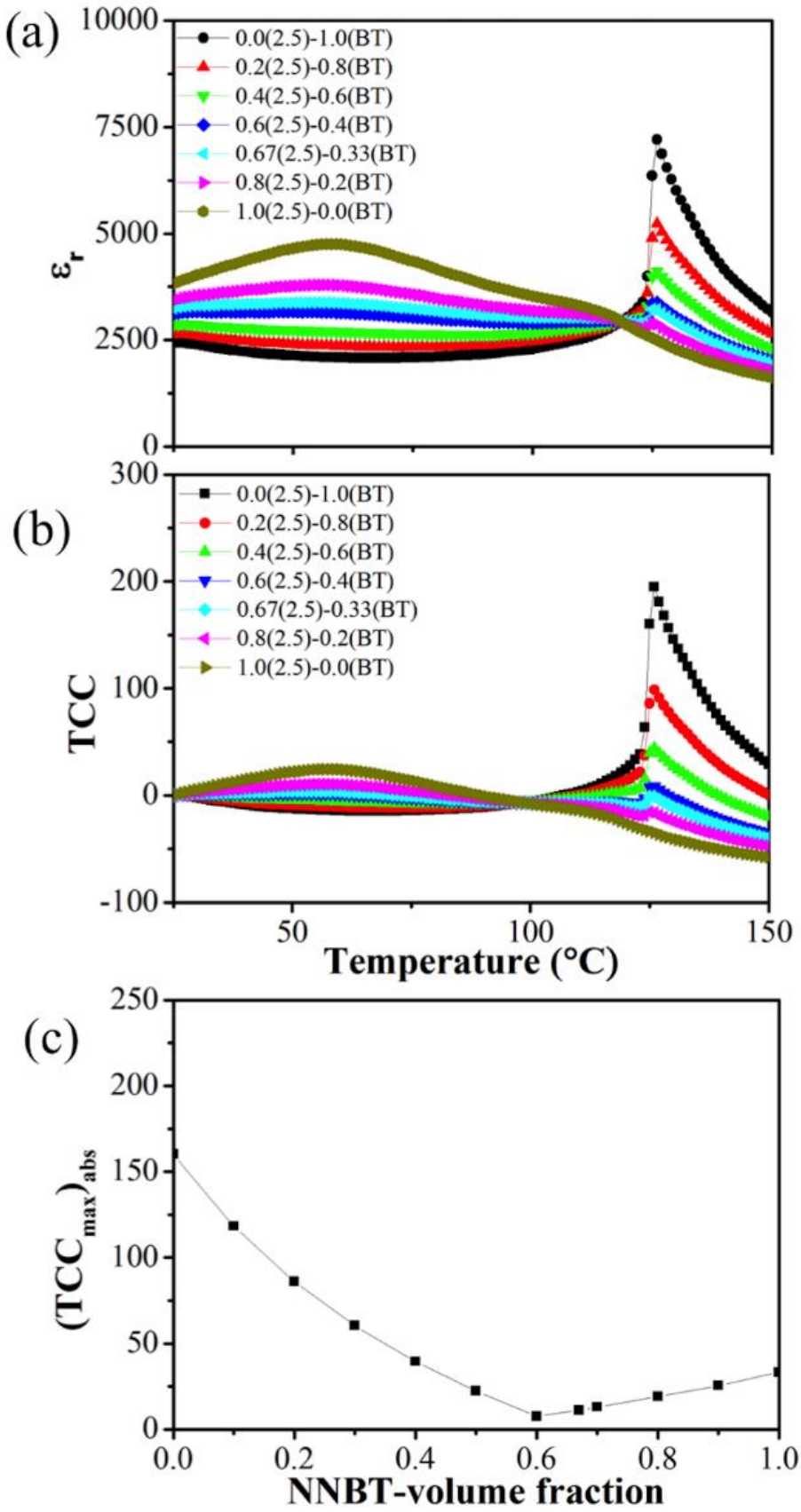

Figure 6.9. (a) Experimentally measured permittivity-temperature profiles of BT (filled black symbols) and 2.5NNBT (filled olive symbols) ceramics with simulated

permittivity-temperature data from the series bilayer model for various volume fractions, v_f, *e.g.* 0.2(2.5)-0.8(BT) corresponds to v_f = 0.2 (2.5 NNBT) and v_f = 0.8 (BT). (b) Converted TCC values and (c) the absolute maximum deviation of TCC versus v_f of 2.5 NNBT.

Figure 6.9 is a summary of simulated core-shell volume fraction using the data obtained from BT and 2.5NNBT, respectively. Their permittivity-temperature profiles were used as the input data sets to optimise TCC using equation 6.1. The relative volume fractions from that equation are equivalent to the relative thicknesses of the two ceramics in a series arrangement.

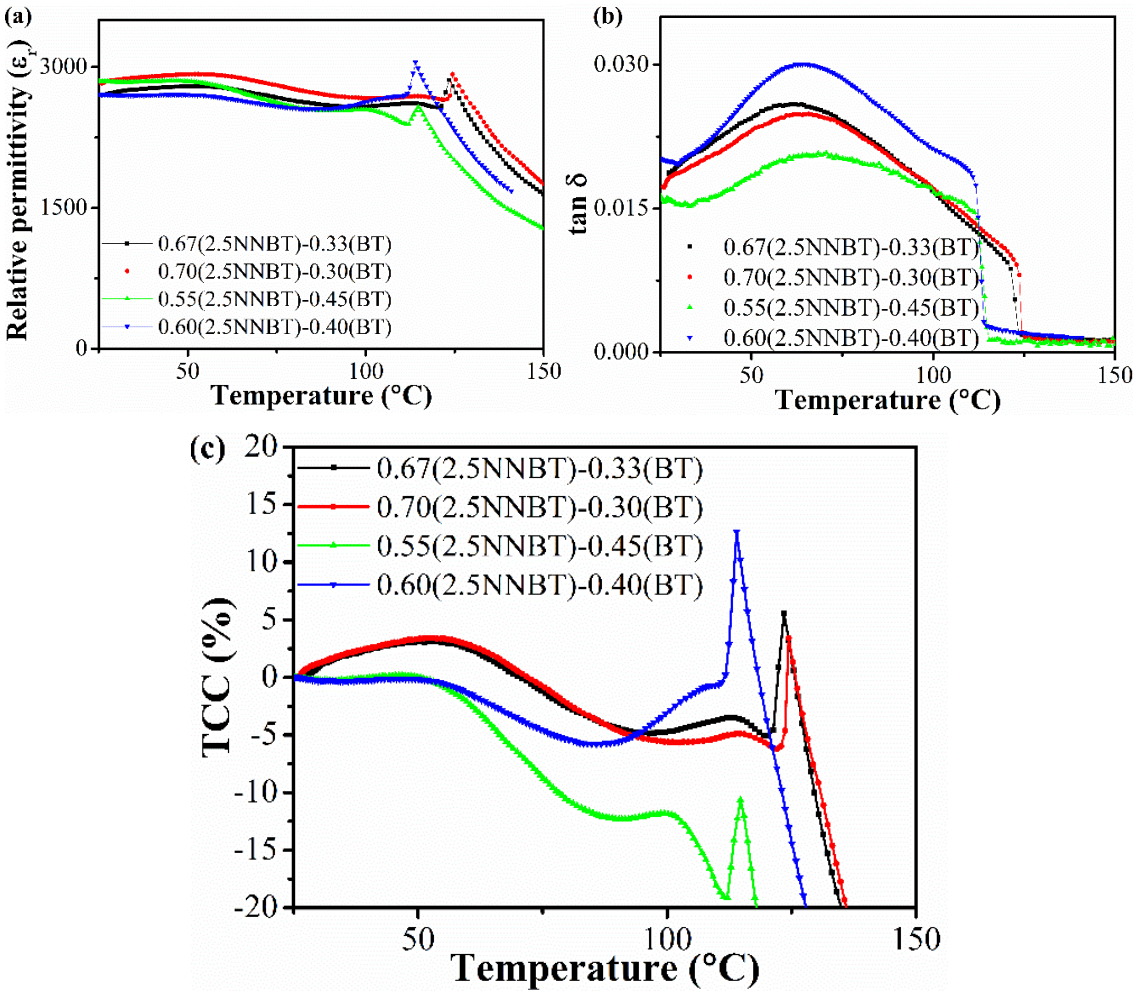

Figure 6.10. Experimental data for a range of bilayers showing (a) their permittivity profiles, (b) their tan δ and (c) their TCC profiles.

The permittivity part (6.9.a) illustrates that it is possible to flatten the permittivity profile using the bilayer method. The simulation clearly shows a strong suppression of the large TCC of BT at its T_C with increasing NN-content. However, it also becomes obvious that improvements of TCC are compensated by a decrease in the permittivity value. This is a reasonable trade-off considering that figure 6.9.b shows an improvement in TCC from extremes such as +200 % (BT) and -55 % (2.5NNBT) down to ±25 % for the temperature range of 25 to 150 °C. This is even more impressive, when considering the temperature range of 25 to only 125 °C, where TCC values lower than 15 % are achieved.

Figure 6.9.c shows the absolute maximum deviation of TCC versus v_f of 2.5. This metric offers a simple coefficient to judge the degree of optimisation for the system. The smaller the absolute maximum TCC, the more optimised the system is and the experimental equivalent should offer the lowest TCC. From this plot it is possible to identify a region of NN-content resulting in the lowest possible TCC between x = 0.6 and 0.7.

To verify the predicted volume ratio, a range of bilayers were produced and a variety of data from them are shown in figure 6.10. The lowest TCC was obtained when the NN-content was x = 0.67. This is a ratio that might be useful when considering this technique in MLCC form, as it is essentially a 2:1 2.5NNBT:BT ratio. This might be easier to manufacture than other more complex ratios.

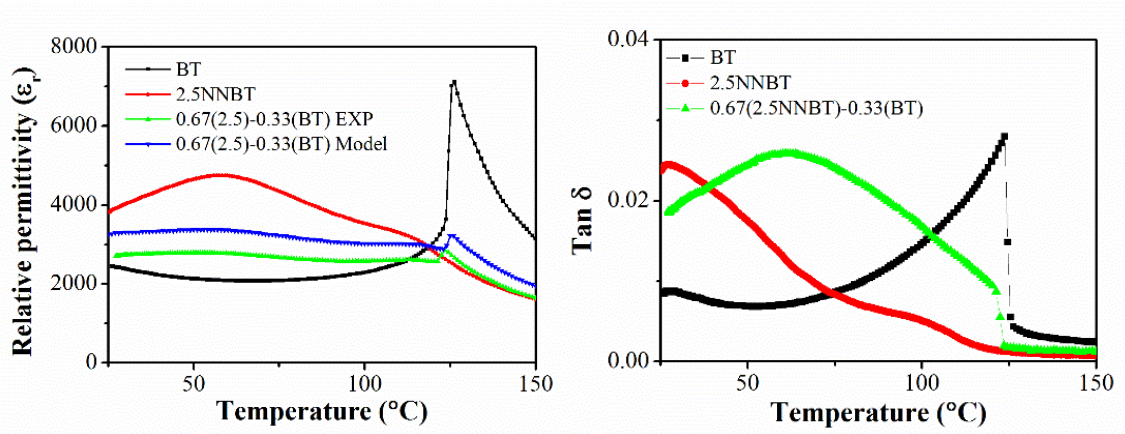

Figure 6.11. Permittivity (left) and tan δ (right) profiles of the chosen bilayer system compared to the end members. The experimental bilayer data is shown in green.

The permittivity and tan δ profile for the 0.67 bilayer are compared to its components profiles in figure 6.11. This comparison shows the bilayer to have a permittivity of ~3000 between 25 and 125 °C, whilst retaining the low tan δ of its components. The comparison also shows a drop in permittivity between the simulated and the experimental bilayer data. This is due to a difference in the interface between the two and will be discussed in more detail in section 6.3.2.

The TCC profiles of the simulated and experimental 0.67 bilayers in figure 6.12 show very close agreement between simulation and the experimental bilayer. The experimental TCC is as low as ±6 % for the temperature range of 25 to only 125 °C. This, in combination with the permittivity being at 3000 and its low dielectric loss makes this an interesting system for MLCCs and therefore offers a viable alternative technique to CS-microstructures.

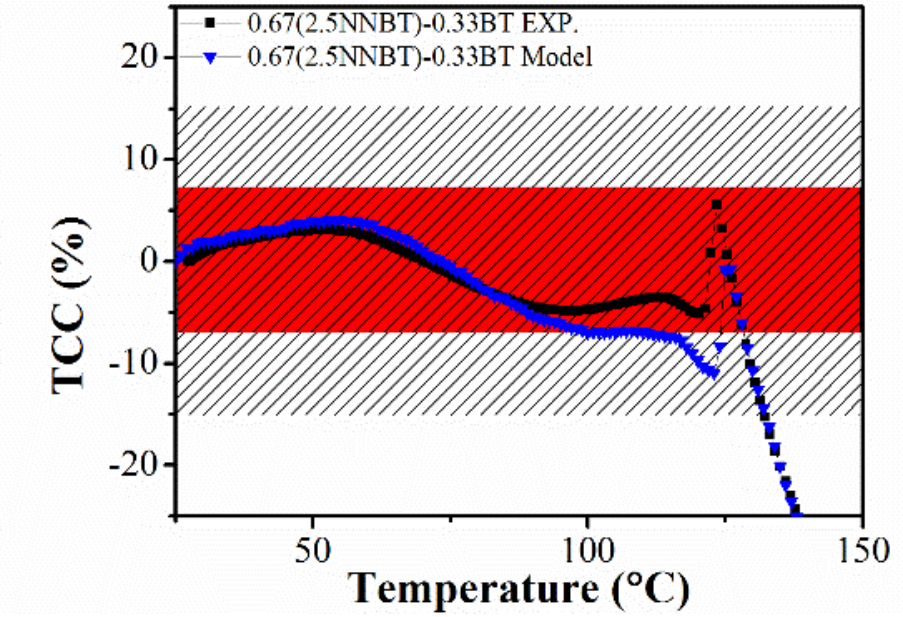

Figure 6.12. Modelled and experimental TCC responses of the chosen bilayer system.

Considering it is the volume ratio of the two materials that results in the TCC optimisation, it was considered if mixing the two materials in the 0.7 ratio would be enough to improve TCC. Figure 6.13 shows the outcome of that attempt in comparison to the end members. It is clear to see that simple mixing does not result in the correct volume fractions, as the dopants diffuse through the BT, effectively ‘diluting’ the dopant

concentration. Going back to the permittivity profiles of the solid solution in figure 4.4, it can be determined that the mixing results in a xNNBT ceramic with x being just below 2 (mol%).

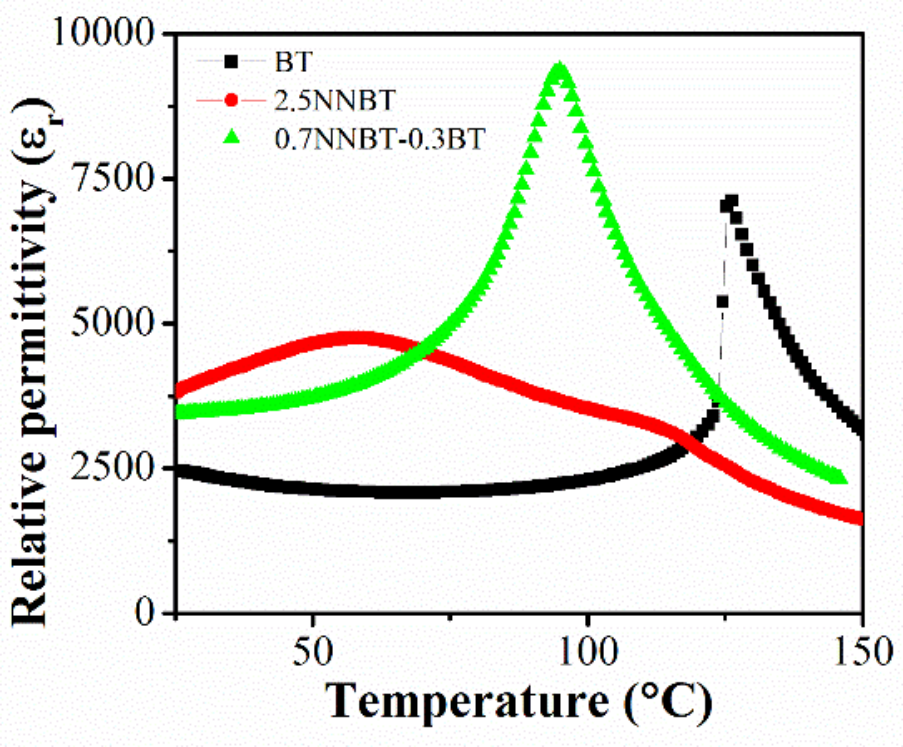

Figure 6.13. Permittivity profiles of the chosen CS-ratio system compared to the end members, when mixing the CS components, rather than layering them.

6.3.2 Comparison of CS and bilayer

This work was based on the assumption that the permittivity profiles of a CS and a bilayer, with the same CS volume fractions, are comparable to each other. In order to justify this assumption it is instructive to compare and contrast the permittivity profiles of the CS and bilayers directly. Figure 6.14 shows a direct comparison between simulated permittivity profiles for a range of CS and bilayers of varying volume fractions. The bilayers profiles were obtained as described in this chapter, whilst the CS-profiles were obtained using a FEM package by Dean *et al*.[2]

The discrepancy between the CS and bilayer profiles appears to follow the trend predicted in the introduction. The bilayer model permittivity profiles follow the smallest

end member permittivity profile at all volume fraction, as the smallest capacitor dominates the response for a series capacitor model.

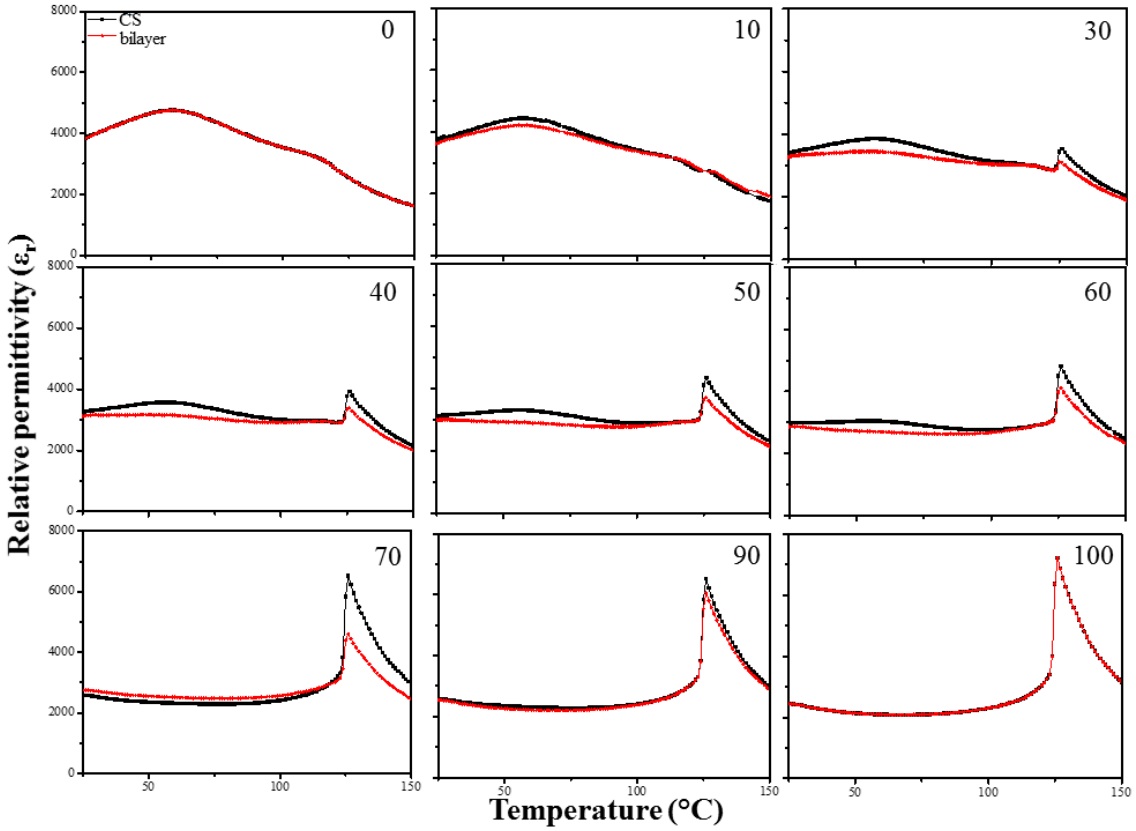

Figure 6.14. Change in permittivity profiles with a change in vol% of the 'core'-part for bilayer- (red) and CS-models (black).

The CS model is in reasonable agreement with the bilayer model at high core volume fractions. However, at low and intermediate core volume fractions it deviates from the bilayer model. This is due to the current pathway and the existence of parallel capacitance at these volume ratios, as shown in figure 6.2. When having capacitors in parallel, the larger capacitance/permittivity dominates. Therefore, the CS-model permittivity profiles at the low and intermediate core volume fractions follow the highest end member permittivity profile.

Following this explanation, it is expected that the largest discrepancy between the two models would occur whenever one of the components runs through a maximum (~60 °C for 2.5NNBT and ~125 °C for BT). The permittivity plots in figure 6.14 clearly show the largest discrepancies at these temperatures.

It should be noted that although these discrepancies exist, the overall difference does not appear to be a significant problem and in fact it looks like the bilayers appear to have better temperature stability than the corresponding CS.

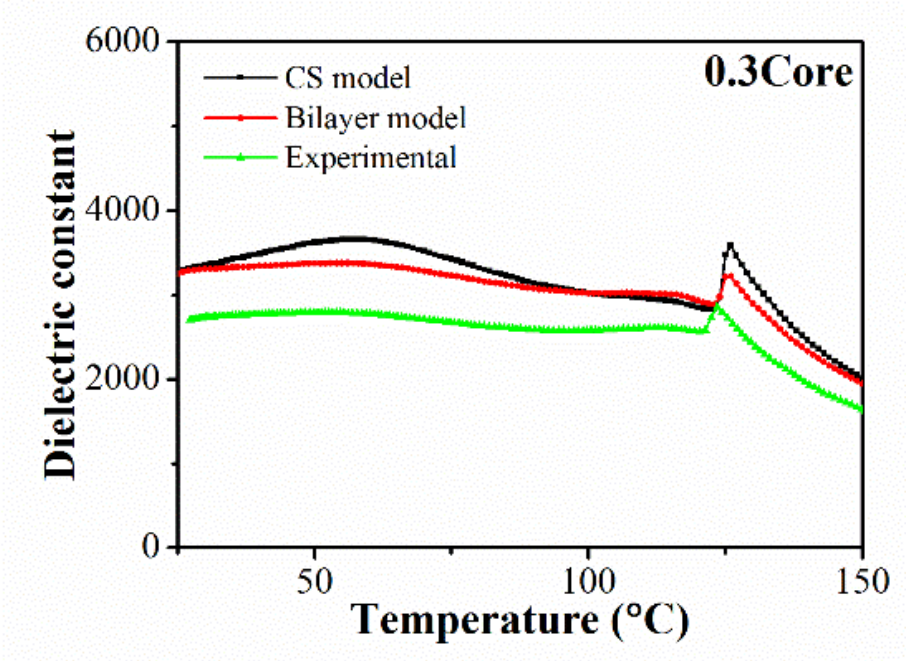

Figure 6.15. Comparison of the modelled CS and bilayer permittivity profiles with the experimental bilayer data for a 0.7(Shell)-0.3(Core) system.

The flatter permittivity profiles of the bilayers is demonstrated by figure 6.15. It shows that for a 0.3Core the two models possess the same RT permittivity but the CS model shows larger variation at the two T_Cs, making it less favourable. It needs to be said that the CS could probably be optimised to show the same response as the bilayer, however the volume fraction would need to be varied for that to occur. The conclusion is therefore that at the same volume fraction, the bilayer possesses the more favourable TCC.

The experimental data in figure 6.15 is again lower than the simulated data. As mentioned previously, this is due to the interfaces associated with each set of data. The modelled data set assumes a perfectly flat interface between the two layers with no porosity or inter-diffusion or any other extrinsic effects. This is however not the case for the experimental data set. The layers will not be perfectly flat, even after polishing and there is the layer of gold paste between the ceramics.

To examine and confirm the effects of the interface, its roughness and electrode coverage, a 60/40 2.5NNBT/BT bilayer was created and different interfaces applied to it. The permittivity profiles for each interface were collected and compared in figure 6.16.

The three interfaces that were compared are Au foil, Au paste and nothing-in-between the pellets. Au paste 1 and 2 were prepared slightly differently. In the case of Au paste 2, the two pellets were directly connected with Au paste. In the case of Au paste 1, each of the pellets was coated individually first and then the already coated and hardened surfaces were combined with more Au paste. In the case of gold foil, a piece of gold foil was placed between the samples and the pellets were subsequently compressed during the dielectric measurements.

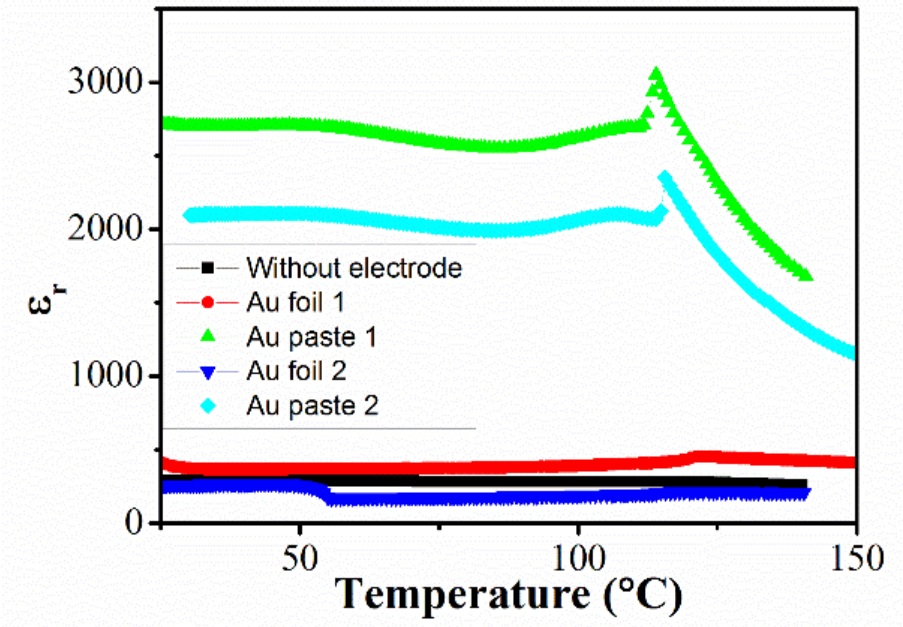

Figure 6.16. Effect of various interfaces on the permittivity-temperature profiles of a bilayer.

Significant drops in permittivity were observed for all interfaces when compared to Au paste 1. In the case of having nothing in between the pellets or using gold foil this is due to the lack of sufficient interfacial contact. Figure 6.17 shows an interface created using gold foil. Although the pellets both possess polished flat surfaces and are compressed in a spring loaded jig, it is possible to see substantial gaps between the foil and the ceramics. This significantly reduces the effective area of the capacitor and essentially introduces large air gaps.

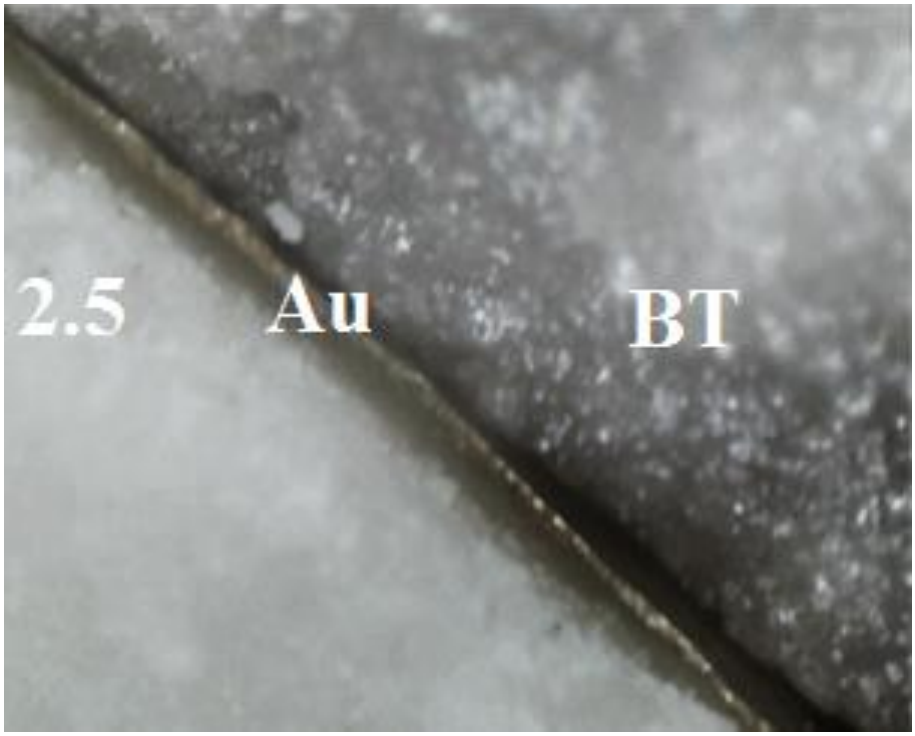

Figure 6.17. Micrographs of the ceramic-(Au-foil)-ceramic interface of a bilayer system.

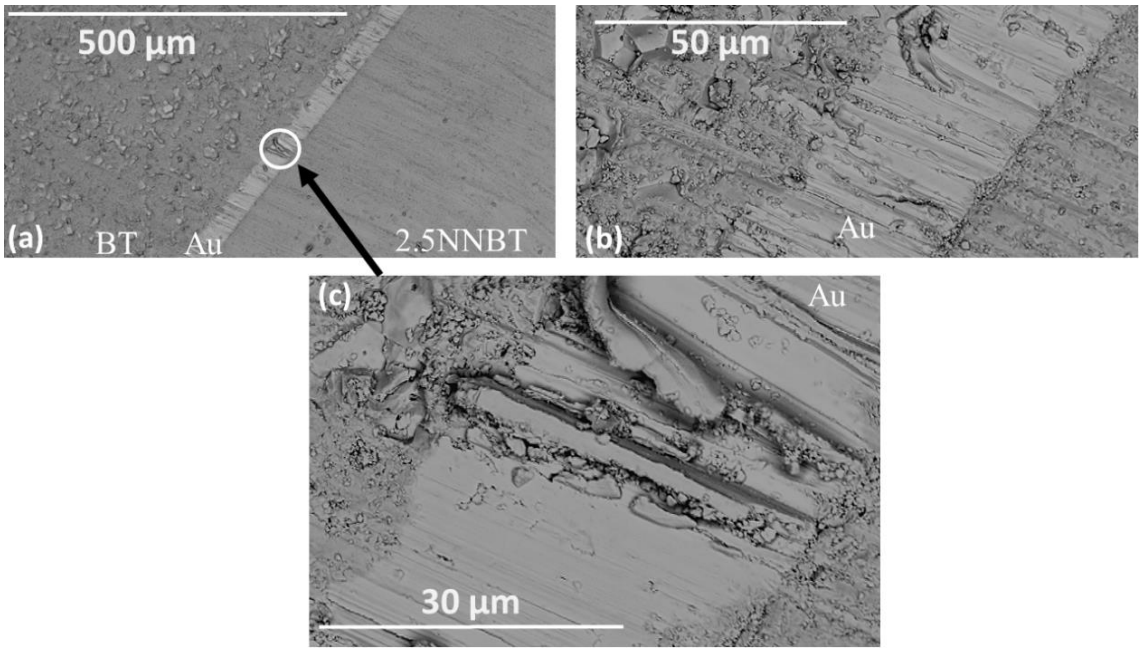

Figure 6.18. SEM micrographs of the ceramic-Au (paste)-ceramic interface of a bilayer system.

The SEM micrographs for the Au paste in figure 6.18 show the ceramic-Au-ceramic interface created when using gold paste. The interface itself is fairly neat, however upon closer inspection it is possible to see that the BT side of the interface particularly shows signs of diffusion, as it is rougher than the interface to the 2.5NNBT ceramic. Furthermore, it is possible to see ceramic inclusions and cracks in the Au-part. It is also possible to see what appears to be small air gaps, figure 6.18.c.

These images together with the results in figure 6.16 highlight the importance of the electrode interface in the performance of the device. Good interfacial contact needs to be achieved to obtain high permittivity bilayer ceramics. Poor internal electrode contacts are due to a combination of incomplete (or no) electrode coverage, as well as surface roughness and porosity, as a result of the processing and fabrication methods.

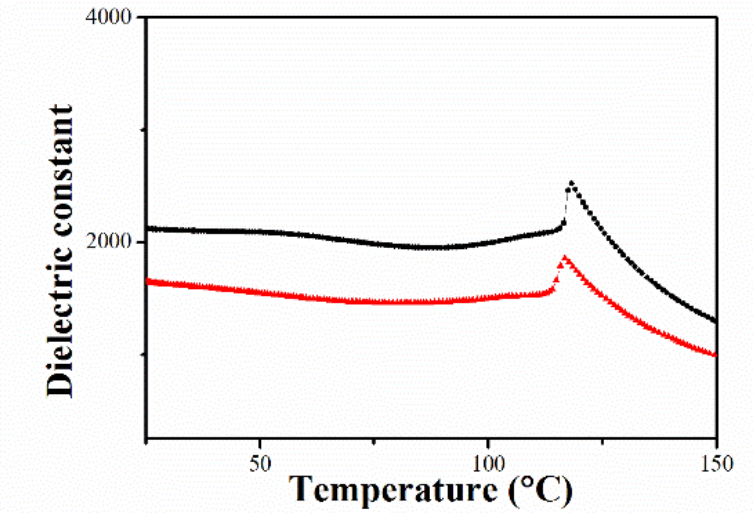

Figure 6.19. Effect of interfaces (black = good, red = bad) on experimental permittivity-temperature profiles of bilayers.

The quality of the internal electrode interface can be judged in several ways. The quickest method is to simply consider the permittivity profile. Figure 6.19 shows very clearly the difference between a good and a bad internal electrode interface. The sample with the poor interface possesses a permittivity that has dropped significantly compared to what is expected from the predicted values. This is due to low permittivity regions in the interface due to air gaps for example.

In the impedance response, the difference between a good and a bad interface becomes even more apparent, as shown in figure 6.20. The existence of air bubbles and other

imperfections causes noisier data and a significant drop in capacitance, particularly at higher frequencies.

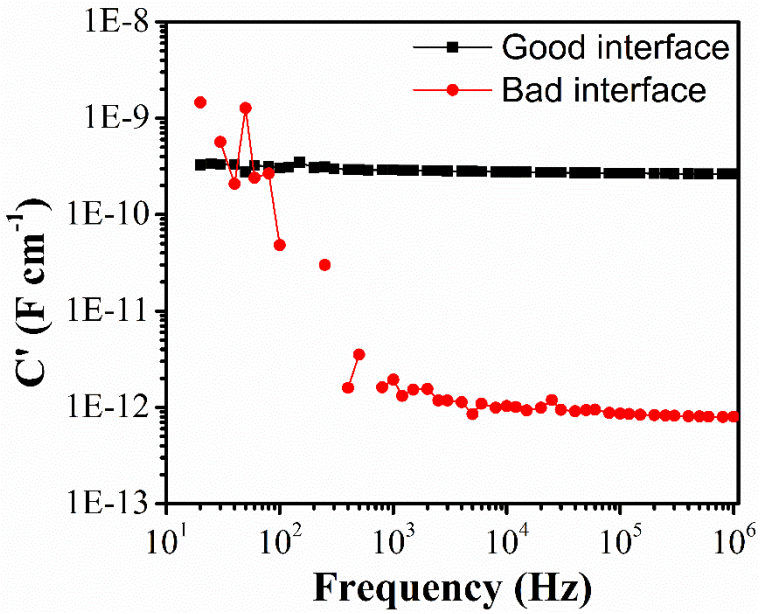

Figure 6.20. Effect of interfaces on the room temperature capacitance of bilayers as a function of frequency.

This shows the importance of consistent and reproducible processing and it should be noted that this is more likely to be achieved on an industrial scale, with more automated machinery. The example here, from figures 6.19 and 6.20 was processed by hand following the same instructions.

6.3.3 Limitations and advantages

The advantage of bilayers is that new suitable combinations are easier to find than new CS-formulations, as it is possible to predict suitable volume ratios beforehand. This eliminates a lot of the time and resource intensive trial and error associated with the current CS method.

Furthermore, the bilayer methodology is applicable to a wide variety of materials and is not limited to the two materials used in this proof of concept. Materials that have been discarded previously due to their TCC being too high might become viable with this new

methodology. This is illustrated by the example that neither of the materials used here would have fit the ±15 % TCC variance by themselves.

The limitation in this study is that the materials used in this proof of concept were optimised for the temperature range of 25 to only 125 °C. To fulfil the complete temperature range for an X7R (-55 to 125 °C) further work is required. This comes on top of the issue of co-sintering the materials, which was not done for this work but would be required for industry. Also, the interface could cause problems and it would be beneficial to exclude it. However, it is likely that a separator, like a floating electrode, would be required in a MLCC device to limit diffusion between the layers and any change in the target volume ratio of the two layers.

6.4 Conclusions

This chapter showed proof of concept for a novel approach to optimise TCC. TCC was successfully optimised by creating a novel 2.5NNBT-BT bilayer system, with a RT permittivity around 3000 and a TCC of ±6 % for a temperature range of 25 to 125 °C, based on a volume ratio of 0.67 2.5NNBT to 0.33 BT. This TCC lies within the benchmark of ±15 % to make it interesting for industry. Further work is required to optimise the permittivity across the whole temperature range of an X7R (-55 to 125 °C). This might require different materials, however this methodology is applicable for any material and could be used by the MLCC industry with very little change, once co-sinter ability has been achieved. This may be possible by varying the levels of sintering aids such as glass additions.

The work has also shown the significance of the internal interfaces. Whether this is between the layers or with an internal electrode. These interfaces can have significant impact on the TCC profile and the permittivity value of the device. It would be beneficial to study this further in actual MLCC devices, as the interface behaviour will be significantly different to the bulk samples used here, due to the large amount of glass and organics required in the MLCC processing having significant impact on mobility and diffusion of the materials used.

6.5 References

1 S. Jeon, B. Yoon, K. Kim and S. L. Kang, *J. Adv. Ceram.*, 2014, **3**, 76–82.

2 J. S. Dean, P. Y. Foeller, I. M. Reaney and D. C. Sinclair, *J. Mater. Chem. A*, 2016, **4**, 6896–6901.

3 F. H. Morshead, P. Y. Foeller, C. L. Freeman, H. Zhang, I. M. Reaney, D. C. Sinclair and J. S. Dean, *J. Eur. Ceram. Soc.*, 2017, **37**, 2795–2801.

4 D. Maurya, F. Sun, S. P. Alpay and S. Priya, *Sci. Rep.*, 2015, **5**, 15144.

5 A. G. Serrano, A. L. Bonaventura, R. B. Junior and E. Antonelli, *Mater. Res. Bull.*, 2017, **87**, 34–39.

6 J. P. Heath, *Priv. Commun.*

7 J. S. Dean, J. H. Harding and D. C. Sinclair, *J. Am. Ceram. Soc.*, 2014, **97**, 885–891.

8 C. Geuzaine and J.-F. Remacle, *Int. J. Numer. Methods Eng.*, 2009, **79**, 1–24.

Chapter 7: Layered structures to optimise TCC

7.1 Introduction

The previous chapter dealt with the proof of concept of bilayers and their potential for being used in the MLCC industry. There was little focus on what general knowledge and experience was gained when working with bilayers and how these help to guide future choices of materials and or temperature ranges.

The aim of this chapter is to summarise the most significant observations on bi-/multi-layered systems. This ranges from the number of layers used to the choice of materials in the system. Whilst most of the observations are based around bilayered systems the knowledge is transferrable to any number of layered-systems. The next chapter will report on trilayered systems and the materials chosen are partially based on the observations gleaned from working with bilayers.

The second part of this chapter is a short summary of $BaZrO_3$-$BaTiO_3$ (BZT-BT) bilayers. This work was carried out to show that the optimisation process works for any material. BZT was chosen as it is well studied and has been widely used. This system, whilst being optimised highlights some limitations that were not encountered previously.

The outcome is that the knowledge described here means that one can rely on the simulations of bi-/multi-layered systems. The limitations, such as the effect of the interface, can be controlled and, if treated correctly, accounted for. Confidence in the method is important as it is unlikely that industry would be prepared to replace current/existing methods with a method they deem unlikely to succeed. In this case the advantage of predictability and potential usage of currently available materials makes the layered method appear favourable compared to CS microstructures.

That said, it has to be reiterated that industrial processing is distinctly different from the processing here and it is advised that when bilayers are actually being considered for the use in MLCCs the input data for the optimisation is based on MLCCs made up of the individual components, rather than bulk properties as is the case here. This would allow to take electrode interfaces and their effect on the materials into account from the start.

7.2 Experimental

Experimental procedures for the data in this chapter can be found in chapters 3 and 4. The BZT-BT bilayers were not co-sintered but prepared as described in chapter 6.

7.3 Results and discussion

7.3.1 Number of layers used

As shown in chapter 6, creating a layered system can be used to imitate a CS microstructure reasonably well. One of the most important factors to consider is the number of layers that will be used. As stated previously, the optimum number is as low as possible to keep the processing as easy as possible.

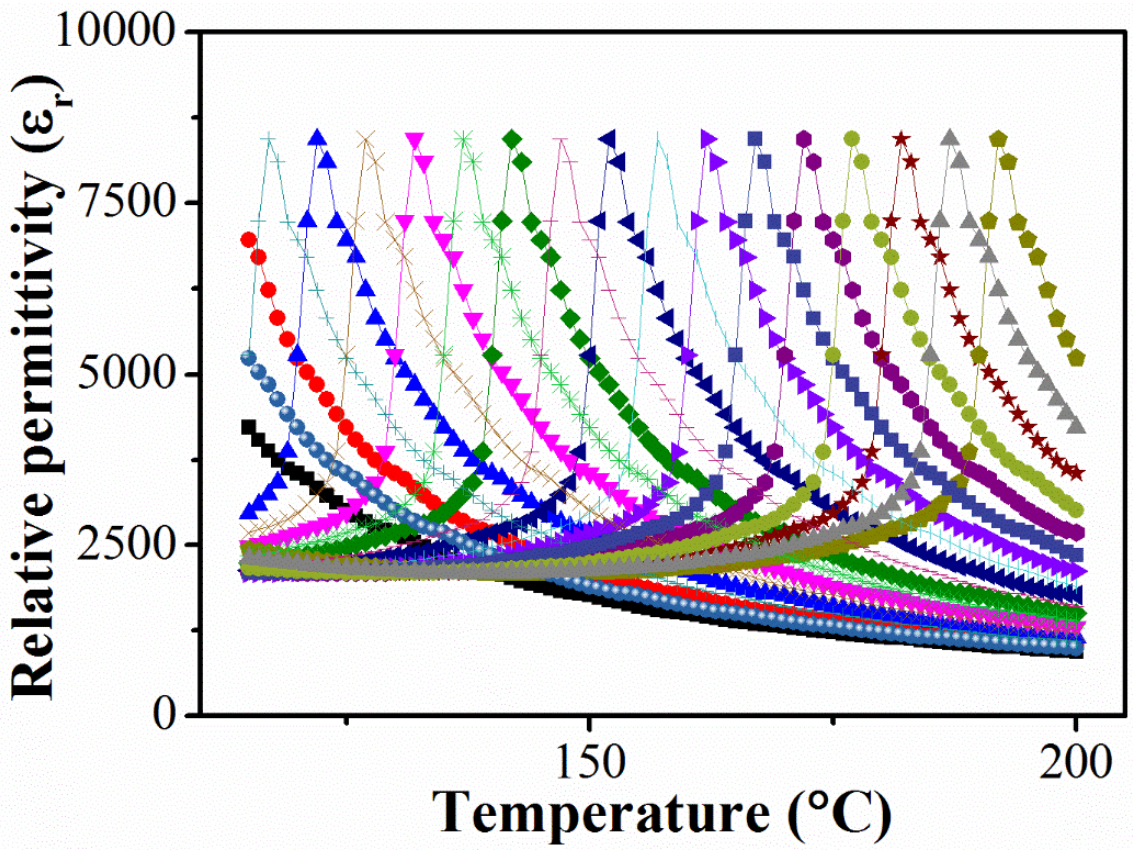

Figure 7.1. The permittivity profiles of the components of an assumed concentration gradient.

In general however, the more layers one can use, the more closely the system will imitate an actual CS microstructure and/or a dopant concentration gradient through the shell. This means a large number of compositions could exist with slightly different dopant concentrations and therefore give small shifts in T_C. Figure 7.1 shows a constructed concentration gradient, based on a BT profile. Each profile is translated by 5 degrees up to 125 + 90 °C. As seen in figure 7.1 each composition has a slightly different T_C, even though real compositions would not share the same temperature profile and/or permittivity maximum. The assumed shift in T_C as a linear function of dopant concentration does correspond to real dopant systems, such as Sr- or Pb-doped BT, as seen in figure 2.12.[1] Unlike the permittivity profiles in figure 7.1, the change in profiles of real data would not be limited solely to a shift in T_C.

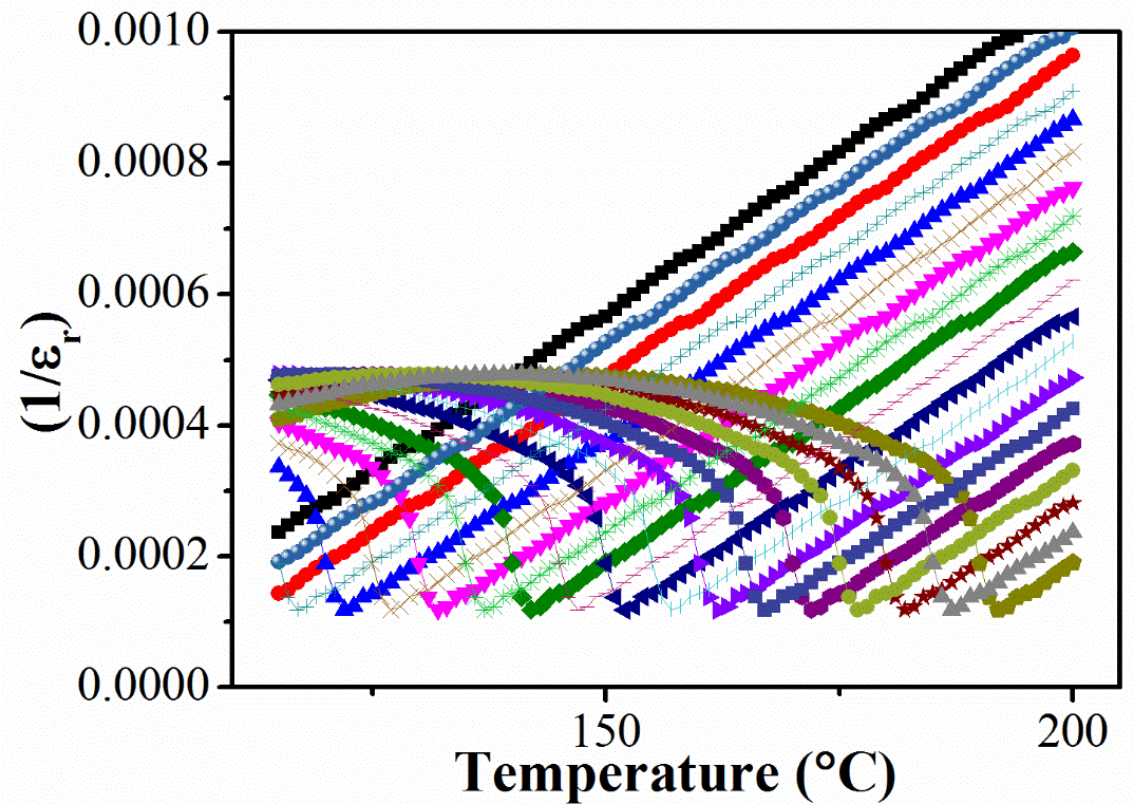

Figure 7.2. The inverse permittivity profiles of the components of an assumed concentration gradient.

When plotting the inverse permittivity of these compositions however it becomes possible to get an impression of how the overall permittivity profile of this continuous

"CS" would appear. Figure 7.2 shows a clear behavioural trend, *i.e.* overlap of curves. This overlap corresponds to a permittivity of ~2500.

The simulated combined system (adapting equation 6.1: capacitors in series with equal volume fractions) in figure 7.3 does indeed show the same trend predicted from figure 7.2 at a permittivity of ~2500, possessing an extremely flat permittivity-temperature profile.

The schematic and its simulation show that TCCs very close to 0 could be achieved over wide temperature ranges but the number of different layers might be prohibitively high when considering the processing, in particular co-sinterability. The conclusion must therfore be that a trade-off can be found that involves getting the flattest possible profile with the fewest number of layers.

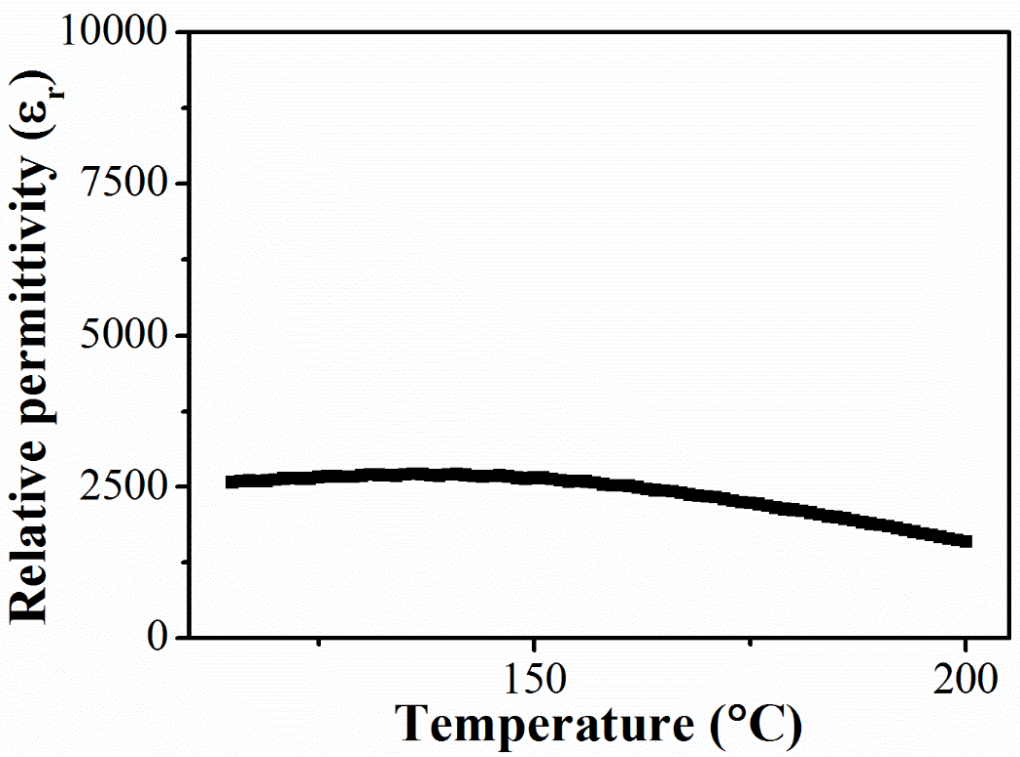

Figure 7.3. The permittivity profile of a layered concentration gradient system.

The temperature range used in the schematic, 100 to 200 °C, is used again in the next chapter to see if a trilayer system would be enough to get a temperature stable plateau in that temperature range. This range is required for high temperature capacitor applications.

7.3.2 Choice of materials

The choice of materials for layered systems is now discussed. There are obvious processing related characteristics that need to be obeyed, for instance their co-sinterability. There is however also their electronic properties to consider, in particular the permittivity profiles.

Certain profiles will optimize better than others. The reason for that is the nature in which permittivity is summed for capacitors connected in series. Assuming a bilayer system, figure 7.4 shows two materials, A and B, which show the ideal permittivity profile to result in a TCC of 0 %, when combined in a 50:50 volume ratio. Therefore, the more the permittivity profiles of the two compositions used in a bilayer are mirror images of each other for a particular temperature range, the better the degree of possible optimisation. Considering the profiles of 2.5NNBT and BT in figure 6.6, it can be said that they come very close to resembling each other's mirror image in the temperature range of RT to 125 °C. Therefore, a significant improvement in TCC can be achieved by optimisation of that temperature range.

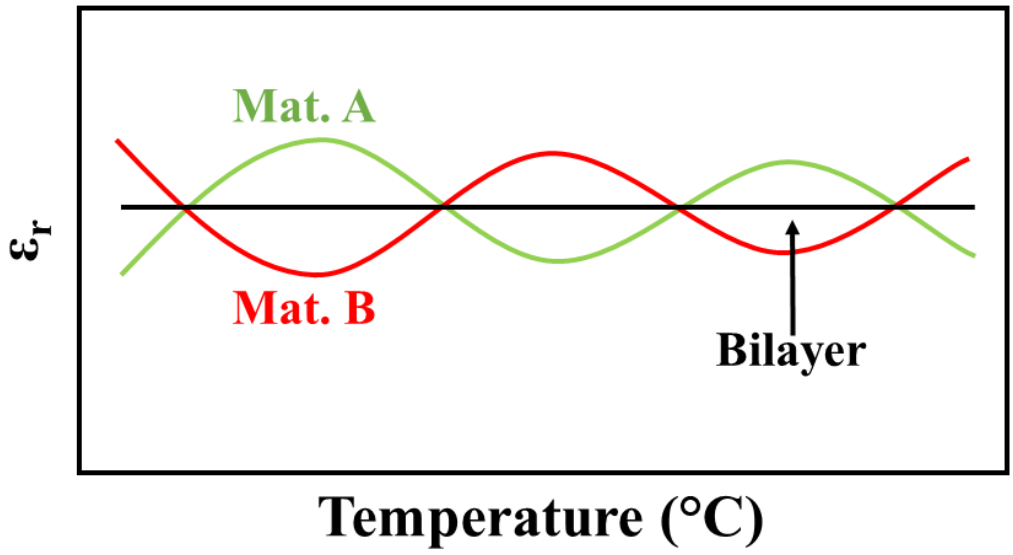

Figure 7.4. Schematic of ideal material choices.

7.3.3 Reasons for changes in TCC profiles

The work presented here and also from examples in the literature,[2,3] allows the observation of certain differences in the permittivity profiles of simulated and experimental data. These shifts can mostly be put down to one of the following three reasons.

This drop in permittivity is predominantly observed for the bilayer processed here, *i.e.* with internal electrode interfaces. This processing involves gold paste, which in the curing process can lead to some diffusion of the materials into the gold electrode, but mainly it allows for the introduction of air bubbles and/or gaps into the system. The result is an observed drop in permittivity for the experimental data compared to the simulated data.

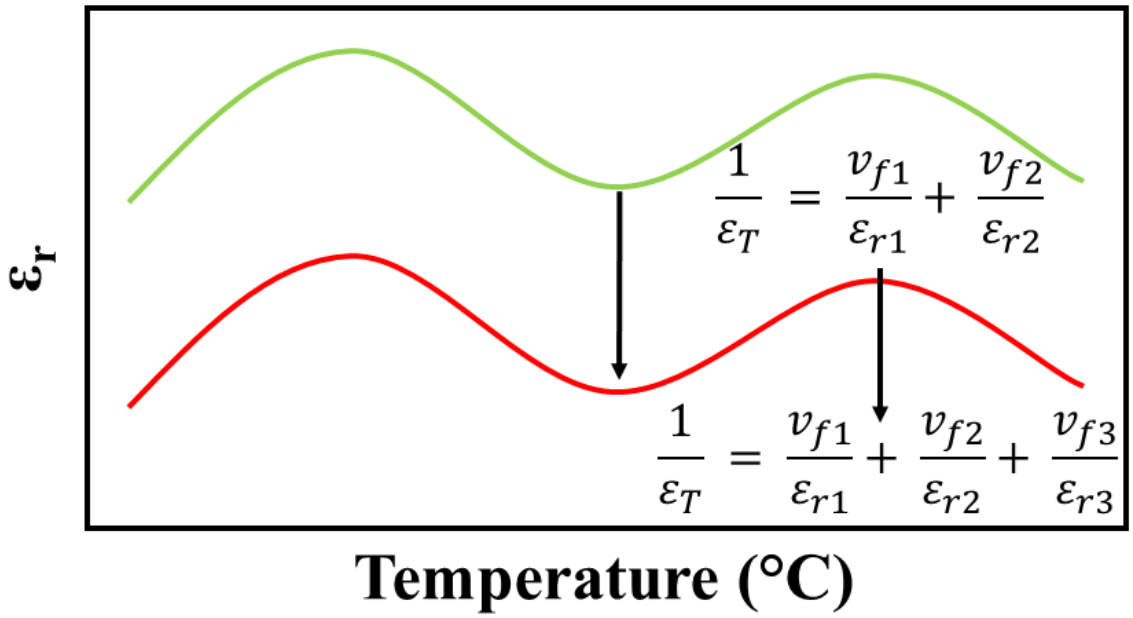

Figure 7.5. Schematic of a change in permittivity profile for a bilayer due to air gaps at the interface.

The reason is explained by the schematic in figure 7.5. The simulated profile consists of two capacitors connected in series, material 1 and material 2. When introducing air gaps, a third component (material 3) with a low permittivity is introduced which means that even at small volume fractions, it will have a significant effect on the permittivity and therefore result in a lower overall permittivity compared to that predicted by the model.

Serrano *et al.* in their work encountered a different kind of shift. Rather than a drop in the permittivity, they observed a change in the shape of the permittivity profile.[2] Again the reason is due to the introduction of additional permittivity profiles. In this case, inter-diffusion of the two materials leads to the creation of a third 'layer'. This extra layer has a comparable permittivity to the others, however with a new T_C. This extra profile will lead to a change in shape, whilst comparable permittivity means that there is no significant drop in permittivity observed.

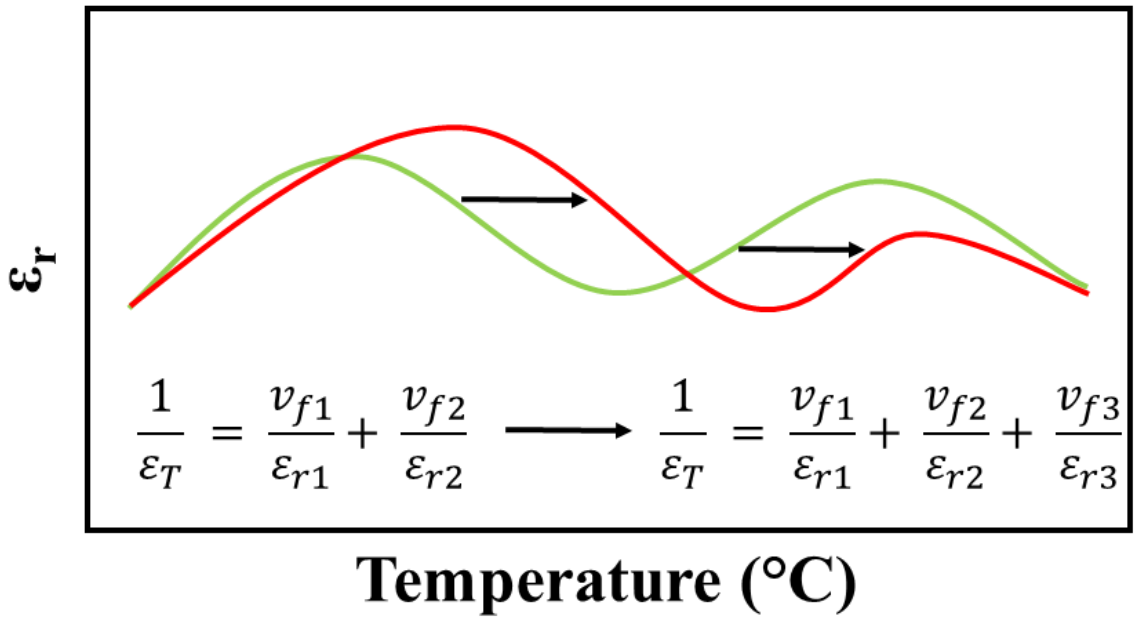

Figure 7.6. Schematic of a change in permittivity profile of a bilayer due to a chemical interface.

Both of the issues mentioned so far can be taken into account for industrial MLCCs and it should be possible to limit their impact, (i) by including internal electrodes in the input data, *i.e.* profiles of end member MLCCs and (ii) by limiting the diffusion between the components, *i.e.* with the use of floating electrodes.

The third reason one might observe differences in simulated and experimental permittivity profiles is if the processing conditions of the input data does not match the processing of the bilayer system. Figure 7.7 shows the vulnerability of the method in regards to reproducing the permittivity-temperature profile of an end member.

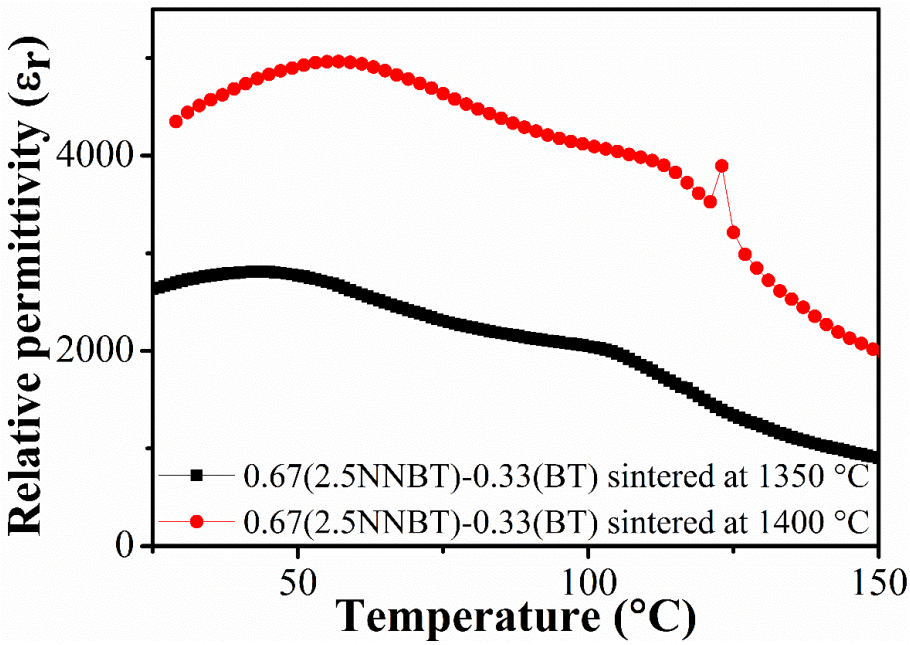

Figure 7.7. Schematic of the change in permittivity-temperature profiles of 2.5NNBT sintered at 1350 and 1400 °C.

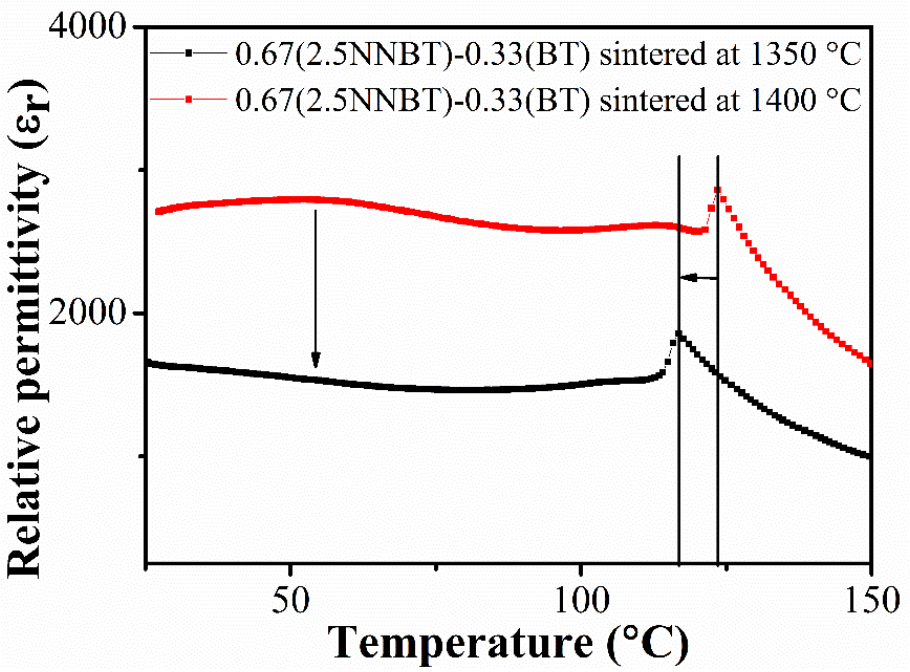

Figure 7.8. Schematic of the change in permittivity-temperature profiles in two bilayers due to a change in processing temperature.

Figure 7.8 shows a significant change in the permittivity-temperature profile for a 2.5NNBT-BT bilayer, where the only difference is the sintering temperature. A change

of 50 °C results in a change in shape as well as magnitude, as the processing conditions affect the permittivity profile of an end member as seen in figure 7.7.

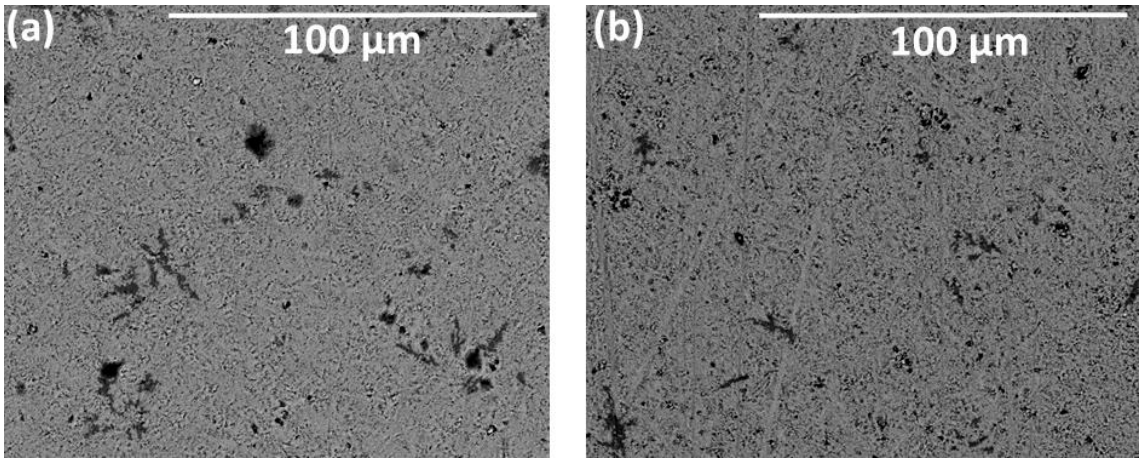

Figure 7.9. SEM micrographs for the surfaces of 2.5NNBT sintered at (a) 1350 °C and (b) 1400 °C.

The reason for that is the extreme reliance of 2.5NNBT on the right sintering conditions. Whilst the BT used here sinters well at both temperatures, 2.5NNBT does not. Figure 7.9 shows significantly larger pores at the lower sintering temperature, it is less dense and a significant drop in permittivity (~1500) can be observed. The magnitude of this drop corresponds to the drop observed in figure 7.8 for the bilayer system. The way capacitors connected in series are summed is responsible for the shift in the peak that can be attributed to the T_C peak of BT. This is a very good example to observe the importance of maintaining consistent processing conditions between input and output when using this model.

7.3.4 Dielectric loss

Another important aspect for these systems to be used in the MLCC industry is the need to maintain a low tan δ. Unlike permittivity there is no easy way to predict tan δ of a bilayer system and so far, there has been no success when attempting to come up with a model. The observation in this work has been that tan δ will remain low over required temperature ranges, if the components of the system possess low tan δ's over the same temperature range.

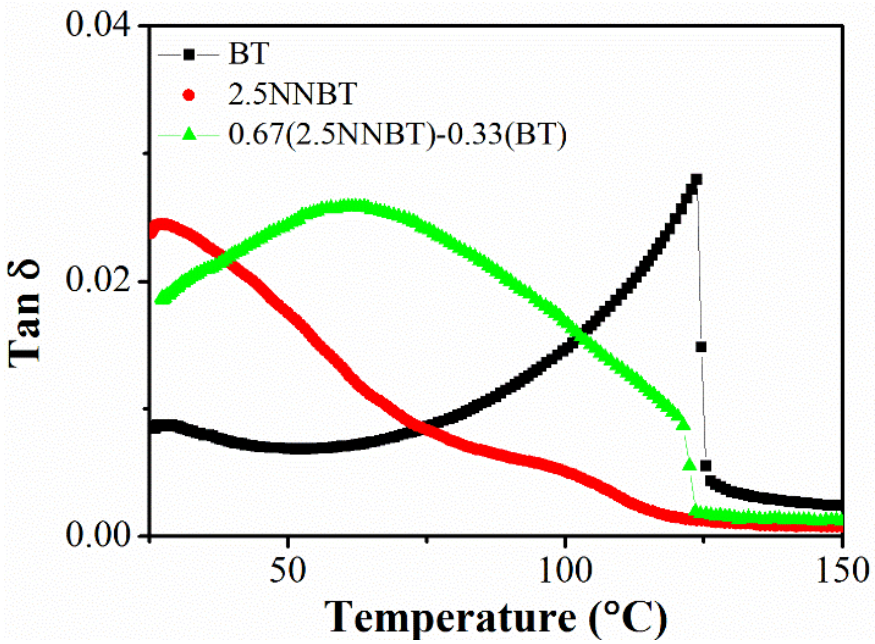

Figure 7.10. tan δ versus temperature profiles of a 2.5NNBT-BT bilayer system compared to the end members.

The bilayer in figure 7.10 shows that tan δ of the bilayer system does not exceed tan δ of the individual components.

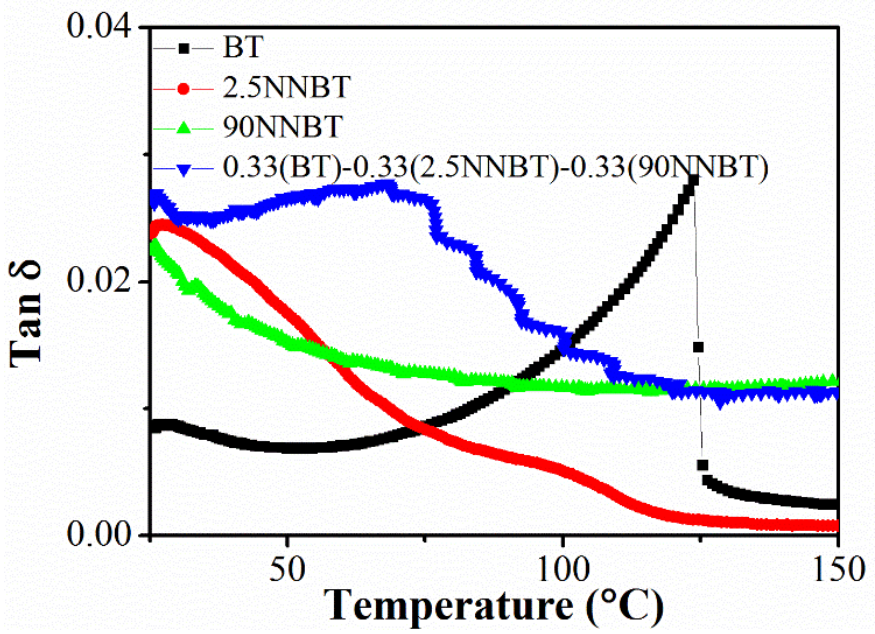

Figure 7.11. Example of tan δ-temperature profiles of BT-2.5NNBT-90NNBT trilayer system compared to the end members.

The same is true for the 0.33(BT)-0.33(2.5NNBT)-0.33(90NNBT) and 0.15(BT)-0.55(85NNBT)-0.30(90NNBT) trilayer systems shown in figures 7.11 and 7.12, respectively. In neither case does the trilayer tan δ exceed that of its individual components, there is no trend. The rule when choosing materials for bi-/multi-layer systems is therefore to choose materials with low tan δ in the temperature range of interest. This has the best possibility to lead to low tan δ in the finished system and is one of the requirement for a competitive device.

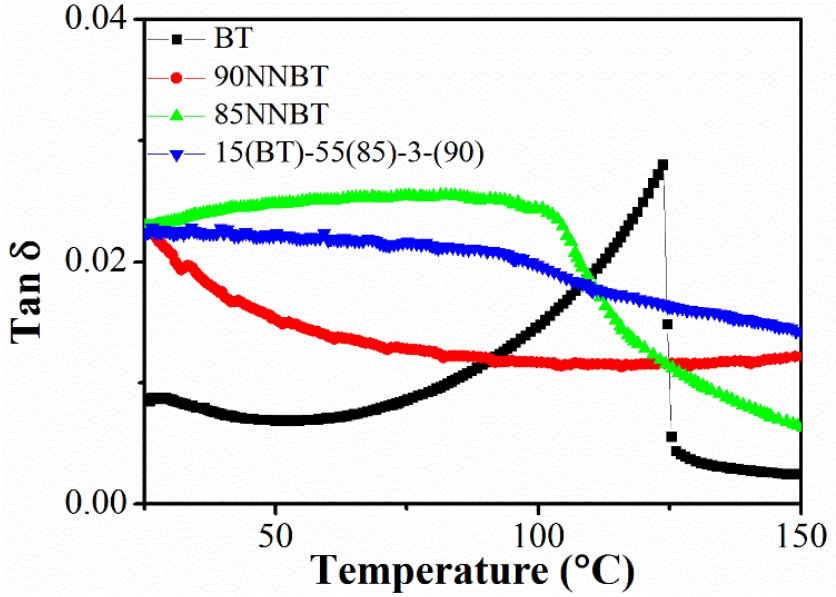

Figure 7.12. Example of tan δ-temperature profiles of a BT-85NNBT-90NNBT trilayer system compared to end members.

7.3.5 Temperature range of interest

The temperature range associated with a low TCC is of significant importance. The outcome of this work has been that it is important to decide on the required temperature range before starting the optimisation. It is very difficult to extend the temperature range of an already optimised system. Materials might have permittivity profiles that suit certain temperature ranges better than others.

The 2.5NNBT-BT bilayer is a good example. In chapter 6 the system was optimised for the temperature range of RT to 125 °C. Extending this temperature range to -55 °C was not possible, as explained in more detail below.

7.3.6 90NNBT *vs.* BT as a core material – the T_C effect

In a 2.5NNBT-BT bilayer, BT proves to be the down fall when attempting to extend the lower temperature range. The reason is the presence of the O-T phase transition around 25 °C as shown in figure 7.13. The relatively sharp and steep change in permittivity at this O-T transition cannot be smoothed enough by the 2.5NNBT permittivity profile, resulting in a TCC larger than ±15 % below this transition.

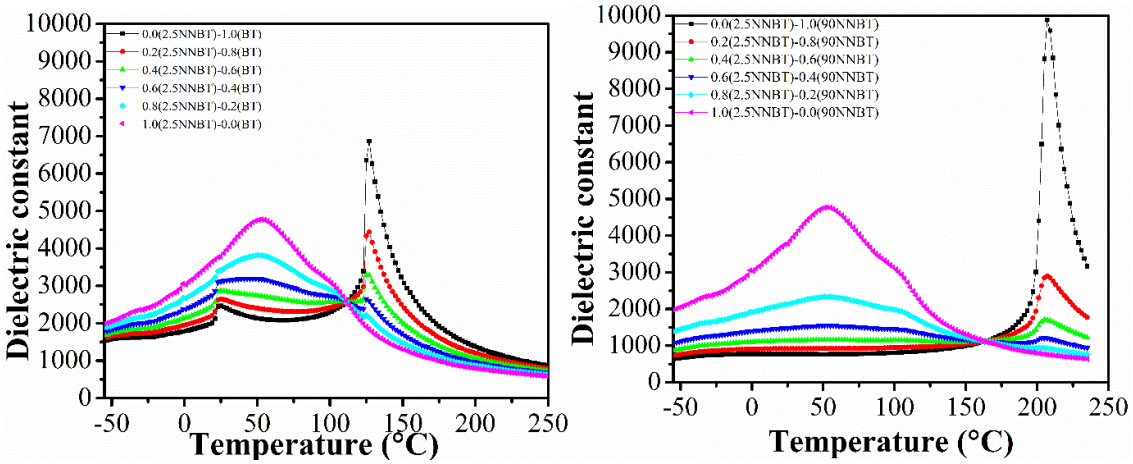

Figure 7.13. Expected changes in predicted permittivity-temperature profiles when substituting BT (left) for 90NNBT (right) in a bilayer with 2.5NNBT.

The main strength of BT above this temperature is its large and reasonably temperature stable plateau, controlling the overall permittivity-temperature stability of the system. Below that temperature BT still dominates, resulting in another fairly stable plateau, as seen in figure 7.13. It is the large shift between these two plateaus that is the issue and results in a TCC greater than 15 % below ~0 °C, as seen in figure 7.14.

The sudden drop in permittivity by ~500 below RT (O-T transition) is significantly larger than the ±15 % allowed by the X7R restrictions on TCC. Figure 7.13 shows that the phase transition even impacts the TCC of bilayers containing very small fractions of BT. Unfortunately, this rules out 2.5NNBT-BT bilayers for industrial applications, as the low temperature range does not adhere to the TCC limitations as seen in figure 7.14.

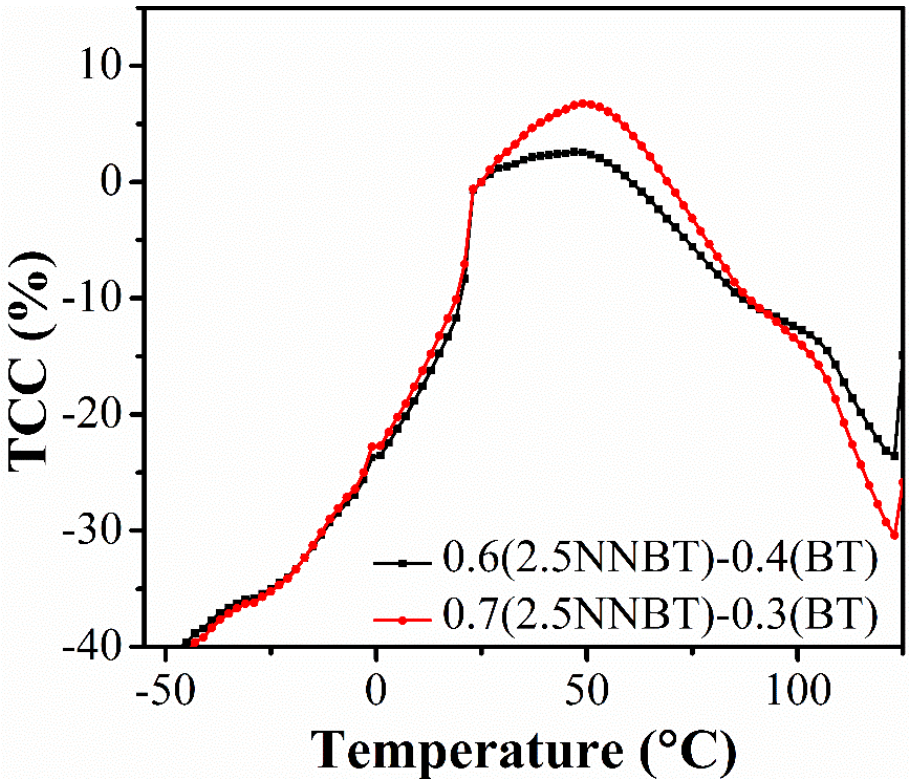

Figure 7.14. Predicted TCC profiles of 2.5NNBT-BT bilayers, highlighting the significant drop in TCC around RT due to the O-T transition in BT.

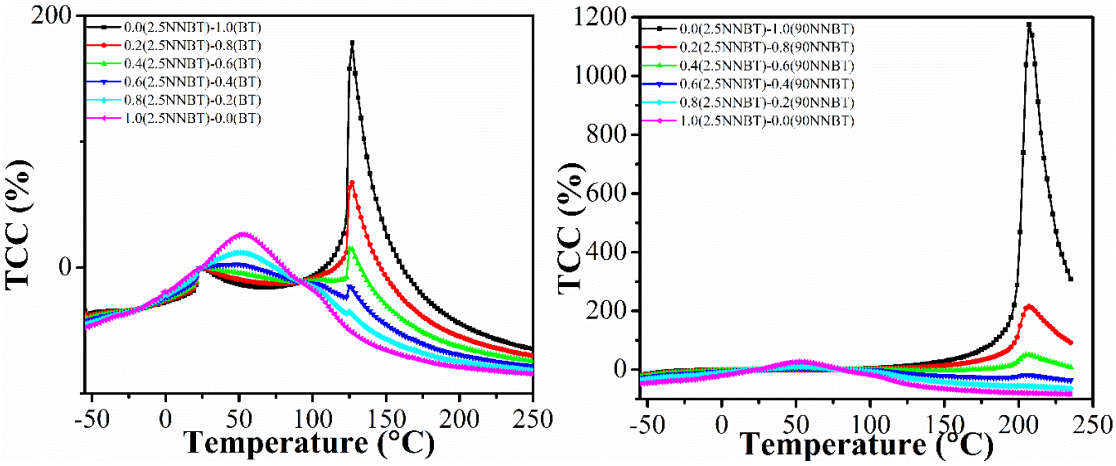

Figure 7.15. Expected changes in predicted TCC-temperature profiles when substituting BT (left) for 90NNBT (right) in a bilayer with 2.5NNBT.

In order to remove this phase transition induced effect, BT needs to be exchanged for a material that possesses a similar permittivity plateau to BT, but does not possess a phase transition in the required temperature range. This description fits 90NNBT, which as discussed previously, possesses an X7R profile on its own merits. However, there is no

phase transition at the lower end and T_C occurs at a significantly higher temperature than that of BT. It is assumed therefore that the switch of BT with 90NNBT will enable an extension of the temperature range of the permittivity plateau in both directions, to lower and higher temperatures, as seen in figures 7.13 and 7.15. However, permittivity will drop significantly compared to the 2.5NNBT-BT bilayer, as 90NNBT has lower RT permittivity. This should not be too problematic, as it is usual in the MLCC industry that capacitors that work to higher temperatures, *i.e.* X8R, have lower RT permittivity.

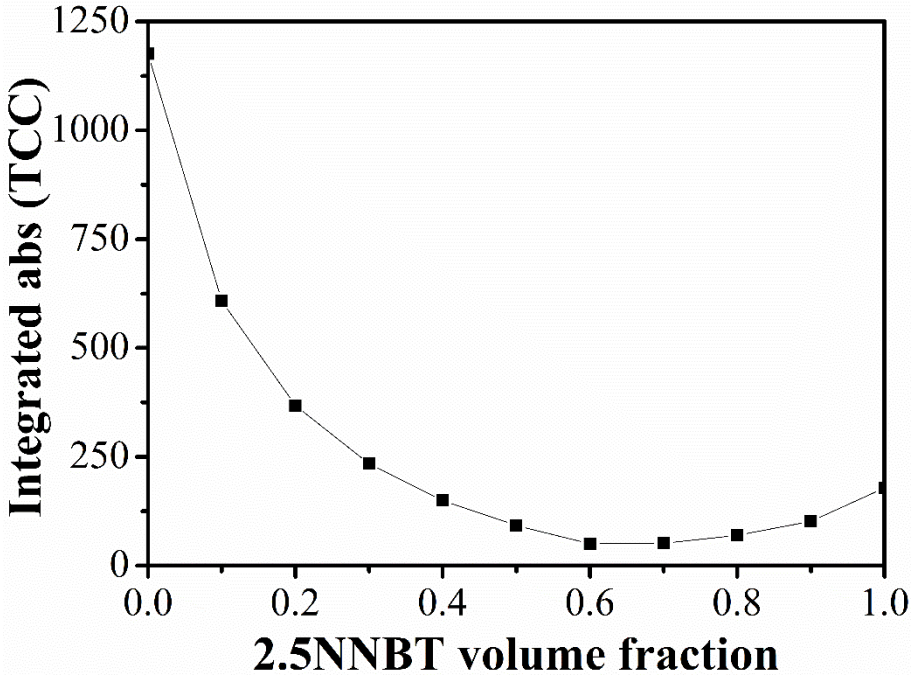

Figure 7.16. The maximum deviation of TCC versus V_f of 2.5NNBT in a 2.5NNBT-90NNBT bilayer for a temperature range of -55 to 250 °C.

Volume fractions play a significant role on the TCC of the bilayer, as shown in figure 7.16. A simple 50:50 ratio could result in a significant optimisation (~25x lower TCC), whilst maintaining a simple volume ratio.

The simulated bilayer can be found in figure 7.17 and shows a RT permittivity of ~1250 and a TCC of ±15 % for the temperature range of ~40 to ~225 °C. Therefore, the suggestion of moving/removing phase transitions for the base-line material has a significant impact on the temperature range.

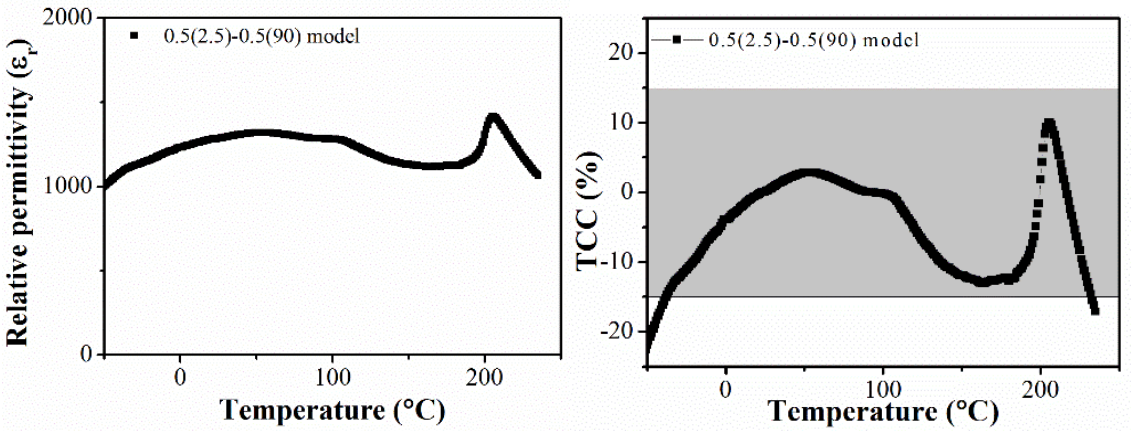

Figure 7.17. Predicted permittivity (left) and TCC (right) profiles for a 0.5(2.5NNBT)-0.5(90NNBT) bilayer.

A small modification in the volume fractions results in a temperature stable plateau at a higher temperature range. As shown in figure 7.18 this bilayer would be temperature stable at ~100 to ~350 °C. This shows that bi-/multi-layer systems might be an interesting way to design capacitors for high temperature applications, without having to rely on Bi or Pb.

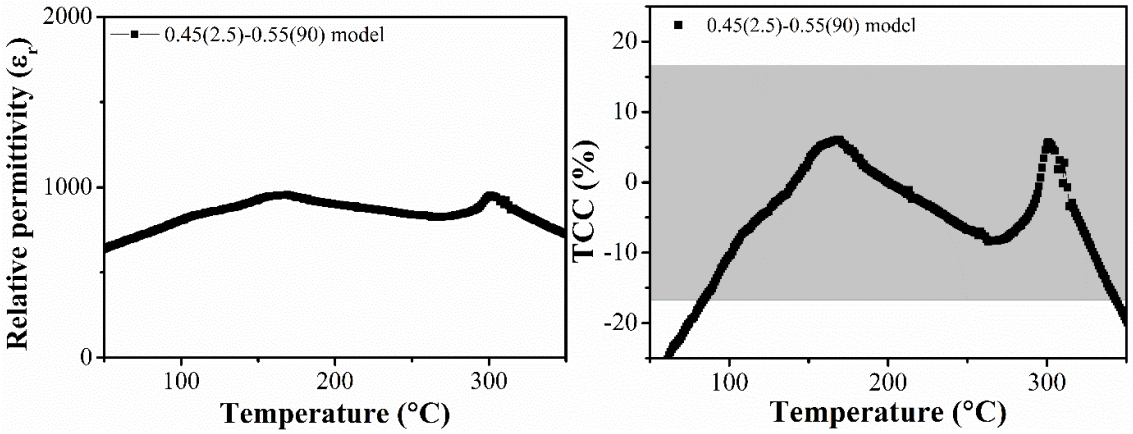

Figure 7.18. Predicted permittivity (left) and TCC (right) profiles for 0.45(2.5NNBT)-0.55(90NNBT) bilayer.

7.3.7 BZT-BT

$BaZr_xTi_{1-x}O_3$ (BZT) is a well-studied solid solution and was chosen to test whether optimisation works for other (i.e. non NN-BT) materials. Three compositions of xBZT were prepared, x = 10, 15, 20 mol%. All were single-phase by XRD, as shown in figure 7.19.

Their permittivity- and tan δ-temperature profiles shown in figure 7.20 show a decrease in T_C with increasing dopant concentration. The relaxor behaviour also increases, with 15BZT showing a similar temperature for T_{max} as 2.5NNBT. The permittivity values for the BZT compositions are significantly higher than those of the NNBT solid solution.

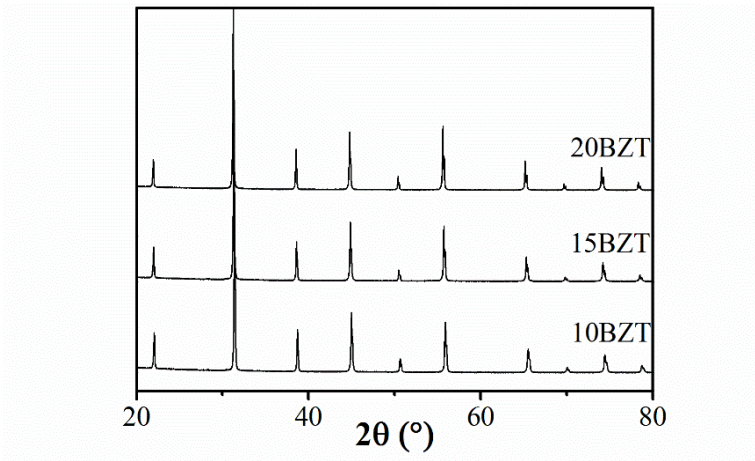

Figure 7.19. XRD patterns of xBZT, 2θ = 20º - 80º, after sintering at 1400 ºC for 8h.

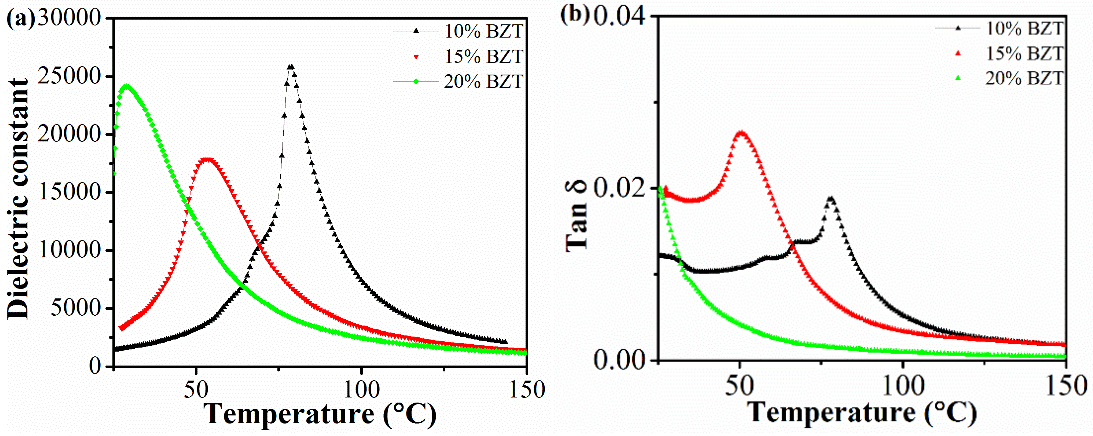

Figure 7.20. (a) Permittivity (100 kHz) vs. temperature profiles and (b) dielectric loss (100 kHz) vs. temperature profiles for xBZT, where x ≤ 20, sintering at 1400 ºC for 8h.

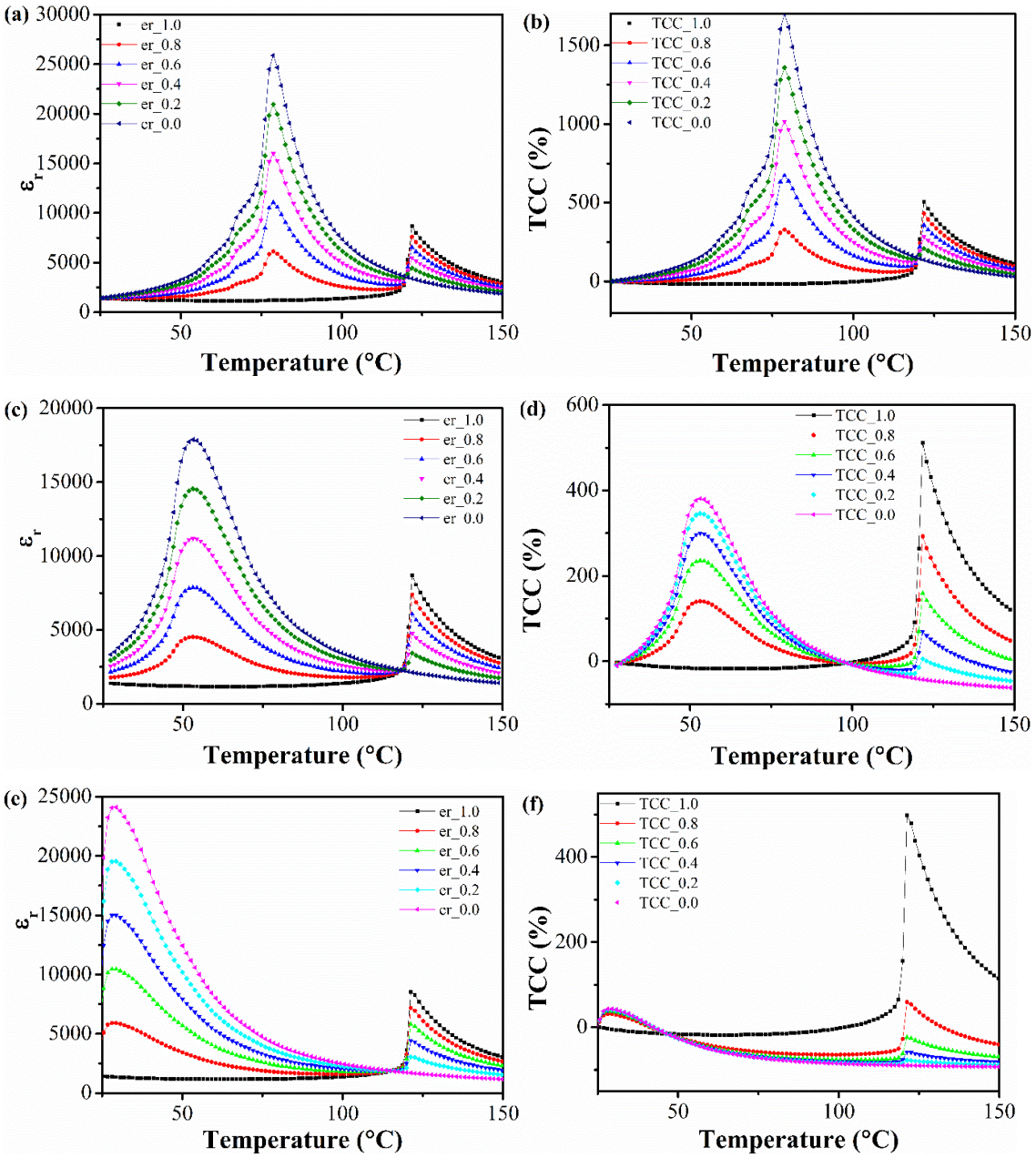

Figure 7.21. Predicted ε_r- and TCC-temperature profiles for xBZT-BT bilayers for a range of CS-ratios, where x = 10 (a, b), 15 (c, d) or 20 (e, f).

The BZT compositions were treated similar to NNBT and the simulated permittivity and TCC profiles for their bilayers are shown in figure 7.21. Figure 7.22 shows the absolute maximum TCC as a function of BT volume fraction for all three bilayer systems. It becomes obvious that the values here are nowhere near as favourable as for the 2.5NNBT-BT or 2.5NNB-90NNBT bilayer systems. However, as observed in figure 7.21,

all three BZT bilayers show significant improvements in TCC, compared to the end members.

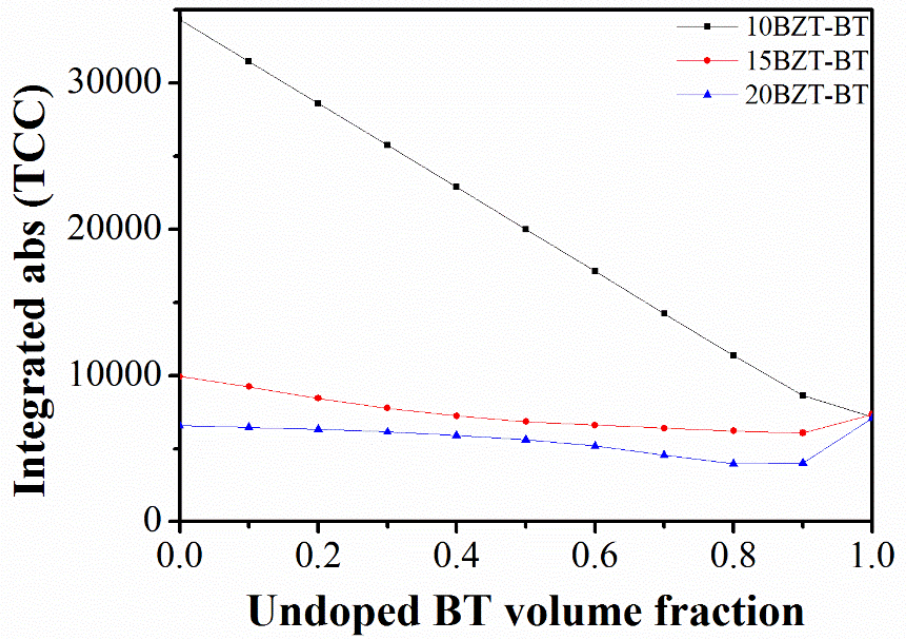

Figure 7.22. The maximum deviation of TCC versus V_f of BT.

Due to its T_{max} being at a similar temperature to 2.5NNBT, 15BZT was chosen to prepare experimental bilayers with BT. The permittivity- and tan δ-temperature profiles are shown in figure 7.23. The bilayers show that small variations in the BZT volume fraction have a significant impact on the overall bilayers 'shell'-dominated half of the profile. This is due to the fact that the permittivity mismatch is a factor of ~10, rather than a factor of ~2, as was the case in the 2.5NNBT-BT bilayers.

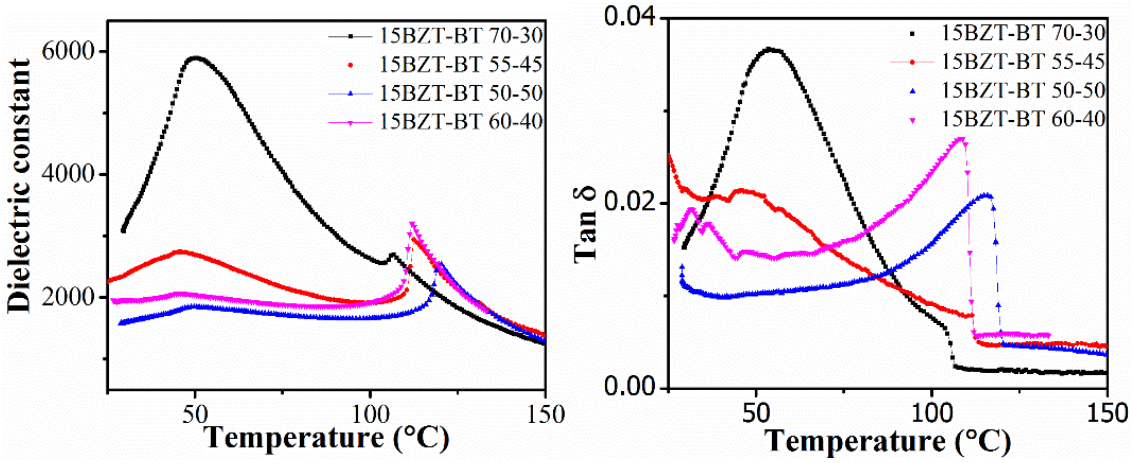

Figure 7.23. Permittivity (left) and tan δ (right) profiles of several 15BZT-BT bilayer systems.

The other problem is that the permittivity maxima of the BZT end member is too large compared to the RT value. This makes it difficult to optimise, as the 15BZT volume fraction dominates TCC, as shown in the 70-30 15BZT-BT bilayer in figure 7.24. Reducing the BZT content in the bilayer improves the optimisation. Improvements can be seen until both permittivity peaks, the one associated with 15BZT and the one associated with BT, are roughly the same magnitude. This is the case for 55-45 15BZT-BT in figure 7.24. Once this point is reached, any deviation from this volume ratio will lead to one of the peaks increasing, depending on the component whose volume fraction is increased. The result of this is that TCC_{max} will increase. This means that 55-45 15BZT-BT is the optimised system for these compositions and shows a TCC of ±25 % from RT to 125 °C. This is outside the ±15 % aimed for, but the improvement in TCC compared to the end members (15BZT: ± ~400 % and BT: ± ~500 %) is significant. Therefore, as another rule, it should be observed that the permittivity maxima of the individual layers should not be too different in magnitude, a 1:1 ratio being best and 1.5:1 being considered a good limit. The temperatures that these maxima lie at plays a significant role, as a T_{max} close to or at RT has a much higher impact on the TCC profile.

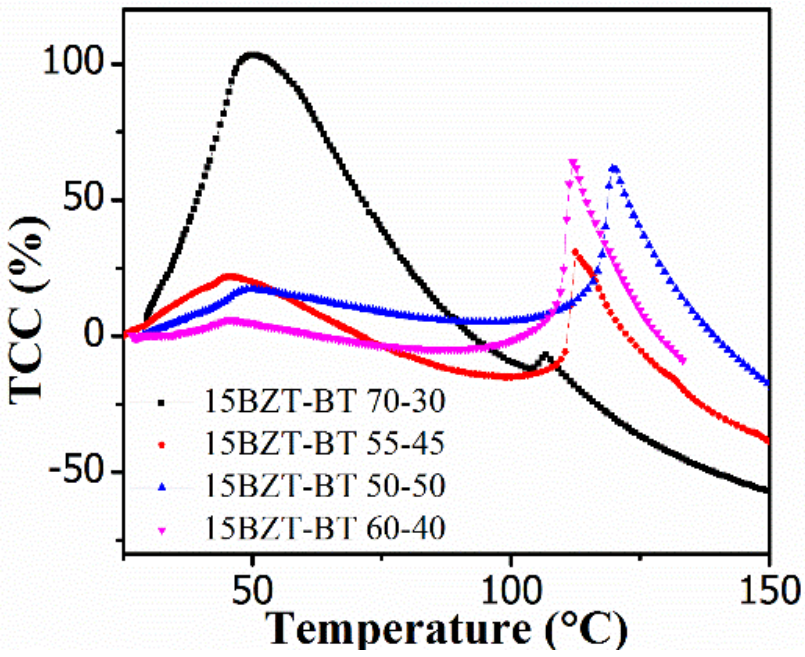

Figure 7.24 TCC profiles of the several 15BZT-BT systems.

7.4 Conclusions

In conclusion, the BZT-BT series showed that mixing of these compositions can also result in significant improvements as TCC for a 15BZT-BT bilayer was shown to improve TCC from several hundred % for the endmembers to just ±25 % for a 55-45 15BZT-BT bilayer. However, the degree of optimisation does not always lead to a TCC of less than ±15 %. In order to achieve these low TCC ranges, it is necessary to choose materials carefully and consider the rules and observations laid out in this chapter. The most important observation to lead to low TCC bilayers is that the permittivity profiles fit better together the closer they are mirror images of each other in the temperature range of interest. This allows for a more easily process-able 50:50 volume ratio.

An important observation is that whilst BT initially seemed to have an excellent profile for a bilayer base-line material, *i.e.* a high permittivity-temperature stable plateau in the range ~ 25 – 100 ^{o}C, the O-T phase transition around RT has a damaging impact on TCC. Similarly, the upper temperature range is limited by a T_C of only 125 °C, which makes obtaining X8R bilayers challenging. 90NNBT with its broader permittivity-temperature plateau with no phase transitions near RT is significantly better suited and increases the temperature range of any bilayer compared to its BT equivalent. The trade-off was found to be the magnitude of the permittivity, as the base value drops from ~3000, in case of the bilayers in chapter 6, down to ~800.

Furthermore, the focus so far has been on bilayered systems. The schematic in figure 7.1 has led to the conclusion that high temperature permittivity-stable capacitors could be obtained by the following process: (i) choose a temperature range, *i.e.* 100-200 °C; (ii) choose a material that possesses a T_C of around 100 °C; (iii) choose a material with T_C a little above 200 °C and (iv) chose a third material that possesses a T_C or T_{max} that sits in the middle of the previous two materials, or has a broad shoulder that spans the gap between the other two T_Cs. As this involves at least three layers, the experimental work for this is the focus of the next chapter, which is based on trilayers.

7.5 References

1 A. J. Moulson and J. M. Herbert, *Electroceramics - Materials, Properties, Applications*, Chapman & Hall, London, 1990.

2 A. G. Serrano, A. L. Bonaventura, R. B. Junior and E. Antonelli, *Mater. Res. Bull.*, 2017, **87**, 34–39.

3 P. Y. Foeller, J. S. Dean, I. M. Reaney and D. C. Sinclair, *Appl. Phys. Lett.*, 2016, **109**, 082904.

Chapter 8: Trilayers and ternary phase diagrams

8.1 Introduction

Previous chapters have limited the multilayer systems to two layers. This chapter deals with the possibility of using three layers. Trilayers are deemed less practical compared to bilayers, as an extra material in the system would involve additional processing as there are now four materials to stack and co-sinter. Nonetheless there are two main points to focus on for this chapter, which build on the previous chapter.

The first point is the difference between the 2.5NNBT-BT and 2.5NNBT-90NNBT bilayers. The BT bilayer has high permittivity but a limited temperature range whereas the 90NNBTR bilayer has an extensive temperature range but significantly lower permittivity. One question is, would adding 90NNBT as a third layer to a 2.5NNBT-90NNBT bilayer expand its temperature range, whilst maintaining a high permittivity value?

The second point of investigation has been hinted at in the conclusion of chapter 7 and is based on figure 7.1. The idea is the creation of a temperature stable system over a temperature range of 100 to 200 °C to test the validity of the set of rules constructed as part of the conclusions in chapter 7. Whilst this is a limited temperature range, it can be seen as proof of concept and if it works wider temperature ranges can be explored in future work.

The three materials for the trilayer are chosen from the material range in this work and their permittivity maxima are within the temperature range required. This is designed to replicate CS-like behaviour, without having to result to 20+ materials as suggested by figure 7.1. High temperature range materials have seen increasing interest in the literature but are mostly based around solid solutions with bismuth-based materials that are unsuitable at ambient conditions.[1–6] Ternary trilayers might offer a bismuth-free alternative to these materials.

8.2 Experimental

The experimental procedures can be found in chapters 3 and 4. The variation is the addition of a third layer but this is the same as described for a second layer in chapter 4.

8.3 Results and discussion

8.3.1 Material choice

The material choices were made by using the materials from the NNBT solid solution, which fit the needs. The first choice was discussed above and simply meant adding 90NNBT to the previous 2.5NNBT-BT bilayer, as this should extend the temperature range of the system and not drop the permittivity as significantly as completely foregoing the BT component in favour of 90NNBT.

The aim for the second objective is a system that is temperature stable between 100 and 200 °C. The strategy here requires a system with at least three components, one with a T_C / T_{max} near 100 °C, one with a T_C / T_{max} of ~200 and one that has a reasonably high permittivity in-between these two temperatures, which emulates a range of T_C / T_{max}. With that in mind and going through the materials prepared for this work, BT, 85NNBT and 90NNBT were chosen as the three materials for the system, as they fit the criterion reasonably well, as shown in figure 8.1.

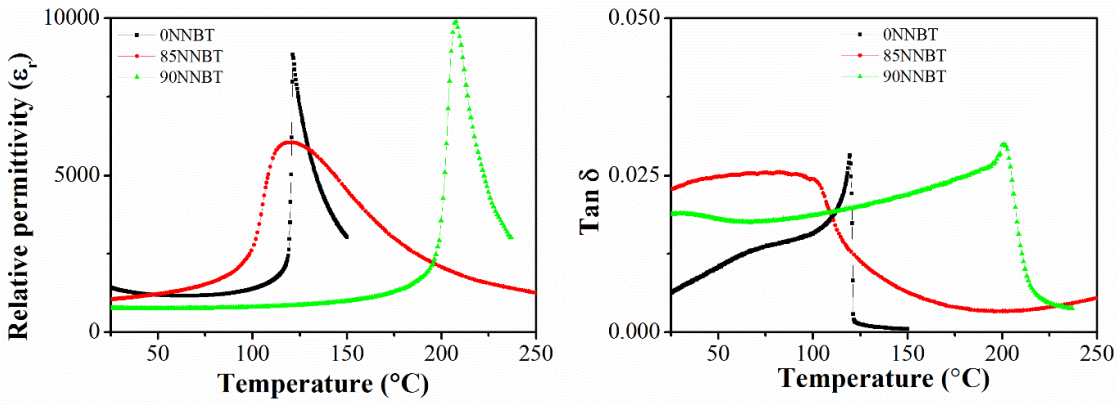

Figure 8.1. Permittivity (left) and tan δ (right) profiles for the end members of the BT-85NNBT-90NNBT trilayer system.

85NNBT has a T_C that is probably just too low and it would be preferable to be around 160 °C, however the broad decline of its profile is nonetheless suitable. All three materials possess low tan δ profiles, which makes it reasonable to expect low tan δ for the trilayer system.

8.3.2 Modelled *vs.* experimental

For the 90NNBT infused 2.5NNBT-BT trilayer, two compositions were prepared and tested. One was a 0.33(BT)-0.33(2.5NNBT)-0.33(90NNBT) volume ratio trilayer and the other a more randomly fabricated trilayer with a volume ratio of 0.106(BT)-0.463(2.5NNBT)-0.431(90NNBT) trilayer.

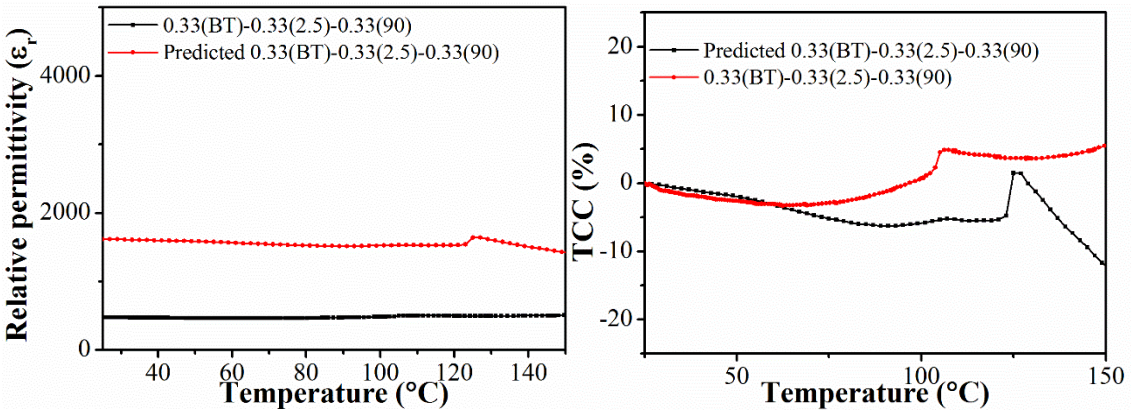

Figure 8.2. Predicted and experimental permittivity- (left) and TCC-temperature (right) profiles for a 0.33(BT)-0.33(2.5NNBT)-0.33(90NNBT) trilayer.

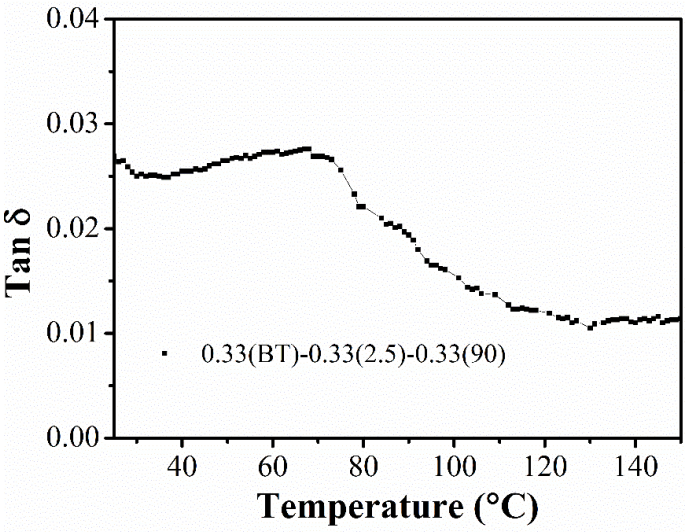

Figure 8.3. tan δ-temperature profile for a 0.33(BT)-0.33(2.5NNBT)-0.33(90NNBT) trilayer.

The experimental and simulated permittivity and TCC profiles for the 0.33(BT)-0.33(2.5NNBT)-0.33(90NNBT) trilayer are shown in figure 8.2. Firstly, there is a

significant drop in permittivity due to the interfaces. This is something that can be overcome by improvements made to the processing/device fabrication procedures. Secondly, the temperature range the system can operate within a ±15 % TCC window has been pushed up to 150 °C. Although in this instance the experimental permittivity is lower than the ~1000 expected for a direct replacement of BT by 90NNBT, the modelled permittivity data shows there is potential for this trilayer to maintain a higher permittivity. Figure 8.3 shows the trilayer is capable of maintaining the low tan δ of its component materials.

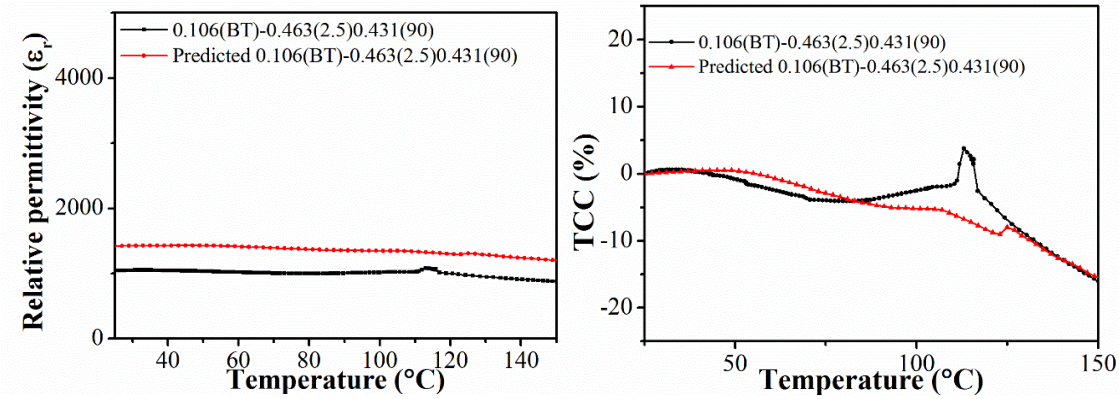

Figure 8.4. Predicted and experimental permittivity- (left) and TCC-temperature (right) profiles for a 0.106(BT)-0.463(2.5NNBT)-0.431(90NNBT) trilayer.

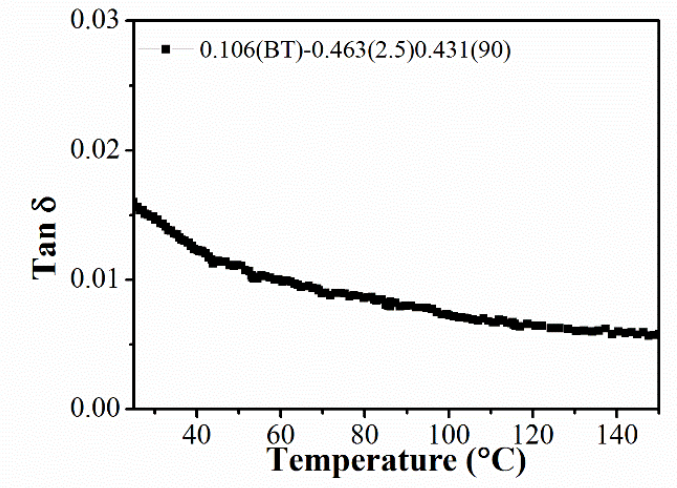

Figure 8.5. tan δ-temperature profile for a 0.106(BT)-0.463(2.5NNBT)-0.431(90NNBT) trilayer.

The simulated and experimental data collected for the 0.106(BT)-0.463(2.5NNBT)-0.431(90NNBT) trilayer are shown in figure 8.4. Again, an interface related drop in permittivity is observed but this is significantly smaller, suggesting a better processed/fabricated device. Once again, the TCC range has been extended to a higher temperature of 150 °C. It appears that extending the TCC beyond that requires removal of BT but since the ~10 vol % BT layer results in a higher permittivity than the system with no BT this is a trade-off that needs to be considered.

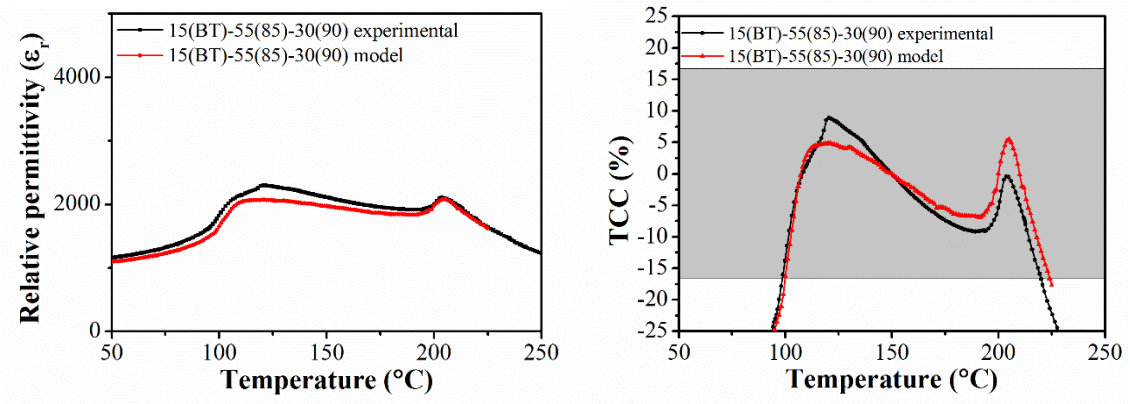

Figure 8.6. Predicted and experimental permittivity- (left) and TCC-temperature (right) profiles for a 0.15(BT)-0.55(85NNBT)-0.30(90NNBT) trilayer.

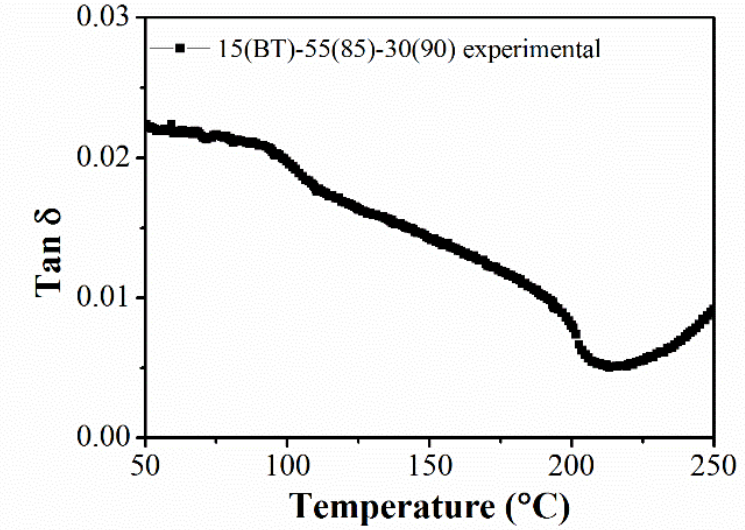

Figure 8.7. tan δ-temperature profile for a 0.15(BT)-0.55(85NNBT)-0.30(90NNBT) trilayer.

The experimental and simulated data for the BT-85NNBT-90NBT trilayer is shown in figure 8.6. The permittivity-temperature profile shows a plateau between ~100 and ~200 °C. The TCC-temperature profile shows the change in permittivity relative to the permittivity at 150 °C. The permittivity changes ~ ±10 % in that temperature range. Figure 8.7 shows the retention of the low dielectric loss of the individual components of the trilayer. Whilst not being as flat a profile as compared to high temperature bismuth-based compositions[2,6], this is an encouraging result. As mentioned previously, the 85NNBT could be replaced with a more suitable material for example a material with the permittivity profile similar to one proposed in figure 8.8. Nonetheless, it offers an alternative bismuth-free way to create temperature stable systems that work at a higher temperature range.

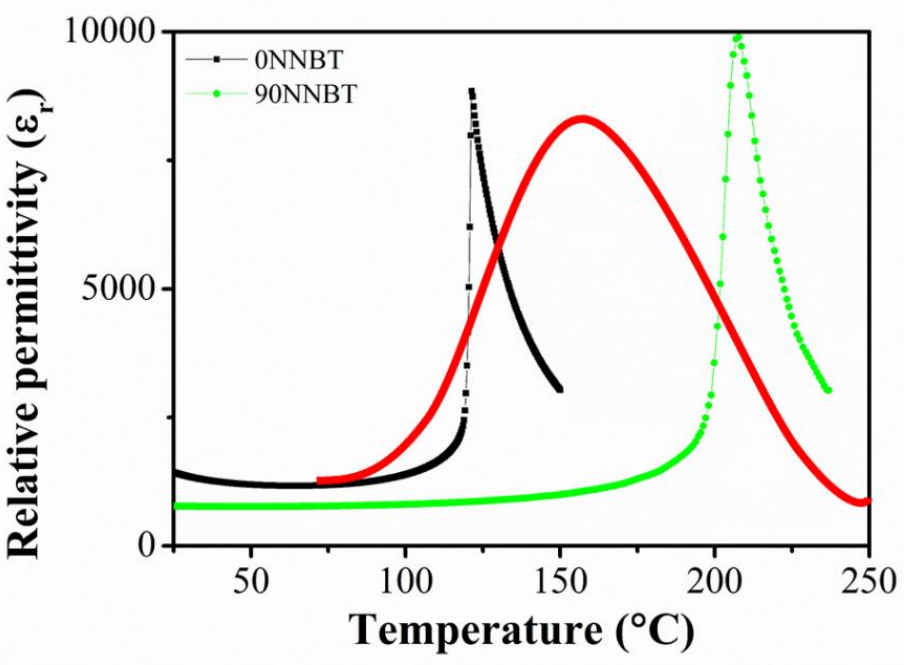

Figure 8.8. Trilayer of BT, 90NNBT and a proposed permittivity profile (red) that would be more ideal for TCC than that of 85NNBT.

8.3.3 Layered *vs.* composites

Similar to the bilayers, there is an argument that composites may be easier to process than trilayers and should therefore be considered, especially as they are the current industry norm. A comparison of a trilayer with its composite equivalent, *i.e.* same quantities of

components used, is shown in figure 8.9. The trilayer clearly shows a flatter permittivity profile, whereas the composite has a lower tan δ. The TCC profiles in figure 8.10 show the composite falls out of the ±15 % specification very quickly. In this particular case, therefore, the trilayer has a significant advantage over the composite system.

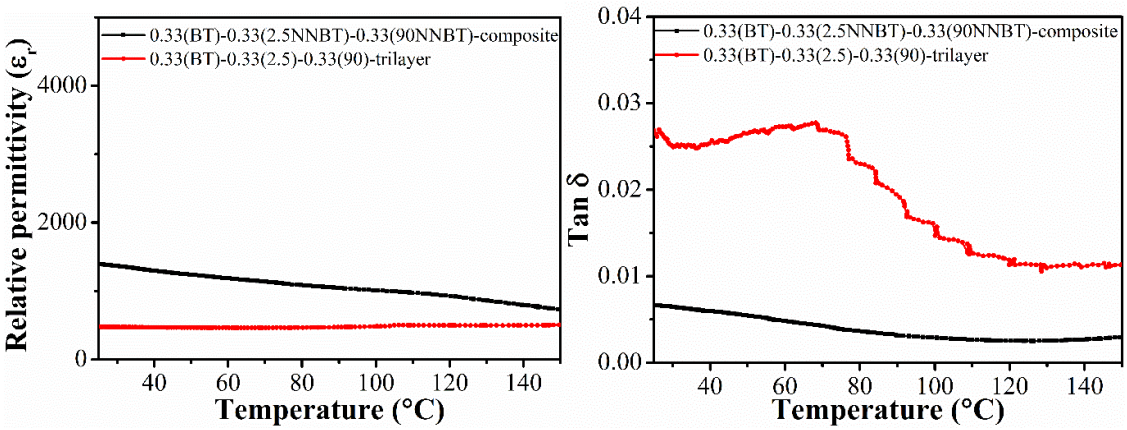

Figure 8.9. Permittivity- (left) and tan δ-temperature (right) profiles for a 0.33(BT)-0.33(2.5NNBT)-0.33(90NNBT) trilayer and an equivalent composite ceramic.

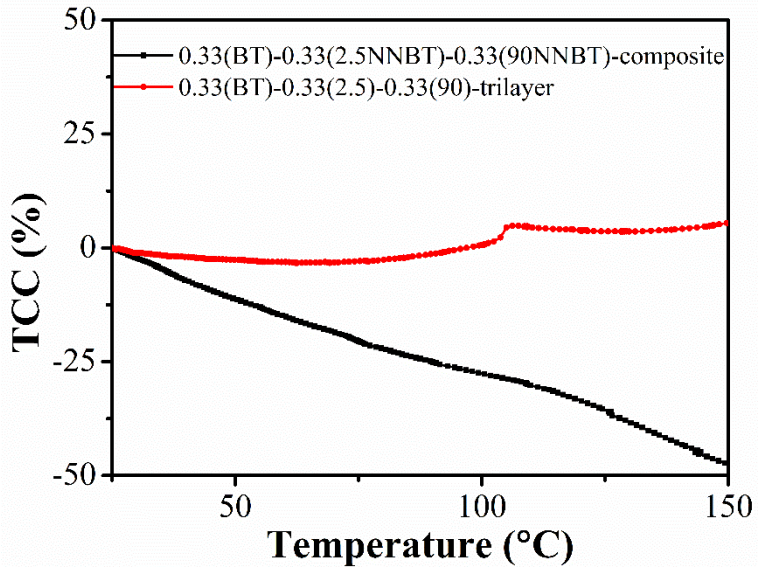

Figure 8.10. TCC-temperature profiles for 0.33(BT)-0.33(2.55NNBT)-0.33(90NNBT) trilayer and an equivalent composite ceramic.

Much of this difference is due to chemical diffusion in the composite ceramic. If this could be controlled/limited in a way that the resulting composite has the same volume

ratio of components as the trilayer then it should show similar temperature stability and would be a better choice in terms of ease of fabrication. To obtain that is a long and repetitious based process, similar to obtaining optimised CS-microstructures for current industrial use.

It is not possible to use the prediction method developed here to optimise composites in an easy fashion compared to the bi-/trilayers. It could, however, be used to predict what kind of composite compositions would be favourable to end up with.

8.3.4 Modelled ternary diagrams

Considering that trilayer systems appear to work as well as bilayers, there was consideration of how to simplify their optimisation. The bilayers optimisation was simplified *via* the maximum |TCC| *vs.* volume fraction of one component. To put that concept to use for a trilayer system, it was combined with the concept of a ternary phase diagram with the result being shown in figure 8.11.

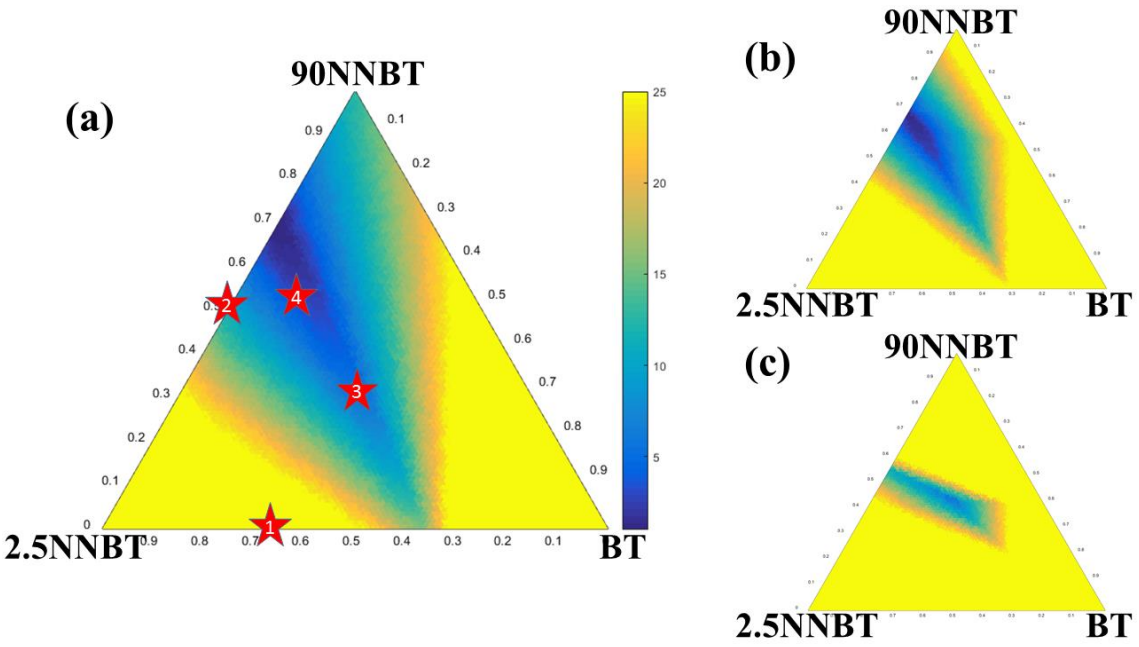

Figure 8.11. Ternary phase diagram for a BT-2.5NNBT-90NNBT trilayer with the TCC over a temperature range of (a) 30 to 125 °C, (b) 30 to 150 °C and (c) 30 to 200 °C. The stars in (a) refer to compositions discussed in (1) Chapter 6, (2) Chapter 7, (3) Chapter 8 and (4) Chapter 8.

Figure 8.11 allows for extracting the volume fractions of the three components and the associated TCC for each possible trilayer system. The volume fractions are extracted from this ternary diagram in the same way as a ternary phase diagram reveals composition. The use of a colour scale allows for the 2D representation of the 3D-TCC map which is created when investigating all possible combinations.

Here it was chosen to use ±25 % as the cut-off point for a useful TCC, *i.e.* all unsuitable materials with TCC ≥ 25% are presented as yellow regions. In contrast, all regions that are a deep blue colour are likely to yield TCCs of ≤ 5 %.

Another factor is the temperature range over which the TCC is determined. Figures 8.11 and 8.12 show the contrast between different temperature ranges. Whilst the former shows the TCC from 30 °C to a changing upper temperature limit, the latter shows the change in TCC for a fixed upper temperature (150 °C) and a changing lower temperature.

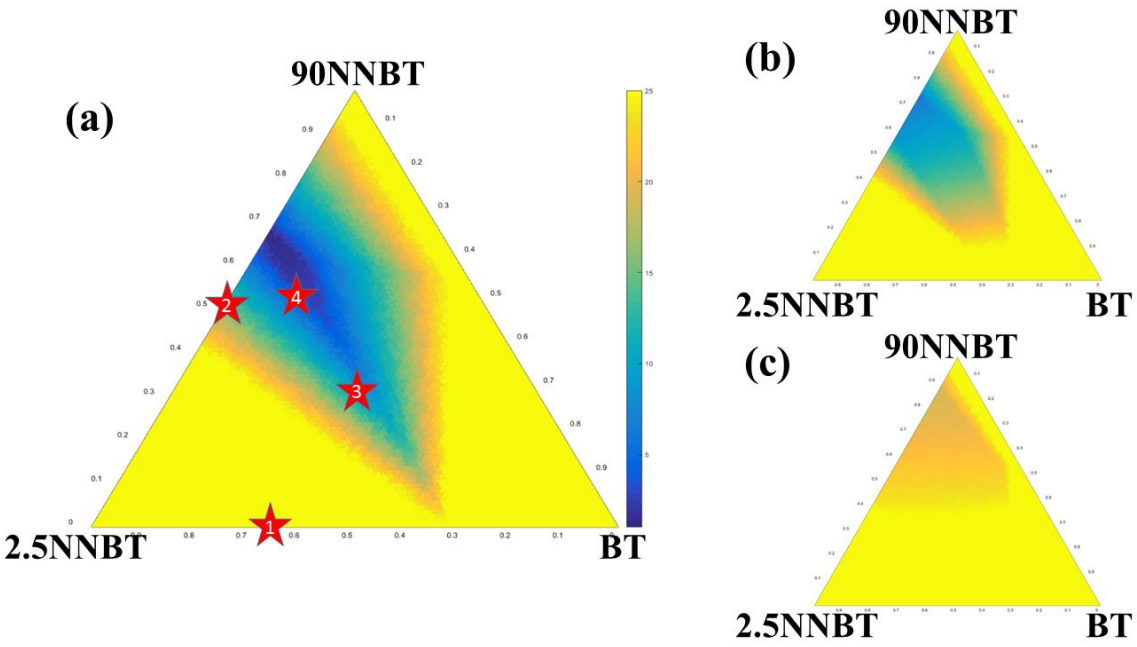

Figure 8.12. Ternary phase diagram for a BT-2.5NNBT-90NNBT trilayer with the TCC over a temperature range of (a) 30 to 150 °C, (b) -30 to 150 °C and (c) -55 to 150 °C. The stars in (a) refer to compositions discussed in (1) Chapter 6, (2) Chapter 7, (3) Chapter 8 and (4) Chapter 8.

8.3.5 Limitations

Limitations for trilayers are mostly processing related. Co-sinterability and chemical compatibility are more difficult to achieve than with a bilayer or composite system. The other limitation is size, as in an MLCC a 'layer' of a trilayer system is likely to be larger than a 'layer' made from a composite.

One limitation that plays a major role to start with is the need for a data-bank for suitable permittivity profiles. This data-bank could also include information like RT permittivity, BME-compatibility, sintering profiles and other processing related information.

8.4 Conclusions

Overall, trilayers have been shown to work similarly well as bilayers. They could be of particular interest for high temperature systems and offer alternatives to the bismuth-based materials that are of current interest.

These trials with trilayers show that multilayer-systems offer quick solutions for any temperature range, as the method mentioned in the previous chapter holds true and temperature stable ranges can be formed by; (i) choosing a temperature range, (ii) choose a material that possesses a T_C or T_{max} close to the low end of the chosen temperature range, (iii) choose a material with T_C or T_{max} a little above the chosen temperature range and (iv) chose at least one material that possesses a T_C or T_{max} mid-range between the previous two materials.

Adapted ternary diagrams can be used to quickly identify material combinations of interest for trilayers and therefore significantly reduce the amount of time and resources required to optimise systems.

8.5 References

1 N. Kumar and D. P. Cann, *J. Mater. Sci.*, 2016, **51**, 9404–9414.

2 N. Kumar, A. Ionin, T. Ansell, S. Kwon, W. Hackenberger and D. Cann, *Appl. Phys. Lett.*, 2015, **106**, 252901.

3 A. Zeb, Y. Bai, T. Button and S. J. Milne, *J. Am. Ceram. Soc.*, 2014, **97**, 2479–2483.

4 A. Zeb and S. J. Milne, *J. Am. Ceram. Soc.*, 2013, **96**, 2887–2892.

5 L. Bisco, F. Zhu, M. B. Ward, J. Li and S. J. Milne, *Acta Mater.*, 2015, **90**, 204–212.

6 A. Zeb and S. J. Milne, *J. Eur. Ceram. Soc.*, 2014, **34**, 1727–1732.

Chapter 9: Industrial Trials

9.1 Introduction

Pre-production trials of multilayer compositions based on the hypotheses presented in this thesis were carried out by AVX Ltd in Coleraine, Northern Ireland. The compositions of the dielectric is commercially sensitive but one layer had a composition close to a typical commercial core whilst the second was similar to a commercially doped-shell composition.

9.2 Experimental

The processing was performed by AVX Ltd. and mostly followed their normal processing route, with the exception of adding in two layers for each dielectric layer, *i.e.* the 'core'- and 'shell' layers.

The general route of preparing MLCCs can be found in the schematic in figure 2.23.[1]

The MLCC prepared are internally labelled as Jobs A-E and due to commercial interests their compositions are kept in confidence. They can be defined as follows:

- Job A possesses a 'shell'-like permittivity profile,
- Job B possesses a 'core'-like permittivity profile,
- Job C is a bilayered MLCC of Job A and B,
- Job D possesses a 'core'-like permittivity profile,
- Job E is a bilayered MLCC of Job A and D.

HALT testing is performed at 278 V and 125 °C.[2,3]

9.3 Results and discussion

The SEM micrograph in figure 9.1.a shows the shell formulation, 9.1.b and 9.1.d the core compositions whereas 9.1.c and 9.1.d show the nominal interface region between the two layer compositions. Figures 9.1a, b and d are typical dense ceramic microstructures with grain sizes varying from 0.25 – 0.75 micron. The 'shell' composition shows the smallest grain size distribution and the smallest grains with core formulations showing a

marginally larger average grain size, especially for Job D. Control of particle size is important, particularly when trying to miniaturise MLCCs. It is noted that figures 9c and d show no evidence of an interface between the two layers, indicating that interdiffusion had occurred during sintering. In previous chapters, homogenisation through diffusion in compositions designed to be core-shell resulted in values of TCC lower than predicted. To eliminate interdiffusion during sintering, it is proposed that floating internal electrodes could be utilised in future studies or if possible the sintering temperature could be decreased.

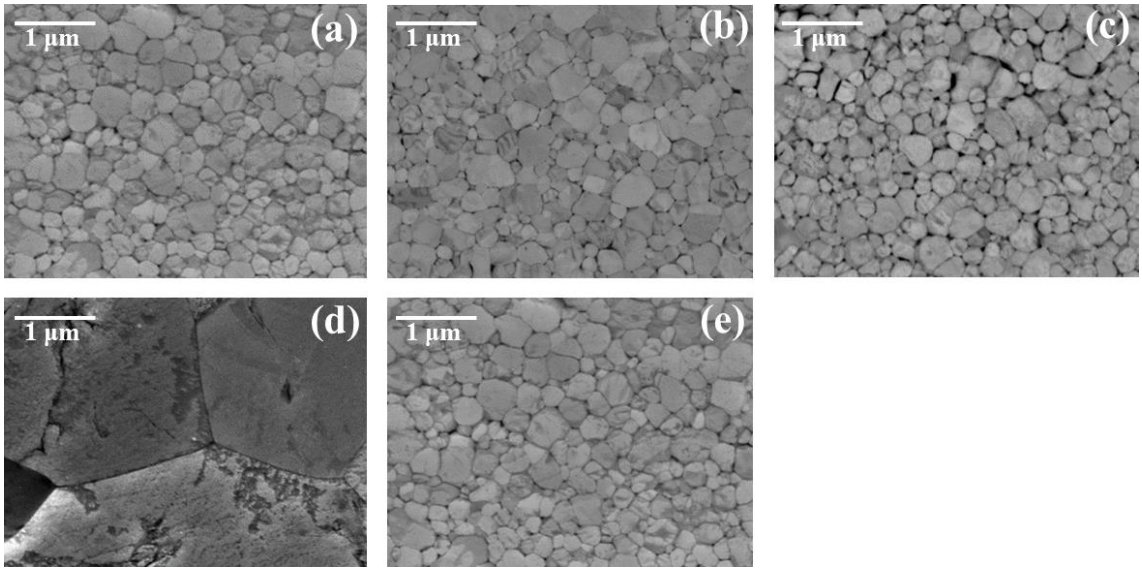

Figure 9.1. Chemically etched SEM micrographs of (a) a 'shell'-like layer Job A, (b) a 'core'-like layer Job B, (c) a bilayer of Job A and B, Job C, (d) a 'core'-like layer Job D and (e) a bilayer of Job A and D, Job E.

Results of the electrical characterisation of Jobs A to E are summarised in table 9.1 and compared with a commercially availabe MLCC equivalent part, Job F. The table shows that there is a significant difference between 'core'- and 'shell'-materials, with the 'core' having a higher permittiivy, (~1400) compared to the 'shell' (~1000). However, the 'core' HALT lifetimes (0.02 and 1.5 hours), differ markedly to those of the 'shell' (>184 h) which showed no evidece of breakdown over the course of the HALT measurements. Bilayer HALT lifetimes are also high, which offers a significant commercial advantage with respect to Job F (16 h) but with no decrease in permittivity.

TCC of the ‘shell’ is -16.48 %, whereas the cores are -14.21 and 462.24 for Jobs B and D, respectively. As a result of the interdiffusion, TCC is not optimised as predicted in the bilayers with Jobs C and E, -16.13 and -17.54 %, respectively. We note that Job C nonetheless shows a comparable TCC to commercialy available Job F.

Table 9.1. Summary of electrical characterisation.

Job	Cap / μF	tan δ	TCC at 125 °C / %	TCC at 150 °C / %	HALT / h
A	0.93	0.71	-16.48	-37.18	>184
B	1.32	1.08	-14.21	-39.57	1.5
C	0.96	0.77	-16.13	-37.51	>184
D	1.48	n/a	462.24	42.85	0.02
E	1.00	0.84	-17.54	-38.77	>184
F	1.03	1.56	-15.9	-39.3	16

9.4 Conclusions

The multilayer methodology hypothesised in this thesis has therefore been shown to have commercial potential for the manufacture of MLCCs. The TCC is similar to commercial systems at AVX Ltd but the HALT lifetime is significantly improved. The predicted improvement in TCC through layering was not however achieved due to interdiffusion of the layers.

9.5 References

1 M.-J. Pan and C. A. Randall, *IEEE Electr. Insul. Mag.*, 2010, **26**, 44–50.

2 J. L. Paulsen and E. K. Reed, *Microelectron. Reliab.*, 2002, **42**, 815–820.

3 *AVX Ltd. Priv. Commun.*

Chapter 10: Conclusions and future work

10.1 Conclusions

This work was conducted to find novel materials and ways to reduce TCC of BT-based systems without the use of RE-dopants, without the need for CS microstructures and to further understand/establish RE-free BT-based materials for MLCC applications.

The NNBT solid solution series provided RE-free components for the bilayer systems as the relaxor properties in that series allow for a range of suitable materials to be selected. The study of this solid solution series revealed that relaxor behaviour can be observed for compositions with at least 2 mol % NN, which is significantly lower than previously reported in the literature.[1,2] The processing conditions chosen for this work induce CS behaviour, which is favourable when trying to obtain temperature-stable permittivity profiles. This means that ferroelectric BT behaviour is found alongside relaxor behaviour in most compositions. The inhomogeneity induced by processing conditions limits any further use for IS analysis, as no observable trends emerge from these kinetically controlled samples.

From the compositions of the NNBT solid solution series 90NNBT stands out, as it possesses an X7R permittivity profile under certain processing conditions. As it is a RE-free material, possesses a low TCC and does not rely on a CS microstructure it essentially fulfils all the aims set out here. The limitation is that its permittivity of ~800 is significantly lower than the target of ~1500 that is generally required.

The first successful bilayer system and proof of concept of layers imitating CS microstructures was a 2.5NNBT-BT system. It possesses a RT permittivity of around 3000 and TCC of ±6 % for a temperature range of 25 to 125 °C, based on a volume ratio of 0.67 2.5NNBT to 0.33 BT. This TCC is significantly below the ±15 % benchmark set for this project. An important point from these initial prototypes was the importance of interfaces on the magnitude of permittivity. Smooth interfaces give higher permittivity than rough interfaces, due to air bubbles/gaps creating regions of low permittivity.

The layering method can improve TCC but the degree of optimisation and the temperature range over which optimisation is achieved can be attributed to several factors. The major factor determining the degree of success is the chosen materials, followed by the number of layers/materials used. A major observation was that BT, whilst an obvious

choice at first due to high permittivity and reasonable permittivity plateau has only a limited degree of success due to its limitation to the temperature range, with the O-T phase transition at around RT and a T_C at only 125 °C. The fact that it keeps the overall permittivity of a system at a high level does not offset this limitation. The result is that for layered systems a lot of compromises in terms of TCC, permittivity, temperature range and number of materials need to be found. Once these compromises are identified it is a very reliable method.

Trilayers were found to offer decent compromises. They still possess a low number of materials in an attempt to keep processing simple and the temperature range is significantly more variable than in bilayers. Temperature stable ranges can be formed by; (i) choosing a temperature range, (ii) choose a material that possesses a T_C close to the low end of the chosen temperature range, (iii) choose a material with T_C a little above the chosen temperature range and (iv) choose at least one material that possesses a T_C mid-range between the previous two materials. This was shown to work, resulting in trilayer systems with a TCC of ±15 % in temperature ranges of 25 – 150 °C (ε_r ~ 1000) and 100 - 225 °C (ε_r ~ 2000). Adapted forms of ternary phase diagrams can be used to visualise the TCC optimisation of trilayer systems. It was however also shown that composites of the trilayers do not work based on the given prediction model.

Initial industrial results from AVX Ltd. have shown that bilayers can create competitive devices, even though the initial TCC optimisation was limited due to higher than expected inter-diffusion of the two layers. Lifetime of the devices was improved compared to commercial ones. Limiting the diffusion will be an objective going forward with this work.

10.2 Future work

The results obtained for this work open up a range of questions and therefore lead to a variety of future work that should be considered to further the understanding of the materials and to improve the solutions discussed previously.

Firstly, the permittivity profiles of the NNBT solid solution exhibit clear signs of a CS microstructure. TEM should be carried out on these samples to confirm the CS. Furthermore, the same compositions should be processed so that the samples obtain a

thermodynamically controlled state, which should yield more information when further IS is carried out.

There is more work to be done for the 90NNBT samples as MLCC prototypes should be fabricated and tested. This can be done for a range of electrodes to obtain an idea of its suitability for these metals. This includes the Li-coated Ni-electrodes discussed in chapter 5, as they would be the cheapest and therefore most favourable option. More work should also go into the analysis of the secondary phases obtained under varying processing conditions and their effects on the materials. This includes further investigation into the ionic conduction observed for 90NNBT.

Whilst the first bilayer system showed a very low TCC over the studied temperature range, it is necessary to look at other materials to extend this temperature range. This was partly achieved in this work, however other alternatives should be investigated in the future. Furthermore, more work should be carried out to investigate interfaces and pores and their effects on permittivity and breakdown of devices, as the results here showed that they clearly play a significant role. MLCC prototypes would be best suited for this, as they incorporate the processing and organic and glass components used in industry, making the results more relevant and significant.

Future work on the trilayer systems should include the investigation of broader temperature ranges than the ones reported here. This is important particularly for high temperature capacitors to make them competitive with Bi-containing systems. Other work should include constructing MLCC prototypes and potentially a way to predict the change from a trilayer to a composite. Cold sintering of the composites might provide a way forward for this, as it might limit the diffusion significantly enough for this to work.[3–7]

10.3 References

1 D. Kwon, Y. Goh, D. Son, B. Kim, H. Bae, S. Perini and M. Lanagan, *J. Electroceramics*, 2016, **45**, 631–638.

2 J. T. Zeng, K. W. Kwok and H. L. W. Chan, *J. Am. Ceram. Soc.*, 2006, **89**, 2828–2832.

3 H. Guo, J. Guo, A. Baker and C. A. Randall, *ACS Appl. Mater. Interfaces*, 2016,

8, 20909–20915.

4 H. Guo, A. Baker, J. Guo and C. A. Randall, *ACS Nano*, 2016, **10**, 10606–10614.

5 J. Guo, A. L. Baker, H. Guo, M. Lanagan and C. A. Randall, 2016, **7**, 1–7.

6 S. Funahashi, J. Guo, H. Guo, K. Wang, A. L. Baker, K. Shiratsuyu and C. A. Randall, *J. Am. Ceram. Soc.*, 2016, **100**, 491–495.

7 J. Guo, H. Guo, A. L. Baker, M. T. Lanagan, E. R. Kupp, G. L. Messing and C. A. Randall, *Angew. Chem. Int. Ed.*, 2016, **55**, 11457–11461.